



Switching and magnetic properties of spin-crossover molecule/metal interfaces

Massine Kelai

► To cite this version:

Massine Kelai. Switching and magnetic properties of spin-crossover molecule/metal interfaces. Condensed Matter [cond-mat]. Université Paris Cité, 2022. English. NNT: 2022UNIP7002 . tel-03684151

HAL Id: tel-03684151

<https://theses.hal.science/tel-03684151>

Submitted on 1 Jun 2022

HAL is a multi-disciplinary open access archive for the deposit and dissemination of scientific research documents, whether they are published or not. The documents may come from teaching and research institutions in France or abroad, or from public or private research centers.

L'archive ouverte pluridisciplinaire **HAL**, est destinée au dépôt et à la diffusion de documents scientifiques de niveau recherche, publiés ou non, émanant des établissements d'enseignement et de recherche français ou étrangers, des laboratoires publics ou privés.

Université Paris Cité

École doctorale Physique en Île-de-France (ED564)

Laboratoire Matériaux et Phénomènes Quantiques, CNRS UMR 7162

Switching and Magnetic Properties of Spin-Crossover Molecule/Metal Interfaces

Par Massine KELAI

Thèse de doctorat de *physique de la matière condensée*

Dirigée par Vincent REPAIN

Présentée et soutenue publiquement le 28 Mars 2022

Devant un jury composé de :

Manuel GRUBER, professeur associé, Université Duisburg-Essen, Rapporteur.

Maciej LORENC, directeur de recherche, Université de Rennes 1, Rapporteur.

Delphine CABARET, professeur des universités, Sorbonne Université,
Examinatrice.

Wolfgang KUCH, professeur des universités, Université libre de Berlin,
Examineur.

Amandine BELLEC, chargé de recherche, Université de Paris, membre invité.

RÉSUMÉ

Les molécules de type Spin-Crossover sont une classe importante de matériaux de commutation multifonctionnels qui changent de manière réversible leur état de spin, de l'état bas spin à l'état de haut spin, et de nombreuses autres propriétés physiques : optiques, magnétiques, conductivité et propriétés mécaniques, lors d'une perturbation externe. En raison de leur multifonctionnalité et de la bistabilité dérivant de l'existence de deux états de spin, les molécules SCO ont été proposées comme blocs de construction prometteurs pour une variété d'applications technologiques telles que le stockage d'informations, les capteurs, l'affichage numérique, etc. Cependant, l'incorporation d'un tel matériau dans des dispositifs à l'échelle nanométrique nécessite une compréhension approfondie des propriétés de transition de spin pour les couches moléculaires déposées sur divers substrats. Ces dernières années, des physiciens et des chimistes ont déployé des efforts considérables pour synthétiser des SCO évaporables sous vide qui peuvent être déposés sur des surfaces et pour caractériser la transition de spin sur les surfaces, sous l'effet de divers stimuli externes. Les travaux sur les couches ultra-minces de SCO sur des métaux, ferromagnétiques ou non, sont cependant assez rares, en raison de la fragilité de ces molécules qui peuvent subir une décomposition et/ou un blocage d'état de spin lorsqu'elles sont adsorbées sur des surfaces. Au cours de ce travail de thèse, nous avons principalement utilisé les molécules $\text{Fe}(3,5-(\text{CH}_3)_2\text{pz})\text{BH}_2$ qui sont l'une des seules molécules SCO actives évaporables sous vide sur substrat métallique. La question centrale de ce travail est la suivante : Comment la transition de spin et les propriétés magnétiques de la molécule $\text{Fe}(3,5-(\text{CH}_3)_2\text{pz})\text{BH}_2$ sont-elles modifiées en contact avec des surfaces métalliques, semi-métalliques et ferromagnétiques ?

Le premier chapitre de la thèse est consacré à la présentation des molécules SCO. Dans la première partie, la commutation induite par la chaleur, la lumière et les rayons X pour les molécules en vrac est détaillée. Dans la seconde partie, nous discutons, molécule par molécule, les avancées réalisées ces dernières années dans le domaine des SCO évaporables sous vide sur surface, des films épais aux films ultraminces.

Pour ce travail de thèse, nous avons principalement utilisé deux techniques expérimentales complémentaires, à savoir la spectroscopie d'absorption des rayons X (XAS) et la microscopie à effet tunnel (STM) qui sont présentées dans le deuxième chapitre. Nous présentons également la molécule que nous avons utilisée et d'autres aspects techniques comme la préparation du substrat, les techniques de dépôt de la molécule et du métal sous ultravide.

Les résultats obtenus au cours de ce travail de thèse sont décrits dans les quatre derniers chapitres. Nous nous intéresserons tout d'abord aux propriétés de commutation thermique (chapitre 3) et induite par la lumière (chapitre 4) du $\text{Fe}(3,5-(\text{CH}_3)_2\text{pz})\text{BH}_2$ adsorbé soit sur des substrats métalliques soit sur HOPG. Nous discuterons ensuite dans le chapitre 5 de l'anisotropie magnétique des molécules de $\text{Fe}(3,5-(\text{CH}_3)_2\text{pz})\text{BH}_2$ dans des films moléculaires 2D adsorbés sur Cu(111). Enfin, nous ferons état dans le chapitre 6 de leur adsorption et de leur couplage sur des substrats ferromagnétiques

Mots-clés : Spin-Crossover, Magnétisme Moléculaire, Magnétisme, Spectroscopie d'Absorption de Rayons X, Dichroïsme Circulaire Magnétique des Rayons X, Synchrotron, Microscopie à effet Tunnel, Spintronique, Spintronique Moléculaire, Electronique Moléculaire, Couches Ultraminces, Physique des Surfaces.

Spin-crossover (SCO) molecules are an important class of multifunctional switching materials that change reversibly their spin-state from low spin (LS) to high spin (HS) states, and many other physical properties: optical, magnetic, conductivity and mechanical properties, upon external perturbation. Due to their multifunctionality and the bistability deriving from the existence of two spin-states, the SCO molecules have been proposed as promising building blocks for a variety of technological applications such as information storage, sensors, digital display, and so on. However, the incorporation of such a material in nanoscale devices requires a deep understanding of the spin transition properties for molecular layers deposited on various substrates. In the last years, a considerable effort was made by physicists and chemists to synthesize vacuum-evaporable SCO which can be deposited on surfaces and also to characterize the spin transition on surfaces, under various external triggers. Works on ultrathin SCO layers on metals, ferromagnetic or not, are however rather scarce, due to the fragility of such molecules which can undergo a decomposition and/or a spin-state blocking when adsorbed on surfaces. During this thesis work, we mainly used $\text{Fe(3,5-(CH}_3)_2\text{pz)BH)}_2$ molecules which are one of the only reported active vacuum-evaporable SCO molecule on metallic substrate. The central question of this work is: How the spin transition and the magnetic properties of the $\text{Fe(3,5-(CH}_3)_2\text{pz)BH)}_2$ molecule are modified in close contact with metallic, semi-metallic and ferromagnetic surfaces ?

The first chapter of the thesis is dedicated to the presentation of SCO molecules. In the first part, the thermal-, light- and X-ray-induced switching for molecules in bulk is detailed. In the second part, we discuss, molecule by molecule, the advances made in the recent years in the field of vacuum-evaporable SCO on-surface, from thick films to ultrathin films.

For this thesis work, we mainly used two complementary experimental techniques, namely X-ray absorption spectroscopy (XAS) and Scanning Tunneling Microscopy (STM) which are presented in the second chapter. We also present the molecule we have used and other technical aspects like the substrate preparation, molecule and metal deposition techniques under ultrahigh vacuum.

The results obtained during this thesis work are described in the four last chapters. We will first focus on the thermal- (chapter 3) and light-induced (chapter 4) switching properties of $\text{Fe(3,5-(CH}_3)_2\text{pz)BH)}_2$ adsorbed either on metallic substrates or on HOPG. We will then discuss in chapter 5 the magnetic anisotropy of the $\text{Fe(3,5-(CH}_3)_2\text{pz)BH)}_2$ molecules in 2D molecular films adsorbed on Cu(111). Finally, we will report in chapter 6 on their adsorption and coupling on ferromagnetic substrates.

Keywords : Spin-Crossover, Molecular Magnetism, Magnetism, X-ray Absorption Spectroscopy, X-ray Magnetic Circular Dichroism, Synchrotron, Scanning Tunneling Microscopy, Spintronics, Molecular Spintronics, Molecular Electronics, Thin Films, Surface Physics.

Le développement de nouvelles technologies et de nouveaux dispositifs découle de la compréhension des propriétés des matériaux à l'échelle du nanomètre. Dans la recherche actuelle dans le domaine du magnétisme, exploiter le spin de l'électron ainsi que de ses degrés de liberté externes (la charge), nous permet d'introduire de nouvelles fonctionnalités, nous appelons cette nouvelle électronique : l'électronique de spin ou spintronique. Elle offre de nouvelles applications qui ont révolutionné le stockage et le traitement de l'information, comme les valves de spin ou les jonctions tunnel magnétiques. Historiquement, les matériaux utilisés pour la spintronique sont inorganiques (métaux ou semi-conducteurs). Ainsi ces systèmes suscitent un grand intérêt de la part des communautés de physiciens et de chimistes. A cet égard, les jonctions hybrides de type molécules magnétiques-métal sont des candidats intéressants pour trouver de nouvelles propriétés et les modular à l'échelle du nanomètre. En effet, il a déjà été démontré que des molécules pouvaient s'hybrider avec des métaux, ce qui peut conduire à de nouvelles fonctionnalités aux interfaces de ces nanostructures. De plus, les développements récents dans le domaine de la spintronique organique montrent la possibilité de créer des dispositifs spintroniques efficaces avec différents types de molécules organiques. Par exemple, Mannini *et al.* ont observé sur l'aimant moléculaire unique (SMM pour *single molecular magnet*) Fe_4C_5 sur Au(111), l'ouverture d'un cycle d'hystérésis magnétique à 0.5 K et qui témoigne de la manifestation d'effets de mémoire magnétique dus à une dynamique de relaxation de spin lente. Un autre type de complexe est prometteur, les composés dits molécules à transition de spin (SCO pour *Spin-Crossover molecules*). Il s'agit de matériaux dont l'état de spin passe de manière réversible d'un état bas spin (LS) à un état haut spin (HS), et de nombreuses autres propriétés physiques : optiques, magnétiques, conductivité et mécaniques, lors de l'application d'une perturbation externe. En raison de leur multifonctionnalité et de la bistabilité dérivant de l'existence de deux états de spin, les molécules SCO ont été proposées comme blocs de construction prometteuses pour une variété d'applications technologiques telles que le stockage d'informations, les capteurs, l'affichage numérique, etc. En outre, et dans la perspective de la miniaturisation des dispositifs, l'utilisation de ce type d'interfaces nécessite une compréhension approfondie des propriétés de transition de spin de la molécule déposée sur un substrat par rapport à la même molécule en volume. Ces dernières années, un effort considérable a été fait par les physiciens et les chimistes pour synthétiser des SCO évaporables sous vide qui peuvent être déposés sur des surfaces et aussi pour caractériser la transition de spin sur les surfaces, sous différents stimuli externes. Cependant, il n'y a pas beaucoup de littérature qui témoigne de la préservation de la propriété SCO sur des substrats métalliques en raison de l'interaction avec le substrat, et qui conduit à la fragmentation ou au blocage de l'état de spin de la majorité des composés SCO. La seule molécule SCO active et évaporable sous vide sur un substrat métallique est celle que nous allons étudier au cours de cette thèse, à savoir le complexe $\text{Fe}((3,5-(\text{CH}_3)_2\text{Pz})_3\text{BH})_2$, prononcé *Fer-pyrazolyl-dimethyl-borate*. Tout au long de cette thèse, la question centrale qui est question adressée : Comment la transition de spin et les propriétés magnétiques du $\text{Fe}((3,5-(\text{CH}_3)_2\text{Pz})_3\text{BH})_2$ sont modifiées en contact étroit avec des surfaces métalliques, semi-métalliques et ferromagnétiques ?

Le premier chapitre de la thèse est consacré à la présentation des propriétés des systèmes spin-crossover (SCO), du bulk à l'échelle de la molécule unique sur différentes surfaces. Nous commencerons par une description détaillée du mécanisme de base de la commutation induite par la température, la lumière et les rayons X. En ce qui concerne la transition thermique, nous montrerons un modèle thermodynamique simple à l'échelle de la molécule unique. Ensuite, nous montrerons dans le cadre d'un modèle de champ moyen, comment

les effets coopératifs transforment la transition thermique. En ce qui concerne la commutation induite par la lumière (ou LIESST pour *Light-Induced Excited Spin-State Trapping*), le mécanisme de transition d'un état à l'autre, ainsi que la relaxation de l'état photoexcité à l'état fondamental seront discutés. De plus, l'influence des paramètres structuraux des molécules sur les propriétés de transition (transition thermique, relaxation de l'état photo-induit) sera discutée. Cette partie se terminera par l'étude d'un type spécial de bistabilité, l'hystérésis thermique induite par la lumière (LITH). Nous verrons précisément que cet effet provient de la compétition entre deux effets cinétiques différents conduisant à une bistabilité autour de la température de relaxation pour les systèmes SCO à haute coopérativité. La deuxième partie du chapitre présente une couverture exhaustive des avancées réalisées dans le domaine des SCO évaporables sous vide en surface, des films épais aux films ultramincés. Nous discutons, molécule par molécule, les différentes études qui montrent comment les propriétés thermiques et photo-induites sont modifiées à des dimensions réduites. La commutation induite par la tension électrique sera également présentée, pour des molécules uniques. Une attention particulière sera accordée aux substrats métalliques et au graphite, puisque ce sont les substrats les plus utilisés dans cette thèse. De plus, le couplage magnétique entre les molécules et le substrat ferromagnétique sera discuté.

Afin d'étudier l'interface entre les molécules et le substrat, deux techniques expérimentales sont principalement utilisées, à savoir la spectroscopie d'absorption des rayons X (XAS) et la microscopie à effet tunnel (STM). En effet, la XAS nous permet de caractériser en temps réel l'évolution de la propriété de transition de spin sous une perturbation externe et d'accéder aux propriétés globales du matériau. Au contraire, la STM est une technique de champ proche qui permet d'accéder aux propriétés locales et permet également de suivre dans l'espace réel la transition de spin. Le chapitre 2 se concentrera sur une présentation générale des molécules, de la théorie et des aspects expérimentaux de la XAS et de la STM et se terminera par la préparation du substrat, les techniques de dépôt de molécules et de métaux sous ultravide (UHV). Tout d'abord, nous nous concentrons sur la présentation des différentes molécules inorganiques que nous allons étudier dans ce travail, à savoir, $\text{Fe}((3,5\text{-(CH}_3)_2\text{Pz)}_3\text{BH})_2$ et $\text{Fe}((3\text{-(Phen)Pz)}_3\text{BH})_2$. La première nommée est la molécule SCO qui sera étudiée dans tous les chapitres, tandis que la seconde est une molécule HS à toutes les températures et sera étudiée dans le chapitre 5. Par des arguments thermodynamiques, nous verrons pourquoi la denticité de ces molécules en font des candidats idéaux pour les études sur les surfaces. Ensuite, nous discuterons de leur structure moléculaire ainsi que les propriétés induites par la lumière, la température et LITH sous forme de poudre. Ensuite, nous décrirons la théorie du XAS en mettant l'accent sur la théorie des multiplets (LFM pour *ligand field multiplet*). En partant de l'hamiltonien quantique à N corps en seconde quantification, nous nous concentrerons sur la description de chaque terme et dériverons les quantités d'intérêt pour la compréhension des spectres XAS. L'objectif est de pouvoir simuler les spectres XAS des seuils $L_{2,3}$ de l'ion Fe^{II} , et qui seront utilisés pour caractériser macroscopiquement la transition de spin. Nous présenterons également le programme *QUANTY*, qui est un programme de calculs quantiques, réalisé en LUA, et capable de calculer des spectres XAS et autres types de spectroscopies des niveaux de cœur. Afin d'étudier le magnétisme à faible dimension, la technique du dichroïsme circulaire magnétique des rayons X (XMCD) est de loin la plus utilisée, et que l'on va décrire aussi. Ensuite, nous passerons aux aspects expérimentaux de la thèse. Tout d'abord, une description détaillée de la ligne de lumière *DEIMOS* du Synchrotron *SOLEIL*. Après cela, nous développerons brièvement les aspects théoriques du STM en décrivant les dispositifs expérimentaux, à savoir un STM

à température variable et un STM à basse température. Enfin, étant donné que toutes nos expériences impliquent soit une monocouche soit quelques couches atomiques ou moléculaires, elles sont toutes réalisées sous ultravide (UHV). Ainsi, nous décrirons les principes de la préparation du substrat, du dépôt de molécules et autres métaux dans cet environnement.

La première investigation, dans le chapitre 3, repose sur la thermobistabilité de films ultraminces de $\text{Fe}((3,5\text{-(CH}_3)_2\text{Pz)}_3\text{BH})_2$ sur des surfaces de Cu(111) et de graphite pyrolytique hautement orienté (HOPG). Tout d’abord, nous constatons que les molécules conservent leur intégrité sur les substrats, ce qui donne lieu à des réseaux moléculaires bidimensionnels ordonnés. De plus, sur la base d’une analyse comparative entre le taux de couverture moléculaire extraite des images STM et le saut au seuil L_3 de Fe^{II} extraite par XAS, nous déduisons une calibration en termes de nombre de couches (en unités de ML pour *monolayer*). Toutes les données expérimentales XAS ont été ajustées grâce aux calculs LFM en utilisant QUANTY. Avec les calculs *ab initio* effectués par nos collaborateurs, les niveaux d’énergie multiélectroniques ont été très bien reproduits en utilisant le groupe de symétrie C_{3v} avec un ensemble de trois paramètres de champ cristallin. Ainsi, les spectres simulés pour HS et LS sont en très bon accord avec les spectres expérimentaux pour HS à haute température et LS à basse température sur un composé de référence. Par conséquent, nous reconstruisons la dépendance en température des spectres XAS du HS. Le spectre du LS est indépendant de la température, puisque son état fondamental n’est pas dégénéré. En conséquence, la combinaison linéaire des spectres LS et HS reconstruits s’ajuste parfaitement bien aux spectres expérimentaux. La courbe de conversion thermique obtenue montre, pour la première fois, l’apparition d’une boucle d’hystérésis thermique pour les couches ultrafines de 3.0 ML et 1.4 ML de SCO adsorbés sur Cu(111) et HOPG, respectivement. Ceci est une indication des forts effets coopératifs malgré l’influence du substrat. En effet, lorsque nous augmentons l’épaisseur moléculaire, les interactions intermoléculaires deviennent plus coopératives et font écran à l’interaction molécule-substrat. En conséquence, nous obtenons la boucle d’hystérésis. L’augmentation de la coopérativité est accompagnée d’une diminution de la population de HS à basse température, donc d’une augmentation de l’enthalpie totale du système. Ceci conduit à une augmentation de la température de transition. De plus, tous ces résultats peuvent être bien reproduits par des simulations Monte Carlo dans le cadre du modèle mécano-élastique. Dans ce modèle, nous extrayons la force intermoléculaire à partir de simulations de la molécule en volume. Ensuite, en incluant une interaction spécifique avec le substrat et pour différentes épaisseurs moléculaires, nous extrayons l’interaction molécule-substrat. Les paramètres obtenus reproduisent qualitativement bien la tendance observée dans les résultats expérimentaux. En outre, nous étudions numériquement l’influence de la force de l’interaction molécule-substrat sur la transition thermique. Nous constatons que lorsque nous augmentons l’interaction avec le substrat, la fraction résiduelle de la molécule HS à basse température augmente. De plus, lorsque nous diminuons l’interaction molécule-substrat, le nombre de couches nécessaire pour avoir une commutation complète est diminué. Pour notre système, nous attendons une commutation complète à partir de 8 ML. Cependant, nous montrons que la distribution des molécules HS à l’intérieur de chaque couche n’est pas homogène sur l’épaisseur du film et plus spécifiquement, nous mettons en évidence le rôle de la couche d’interface. En effet, la fraction résiduelle de molécules HS à basse température dans la couche d’interface dépend fortement de la compétition entre l’augmentation des effets coopératifs (augmentation de la taille du système) et de l’interaction molécule-substrat qui bloque la molécule dans l’état HS. Ces résultats démontrent l’importance de la taille du système et de la nature

du substrat sur la transition thermique et ce qui peut être important pour les propriétés de transport électronique à travers de telles couches moléculaires.

Dans le chapitre 4, nous étudions les propriétés induites par la lumière de $\text{Fe}((3,5\text{-(CH}_3)_2\text{Pz)}_3\text{BH})_2$ en contact direct avec Au(111), Ag(111), Cu(111) et HOPG. Tout d’abord, la molécule sur Au(111) et Ag(111) ne se fragmente pas et forme des réseaux 2D bien ordonnés. Par la même analyse que dans le chapitre 3, nous avons déduit une calibration en termes de nombre de couches sur les deux surfaces. Par XAS, en utilisant différentes longueurs d’onde qui déclenchent normalement la transition $\text{LS} \rightarrow \text{HS}$, une transition anormale de $\text{HS} \rightarrow \text{LS}$ dans la gamme des sous-monocouches est observée. Cet effet anormal induit par la lumière n’a jamais été rapporté auparavant. Ainsi, afin d’interpréter nos observations, un nouveau mécanisme est proposé pour la conversion de spin médiée par les photo-électrons de valence issus des transitions interbandes des substrats métalliques. De plus, des études STM sur des sous-monocouches de la molécule sur Au(111), Ag(111) et Cu(111) confirment bien cet effet anormal. En préparant différentes épaisseurs allant de la sous-monocouche aux multicouches sur les mêmes substrats Cu(111) et HOPG, les mesures XAS démontrent que nous récupérons le LIESST et donc, que cet effet est confiné sur la première couche. Si nous comparons le nombre de molécules converties sous l’effet de la lumière sur les deux surfaces, il apparaît que la commutation est plus efficace sur HOPG que sur Cu(111). L’ensemble de ces résultats démontre le rôle crucial de l’interface molécule/substrat sur la modification des propriétés de commutation induites par la lumière. Toujours sur Cu(111), nous mesurons le T_{LIESST} pour les trois plus faibles épaisseurs de SCO. Nous montrons que les T_{LIESST} pour 1.7 ML et 3.0 ML sont presque égaux (dans les barres d’erreur). Plus intéressant encore, l’épaisseur de 1.7 ML semble confirmer le fait que seule la première couche passe en LS sous l’effet du laser bleue. Enfin, nous démontrons l’existence d’une boucle LITH sur les deux surfaces. En effet, comme discuté dans le chapitre 3, les effets coopératifs sont importants au fur et à mesure que nous augmentons l’épaisseur moléculaire et à la couverture dans laquelle l’hystérésis thermique apparaît, alors une boucle de LITH apparaît. Cependant, pour des épaisseurs où la transition va de HS à LS, nous soupçonnons l’apparition d’une phase dite cachée qui prolonge l’hystérésis thermique vers des valeurs de proportion de HS très inférieures à celles que nous aurions obtenues sans lumière. L’apparition de la phase cachée, révélée par les LITH, est due au chevauchement de la plage de température de la transition thermique et de la plage de température transition anormale induite par la lumière est effective. Ces résultats ouvrent de nouvelles possibilités pour concevoir des dispositifs de stockage d’informations à l’échelle nanométrique : écrire de l’information avec de la lumière et la supprimer ensuite avec la température.

Dans le chapitre 5, nous étudions la robustesse de l’anisotropie magnétique de $\text{Fe}((3,5\text{-(CH}_3)_2\text{Pz)}_3\text{BH})_2$ sur Cu(111) par rapport à un composé référence, la molécule HS $\text{Fe}(3\text{-(Phen)Pz)}_3\text{BH})_2$. Tout d’abord, l’analyse numérique et théorique des mesures de susceptibilité magnétique sur le composé massif de référence permet d’extraire les paramètres d’anisotropie magnétique (ZFS pour *zero field splitting*), à savoir D et E , ainsi que le facteur de Lande effectif (g). La valeur positive de D prouve que le composé possède un axe de difficile aimantation. Sur la sous-monocouche de la molécule SCO sur Cu(111), les mesures XMCD démontrées à trois températures ont révélé l’existence d’une anisotropie magnétique. Avant de procéder à l’ajustement, il est utile de réfléchir aux paramètres les plus importants : tout d’abord, il y a le facteur de Lande effectif qui est extrait à partir des règles de la somme et qui est très proche du composé de référence massif. Ensuite, il y a

l'angle entre l'axe magnétique principal de la molécule (axe C_3) et la surface. Les calculs numériques montre que le meilleur ajustement est obtenu pour $50 \pm 10^\circ$ entre l'axe C_3 et la surface. Plus important encore, la valeur de D obtenue est positive et ceci confirme la présence d'un axe de difficile aimantation pour une monocouche de la molécule SCO sur Cu(111), comme dans le cas de la molécule de référence. L'anisotropie magnétique semble ne pas être affectée par l'interface substrat/vide. Ceci a été confirmé par des calculs *ab initio* effectués par nos collaborateurs. Pour les deux molécules, le référentiel d'axes magnétiques sont presque les mêmes pour les deux molécule. En outre, la nature de l'axe d'aimantation difficile/facile est régie par un paramètre structural, à savoir l'angle de torsion entre l'axe magnétique de haute symétrie et les cycles pyrazole à cinq chaînons du ligand tridenté. Pour comprendre pourquoi, nous avons examiné le *Cambridge Crystallographic Data Centre* pour les complexes hexacoordonnés avec n'importe quel dérivé du ligand tridenté (pz_3HB) et différents ions métalliques (Fe^{II} , Co^{II} et Ni^{II}), les valeurs de l'angle de torsion ne sont jamais supérieures à 9° . En revanche, l'étude du complexe $[\text{Fe}(\text{ptz})_6]^{2+}$ (ptz = propyltétrazole) qui présente des distances de longueur de liaison similaires mais un angle de torsion assez différent (63.3°) et possède un axe facile d'aimantation. Pour rationaliser la relation entre la nature de l'axe magnétique et cet angle de torsion, les calculs de l'énergie des orbitales moléculaires montrent que la raison principale est liée au fait que l'orbitale d_{z^2} ne s'hybride pas avec les orbitales de type π ou σ des ligands (azote) et conduisant à une orbitale presque non-liante. De plus, les calculs des états électroniques des deux molécules montrent que les excitations magnétiques obtenues par couplage spin-orbite aux états de plus haute énergie contribuent positivement à la valeur de l'anisotropie magnétique. Au contraire, l'ordre des niveaux d'énergie moléculaires est inversé pour $[\text{Fe}(\text{ptz})_6]^{2+}$ puisque l'orbitale d_{z^2} de la molécule hybride l'orbitale de l'azote, ce qui rend l'orbitale d_{z^2} anti-liante. Ainsi, l'orbitale d_{z^2} n'est plus l'état fondamental et les excitations magnétiques de l'état fondamental vers les niveaux d'énergie supérieurs obtenues par couplage spin-orbite impliquent une contribution négative à l'anisotropie magnétique. Ceci soutient un degré assez élevé de rigidité contre la déformation, conduisant à la conclusion que l'anisotropie axiale de la famille des complexes $[\text{Fe}^{\text{II}}((\text{pz})_3\text{BH})_2]$ (et autres dérivés) ne devrait pas être facilement altérée par leur environnement.

Dans le chapitre 6, nous avons proposé l'étude de sous-monocouches de molécules SCO sur des substrats ferromagnétiques par STM, XAS et XMCD. Tout d'abord, nous avons constaté que les molécules conservent leur intégrité sur les îlots de Co mais qu'elles sont bloquées dans l'état HS quels que soient les stimuli externes. Le STM montre que sur le Co, les molécules adoptent différentes orientations. Ensuite, nous présentons la préparation molécule/substrat sur les différents substrats de Co. Dans ce cas, la calibration du taux de couverture moléculaire diffère drastiquement puisque les images STM montrent un système totalement désordonné, ce qui rend la calibration par STM très difficile. De plus, la complexité des systèmes préparés conduit à des contributions différentes du fond du XAS. Ainsi, afin d'obtenir une calibration correcte, nous avons décidé de normaliser tous les sauts de bord XAS sur les différentes surfaces par rapport au fond Cu(111). Deuxièmement, nous démontrons par XAS que la molécule est complètement bloquée par l'effet du substrat. En effet, la barrière énergétique entre les deux états est plus élevée sur Co que sur les métaux. Par ailleurs, les mesures XMCD démontrent l'existence d'un couplage antiferromagnétique (AFM) entre les molécules et les moments magnétiques du Co, quelle que soit l'aimantation du Co. De plus, pour l'aimantation hors plan du Co, nous démontrons l'existence d'une aimantation rémanente qui est robuste jusqu'à environ 40 K, et qui diminue lorsque nous

augmentons la couverture moléculaire, même en sous-monocouche. Ensuite, afin de favoriser la commutation et de réduire la barrière énergétique entre les deux états, nous avons décidé d'intercaler différentes épaisseurs de cuivre entre les molécules et le cobalt. Les mesures XAS montrent que les molécules sont toujours bloquées dans l'état HS sur les couches de Cu découplées comme sur le cobalt. Nous observons que le signe du couplage magnétique a changé et est devenu ferromagnétique (FM). C'est la première fois qu'un couplage entre des molécules de SCO sur des surfaces ferromagnétiques a été démontré aussi clairement. Selon la littérature sur d'autres systèmes moléculaires, ce couplage entre les moments magnétiques est médié par l'interaction entre les ligands méthyles et le Co ou les moments magnétiques polarisés en spin du Cu et est certainement du type superéchange. Alors que le changement de signe peut être attribué au couplage dit d'échange intercouche, comme il a été observé pour d'autres systèmes moléculaires ou atomiques sur des surfaces ferromagnétiques. Cependant, au-delà d'une certaine épaisseur de couche de découplage en cuivre, la molécule retrouve son comportement paramagnétique. Les points de données obtenus sont en parfait accord avec ceux obtenus sur Cu(111) et confirme ainsi la robustesse de l'anisotropie magnétique de cette molécule sur les surfaces. Enfin, nous avons utilisé l'or comme couche de découplage. En effet, nous avons préparé un système Au/Co/Au(111) par recuit contrôlé de Co/Au(111). Nous montrons qu'une sous-monocouche de molécules commutent sous l'effet de la lumière et de la température en utilisant cette couche de découplage, et aucun couplage magnétique n'a été mesuré.

Nous pensons que ce travail peut être intéressant pour les communautés de magnétisme et des commutateurs moléculaires, et ouvre des perspectives pertinentes quant à l'utilisation des SCO pour la spintronique moléculaire.

CONTENTS

Contents	xiii
General Introduction	1
1 Spin-Crossover Molecules: from Bulk to Monolayer	3
1.1 What is a spin-crossover (SCO) complex ?	3
1.2 Switching mechanism in spin-crossover complexes	5
1.2.1 Thermal-induced switching at the molecular scale	5
1.2.2 The role of cooperativity	6
1.2.3 Light-induced switching : Light-Induced Excited Spin State Trapping (LIESST)	9
1.2.4 The relaxation mechanism	10
1.2.5 What can affect the relaxation rate ?	11
1.2.6 Light-Induced Thermal Hysteresis (LITH)	15
1.2.7 Soft X-ray Induced Excited Spin State Trapping (SOXIESST)	16
1.3 On-surface SCO	17
1.3.1 Fe(phen) ₂ (NCS) ₂	18
1.3.2 Fe(H ₂ B(pz) ₂) ₂ (L) and functionalized analogues	19
1.3.2.1 L = phen	19
1.3.2.2 L = bipy	22
1.3.3 Fe(pypyr(CF ₃) ₂) ₂ (phen)	24
1.3.4 Fe(qnal) ₂	25
1.3.5 [Fe ^{III} (pap) ₂] ⁺	26
1.3.6 Fe(HB(L) ₃) ₂	26
1.3.6.1 L = tz	26
1.3.6.2 L = pz	27
1.3.6.3 L = (CH ₃) ₂ pz	28
1.4 Conclusions	30
2 Materials, Experimental Methods and Simulations	33
2.1 Organic Materials	33
2.1.1 The stability of the molecules on surfaces	33
2.1.2 Molecular structure	34
2.1.3 Photoswitching and thermodynamic properties of Fe-Pyrz	35

2.2	Theoretical Aspects of X-ray Absorption Spectroscopy (XAS)	36
2.2.1	Introduction	36
2.2.2	Light-Matter interaction	37
2.2.3	Ligand Field Multiplet Theory (LFM) of transition metal $L_{2,3}$ edges	39
2.2.3.1	Single particle picture versus many-body effects in XAS	39
2.2.3.2	The basis	39
2.2.3.3	Treatment of the electron-electron repulsion	40
2.2.3.4	Treatment of the spin-orbit coupling	41
2.2.3.5	Treatment of the crystal field	42
2.2.3.6	The XAS spectra	43
2.2.4	The <i>QUANTY</i> software	44
2.2.5	X-ray Magnetic Circular Dichroism (XMCD)	45
2.3	Experimental aspects of X-ray Absorption Spectroscopy and Magnetic Circular Dichroism	46
2.3.1	Description of the Dichroism Experimental Installation for Magneto-Optical Spectroscopy (<i>DEIMOS</i>) beamline	46
2.3.1.1	Detection technique: The Total Electron Yield (TEY) method	49
2.3.1.2	Let's run a spectrum !	49
2.4	Scanning Tunneling Microscopy (STM)	50
2.4.1	Theoretical models for STM	51
2.4.2	Principle of operation	52
2.4.3	Modes of operation	52
2.5	Experiment under ultrahigh vacuum (UHV)	53
2.5.1	Substrate preparation	53
2.5.2	Metal deposition	54
2.5.3	Calibration of the Co thickness	55
2.5.4	Molecule deposition	56
3	Thermal Switching of Surface-Supported Fe-Pyrz Ultrathin Layers	59
3.1	Monte Carlo Arrhenius simulations in the framework of the mechanoelastic model	60
3.1.1	Description of the model	60
3.1.2	Implementation of the model	62
3.1.3	Implementation of the model on surfaces	64
3.2	Thermal bistability of an ultrathin film of Fe-Pyrz on Cu(111) surface . . .	65

3.2.1	Preparation of the sample and determination of molecular coverage on Cu(111)	65
3.2.2	Temperature-dependant XAS measurements and determination of the high-spin fraction as a function of temperature	67
3.2.2.1	Temperature-dependant XAS measurements at different coverages	67
3.2.2.2	Determination of the high-spin fraction as a function of temperature and calculation of temperature-dependant XAS spectra	67
3.2.2.3	Thermal diffusion model for temperature correction . . .	71
3.2.3	The thermal hysteresis cycles	73
3.2.4	Mechanoelastic simulations	74
3.2.4.1	Determination of the molecule-molecule interaction and Monte Carlo time	74
3.2.4.2	Effect of the molecule-substrate interaction	75
3.2.4.3	Effect of the number of layers on the switching properties	77
3.2.4.4	Distribution of the high spin fraction inside the layers .	77
3.2.4.5	Role of the interface layer	77
3.3	Thermal bistability of an ultrathin film of Fe-Pyrz a Highly Oriented Pyrolytic Graphite (HOPG) surface	79
3.3.1	Preparation of the sample and determination of molecular coverage on HOPG	79
3.3.2	Temperature-dependant XAS measurements and determination of the high-spin fraction as a function of temperature	80
3.4	Conclusions	81
4	Effect of the Substrate on the Transition under Light	83
4.1	Effect of light on submonolayer to monolayers of Fe-Pyrz on Cu(111), Au(111) and Ag(111)	83
4.1.1	Sample preparation of submonolayer of Fe-Pyrz and determination of molecular coverage	84
4.1.2	Anomalous LIESST of submonolayer of Fe-Pyrz on Cu(111), Au(111) and Ag(111)	85
4.1.2.1	XAS measurements	85
4.1.2.2	Dynamics of the anomalous switching under light	87
4.1.3	STM study of the anomalous switching	89
4.1.4	Model for the light anomalous switching: substrate-mediated switching	91

4.2	Effect of light on submonolayer to monolayers of Fe-Pyrz on Cu(111) and HOPG	92
4.2.1	On Cu(111)	93
4.2.2	On HOPG	94
4.3	Light Induced Thermal Hysteresis (LITH) measurements on Cu(111) and HOPG	95
4.3.1	T_{LIESST} measurements on Cu(111)	95
4.3.2	LITH measurements on Cu(111) and HOPG	96
4.4	Conclusions	99
5	Robust Magnetic Anisotropy of an Ultrathin Film of Fe-Pyrz Assembled on Cu(111)	101
5.1	What is the difference between single molecular magnets and paramagnetic molecules ?	103
5.2	The Spin Hamiltonian formalism	105
5.2.1	Origin of the magnetic anisotropy	106
5.2.2	The Pryce's Spin Hamiltonian	106
5.2.3	Properties of the Spin Hamiltonian	108
5.2.4	Calculation of magnetization curves using the <i>PHI</i> software	109
5.2.5	Exact calculation of magnetization curves	109
5.2.5.1	$E = 0, \vec{B}(\theta, \phi), S = 2$	110
5.2.5.2	$E = 0, \vec{B} \parallel (\mathbf{OZ}), S = 2$	110
5.2.5.3	$E = 0, \vec{B} \parallel (\mathbf{OZ}), S$ is integer	111
5.2.5.4	$E = 0, \vec{B} \parallel (\mathbf{OZ}), S$ is half-integer	111
5.3	Magnetic properties of a powder of Fe-Phen	112
5.4	XAS and XMCD measurements of an ultrathin layer of Fe-Pyrz on Cu(111)	113
5.4.1	XAS, XMCD and magnetization measurement on Fe-Pyrz	113
5.4.1.1	The effective g -factor	115
5.4.1.2	The normalization factor	115
5.4.1.3	The angle between the magnetic field and the principal anisotropy axis	116
5.5	<i>Ab initio</i> calculations	117
5.5.1	Is Fe-Phen a good reference for Fe-Pyrz ?	117
5.5.2	The magnetic axis frame of Fe-Pyrz and Fe-Phen	117
5.5.3	Role of the torsion angle	118
5.5.3.1	Molecular orbitals energy diagram	119

5.5.3.2	Electronic structure energy diagram	120
5.5.4	How to tune the magnetic anisotropy ?	121
5.6	Conclusion	122
6	Switching and Magnetic Properties of Spin-Crossover Molecules/Ferromagnetic Interfaces	125
6.1	Fe-Pyrz on ferromagnetic cobalt surface	126
6.1.1	STM of Fe-Pyrz on Co/Cu(111)	126
6.1.2	Sample preparation and determination of cobalt and molecular coverages for Fe-Pyrz/Co/Au(111) system	127
6.1.3	Thermal and light-induced switching properties for Fe-Pyrz/Co/Au(111) interface	129
6.1.4	XMCD and magnetic hysteresis measurements for Fe-Pyrz/Co/Au(111) interface	129
6.2	Effect of different decoupling layers on the switching and magnetic properties between Fe-Pyrz and Co/Au(111)	132
6.2.1	Copper as a decoupling layer	133
6.2.1.1	Thermal and light-induced switching properties	134
6.2.1.2	XMCD and magnetic hysteresis measurements	135
6.2.2	Gold as a decoupling layer	137
6.2.2.1	Thermal and light-induced switching properties	139
6.2.2.2	Magnetic properties	140
6.3	Conclusion	142
	General Conclusions	145
	List of Publications	147
	Bibliography	171

GENERAL INTRODUCTION

Spintronics is a branch of electronics which exploits not only the charge of the electron but also its spin degree of freedom. It has opened a way to new devices such as spin valves or magnetic tunnel junctions which have revolutionized the field of sensors and information storage. As usual, the development of breaking-through nanoscale technologies is based on the understanding of the material properties at the nanometer scale. Historically, the materials used for spintronics are inorganic ones (mainly metals and oxydes). However, the need of new materials arouses a huge interest from physicists and chemists communities. In this respect, incorporating molecular materials in devices is promising as molecules can be designed and tuned at will to create new functionalities. Among them spin-crossover compounds present the interesting and rather rare property to be switchable and addressed by various external stimuli.

Spin-crossover (SCO) molecules are an important class of multifunctional switching materials that change reversibly their spin-state from low spin (LS) to high spin (HS) states, and many other physical properties: optical, magnetic, conductivity and mechanical properties, upon external perturbation. Due to their multifunctionality and the bistability deriving from the existence of two spin-states, the SCO molecules have been proposed as promising building blocks for a variety of technological applications such as information storage, sensors, digital display, and so on. However, the incorporation of such a material in nanoscale devices requires a deep understanding of the spin transition properties for molecular layers deposited on various substrates. In the last years, a considerable effort was made by physicists and chemists to synthesize vacuum-evaporable SCO which can be deposited on surfaces and also to characterize the spin transition on surfaces, under various external triggers. Works on ultrathin SCO layers on metals, ferromagnetic or not, are however rather scarce, due to the fragility of such molecules which can undergo a decomposition and/or a spin-state blocking when adsorbed on surfaces. During this thesis work, we mainly used $\text{Fe}^{\text{II}}((3,5-(\text{CH}_3)_2\text{Pz})_3\text{BH})_2$ molecules which is one of the only reported active vacuum-evaporable SCO molecule on metallic substrate. The central question of this work is: How the spin transition and the magnetic properties of the $\text{Fe}^{\text{II}}((3,5-(\text{CH}_3)_2\text{Pz})_3\text{BH})_2$ molecule are modified in close contact with metallic, semi-metallic and ferromagnetic surfaces ?

The first chapter of the thesis is dedicated to the presentation of SCO molecules. In the first part, the thermal-, light- and X-ray-induced switching for molecules in bulk is detailed. In the second part, we discuss, molecule by molecule, the advances made in the recent years in the field of vacuum-evaporable SCO on-surface, from thick films to ultrathin films and down to single molecules.

For this thesis work, we mainly used two complementary experimental techniques, namely X-ray absorption spectroscopy (XAS) and Scanning Tunneling Microscopy (STM) which are presented in the second chapter. We also present the molecule we have used and other technical aspects like the substrate preparation, molecule and metal deposition techniques under ultrahigh vacuum.

The results obtained during this thesis work are described in the four last chapters. We will first focus on the thermal- (chapter 3) and light-induced (chapter 4) switching properties of $\text{Fe}^{\text{II}}((3,5-(\text{CH}_3)_2\text{Pz})_3\text{BH})_2$ adsorbed either on metallic substrates or on HOPG. We will

then discuss in chapter 5 the magnetic anisotropy of the $\text{Fe}^{\text{II}}((3,5\text{-(CH}_3)_2\text{Pz)}_3\text{BH})_2$ molecules in 2D molecular films adsorbed on Cu(111). Finally, we will report in chapter 6 on their adsorption and coupling on ferromagnetic substrates.

SPIN-CROSSOVER MOLECULES: FROM BULK TO MONOLAYER

Spin-crossover [1–9] (SCO) molecules are an important class of multifunctional [10–14] switching materials that change reversibly their spin-state and many other physical properties, such as, the optical, vibrational and electronic properties, upon external perturbation. Due to their bistability [4, 12, 15] deriving from the existence of two spin-states, the SCO molecules have been proposed as promising building blocks for a variety of technological applications such as in spintronics [16–20], information storage [21–24], sensors and digital display [21, 25]. However, the use of SCO in applications require a detail understanding of both physics and chemistry of the molecule from bulk form to on-surfaces in thick, thin, ultrathin and isolated molecule levels. The key point is the preservation of the molecular functionalities in reduced dimensions.

This chapter starts with a detailed description of the basic mechanisms of the thermal, light, and X-ray-induced SCO and the relevant parameters that drive the molecular switching in bulk. Then, we propose a complete coverage of advances made in the field of on-surface SCO.

1.1 What is a spin-crossover (SCO) complex ?

The general structure of SCO consists of a central transition metal ion ($3d^n$ with $n=4,5,6,7$) that is surrounded by organic ligands which apply a crystal field (CF)[1, 12, 26–28] and thus splits the degeneracy of the $3d$ orbitals according to the symmetry of the ligands (cf. Figure 1.1-a/b in octahedral symmetry). These molecules are characterized by two spin-states, one called low-spin (LS) and one called high-spin (HS). Among the molecules synthesized by chemists, those based on Fe^{II} are by far the most investigated[2–4, 7–9, 29, 30]. For simplicity of discussion, let us consider the simple case of an octahedral crystal field (O_h point group) which breaks the degeneracy of the d orbitals into two collective sets of orbitals. As shown in figure 1.1-b, the first set is constituted by the non-bonding d_{xy} , d_{xz} , d_{yz} orbitals called t_{2g} and the second set of orbitals is constituted by the anti-bonding $d_{x^2-y^2}$, d_{z^2} also called e_g orbitals. They are separated by the CF splitting, called $10D_q$. The electronic struc-

ture of Fe^{II} is $[\text{Ar}]4s^03d^6$ configuration and depending on the competition between the CF and the spin-dependent coulomb repulsion between the six electrons of the partially filled d orbitals, also called the pairing energy (Π), two spin-states can occur. Indeed, if $10D_q$ is lower than Π , the ground state results from the configuration where the d -electrons first maximize the total spin of the t_{2g} orbitals of lower energy, then the e_g orbitals of higher energy. The ground state is then HS and obeys the Hund's rule [26]. On the contrary, for $10D_q$ larger than Π , the Hund's rule is not respected and the electrons occupy only the t_{2g} orbitals. Consequently, the spin-state of a Fe^{II} ion in an octahedral environnement is characterized by its diamagnetic LS state ($^1A_{1g}$, $t_{2g}^6 e_g^0$, $S = 0$) or by its paramagnetic HS state ($^5T_{2g}$, $t_{2g}^4 e_g^2$, $S = 2$). This discussion is summarized in figure 1.1-b/c. Finally, a SCO molecule has a CF splitting close to its pairing energy, allowing the switching from one state to another under various excitations.

Moreover, another important parameter during the transition is the change of the average distance between the metal and the neighboring ligands, as shown in figure 1.1-c. A typical value of the change of the distance between the ion and the ligand, encoded by $r_{\text{Fe-L}}$ (or r_{HL} in figure 1.1-c), from LS to HS is 0.2 Å [31, 32]. As a consequence, it induces an increase of volume of the $[\text{FeL}_6]$ coordination sphere. This change of volume at the scale of the molecule induces macroscopically, the so-called the cooperativity [1, 4, 30, 33] and which is an important parameter of the thermal transition. Besides, the change of electronic configuration can be accompanied by an anisotropic distortion of the octahedral cage (trigonal and octahedral distortion, cf. figure 1.1-a) which has important consequences on the transition properties under light [34–40]. All this will be discussed in more detail in the following sections.

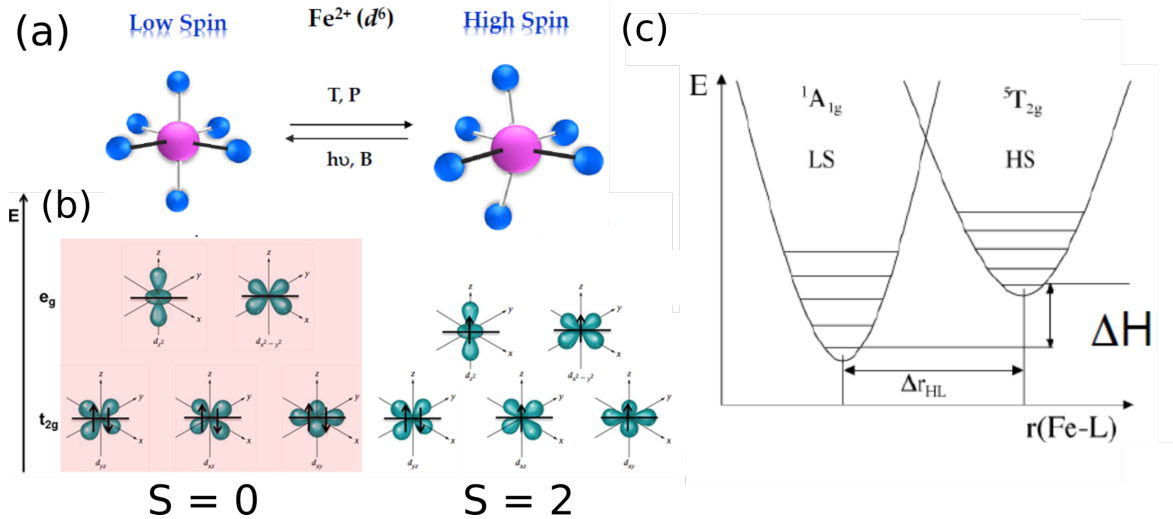


Figure 1.1: (a) FeN_6 coordination sphere of SCO. (b) Change of electron distribution between LS and HS states of an octahedral iron(II) coordination compound. The orbitals e_g and t_{2g} arise from the splitting of the 3d orbitals in an octahedral (O_h) ligand field symmetry. (c) potential well energy of LS (1A_1) and HS ($^5T_{2g}$) states as a function of Fe-L bond length.

1.2 Switching mechanism in spin-crossover complexes

Among the different stimuli that induce spin transition in SCOs, thermal and light-induced transition also called Light-Induced Excited Spin-State Trapping (LIESST) [3–5, 7, 29, 41–43], have been the most studied in the literature. The description of the mechanisms that induce the switching at the molecular scale will be discussed for both stimuli. Moreover, we will see how collective and structural effects modify the transition.

1.2.1 Thermal-induced switching at the molecular scale

To understand the switching mechanism under the effect of temperature, we must invoke thermodynamic arguments. The thermodynamic function that describes the system is the Gibbs free energy $G(T, p)$ with temperature and pressure as variables. Thus we can note the difference in Gibbs free energy for the HS and LS states as:

$$\Delta G(T, p) = G_{HS}(T, p) - G_{LS}(T, p) = \Delta H - T\Delta S \quad (1.1)$$

Where ΔH and ΔS represent the difference of enthalpy and entropy between HS and LS states, respectively. The thermodynamic stable state is given by the lowest Gibbs energy and thus the competition between the enthalpy and entropy. As shown in figure 1.1-c, the enthalpy term fixes the difference of the zero point energies of the HS and LS potential wells. While the energy barrier from HS to LS (resp. LS to HS) is given by the difference between the zero point energy of the HS (resp. LS) state and the crossing point between the two potential wells.

With regard to entropy, there are three different contributions to the total entropy change term, namely, vibrational (ΔS_{vib}), electronic (ΔS_{elec}) and rotational (ΔS_{rot}) [2, 5, 7, 44, 45]. The vibrational contribution comes from the fact that the stretching frequencies change between the HS and LS states. Indeed, the vibrational entropy is more pronounced for the HS state than in the LS state owing to the longer metal-ligand bond lengths. It has been shown that this contribution to the Gibbs free energy is the most dominant for SCO molecules and is determined to be in the range 40–80 J.mol⁻¹.K⁻¹ [45]. The electronic contribution comes from the fact that the orbital and spin degeneracies are different between the two states. Moreover, in the case of transition metal ions in an octahedral environment, there is a quenching of the orbital momentum and thus the major contribution to this entropy comes from the difference in spin multiplicity and is related to the ratio of the degeneracies Ω_{HS}/Ω_{LS} between the HS and LS states according to the Boltzmann law. This contribution for Fe^{II} ions is 13.4 J.mol⁻¹.K⁻¹ [45]. Finally, the rotational contribution is the one that contributes the least, and is around 1 J.mol⁻¹.K⁻¹ [44]. In a SCO compound, the enthalpy and entropy variations between the LS and HS states are positive and the equation can be written as a function of the transition temperature $T_{1/2}(=\frac{\Delta H}{\Delta S})$ for which $\Delta G = 0$, such that equation 1.1 becomes:

$$\Delta G = \Delta H(1 - \frac{T}{T_{1/2}}) \quad (1.2)$$

From the previous equation, we just have to distinguish the cases $T < T_{1/2}$, $T = T_{1/2}$ and $T > T_{1/2}$. For the first case, the enthalpy term dominates over the entropy and the LS state is favored because $\Delta G > 0$ (see figure 1.2-a/b in blue). It is worth noting here that two very distinct cases can occur for $\Delta G = 0$ (cf. figures 1.2-a versus b in orange) with either one minimum or two minima separated by an energy barrier, depending on the coupling between the LS and HS states (in a rather similar manner than textbooks on the mixing of alloys, with the regular solution model). Finally, for $T > T_{1/2}$, the HS potential well is lower in energy because the entropy term dominates and so the HS state is favored ($\Delta G < 0$, see figure 1.2-a/b in green). As a summary, the thermal transition is driven by entropy. An elegant approach to the problem is given by Landau's theory of phase transition by [46], from which the following figure was taken.

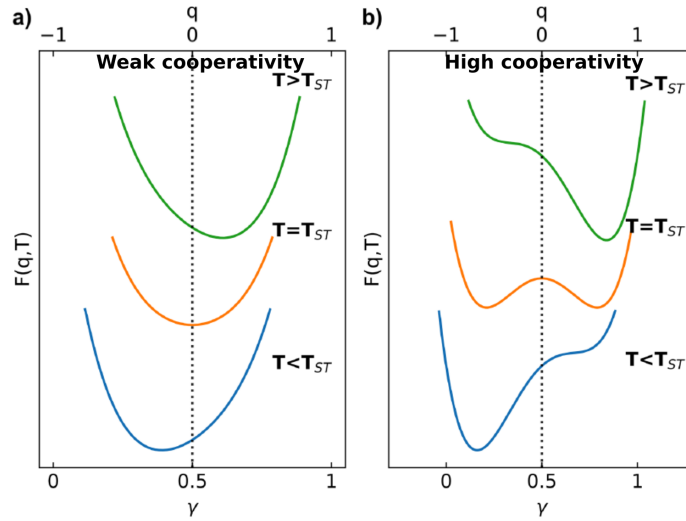


Figure 1.2: Evolution with temperature of the thermodynamic functional $F(q, T)$ with the order parameter q (top axis) and the HS proportion (bottom axis) $\gamma = \frac{1+q}{2}$ (a) without bistability (weak cooperativity) (b) with bistability (strong cooperativity). Note that T_{ST} is the same as $T_{1/2}$. This figure was adapted from [46].

1.2.2 The role of cooperativity

In the previous section, we discussed the effect of the thermal transition at the molecular scale. Now, we will focus on the case where the intermolecular interactions are included. Indeed, a thermally induced SCO is characterized by the evolution of the HS proportion as a function of temperature ($x_{HS}(T)$). Several techniques are currently used to obtain such curves. In bulk, the simplest method consists of measuring the temperature dependence of the molar magnetic susceptibility ($\chi T(T)$). However, other techniques exist such as Mössbauer spectroscopy, temperature-dependent infrared studies and electron paramagnetic resonance. At the thin and ultrathin film levels, the best technique is to measure $L_{2,3}$ edges of X-ray absorption spectra of the Fe^{II} . However, regardless of the experimental method used, thermal transitions can be classified into four types:

- The transition may be smooth (cf. Fig. 1.2-a, Fig. 1.3-a/b and d in black and red), occurring within a large temperature range, or abrupt (cf. Fig. 1.3-d in green), occurring

within a few Kelvin range (2nd order phase transition).

- The $x_{HS}(T)$ curves may exhibit a hysteresis (1st order phase transition, see figures 1.2-b, fig. 1.3-c and d in blue).
- The transition may be complete both at low temperature ($x_{HS} = 0$) and at high temperature ($x_{HS} = 1$), or incomplete. The incompleteness may occur at low temperature and/or at high temperature although it is more often observed at low temperature.
- The transition may occur in multiple steps [40, 46, 47] in rare cases for mononuclear SCO.

To account for the experimental observations, it is necessary to introduce the intermolecular interactions in an assembly of molecules also called cooperativity. The cooperativity is of elastic origin [30, 42, 48–51] and is caused by the volume change between the HS and LS states that creates an internal pressure at the position of the switched molecule. Therefore, several models have been proposed, such as the Slichter-Drickamer model [1, 33] which treats these interactions in the mean field approximation, the Ising-type model [49, 52–64], the mechanoelastic model [63–73] (see chapter 3 for more details) and recently the model of phase transitions which also treats the case of the structural symmetry breaking or non-symmetry breaking that accompanies the spin transition [40, 46, 47, 74–79]. For simplicity, I will discuss the Slichter-Drickamer mean field model [33] which gives a good idea of the different types of thermal transitions.

The Slichter-Drickamer model encodes the cooperativity term via a phenomenological parameter Γ which couples the proportions of HS and LS, in a similar way than a regular solution model. In addition, we must introduce an additional entropy term, the mixing entropy, to the Gibbs free energy that accounts for the fact that within the assembly of N molecules, there are many ways of distributing $x_{HS}N$ HS molecules and $(1 - x_{HS})N$ LS molecules. We can then rewrite equation 1.1 as:

$$G(x_{HS}, T, p) = x_{HS}G_{HS} + (1 - x_{HS})G_{LS} - RT[x_{HS} \ln(x_{HS}) + (1 - x_{HS}) \ln(1 - x_{HS})] + \Gamma x_{HS}(1 - x_{HS}) \quad (1.3)$$

The state of equilibrium is defined by the extrema of $G(x_{HS}, T, p)$ and is given by the vanishing point of the partial derivative of the free energy with respect to x_{HS} at constant pressure and temperature and leads to the implicit equation:

$$T = \frac{\Delta H + \Gamma(1 - 2x_{HS})}{R \ln(1 - \frac{1 - x_{HS}}{x_{HS}}) + \Delta S} \quad (1.4)$$

When Γ is null (cf. Fig. 1.3-a and d in black), we find the case discussed in the previous section and the transition is smooth and follows a Boltzmann law. The introduction of the cooperativity induces additional effects which can change the nature of the phase transition. We can then have a second order phase transition when $\Gamma < 2RT_{1/2}$ (cf. Fig. 1.3-a/b

and d in black and red) and a first order one when $\Gamma > 2RT_{1/2}$ (cf. Fig. 1.3-c and d in blue). Strictly speaking, in the case where $\Gamma < 2RT_{1/2}$ the transition is smooth and without hysteresis because of the weakness of the intermolecular interactions and it is called *crossover*. While in the second case, where the transition is more abrupt, we call it a *transition* and it could be accompanied by thermal hysteresis if the intermolecular interactions are strong enough [67].

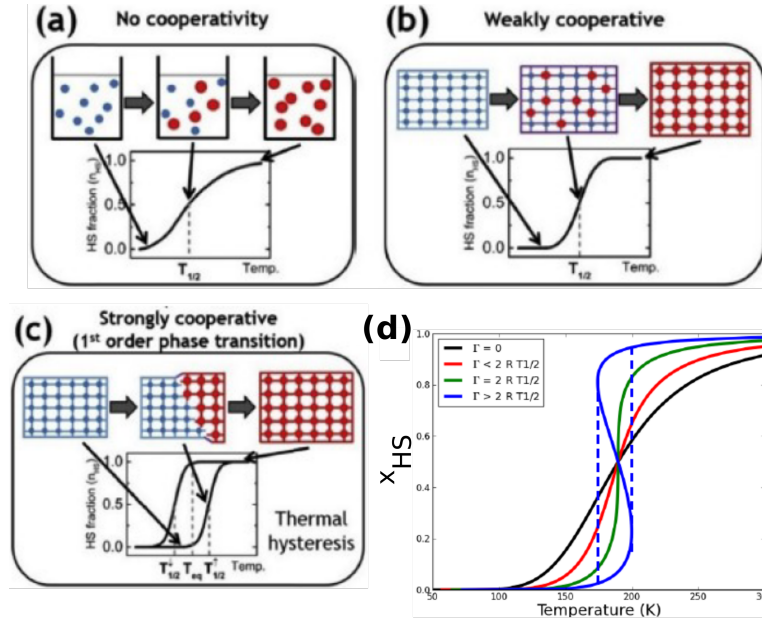


Figure 1.3: Schematic representation of the transition mechanisms and associated thermal spin transition curves in three characteristic SCO systems having different degrees of cooperativity. (a) in solution (no cooperativity, gradual conversion); (b) in a solid exhibiting a weakly cooperative spin conversion (intermediate cooperativity, more abrupt transition) and (c) in a solid exhibiting a first-order spin transition (high cooperativity, abrupt transition with thermal hysteresis loop). LS and HS molecules are depicted by blue and red circles, respectively. This figure was adapted from [80]. (d) Different $x_{HS}(T)$ conversion curves for different values of cooperativity Γ in the Slichter-Drickamer model.

The Slichter-Drickamer model, in addition to being a mean field model, does not account for all the experimental observations on the thermal transition. Indeed, some spin transitions can be accompanied by a structural phase transition which can give rise to steps or asymmetries in the curves describing the thermal transition [40, 76, 80–82]. All these cases are very well explained from the Landau theory of phase transitions made by reference [46]. Finally, this mean-field does not explain also some observations like the nucleation-propagation of domains of same spin-state [54, 63, 64, 66, 68, 83–86] as shown in figure 1.3-c. Therefore, several models such as the mechanoelastic model (which will be presented in more detail in chapter 3) have been designed to take into account the finite-size effects and which encodes short and long-range interactions.

1.2.3 Light-induced switching : Light-Induced Excited Spin State Trapping (LIESST)

The existence of two minima in the potential energy curves (as shown in figures 1.1-c and 1.4-a), such as the LS minimum being lower in energy than the HS minimum, has allowed the observation of a very interesting phenomenon called Light-Induced Excited Spin-State Trapping (LIESST). In 1982, the first experiment to demonstrate the LIESST effect, i.e the LS to HS transition, was carried out by McGarvey [87] in solution. Using pulsed-laser irradiation to trigger the spin- and parity-allowed metal-ligand charge transfer ($^1\text{MLCT}$) absorption band of the low spin-state, they demonstrate the LS ($^1A_{1g}$) to HS($^5T_{2g}$) transition (cf. Fig 1.4-a in green arrows). Two years after, in order to investigate if this transition occur in cooperative systems, Descurtins[88] carried the experiment on a solid-state $\text{Fe}(\text{ptz})(\text{BF}_4)$ compound. They demonstrate the LIESST effect in a temperature range below 50 K, using wavelengths that pointed to the $^1\text{MLCT}$ states but also to the lower-energy spin-permitted absorption bands called ligand-field states (or $d-d$ excitations), namely, 1T_1 and 1T_2 (cf. Fig 1.4-a in green arrows) and the metastable state decay in a non-radiative way to the $^5T_{2g}$ state through transient states (cf. Fig 1.4-a in black arrows), this the so-called intersystem crossing processes [34, 89–91]. Besides that, in reference [88], it was shown that LIESST also appears when irradiating at 530 nm to the spin-allowed bands of the ligand-field of LS species which do not have a transition to MLCT. In addition, LIESST is also observed on irradiation directly into the spin-forbidden $d-d$ absorption band of the LS species, namely, the $^3T_{1g} \rightarrow ^5T_{2g}$ transition [92]. Moreover, in 1986, they demonstrate that the LIESST phenomenon was reversible. Indeed, when irradiating a sample trapped in the HS state at 10 K, using a light corresponding to the $^5T_{2g} \rightarrow ^5E_g$ transition at 820 nm, a pumping back to the normal LS state is observed and this phenomenon is called reverse-LIESST (r-LIESST) [29, 89, 93]. However, it was observed that this phenomenon was not as efficient as LIESST (85 % of conversion), and this comes from the fact that the spin-forbidden excited state of the LS state ($^3T_{2g}$ and $^3T_{1g}$) overlaps with the 5E and gives a steady state situation. All this discussion is summarized in figure 1.4-a. Recently, ultrafast pump-probe experiments coupled with structural measurements have been conducted [23, 38, 40, 92, 94–101], in order to visualize the time-scales of all these phenomena and access to intermediate states (cf. figure 1.5-c) that are induced by the LIESST effect.

Below 10 K and as shown in figure 1.4-b (blue arrow), the thermal energy is too low for the system to overcome the energy barrier between the HS and LS states, thus the HS state is trapped and does not decay within several hours or days, this is the quantum tunneling regime. Above 50 K and as shown in figure 1.4-b (red arrow), the HS state relaxes back to the stable LS state because of the temperature; this is the thermally activated regime. Consequently, at cryogenic temperatures, it seems that the relaxation rate is less efficient than at higher temperatures. The word "trapping" in LIESST comes from the fact that we trap the molecules in a metastable HS state with a long lifetime at low temperatures.

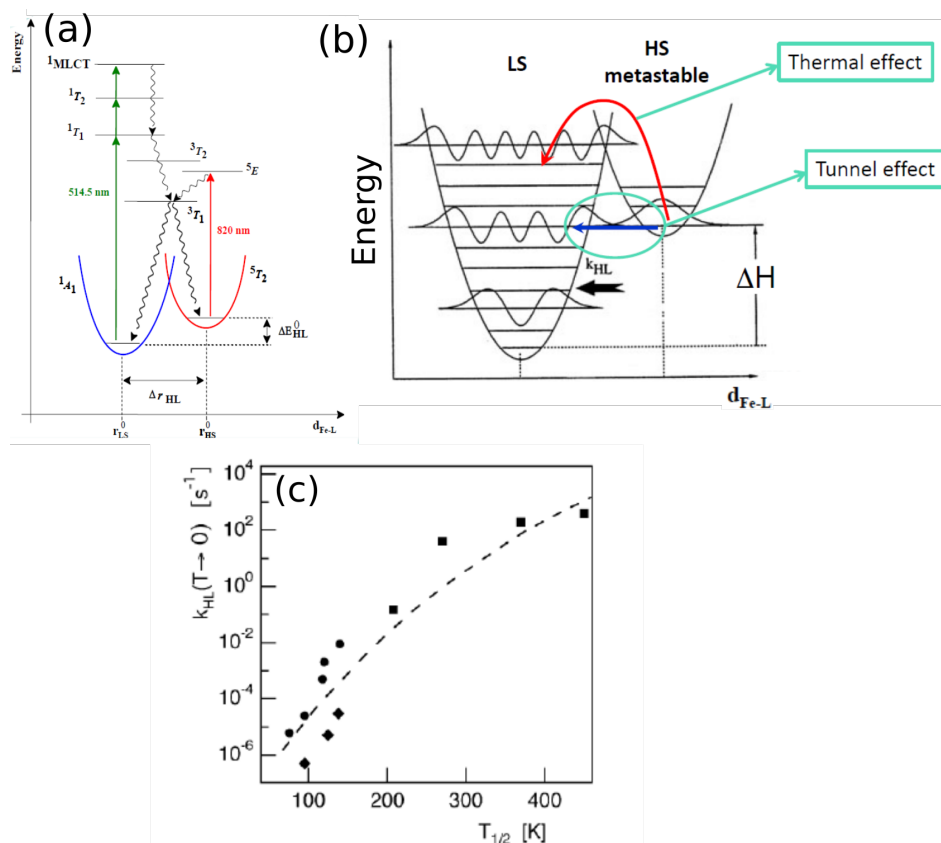


Figure 1.4: (a) The electronic structure of iron(II) spin-crossover complexes. The mechanisms of LIESST and reverse-LIESST are indicated by curly arrows. At low temperatures, the barrier effectively traps the complex in the high spin-state. (b) Potential wells of the high-spin and the low spin-state along the totally symmetric normal coordinate. At low temperatures, tunnelling occurs exclusively from the lowest vibrational state of the HS state. At elevated temperatures, tunnelling occurs as an activated process from thermally populated vibrational levels of the high spin-state. The zero-point energy difference is denoted either ΔE_{HL} or ΔH . (c) The low-temperature tunnelling rate constant on a log scale as a function of chemical variation of the zero-point energy difference between the HS and the LS state as expressed by the transition temperatures of a series of spin-crossover complexes, (filled circles) picolylamine, (filled diamonds) tetrazoles, (filled squares) $(mepy)_{3-x}(py)_x$ series, (dashed line) theoretical. These figures were taken from [29].

1.2.4 The relaxation mechanism

After the discovery of LIESST, a lot of experimental and theoretical works have been done to understand the relaxation rate k_{HL} ¹ from HS to LS with temperature [29]. At the beginning and because of the limitations to go down to very low temperatures, the majority of the studies concerned SCO in solutions with $T_{1/2}$ near room temperature and the k_{HL} obtained were all between 10^6 and 10^8 s⁻¹. With the generalization of cryogenics techniques as well as new SCO complexes in solid-state with $T_{1/2}$ much lower than 300 K, it has been shown experimentally that there are two regimes of relaxations: i) quantum tunneling at very low temperature; ii) thermally-activated regime at higher temperature. This was also

¹HL refers to the relaxation of the metastable HS state to the LS state.

confirmed by the Buhks theory [102, 103] the so-called non-adiabatic multiphonon process. Classically, if a complex is trapped in the HS state, it can pass to the LS state only by thermal energy. While quantitatively, there is a non-zero probability of passing the energy barrier by quantum tunneling and which is given by the Fermi golden rule:

$$w_{m,m'} = \frac{2\pi}{\hbar^2\omega} \langle \Phi_{LS} | \hat{H}_{SO} | \Phi_{HS} \rangle | \langle \chi_{m+n} | \chi_m \rangle |^2 \delta(E_{m'}, E_m) \quad (1.5)$$

Where \hat{H}_{SO} is the spin-orbit coupling operator, $|\Phi_{HS}\rangle$ and $|\Phi_{LS}\rangle$ are the electronic wavefunctions of the HS and LS states, respectively. The above equation describes the transition probability from a vibrational state m' of the LS state to a vibrational state m of the HS state, such that the energy spacing between two consecutive levels is $\hbar\omega$. The matrix element is given by the second order correction of the spin-orbit coupling. $\langle \chi_m | \chi_{m'} \rangle$ is the Franck-Condon factor and which describes the overlap between the vibrational wavefunctions of the LS and HS states. The conservation of energy ensures that $m' = m + n$ such that $n = \Delta H / \hbar\omega$ and is called the reduced energy gap. The transition rate $k_{HL}(T)$ can be written as:

$$k_{HL}(T) = \frac{2\pi}{\hbar^2\omega} \langle \Phi_{LS} | \hat{H}_{SO} | \Phi_{HS} \rangle \frac{\sum_m | \langle \chi_{m+n} | \chi_m \rangle |^2 \exp(-m\hbar\omega/k_B T)}{\sum_m \exp(-m\hbar\omega/k_B T)} \quad (1.6)$$

When the temperature decreases and in the limit where T tends to 0 K, only the low energy vibrational levels of the HS state can be populated and it can be shown that the previous equation becomes temperature-independent. Thus, the temperature-independent process corresponds to a pure tunneling process in which the electronic energy of the HS state is transformed into a vibrational energy contribution of the LS state. At higher temperatures, the relaxation from HS to LS becomes thermally active and is seen as tunneling from thermally populated levels of the high spin-state having much larger Franck-Condon factors with the corresponding vibrational levels of the low spin-state.

Finally, another aspect we can add is that the relaxation time becomes faster when the transition temperature of the compound increases. This is due to the fact that $T_{1/2}$ increases when ΔH increases and so the energy barrier from HS to LS decreases, this is called the inverse gap energy law. As shown in figure 1.4-c for several SCO complexes, it was reported that the tetrazole-based (filled squares) SCO complexes possesses higher relaxation rates (10^{10} order of magnitude) comparing to the picolylamine-based (filled diamonds) SCO. This is an experimental evidence of the inverse gap energy law.

1.2.5 What can affect the relaxation rate ?

To study the relaxation to the LS state after obtaining the HS photoexcited state, different methods have been proposed. The first one consists in measuring the isothermal relaxation curves between the HS photoexcited state and the LS state at different temperatures. The goal is to build an Arrhenius type curve to extract the energy of the barrier between the HS and LS states. It has been proposed by Hauser, a mean field treatment of the relaxation curves in a model called self-acceleration [56, 89, 103–106]. The second way to measure the

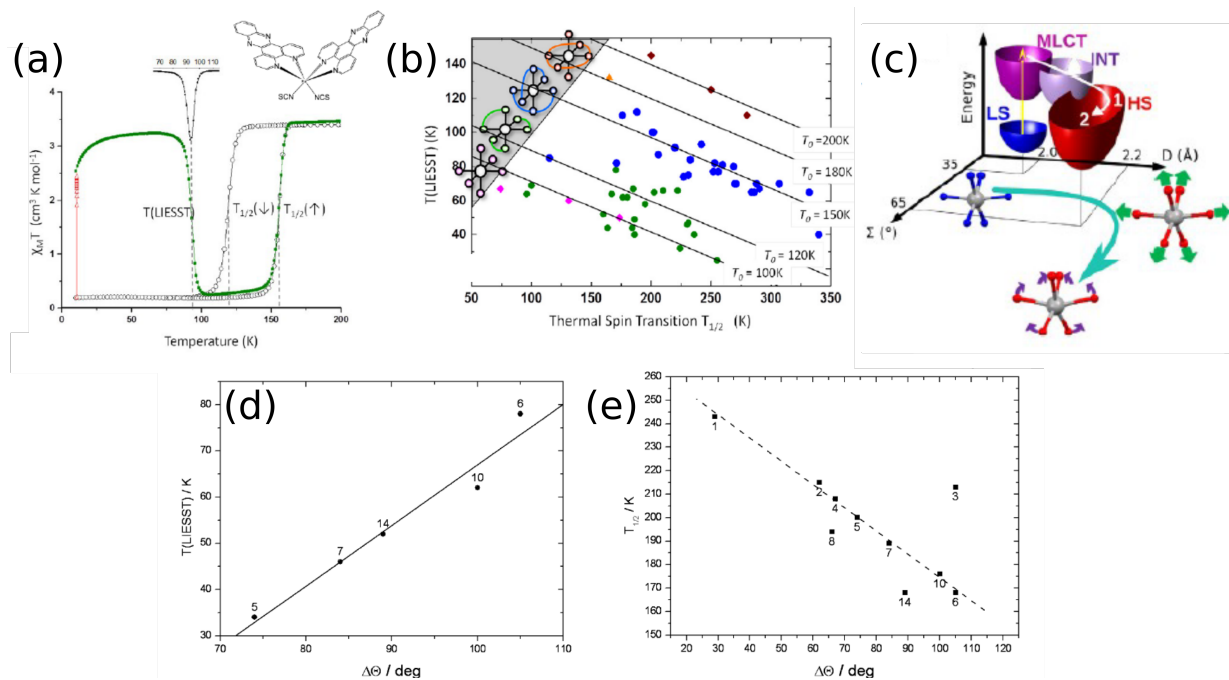


Figure 1.5: (a) T_{LIESST} experiment recorded for the mononuclear $[\text{Fe}(\text{dpp})_2(\text{NCS})_2]$ complex with (green) the temperature dependence of $\chi T(T)$ recorded in the cooling and warming modes without irradiation, (red) the change recorded during 1h of irradiation at 10 K, and (black) the behaviour recorded during the warming mode (0.3 K/min) when the light irradiation was switched off. The inset reports the $\frac{\partial \chi T}{\partial T}$ curve where the peak represents the T_{LIESST} . (b) $[T_{1/2}; T_{\text{LIESST}}]$ database. Violet diamonds and green circles stand for complexes based on mono- and bidentate ligands. Blue circles stand for tridentate ligand-based complexes, belonging mainly to the $[\text{Fe}(\text{bpp})_2]\text{X}_2 \cdot \text{S}$ family. The orange triangle relates to a macrocyclic ligand and purple stars to 3D Prussian blue analogs. The figures (a) and (b) were adapted from [39]. (c) Transformation pathway in the 2D (elongation ζ and bending Σ) space. Fast intersystem crossing [34, 90, 91], through possible intermediate states, first drives the Fe-ligand elongation with the activation and damping of a stretching mode, followed by the activation of bending modes. This figure was adapted from [97]. (d)-(e) Plot of the variation at the spin-crossover of the metal environment distortion, $\Delta\Theta$, versus (d) T_{LIESST} and (e) $T_{1/2}$ for a series of $[\text{Fe}(\text{L})(\text{NCS})_2]$ complexes with L is the ligand. The last two figures were taken from [37].

relaxation is to measure the temperature for which the thermal effects prevail, this temperature is called T_{LIESST} . This method was proposed by Herber in 1986 [41, 107] by following the thermal evolution of the photoexcited HS state under a temperature ramp. Note that T_{LIESST} is not an intrinsic quantity of the system and depends on the temperature ramp as well as on the measurement technique. Therefore, Letard [108] proposed the measurement of T_{LIESST} by irradiating at 10 K to promote the photoexcited HS state before turning off the light and ramping at 0.3 K/min (by convention). Thus, looking at the inflection point of the curve describing the $x_{\text{HS}}(T)$ in the dark, we find the T_{LIESST} as shown in figure 1.5-a.

Thanks to the standardization of the T_{LIESST} measurement, it enables the comparison of different compounds, the synthesis of molecules with the highest T_{LIESST} and also to rationalize the T_{LIESST} values obtained. Indeed, it has been found by Letard an empirical law that links the T_{LIESST} and the $T_{1/2}$, such that $T_{\text{LIESST}} = T_0 - 0.3 T_{1/2}$. The same result was found by Hauser [29, 39, 43, 104]. When $T_{1/2}$ increases then the relaxation becomes faster

(T_{LIESST} decreases), as expected from the inverse gap energy law. Moreover, thanks to this empirical law and as shown in figure 1.5-b, it has been demonstrated that many compounds depending on their ligand denticity (monodentate, bidentate, tridentate, etc.) belong to the same T_0 lines. However, some compounds do not fall into these T_0 lines and it has been shown that the main reason is the distortion (octahedral and trigonal) of the coordination sphere[34–40] of the molecule. Indeed, in addition to the change of the metal-ligand bond length, an anisotropic distortion of the coordination sphere can take place². Therefore, the energy diagram of the HS and LS potential wells should be represented taking into account the induced distortions as additional reaction coordinates, as shown in figure 1.5-c. These distortions have the effect of increasing the energy of the barrier and thus the stronger the distortion is, the higher the T_{LIESST} will be (as shown in figures 1.5-d/e). So the molecular scale is a good scale to tune the T_{LIESST} . Moreover, as the scale increases, the molecular packing acts as a perturbation that modulates the lifetime of the metastable HS state but it is a higher order effect.

The most striking example of the effect of distortion on the T_{LIESST} is that of the bidentate $\text{Fe}(\text{PM-BiA})_2(\text{NCS})_2$ (with PM-BiA = N-(2-pyridylmethylene)aminobiphenyl) [36, 108–111] which has two polymorphic phases I and II. Most of the bidentate compounds should fall in the $T_0 = 100$ K line, except for the polymorph I which falls in the $T_0 = 120$ K line which should normally be that of the tridentate. The reason is that the phase I is much more distorted than the II phase. In addition to these polymorphic effects, there are also reasons for symmetry breaking of the crystal packing as seen from reference [112] for the $\text{Fe}(\text{M}_1)_2(\text{BF}_4)_2 \cdot \text{S}$ ($\text{M}_1 = 4$ -(Isopropylsulfanyl)-2,6-di(pyrazol-1-yl)pyridine) compound. Thus, when the symmetry decreases, it is accompanied by a reduction of the total entropy of the system which consequently has the effect of increasing the $T_{1/2}$ and decreasing the T_{LIESST} , according to the empirical law of T_{LIESST} vs $T_{1/2}$ and thus respecting the inverse gap energy law.

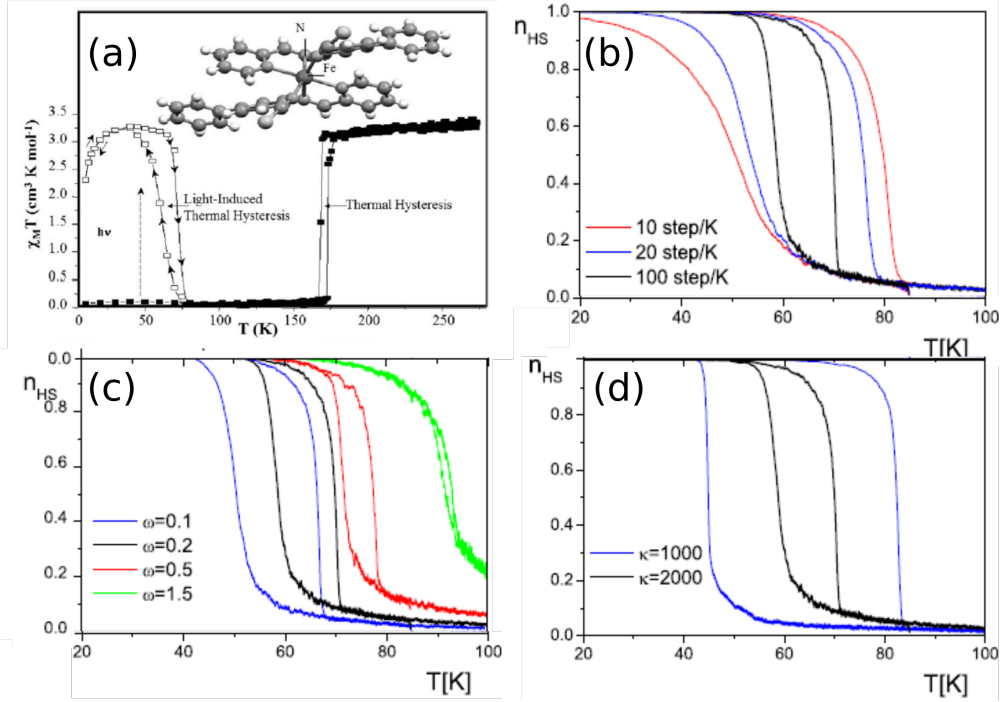


Figure 1.6: (a) Temperature dependence of the magnetic susceptibility times the temperature χT on cooling and heating modes for the $[\text{Fe}(\text{PM-BiA})_2(\text{NCS})_2]$ compound represented here. The first-order transition occurs around 170 K with a thermal hysteresis of 5 K. Under continuous laser irradiation 5 mW/cm^2 at 830 nm the HS state can be photoinduced and a quasi-static light-induced thermal hysteresis (LITH) appears between the cooling and warming modes. This figure was taken from [111]. Mechanoelastic simulations of the Light-induced thermal hysteresis: (b) dependence on temperature sweep rate, (c) irradiation intensity, and (d) interaction strength. This figure was taken from [113].

1.2.6 Light-Induced Thermal Hysteresis (LITH)

Among multiple kinds of hysteresis observed in spin-crossover compounds, the light-induced thermal hysteresis (LITH) is maybe the most spectacular [108, 114]. This was first demonstrated experimentally on $\text{Fe}(\text{PM-BiA})_2(\text{NCS})_2$ [108] solid and $[\text{Fe}_x\text{Co}_{1-x}(\text{btr})_2(\text{NCS})_2]\cdot\text{H}_2\text{O}$ solid-solution [114]. As shown in figure 1.6-a, the LITH is characterized by the appearance of a new thermal hysteresis loop within the photo-induced region, in the thermally-activated regime (below 100 K), during thermal cycles under constant irradiation. This new bistability induced by light is due to the direct competition between the $\text{LS} \rightarrow \text{HS}$ molecular photoexcitation and the $\text{HS} \rightarrow \text{LS}$ thermal relaxation of the metastable state and it has been interpreted as coming from the cooperativity of the system [108, 115–119]. Indeed, the relaxation process can be affected by cooperativity such that: i) for weakly cooperative systems: the relaxation rate obeys single-exponential and only a single photostationary state is established at all times, with a continuously lower steady state HS fraction for increasing temperature; ii) for strongly cooperative systems: the relaxation rate is highly non-linear and follows a sigmoidal kinetics ascribed to the so-called self-acceleration phenomenon [43, 104, 106, 108, 114–118, 120–124] and this leads to a two steady-state situation. This is explained in terms of an internal pressure which is built-up by the depopulation of the metastable HS state, owing long-range elastic interactions [104, 115, 116] which lowers the energy barrier. As a result, similarly to the thermal hysteresis, it was shown that the LITH is driven by domain nucleation process and leads to the coexistence of domains of two stable steady-states [86, 106, 108, 111, 125] and this gives rise to spectacular patterns in materials under constant illumination [111].

The LITH shape and width depend not only on the intrinsic properties of the material but also on experimental inputs, namely light intensity and temperature sweep rate [113, 126]. Firstly, as shown in figure 1.6-b, the LITH is a kinetic phenomenon by nature because it results from kinetic processes occurring simultaneously within the experimental time *i.e.* relaxation and photoexcitation. Therefore, one can measure an experimental LITH even if the molecular interactions are so small that a thermal hysteresis is not visible, so the LITH is magnified by kinetic effects and may be real or apparent. Indeed, to measure a real LITH,

²The first distortion parameter is denoted ζ and is defined as the average of the sum of the deviation of metal-ligand distance (Fe-L_i), from the mean distance:

$$\zeta = \frac{1}{6} \sum_{i=1}^6 |(\text{Fe-L}_i) - \langle \text{Fe-L} \rangle| (\text{\AA})$$

The octahedral distortion (Σ) is defined as the sum of the deviations from, 90° , of the 12 *cis* α angles and is written as:

$$\Sigma = \sum_{i=1}^{12} |90 - \alpha_i| (^\circ)$$

The trigonal distortion (Θ) is defined as the sum of the deviations, from 60° , of the 24 possible θ angles and is written as:

$$\Theta = \sum_{i=1}^{24} |60 - \theta_i| (^\circ)$$

You can consult the OctaDist (Octahedral Distortion calculator) website: <https://octadist.github.io/> which is an inorganic chemistry and crystallography program for computing the distortion parameters in coordination complexes.

one needs to sweep the temperature rate in an infinitesimally slow way [119, 127–130] to achieve the steady-state situation between the two processes and avoid extrabroadening effects. Secondly, as shown in figure 1.6-c, the LITH moves to higher temperature with increasing irradiation intensity because the relaxation processes are faster. However, the shift is larger for the descending temperature branch, and consequently the width of LITH decreases with increasing irradiation intensity; at the critical value the LITH is expected to disappear. Thirdly, as the LITH originates from the cooperativity of the system, mechanoe-lastic calculations in figure 1.6-d show that as the intermolecular interaction (encoded by κ here) increases, the LITH cycle is larger. Another experimental precaution is to ensure that the crystal should remain in the same crystallographic phase during one measurement cycle [128], because of the very different relaxation kinetics in two phases which may drastically influence the shape of the hysteresis. The observation of the LITH is achieved under suited conditions of temperature, light intensity and large intermolecular interaction.

LITH has been mostly studied in bulk Fe(II)-based spin-crossover compounds [51, 75, 79, 105, 108, 111, 113, 114, 117, 119, 124, 127, 128, 131–137], also in a SCO Fe(III)-based compound [138], Co-Fe Prussian Blue Analogues [139] and on cobalt valence tautomeric systems [140]. In a more original way, reference [14] demonstrated the existence LITH on an electronic device composed of $\text{Fe}^{\text{II}}((3,5-(\text{CH}_3)_2\text{Pz})_3\text{BH})_2$ on graphene and this by transport measurements of graphene electron conductivity. This proves a coupling mechanism between SCO molecules and graphene, providing electrical reading of the molecules/2D substrate interfaces. LITH belongs to the large family of light-induced instabilities [108, 113, 114, 125] including Light-Induced Optical Hysteresis (LIOH) [106, 114, 120, 135–137, 141], Light-Induced Pressure Hysteresis (LIPH) [79, 105, 106, 135] and Light-Induced Perturbed Thermal Hysteresis (LIPTH) [142, 143].

1.2.7 Soft X-ray Induced Excited Spin State Trapping (SOXIESST)

At low temperatures, the exposure of the soft X-rays to the SCO complexes can give rise to a Soft X-ray Induced Excited Spin-State Trapping (SOXIESST), i.e. $\text{LS} \rightarrow \text{HS}$ transition. In 1997, Collison [144] observed this phenomenon. It can be attributed to the similar trapping of the metastable HS state through a cascade of excited states as observed in the case of LIESST effect. However, the LIESST and SOXIESST cross sections are different. Then the mechanism of direct optical excitations of the molecule's electronic states is discarded. The proposed mechanism of SOXIESST by reference [145] stated that for the LS molecule, the injection of the x-ray induced secondary electrons to the unoccupied orbitals which leads to a weakening of the $\langle \text{Fe} - \text{N} \rangle$ coordination bond. Consequently, the bond lengthens, resulting in a reduction of the ligand field strength. These secondary electrons originate from a remote ionization caused by the X-rays [145, 146].

An important drawback of the X-rays is that in some cases the effect might not be reversible, this the so-called Soft X-ray Photochemistry (SOXPC). Indeed, the exposure of the X-ray might permanently damage the molecules or break some of its ligands and hence causing irreversibility of the spin-state switching. Finally, excitation from the LS state to HS state was also observed on the *K*-edge of Fe^{II} using Hard X-rays [146]. This effect is called Hard X-ray-Induced Excited Spin-State Trapping (HAXIESST).

1.3 On-surface SCO

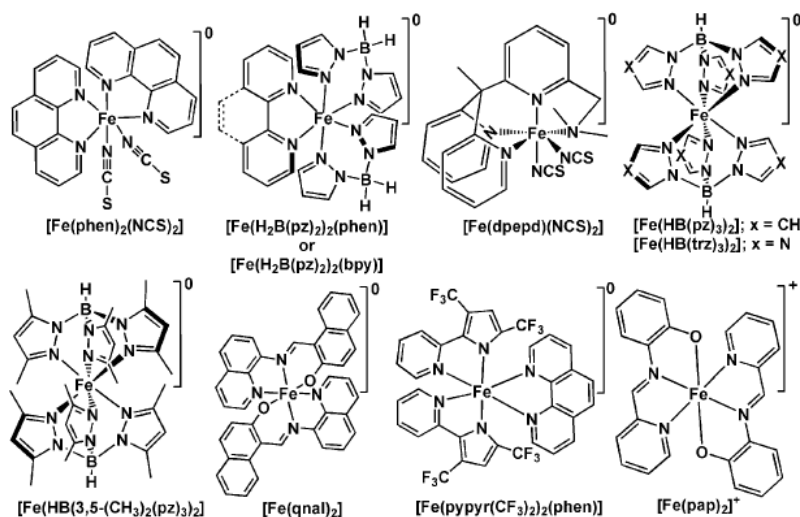


Figure 1.7: Reported sublimable SCO compounds. $\text{Fe}(\text{phen})_2(\text{NCS})_2$; $\text{Fe}(\text{H}_2\text{B}(\text{pz})_2)_2(\text{phen})$; $\text{Fe}(\text{H}_2\text{B}(\text{pz})_2)_2(\text{bipy})$; $\text{Fe}(\text{dpepd})_2(\text{NCS})_2$; $\text{Fe}(\text{HB}(\text{pz})_3)_2$; $\text{Fe}(\text{HB}(\text{tz})_3)_2$; $\text{Fe}((3,5\text{-(CH}_3)_2\text{Pz})_3\text{BH})_2$; $\text{Fe}(\text{qnal})_2$; $\text{Fe}(\text{pypyr}(\text{CF}_3)_2)_2(\text{phen})$; $[\text{Fe}^{\text{III}}(\text{pap})_2]^+$. Abbreviations: *phen* = 1,10-phenanthroline; $\text{H}_2\text{B}(\text{pz})_2$ = bis(hydrido)bis(1H-pyrazol-1-yl)borate; *bipy* = 2,20-bipyridine; *dpepd* = 1,6-[1,1-di(pyridin-2-yl)ethyl]-pyridin-2-yl-N,N-dimethylmethanamine; *pz* = pyrazolyl; *tz* = triazol-1-yl; *pap* = N-2-pyridylmethylidene-2-hydroxyphenylamino; *pypyr* = 2-(20-pyridyl)pyrrolide; *qnal* = quinoline-naphthaldehyde. This figure was taken from [147].

Toward the miniaturization of nanotechnology devices[12, 21, 25, 147–153], the synthesis of SCO molecules that can sublime under vacuum and deposit on surfaces[81, 154–164], without fragmentation, is a great challenge for the chemist community. Indeed, it is essential to understand the modification of SCO properties from powder, single crystals[4, 9, 23, 38, 40, 42, 130], solution[42, 43], nanoparticles[4, 9, 150, 151, 165–171] to on-surface (from thick to ultrathin layers/single molecules) forms[9, 147, 156, 172–175]. Indeed, the key point is thus the preservation of the molecular switching in those particular cases in order to introduce them in molecular electronic or spintronic devices [1, 6, 13, 16–20, 22, 25, 176–183]. The list of molecules studied in the literature are shown in figure 1.7. Moreover, the investigation of the spin transition at the ultrathin level requires more sensitive techniques than standard magnetometry. Indeed, element-sensitive X-ray absorption spectroscopy (XAS) is a powerful tool to investigate the spin transition. Using soft X-ray, the evolution of the L_3 -edge of Fe^{II} is a fingerprint of the HS \rightleftharpoons LS transition under external perturbation.

In the next sections, we will give an overview of what has been done for these molecules on various surfaces.

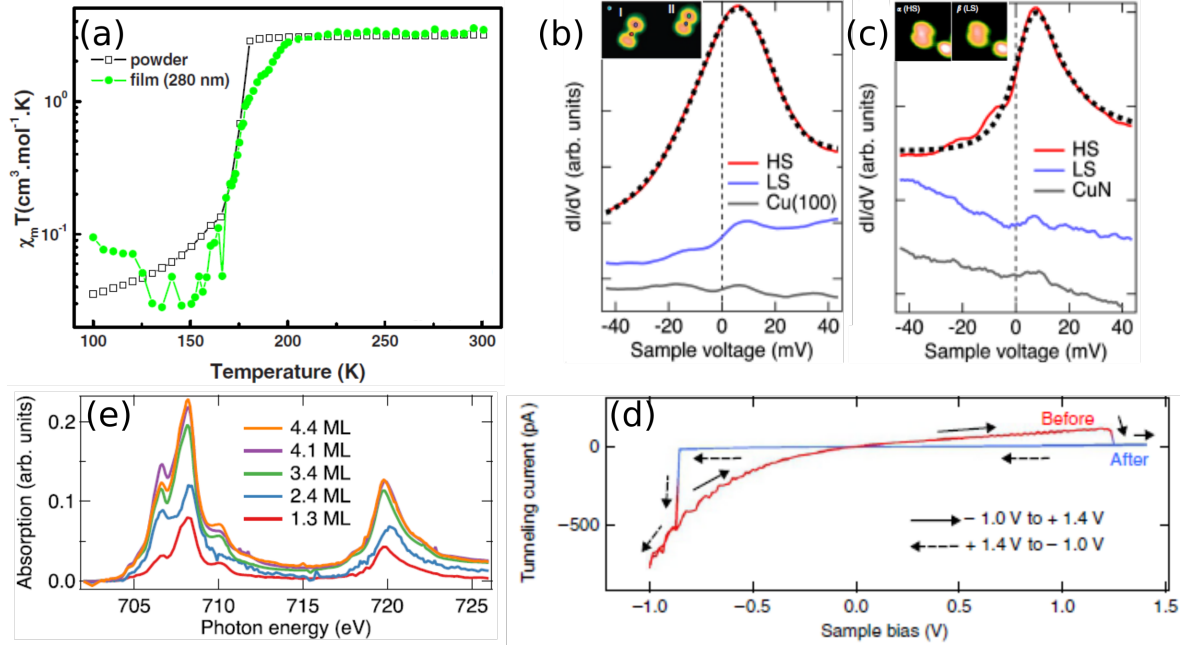


Figure 1.8: (a) Temperature dependence of $\chi T(T)$ for the powder and the 280 nm-thick film on silicon substrate. This figure was adapted from [184]. (b-c) Differential conductance measured on the center of HS molecules (red) and LS molecules (blue) adsorbed on Cu(100) (b) and Cu₂N/Cu(100) (c). Inset: Topography of HS and LS molecules on Cu(100) (b) and Cu₂N/Cu(100) (c). (d) $I(V)$ curves of isolated Fe-phen molecules on the Cu₂N/Cu(100) surface recorded on the centre of the molecule showing a hysteretic switching behaviour (tunnelling conditions for tip stabilization: 1 V, 100 pA). The high (red) and low (blue) junction conductance states are visualized using STM images. The figures (b-d) were adapted from [185]. (e) Fe L_{2,3} XAS spectra recorded for Fe-phen ultra-thin films deposited on Cu(100). This figure was adapted from [156].

1.3.1 Fe(phen)₂(NCS)₂

The first reported example of a successful deposition of SCO molecule was a 280 nm thick film of the Fe(phen)₂(NCS)₂ complex on SiO₂ [184] where the complex exhibits a complete and gradual thermal transition without hysteresis with $T_{1/2} = 175$ K (figure 1.8-a).

For on-surface studies, this molecule was also studied (experimentally and theoretically) on different non-magnetic [156, 185–187] and ferromagnetic [156, 188, 189] metallic substrates. On Cu(111) [156, 185, 187], it has been shown, by STM and XAS, a coexistence of HS and LS states at low temperature with spin-state blocking in the submonolayer range. Reference [185] shows, by STM, that the molecule does not switch due to the strong chemisorption of the molecule on the surface [190, 191], i.e. strong coupling between the NCS groups and the surface. Moreover, Scanning Tunneling Spectroscopy (STS), in figure 1.8-b (red), shows that the HS configuration is characterized by the appearance of a Kondo peak in the density of state of the molecule, due to the coupling between the localized unpaired spins of the molecule with the delocalized electronic states of the substrate. In the contrary, the absence of the Kondo peak reflects the LS configuration, as shown in figure 1.8-b in blue. Thus, in order to regain the spin transition property, the interaction with the substrate must be reduced. To do so, one strategy consists on introducing a Cu₂N

spacer layers between the molecules and Cu(100). The authors demonstrated that there is still a spin coexistence as shown in figure 1.8-c. Moreover, it was possible to switch a single molecule between the two configurations by the electric field produced by the STM tip. It was proposed by reference [192] a simple transition-state model involving modifications to the energy barriers between LS and HS states due to a tip-induced electric field through the Stark effect. Moreover, as shown in figure 1.8-d, by sweeping the voltage bias from negative to positive and reversely, the $I(V)$ characteristic curve shows a hysteretic behavior, where the lower conductance (blue) is the LS state whereas the higher conductance (red) is the HS. This work was supported by Density Functional Theory (DFT) simulations [186]. Another strategy to decrease the molecule-substrate interaction is to increase the molecular thickness. In references [156, 187], they performed temperature-dependent XAS measurements for different molecular thicknesses on Cu(100), as shown in figure 1.8-e, and in which they observe a strong LS character with partial thermal-induced switching. In references [156, 187], you can find the other studies on Cu(111), Au(111) and Au(100).

In the literature, the only ferromagnetic substrate on which this molecule was deposited is on Co/Cu(111) [188]. On the Co islands, the molecules are chemisorbed and some decompose as well. Of those that do not decompose, it has been seen by SP-STM and STS that HS molecules couple magnetically with the magnetic moments of cobalt. This was confirmed by DFT calculations by reference [188, 189] in which they showed a ferromagnetic coupling between the Fe(II) and Co through NCS groups. However, the switching of the molecules on cobalt was not effective, in contradiction with the conclusions of DFT results made by reference [189]. Moreover, they study the effect of introducing several Cu decoupling layers on top of Co/Cu(111). They found that the magnetic coupling changes sign with the Cu thickness, in an oscillatory fashion due to the interlayer exchange coupling [193–196].

1.3.2 $\text{Fe}(\text{H}_2\text{B}(\text{pz})_2)_2(\text{L})$ and functionalized analogues

Historically, this molecule has been synthesized with two ligands, namely $\text{L} = \text{phen}$ or bipy . The first successful example of the deposition by sublimation on surfaces was reported in reference [197]. The deposition of a 480 nm (resp. 410 nm) thick film of the phen (resp. bipy) on glass (resp. silicon) substrate exhibits photoconversion with a T_{LIESST} comparable to bulk as well as a thermal transition with a thermal hysteresis width and $T_{1/2}$ also comparable to bulk. Another study of thick films on Kapton, reported by reference [198], is in agreement with reference [197].

1.3.2.1 $\text{L} = \text{phen}$

At the ultrathin film level, this molecule has been extensively studied on Au(111) by XAS and STM as a mono- and bilayer [199, 201]. By XAS and STM, they have shown that the molecules in the first layer decompose on the surface into the four-coordinate complex $[\text{Fe}(\text{H}_2\text{B}(\text{pz})_2)_2]$ and phen [199]. However, as shown in figure 1.9-a, the STM images confirm the integrity of the molecule for the bilayer but with the first layer of molecules decomposed and acting as a spacer between the molecules and the substrate. As a result, the second layer shows a thermal-induced SCO with a more gradual characteristics compared to the

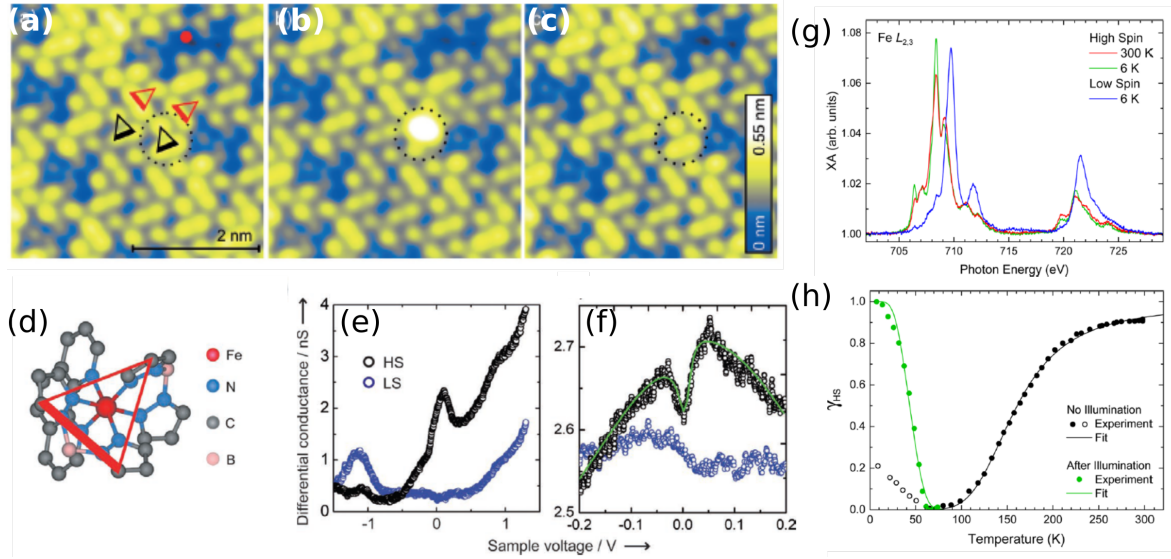


Figure 1.9: (a-c) Constant-current STM topographs with a submolecular resolution of a double layer of the molecule on Au(111) at $V = 1.6$ V and $I = 50$ pA. Triangles in (a) indicate selected molecules (see figure (d)). Dotted circles in (a)-(c) indicate a molecule which is switched from LS (a) to HS (b) and back to LS (c). (d) View of the molecule along a pseudo-trigonal molecular axis. The triangle connecting three pyrazole groups is used to represent the orientation of the molecule. (e-f) Spectra of the differential conductance dI/dV of the molecule in its LS (blue circles) and HS states (black circles). (e) is the wide energy range and (f) is around the Fermi level. The figures (a-f) were adapted from [199]. (g) Temperature-dependent Fe $L_{2,3}$ XA spectra of 0.4 ML of the molecule on HOPG. Spectra before and after illuminating the sample with green light at $T = 6$ K are shown in blue and green, respectively. (h) HS fraction molecules as a function of temperature during cooling the sample without illumination (black solid symbols) and after saturation of the light-induced HS state during heating the sample (green solid symbols). The temperature-induced SCO is fitted with a model without cooperative interactions between the molecules (black line). The relaxation of the light-induced HS state is fitted with an Arrhenius law (green line). Below 70 K (black open symbols), the molecules undergo an X-ray induced transition to the HS state caused by the measurement. The last two figures are adapted from [200].

bulk material. In addition, below 90 K, excitation to the high spin-state is mediated by the SOXIESST for the thicker layer. As for the $\text{Fe}(\text{phen})_2(\text{NCS})_2$ molecule on Cu(100) [185], figures 1.9-e/f show that the HS state is characterized by the presence of a Kondo resonance at the Fermi level in the $I(V)$ curve, whereas the LS state has a lower conductance and do not show this zero-bias anomaly. Furthermore, in reference [199] the authors were able to reversibly switch the parent $\text{Fe}(\text{H}_2\text{B}(\text{pz})_2)_2(\text{phen})$ molecule in the second layer using an STM tip, as shown in figures 1.9-a (HS), b (switching to LS) and c (relaxation to the HS state). This phenomenon is commonly referred to as Electron-Induced Excited Spin-State Trapping (ELIESST) [201]. This effect has been explained as follows: the injection of tunneling electrons from the tip into the unoccupied d -orbitals of the molecule in the LS state will excite the molecule into an LS^- state and it will therefore relax statistically to either the LS or HS (metastable) state with the excess electron tunneling to the substrate. When the molecule goes into the HS state, its spin-state has been shown to be preserved for a few hours.

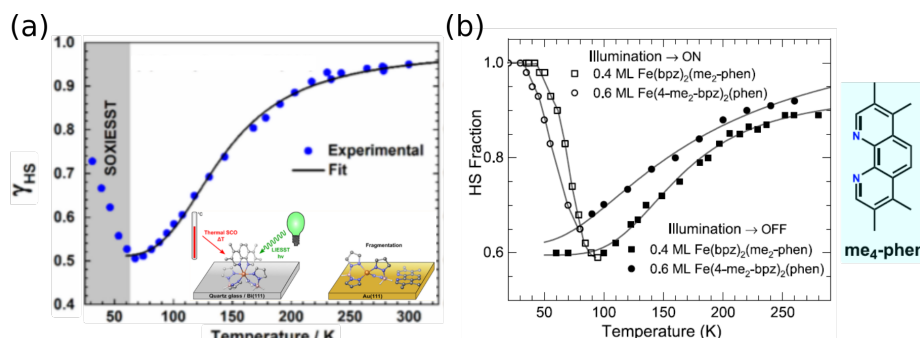


Figure 1.10: (a) Temperature dependence of HS fraction of 0.3 ML of $\text{Fe}(\text{H}_2\text{B}(\text{pz})_2)_2(\text{me}_4\text{-phen})$ on Bi(111) (blue dots). The inset sketches the intact nature and the fragmentation of both molecules on Bi(111) and Au(111) respectively. This figure were adapted from [202]. (b) Thermal-induced SCO of 0.4 ML of $[\text{Fe}(\text{bpz})_2(\text{me}_2\text{-phen})]$ (squares) and 0.6 ML of $[\text{Fe}(4\text{-me}_2\text{-bpz})_2(\text{phen})]$ (circles) on HOPG. The open and solid circles (and squares) represent, respectively, the spin transition with and without light exposure. Solid lines are guides to the eyes. This figures was adapted from [203].

Toward the reduction of the molecule-substrate interaction for the stability of the molecules, two possible approaches are: either changing the substrate or functionalization of the phenanthroline ligand. The first strategy has been explored by reference [200]. Indeed, the deposition of this molecule as a sub-monolayer (0.4 ML) on another surface (HOPG) showed a complete thermal switching, in addition to the complete LIESST transition at 6 K, as shown in figures 1.9-g/h. Moreover, in reference [202], 0.3 ML coverage of the molecule on Bi(111) shows no decomposition (in contrast to Au(111)), and exhibits thermal-, light-, and X-ray-induced spin-state switching. In contrast to the HOPG, at this coverage the transition is incomplete.

To promote the switching on Au(111), reference [202] synthesized a functionalized analogues to the parent molecule the $[\text{Fe}(\text{H}_2\text{B}(\text{pz})_2)_2(\text{me}_4\text{-phen})]$. Indeed, the introduction of methyl groups may enhance the SCO complexes-surface interactions for this class of molecules. The latter complex decays like its parent molecule on Au(111) (see inset of figure 1.10-a) but shows a partial SCO under X-ray, light and temperature on Bi(111), as shown in figure 1.10-a. Moreover, in reference [204], they investigate the influence of methyl and chloro substituents on the spin transition and they synthesized the following analogues of the SCO complex $[\text{Fe}(\text{H}_2\text{B}(\text{pz})_2)_2(\text{L})]$ i.e., $\text{L}_1 = 4\text{-methyl-1,10-phenanthroline}$, $\text{L}_2 = 5\text{-chloro-1,10-phenanthroline}$, $\text{L}_3 = 4,7\text{-dichloro-1,10-phenanthroline}$ and $\text{L}_4 = 4,7\text{-dimethyl-1,10-phenanthroline}$. First, in the solid-state the molecules L_3 and L_4 shows a locking in the HS state, for all temperatures, due to strong $\pi\text{-}\pi$ interactions between the ligands while for the molecules L_1 and L_2 , they showed a complete LS to HS thermal switching. Moreover, 100 nm thick films of all the molecules on quartz surface showed a complete thermal and light-induced SCO. This has been interpreted as a decrease of the intermolecular interactions, at least for L_3 and L_4 in films as compared to the bulk. On the other hand, for a thin film of 4 ML of L_4 on HOPG the spin transition becomes incomplete and this is certainly due to specific interactions with the surface. In reference [205], the phenanthroline ligand was substituted to diarylethene-phenanthroline (L_5) and was successfully evaporated (5nm) on Au(111) and (sub-ML) on HOPG. On the latter, thermally-induced reversible switching and their photo-switching at cryogenic temperatures have been demonstrated. Finally, in reference [203], they functionalized either the $\text{H}_2\text{B}(\text{pz})_2$ or the phen groups by methyl groups,

namely, $\text{me}_2\text{-phen}$ (L_6), $\text{me}_4\text{-phen}$ (L_7) (inset of figure 1.10-b in blue box), $4\text{-me}_2\text{-H}_2\text{B}(\text{pz})_2$ (bpz-1) and $\text{Fe}(\text{H}_2\text{B}(\text{pz})_2)_2(\text{dpq})$ (dpq = dipyrido[3,2-f:2',3'-h]-quinoxaline (dpq), deposited on an HOPG surface. As stated by the author and as seen in reference [204], the addition of methyl groups to the parent SCO complexes always results in a partial or a complete loss of the SCO on the surface. Indeed, 0.4 ML and 0.6 ML of the parent complex functionalized with the L_6 and bpz-1 ligands respectively, shows a partial thermal and light-induced SCO on HOPG as depicted in figure 1.10-b. To rationalize the recovery of the SCO behavior, the authors measured N K -edge XA spectra of the methylated complexes. This indicates that the addition of methyl groups leads to two different classes of molecules. In the case of $[\text{Fe}(\text{H}_2\text{B}(\text{pz})_2)_2(\text{me}_4\text{-phen})]$ on the HOPG surface, the molecule shows an orientation and a geometry similar to the parent molecule, but the complex is HS-locked, probably due to $\text{CH}-\pi$ interactions between the methyl groups and HOPG [198]. In contrast to that, the complexes $[\text{Fe}(\text{H}_2\text{B}(\text{pz})_2)_2(\text{me}_2\text{-phen})]$ undergoes an incomplete SCO on HOPG and shows a random orientation on the surface without observable distortion of the molecule on the surface.

1.3.2.2 L = bipy

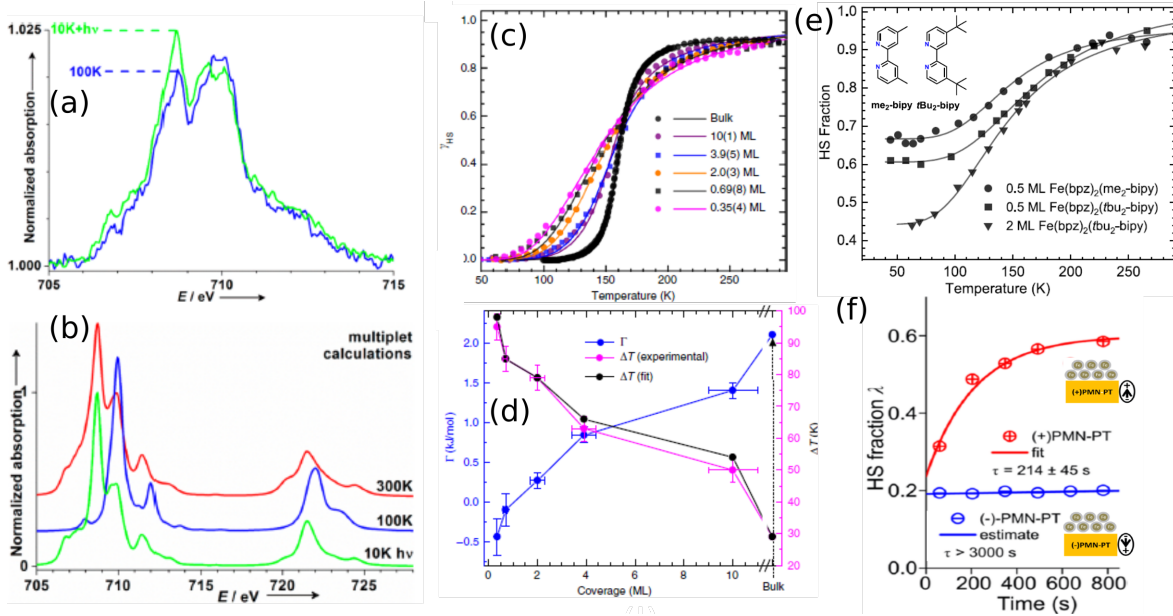


Figure 1.11: (a) Comparison of spectra at the L_3 edge for the submonolayer sample of the molecule at 10 K before (blue) after laser irradiation (658 nm, 15 mW.cm^{-2} , in green). (b) Ligand field multiplet (LFM) calculations of the spectra. The figures (a-b) were taken from [206]. (c) HS fraction as a function of temperature for different coverages of the molecule on HOPG along with that of the bulk data; the dots represent experimental data while the solid lines are fits obtained from the Slichter-Drickamer model. (d) Dependence of the interaction parameter Γ (left-axis) and the transition width ΔT (right-axis) upon the coverage. These figures were taken from [207]. (e) Thermal-induced SCO of 0.5 ML of $[\text{Fe}(\text{bpz})_2(\text{me}_2\text{-bipy})]$ (solid circles); $[\text{Fe}(\text{bpz})_2(\text{tbu}_2\text{-bipy})]$ of 0.5 ML and 2 ML (solid squares and solid triangles, respectively) on HOPG [203]. (f) Time-dependent HS fractions of the molecule on PMN-PT under the SOXIESST effect [208].

References [209–211] reported by STM and XAS the change of the SCO behavior and

the growth of the complex on Au(111) from bilayer to multilayer. STM experiments show that the bilayer level form a well-ordered and uniform film whereas at larger thicknesses, a poorly-ordered and more granular polycrystalline film is obtained. For the bilayer film, they confirm by local spectroscopy, conductance imaging and ultraviolet photoemission spectroscopy (UPS) and XAS the existence of both spin-states at all temperatures. On the contrary, the multilayer film exhibits a more LS feature. This confirms the role of the thickness in the properties of SCO molecules.

In reference [206], the authors were interested in the SCO behaviour of this molecule on Au(111) (see figure 1.11-a). They demonstrate the preservation of the (reversible) thermal and light properties of SCO molecules but the transition is incomplete with a transition of 50% at low temperature and 80% at high temperature. As many molecules are pinned in one state at all temperatures, this demonstrates the effect of the substrate in modifying the SCO properties. In addition, in this paper there are simulations of HS XAS spectra (see chapter 2 and 3), using the LFM calculations, to fit their experimental XAS spectra. Using octahedral symmetry (O_h) with parameters $10D_q = 1$ eV for HS and 2.2 eV for LS, the simulated spectra show good agreement with the experimental spectra, as shown in figure 1.11-b. Note that these crystal field values can be compared with the range predicted for the occurrence of SCO from ligand field theoretical considerations [28].

In references [145, 207], they investigate the thermal, photo and soft x-ray induced SCO on HOPG for various thicknesses. They demonstrate that at the sub-ML level, the transition was complete by light or temperature. Temperature-dependent XAS measurement at different thicknesses shows that the thermal-induced SCO became more and more abrupt as they increase the number of layer while the temperature of transition decreases comparing to the bulk (see figure 1.11-c). They discussed this effect as coming from the cooperativity of the system which increases with the system size. Quantitatively, they used the mean-field Slichter Drickamer model to extract the cooperativity of the system. As depicted in figure 1.11-d, they showed that below 2 ML, the cooperativity is negative which account to antiferroelastic interaction and favors the LS-HS configuration. In the contrary, above 2 ML, the sign of Γ is positive and this accounts to ferroelastic interaction and favors LS-LS or HS-HS configurations.

In reference [203], they functionalized either the $H_2B(pz)_2$ or the bipy groups by me_2 -bipy (L_8) and $[Fe(H_2B(pz)_2)_2(tbu_2-bipy)]$ (tbu_2). Similarly to the previous section, the methylation results [204] in a partial or a complete loss of the SCO due to CH- π interactions between the methyl groups and HOPG [198] as confirmed by N-K edge XAS spectra. However, the complexes L_8 and tbu_2 undergo an incomplete SCO on HOPG (figure 1.11-e). In another ligand functionalization study, reference [212] were able to synthesize the first SCO-amphiphile complex, namely, $[Fe(H_2B(pz)_2)_2(C_{12}-bipy)]$ (C_{12} -bipy = dodecyl[2,2-bipyridine]-5-carboxylate). Studies on the powder and on a 10 nm thin film sublimated on glass or SiO_2 show that the spin properties are retained in both cases. Moreover, in both cases, the structures are the same. To my knowledge, this is the only system that preserves its structural and spin transition properties independently of its size.

This molecule has also been studied on organic ferroelectrics, namely polyvinylidene fluoride with trifluoroethylene (PVDF-TrFE) [213]. These authors found that the molecules located in a ferroelectric saturated 'up' (resp. 'down') state, exhibit an HS (resp. LS) state that persists up to 100 K, well below the SCO transition temperature. This may pave the way

to the use of molecular magneto-electric effect on devices. Reference [214] demonstrates this locking of the spin-state, for ultrathin films, in direct contact with dielectric substrates such as SiO_2 and Al_2O_3 . Another original substrate studied for this molecule is on the ferroelectric PMN-PT $[\text{Pb}(\text{Mg}_{1/3}\text{Nb}_{2/3})\text{O}_3]_{1-x}[\text{PbTiO}_3]_x$, $x = 0.32$) [208]. The temperature conversion shows a complete transition from LS to HS between 100 and 300 K without influence of the ferroelectric polarization of the substrate. However, in the temperature regime in which SOXIESST is effective, it was shown that the conversion rate from LS to HS via the SOXIESST effect was more efficient when the substrate ferroelectric dipoles point towards the substrate compared to the other polarization as shown in figure 1.11-f. Through these studies, the authors shed light on the origin of the SOXIESST as secondary electron scattering generated by X-rays at the molecular level. The reason for this large difference is given by the different electronic affinities of the two differently-polarized substrates. As suggested by the authors of this paper, this experiment tends to give another use to the SCO molecules so that they could be used as detectors of electrons moving in the substrate at energies lower than the electron affinity of the substrate.

Finally, reference [215] studied this molecule on magnetic oxide substrates, namely $\text{NiCo}_2\text{O}_4(111)$ and $\text{La}_{0.65}\text{Sr}_{0.35}\text{MnO}_3(001)$ (LSMO). These substrates lock the spin-state of the molecule predominantly in the LS state, well below the transition temperature for bulk, and which can switch to the HS state with X-rays. The difference between these two substrates is that the relaxations from the photoexcited HS state to the LS state are highly dependent on the competition between X-rays and an applied alternating magnetic field. Indeed, when the applied magnetic field is greater than the coercive field of the substrate, the transition to the LS state is much faster for $\text{NiCo}_2\text{O}_4(111)$ than on LSMO. Indeed, the measurements under magnetic field were made by exposing the molecules as little as possible to X-rays and which then suggest that the relaxation time of the molecules on this substrate is much lower than on the other two because the X-rays promote the molecules from LS to HS while the magnetic field helps them to relax to the LS state. Thus, the authors speculate on the possible existence of magnetic coupling between the molecules and the substrate that would influence this relaxation.

1.3.3 $\text{Fe}(\text{pypyr}(\text{CF}_3)_2)_2(\text{phen})$

This molecule has been deposited on numerous substrates having different electronic properties. The first study is done by reference [216] on 40 ML thick molecules on 1T- TiTe_2 (Te-Ti-Te sandwich layers covalently bound with Van der Waals interactions) in which it was shown that the thermal transition is complete but with a lower transition temperature than the bulk. LIESST and SOXIESST effects have also been shown on this system. On the metals ($\text{Au}(111)$ and $\text{Co/Cu}(100)$), a sub-monolayer of molecules decompose completely (black XAS spectra in figure 1.12-a), so there is no spin-state switching. In contrast, 5 ML of molecules on $\text{Au}(111)$ shows an efficient and fully reversible switching with temperature. Moreover, figure 1.12-b shows that for sub-monolayer coverages on semimetallic (0.4 ML SCO on HOPG) and layered transition metaldichalcogenide semiconductors (0.4 ML SCO on HfS_2 and WSe_2) exhibits a complete LIESST effect for the former while only 80 % of the molecules exhibit LIESST for the latter two. Finally, on 0.4 ML of SCO on graphene/ $\text{Ni}(111)$, there is 80 % residual HS proportion at low temperature. All these experiments show that there

is an effect of the electronic properties of the substrate on the integrity of the molecules. Indeed, the authors propose that the lower the density of state at the Fermi level, the more the molecule keeps its integrity and functionality on the surface.

1.3.4 $\text{Fe}(\text{qnal})_2$

The only surface study relating to this complex was carried out by reference [161] and the main result is shown in figure 1.12-c. The molecule in bulk exhibits a complete LIESST effect and a transition effect under temperature which is also complete, while on 50 nm thick film of the molecule deposited on the Au(111) substrate also exhibits an almost complete photoconversion and a thermal transition very comparable to bulk but with a lower $T_{1/2}$ relative to bulk.

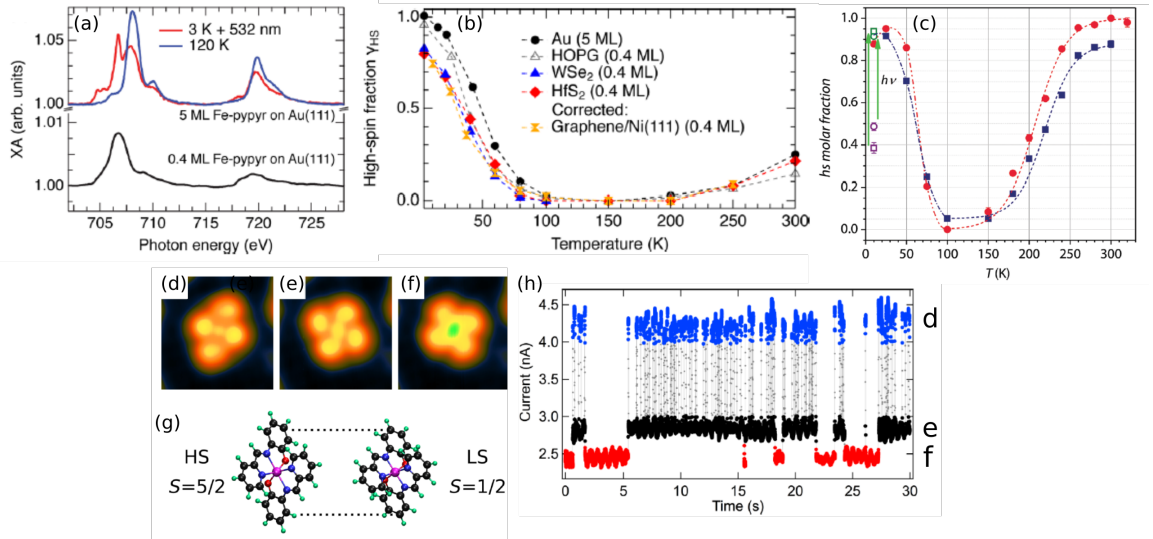


Figure 1.12: (a) XA spectra acquired on 5 ML Fe-pypry on Au(111) at 3 K under illumination with a 532 nm laser (red curve) and at 120 K (blue curve). The lower spectrum (black curve) was measured on 0.4 ML Fe-pypry on Au(111) at 100 K. (b) Evolution of the fraction of HS molecules as a function of temperature for 0.4 ML Fe-pypry on different substrates and 5 ML Fe-pypry on Au(111) as a reference. The samples were constantly illuminated with 532 nm laser light. These figures were adapted from [162]. (c) Temperature variation of the HS molar fraction for $\text{Fe}(\text{qnal})_2$ determined by the interpolation of the corresponding XAS spectra. Purple and green empty symbols refer to the HS molar fraction before and after light-irradiation. Short dashed lines for $T > 100$ K are Boltzmann fits of the experimental data, while dot dashed lines for $T < 100$ K are interpolations of the experimental data and represent only a guide for the eyes [161]. (d-g) STM topographs of the $[\text{Fe}^{\text{III}}(\text{pap})_2]^+$ molecule on $\text{Cu}_2\text{N}/\text{Cu}(100)$ (d) in its initial state (e, f) in the switched states. (g) Molecular structure resulting from gas-phase DFT calculations of HS and LS $[\text{Fe}^{\text{III}}(\text{pap})_2]^+$. (h) Time series of the tunneling current measured with the tip positioned over the center of a $[\text{Fe}^{\text{III}}(\text{pap})_2]^+$ molecule. The current trace shows three current levels colored in blue, black, and red from which the state of the molecule (d, e, and f) can be inferred. The current feedback was opened at a current of 2.4 nA and a voltage of 2.5 V. The figures from (d-h) were taken from [217].

1.3.5 $[\text{Fe}^{\text{III}}(\text{pap})_2]^+$

This molecule has a spin of 1/2 in the LS state and 5/2 in the HS state, as shown in figure 1.12-g. This molecule is a bit special because it differs from the most synthesized SCOs by the fact that it is based on iron(III) and it is a charged molecule. Therefore, it is synthesized with a perchlorate counterion (ClO_4^-) to stabilize the bulk form of the molecule. In reference [163], using standard sublimation technique for deposition, they showed that the molecule is deposited with its counter-ion on Au(111) but this does not affect the STM study of individual $[\text{Fe}^{\text{III}}(\text{pap})_2]^+$. However, in order to remove the counterion, the traditional methods of sublimation does not work. Its deposition is done with another technique namely electrospray ionization deposition (ESID) [21]. Thus, the authors investigate the SCO properties by the STM technique on $\text{Cu}_2\text{N}/\text{Cu}(100)$ [217]. They show that the $[\text{Fe}^{\text{III}}(\text{pap})_2]^+$ molecule switches reversibly between three different configurations, as depicted in figures 1.12-d/e/f, with three tunneling current levels (cf. Fig 1.12-h) but without identification of the spin-state. From comparison with DFT calculations, they deduce that the three spin-states correspond to: a pure HS state and two different LS states with most likely different electronic couplings to the substrate. This represents the first report of combined intrinsic (spin transition) and extrinsic (different coupling to the substrate) switching of a spin-crossover compound on a surface.

1.3.6 $\text{Fe}(\text{HB}(\text{L})_3)_2$

1.3.6.1 $\text{L} = \text{tz}$

In references [218, 219], they investigate the thermal-induced switching for different molecular thicknesses, from 20 nm to 200 nm, on fused silica substrates. As shown in figure 1.13-a, all the thicknesses exhibit an abrupt and complete thermal SCO transition at any thickness with a transition temperature, above room temperature, of 338 K, similarly to the bulk. Surprisingly, the authors find that the thermal transition temperature ($T_{1/2}$) shifts toward high temperatures (about 3 K) when the thickness is reduced from 200 nm to 45 nm. Generally on metals, the reduction of the system size is accompanied by the increase of the residual HS fraction at low temperature and the suppression of the hysteresis cycle. This is clearly not the case here as the volume properties seem to still dominate.

In reference [101], the authors focus on the finite size effect on the out-of-equilibrium switching dynamics using time-resolved optical spectroscopic measurements. They showed that during the transition from LS to HS, in the *ps* timescale (first step on figures 1.13-b), the variation of the HS population (Δn_{HS}) follows a linear law with the laser pulse energy (figure 1.13-d in blue). At the *ns* timescale, we also see the appearance of a second step (figures 1.13-b) which corresponds to a non-linear variation of Δn_{HS} with the laser pulse energy (figure 1.13-d in green) and which tends to disappear when the temperature decreases (figure 1.13-c) and/or the molecular thickness decreases (figure 1.13-e). Figure 1.13-d shows the variation of the HS population in the first step (resp. second step) that the authors have named $\Delta n_{\text{HS}}^{\text{hv}}$ ($\Delta n_{\text{HS}}^{\text{th}}$) in the sub-*ps* (resp. *ns*) regime and at two different temperatures, the non-linearity in the thermal regime appears clearly where in the sub-*ps* regime, the relation is always linear. The authors discuss these non-linearities, which arise at timescales of a few

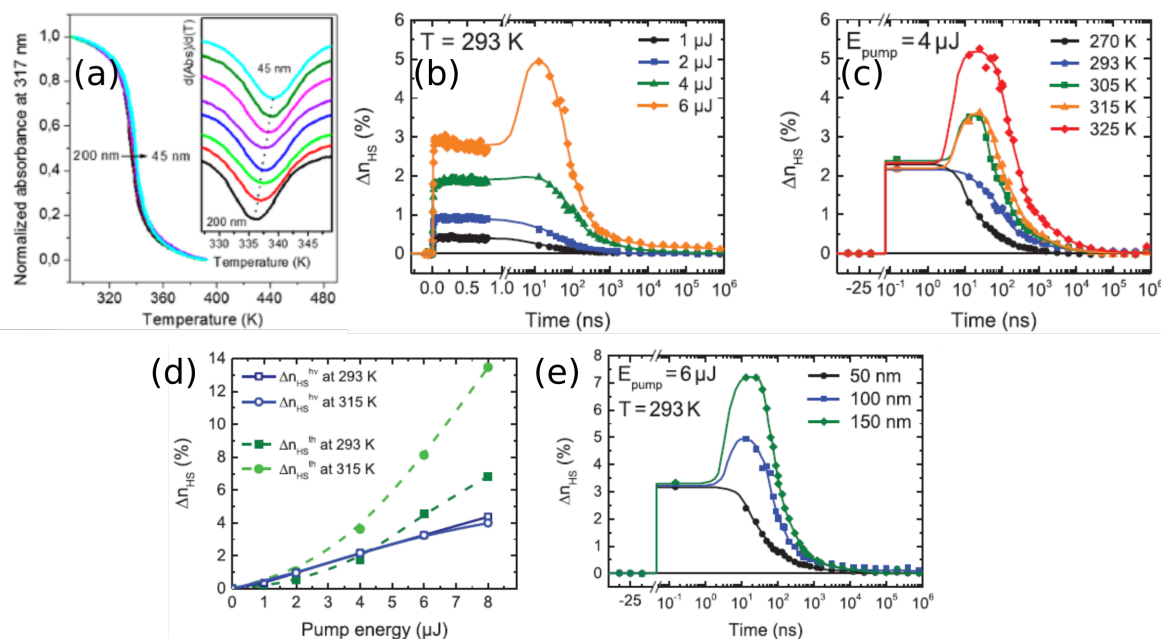


Figure 1.13: (a) Temperature dependence of the normalized absorbance at 317 nm along the fourth heating-cooling cycle recorded at 1 K/min scan rate for eight films with different thicknesses between 45 and 200 nm. The inset shows the derivatives of the absorbance curves in the heating mode. This figure was taken from [218]. (b) Time evolution of the increase of the HS proportion (Δn_{HS}), at room temperature in the 100 nm thick film following a femtosecond laser pulse with various excitation energies. (c) Time evolution of Δn_{HS} in the same film following an identical 4 μJ laser pulse at various temperatures between 270 and 325 K. (d) Evolution of Δn_{HS}^{hv} and Δn_{HS}^{th} , measured respectively at 150 ps and 25 ns, with respect to the pump energy at two different temperatures (293 and 315 K). (e) Comparative photoresponse at room temperature of the three films of the molecules to a 6 μJ femtosecond laser pulse. For each plot, symbols are experimental data points and lines are drawn to guide the eye. These figures were taken from [101].

tens of nanoseconds and disappear for thin samples (50 nm), as effects corresponding to: i) the structural and electronic rearrangements of photoexcited molecules in the HS state; ii) then, the propagation of strain waves at the material scale; iii) and finally, the thermal activation above the molecular energy barrier [38, 40, 220, 221]. The subtlety comes from the fact that the heat transfer to the substrate is more important for the thinner sample and this helps the sample to relax quickly and thus we see the suppression of this second step.

1.3.6.2 L = pz

This molecule undergoes a thermally induced SCO in the 300-450 K temperature range as shown in figure 1.14-a from reference [158]. The thermal SCO curve, in the first cycle of heating and cooling, shows an asymmetric shape in irreversible changes on the magnetic and optical properties of the material. Indeed, the first recorded heating cycle differs drastically from the successive thermal cycles. According to the authors, this irreversibility has a crystallographic origin and is associated with a transformation between a metastable tetragonal and the stable monoclinic forms. Moreover, thin films of 200 nm thickness of the complex were deposited, by thermal evaporation at 10^{-5} mbar, on gold interdigitated micro-

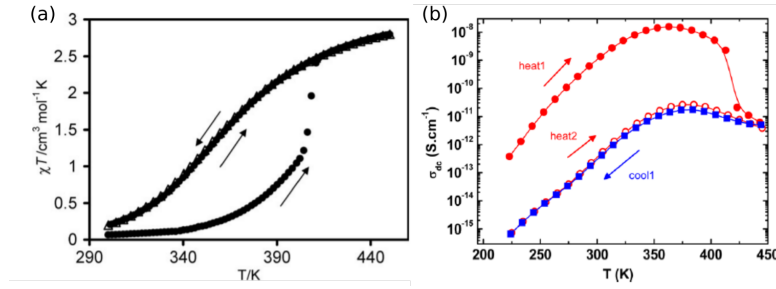


Figure 1.14: (a) The temperature dependence of the $\chi T(T)$ product of the molecule upon two successive thermal cycles (first cycle: closed circles, second cycle: open triangles) [158]. (b) the temperature dependence of the dc conductivity recorded at 10 mHz over two successive thermal cycles [159].

electrodes on a Si wafer covered by SiO_2 insulating layer [159]. As shown in figure 1.14-b, they demonstrated by impedance measurement that the conductivity of the films decreases by 1-2 orders of magnitude when the material goes through the first (irreversible) thermal phase change.

1.3.6.3 L = $(\text{CH}_3)_2\text{pz}$

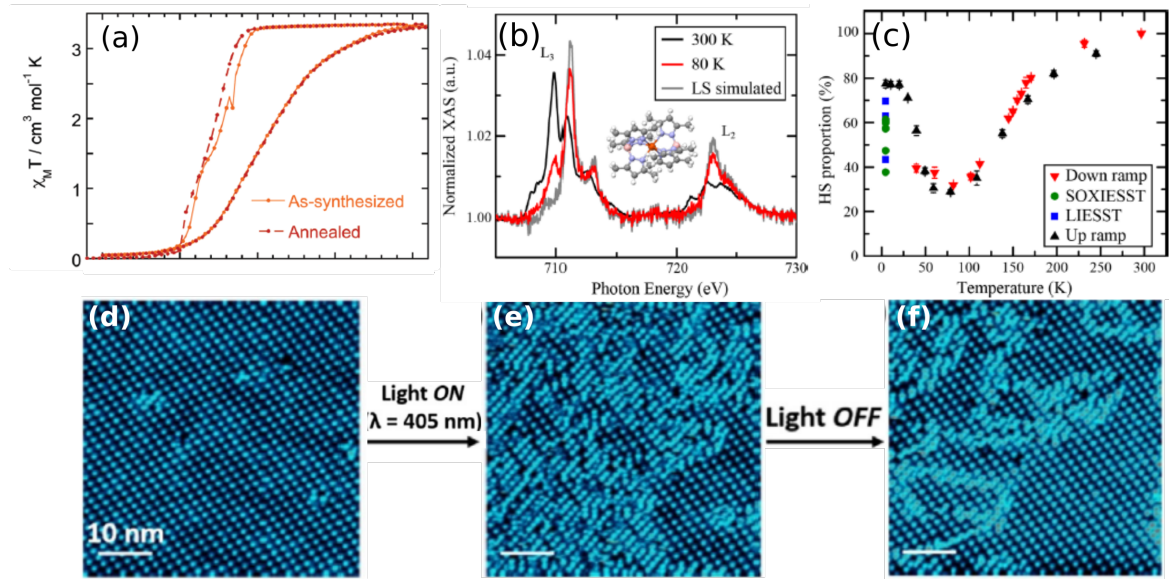


Figure 1.15: (a) Temperature dependence of $\chi T(T)$ (scanning rate = 2 K/min) for the as-synthesized and the in-situ annealed powder. This figure was taken from [81]. (b) Normalized XAS spectra of 1.6 ML of Fe-Pyrz on Au(111) at 300 K (HS) and 80 K and the simulated LS spectrum obtained from a linear combination of the spectra at 300 and 80 K. (c) HS proportion as a function of temperature for the submonolayer of Fe-Pyrz obtained from the linear combination of the HS and simulated LS spectra. The (b) and (c) figures were adapted from [222]. (d-f) Light-induced SCO and thermal relaxation at the molecular scale. Scanning Tunneling Microscopy (STM) images (4.6 K) of the same area (d) in its initial state presenting the $S_{2/3}$ superstructure, (e) under blue light illumination after 9 h and 45 min of exposure and (f) in its relaxed state 9 h and 45 min after stopping the blue light illumination ($V = 0.3$ V, $I = 20$ pA). Scale bars, 10 nm. The last three figures were adapted from [223].

This molecule is the system that I will study in my thesis and which I call Fe-Pyrz. The first study on surface was done by reference [154] with different thick films (150 nm to 50 nm) of Fe-Pyrz on Si/SiO₂ in which they show that the molecule keeps its switching properties (LIESST, SOXIESST and thermal hysteresis) as for the bulk. Except that, it is observed that the decrease in the thickness of the molecular layer leads to a decrease in the transition temperature and also affects the shape of the hysteresis. The authors claim that this change in macroscopic thermal transition property is due to the nanocrystalline growth of the molecule on the substrate which induces cooperativity between the grains of molecules in addition to the cooperativity that exists between molecules in the same grain.

In reference [81], the authors investigate the thermal bistability on powder and as a function of the number of layers (130 nm to 8500 nm). Combining magnetic and thermodynamic measurements on powder, they show that the molecules exhibit a complete hysteretic transition (31 K width and with a transition temperature of 189.5 K) with an asymmetric shape, as shown in figure 1.15-a. On the thickest sample, for the 130 nm film, the $T_{1/2}$ was shifted to a lower temperature (152 K) with a smaller hysteresis width of 17 K. Moreover, the authors observed on the substrate the coexistence of two polymorphic phase for the as-synthesized sample, one with a triclinic phase and a tetragonal phase. This metastable tetragonal phase disappears after annealing the sample at 373 K and without changing the thermal properties, in contrast with the powder which does not show the metastable tetragonal phase (cf. Fig 1.15-a in orange). the asymmetry in the thermal hysteresis can be attributed to the emergence of crystallographic phase transitions, which are partly coupled to the electronic switching. The asymmetric shape of hysteresis can be accounted for distinct structural reorganizations taking place in the cooling and heating mode prior to the SCO. This effect of structural instabilities and reorganizations was already pointed out by reference [2] with similar pyrazolylborate complexes. You can also refer these two theoretical papers [46, 47] in which they explain the coupling between the structural and electronic degrees of freedom.

As far as studies of ultrathin layers of this SCO complex on a metallic Au(111) surface are concerned, the only studies that exist have been done by my team [222, 223]. Firstly, this molecule has the particularity of being the only one that has adsorbed without decomposing metal substrates and to preserve its switching property. In reference [222], the authors investigate the behavior of 1.6 ML of Fe-Pyrz on Au(111). Figure 1.15-b shows that the molecule exhibit switching by temperature, from LS at low temperature to HS at high temperature separated by the CF splitting. Moreover, Ligand Field Multiplet (LFM) calculations [224, 225] confirmed that the molecules do not decompose on the surface since the spectra is reproducible in O_h symmetry with realistic parameters for SCO. Moreover, as shown in figure 1.15-c in blue and green, the LIESST and SOXIESST at low temperature are effective. From the metastable HS state at low temperature, they ramp up the temperature untill the suppression of the photoinduced state, the T_{LIESST} was determined to be around 50 K (see figure 1.15-c in black). Using the same ramp, they measure the thermal transition properties between 50 K to 300 K. Figure 1.15-c (in up and down triangles) shows a continuous phase transition from an incomplete HS phase to a complete HS phase.

In reference [223], they investigate the behavior of a submonolayer of Fe-Pyrz on Au(111). STM image at 4.7 K, presented in figure 1.15-d, shows a unique long-range ordered mixed spin-state phase with two out of three molecules in the HS state (called $S_{2/3}$ superstruc-

ture). By irradiating with a laser diode, figure 1.15 shows that the superstructure evolves into another one with one molecule over two is in the HS state ($S_{1/2}$). Note that the description given here is different than in the paper, where HS and LS states were incorrectly ascribed, on the basis of comparison between STM results and DFT calculations. However, this work was the first observation of a light-induced SCO transition at the molecular scale. Regarding the symmetry relationship between the $S_{2/3}$ and $S_{1/2}$ phases, note that there is no group-subgroup relationship. This is very reminiscent to structural reconstructive phase transitions, as it was previously studied by references [46, 138].

The same authors were interested to understand the structural properties of the molecular film with respect to the Au(111) surface, by grazing incident X-ray diffraction (GIXD) and mechanoelastic simulations [226]. GIXD experiments at 300 K show that there is an epitaxial relationship between the sub-monolayer molecules and the substrate and consequently lead to the experimentally observed high-quality 2D arrangement. To understand the role of this epitaxial relationship on the mixed spin-state phase observed at low temperature, mechanoelastic simulations were realized. It appears that the residual HS fraction at low temperature is due to the epitaxial stress with the surface which induces a partial reduction of the elastic strain energy arising from lattice misfits of the molecular and Au lattices as the system undergoes a transition from the HS to the LS state, leading to the existence of residual HS molecules at low temperatures.

1.4 Conclusions

In this chapter, we have firstly described the thermal-, light- and soft X-ray-induced SCO mechanisms in the bulk. Indeed, the thermal transition is governed by the cooperativity of the system while the LIESST is governed by the lifetime of the photoinduced HS state. With a dedicated wavelength that triggers the metastable HS state, the LIESST effect is reversible, the so-called r-LIESST. Moreover, we have shown how the relaxation of the HS metastable state is measured (T_{LIESST}) and how it is influenced by the distortions of the coordination sphere. Moreover, in highly cooperative SCO materials, another type of bistability involving thermal and photoconversion effects gives rise to light-induced thermal hysteresis (LITH). Concerning the SOXIESST effect, it is proposed that the transition from LS to HS is promoted by secondary electrons.

We have also reported a rather exhaustive overview of experimental studies of vacuum-evaporable SCO materials on-surfaces. The investigations of various complexes on surfaces allowed new discoveries and a better understanding of the mechanisms at play. Under the effect of light or temperature, some submonolayer and multilayer SCO systems exhibit complete/incomplete transition or a loss of the SCO behavior on different substrates. However, a lot more work is necessary to overcome the limits especially on metallic surfaces. Except the case of $\text{Fe}((3,5-(\text{CH}_3)_2\text{Pz})_3\text{BH})_2$, on metallic surfaces, almost all the molecules in the submonolayer are either blocked or decomposed. This constrains the use of spin transition molecules on magnetic and/or non-magnetic metals. To overcome this limitation, different strategies are explored in parallel, consisting in introducing decoupling layers between the metallic substrate and the metallic substrates, increasing the molecular thickness, the synthesis of more robust compounds or incorporating a functional switchable ligands.

In this thesis, we study in particular the case of the $\text{Fe}((3,5\text{-(CH}_3)_2\text{Pz)}_3\text{BH})_2$ adsorbed on different metals (magnetic and non-magnetic) and HOPG. We are particularly interested to know if this molecule does not fragment or block on surfaces. In case these molecules keep their switching properties, we will be particularly interested at the modification of the thermal bistability (chapter 3) and the light-induced switching (chapter 4), for submonolayers and multilayers. In addition, LITH measurements on thin and ultrathin films will also be presented in Chapter 4. Finally, we will investigate the modification of the magnetic anisotropy properties of the molecule on a metal (chapter 5). In chapter 6, we will study the switching and magnetic coupling properties of this molecule on cobalt and we will introduce decoupling layers between the molecules and the cobalt.

MATERIALS, EXPERIMENTAL METHODS AND SIMULATIONS

This chapter is dedicated to the presentation of the organic materials used, the theory and experimental aspects of XAS and STM and will end with the substrate preparation, molecule and metal deposition techniques under ultrahigh vacuum (UHV) environment.

2.1 Organic Materials

In this part, I will describe the molecules that we will study throughout my thesis. First, there is the compound $\text{Fe}^{\text{II}}((3,5-(\text{CH}_3)_2\text{Pz})_3\text{BH})_2$ (Iron-pyrazolyl-dimethyl-borate or Fe-Pyrz) which is the SCO complex. As well as another compound, very similar to the first, which is a high-spin molecule at all temperatures, namely, $\text{Fe}^{\text{II}}((3-(\text{Ph})\text{Pz})_3\text{BH})_2$ (Iron-pyrazolyl-phenyl-borate or Fe-Phen¹). The synthesis of these compounds were made by our chemists collaborators, that I want to thank, of the *Institut de Chimie Moléculaire et des Matériaux d'Orsay* (T. Mallah and M. L. Boillot)..

2.1.1 The stability of the molecules on surfaces

The molecules are composed of a metallic center of Fe^{2+} with a $[\text{Ar}]4s^03d^6$ electronic configuration, surrounded by organic tridentate ligands, namely, $(3,5-(\text{CH}_3)_2\text{Pz})_3\text{BH}$ for the SCO molecule (Fe-Pyrz) [227, 228] or by $(3-(\text{Phen})\text{Pz})_3\text{BH}$ for the HS molecule (Fe-Phen) [229]. The choice of the tridentate ligands is crucial regarding the stability of both molecules on surfaces. To understand this, we must invoke thermodynamic arguments. Indeed, we must calculate the Gibbs free energy ($\Delta G = \Delta H - T\Delta S$ with H being the enthalpy and S is the entropy) of the following reaction: $\text{Fe}^{\text{II}}(\text{L})_2 + \text{surface} \rightarrow \text{Fe}^{\text{II}}(\text{L}) + \text{L/surface}$ (with L is the tridentate ligand). From an enthalpic point of view, the fact that the tridentate ligand is negatively charged gives some extra electrostatic binding energy to the Fe-ligands

¹Beware, here the name Phen (for Phenyl) can be confusing and does not refer to the molecule $\text{Fe}^{\text{II}}(\text{phen})_2(\text{NCS})_2$, where the acronym Phen means 1,10-phenanthroline.

bonds. For comparison, bidentate based molecules generally involve two charged and one neutral ligands. This latter is therefore less binded to the Fe^{II} central ion. From an entropic point of view, the molecule with the tridentate ligands is also more stable. Indeed, the configurational probability to form a molecule with a central ion and three bidentate ligands is less than with two tridentate ligands. It is therefore easier to dissociate a bidentate based molecule which requires the breaking of two Fe-N bonds simultaneously instead of three Fe-N bonds for a tridentate ligand.

2.1.2 Molecular structure

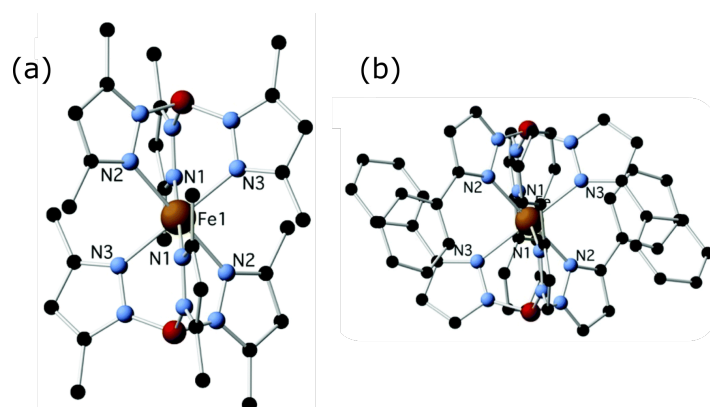


Figure 2.1: View of the molecular structures of Fe-Pyrz in the HS state (a) and Fe-Phen (b); hydrogen atoms are omitted for clarity, N (blue), C (black), B (red), Fe (brown).

Figure 2.1 shows the Fe-Pyrz (a) and Fe-Phen (b). Concerning the Fe-Pyrz molecule, I present the result obtained by crystalline structure studied at three different temperatures in the HS and LS states using single-crystal X-ray diffraction (XRD) measurements from [81, 230]. It was shown that in the HS state at (298 K), the compound crystallizes in the triclinic $P\bar{1}$ space group. The Fe atom sits on an inversion center and it binds with two $\text{HB}(3,5\text{-(CH}_3)_2\text{Pz})_3$ anions to form a $[\text{FeN}_6]$ coordination sphere with a three-fold symmetry axis (C_3) defined by the (B-Fe-B) direction with a symmetry very close to C_{3v} . At 240 K, (mixed spin-state with 80% HS) and at 100 K (LS state), the space group does not change with respect to the spin-state. However, changing the spin-state from HS to LS (resp. LS to HS) decreases (resp. increases) the volume of the crystal and hence of the crystalline lattice by a change in the coordination sphere, i.e., the mean distance of the Fe-N bond ($\langle\text{Fe-N}\rangle$) by 0.2 Å for iron(II) compounds [31, 32], and can also induce distortions [81] such that the LS state is more symmetric than the HS state. Indeed, the LS complex adopts the regular geometry close to the octahedral symmetry whereas the HS one is much more distorted. Concerning the Fe-Phen and as for the Fe-Pyrz, the metallic center is located on an inversion center and is octahedrally coordinated by six N from two ligands. However, the Fe-N bond distances are larger than for Fe-Pyrz and have a larger deviation to their average value. The $\widehat{\text{NFeN}}$ angles have an average value very close to 90° (89.8°) larger than that for Fe-Pyrz. The average value of the $\widehat{\text{BFeN}}$ angles (54.6°) is almost identical to that of a regular octahedron with a deviation of less than 0.2°. Finally, the reason why this molecule does not switch comes from the fact that the phenyl group imposes a long Fe-N bond which is around 2.2 Å at any temperature. Therefore and by construction, the LS form of the

molecule is very destabilized and cannot switch to the LS state [229]. You can find all the structural details of both molecules in supplementary information of reference [231].

2.1.3 Photoswitching and thermodynamic properties of Fe-Pyrz

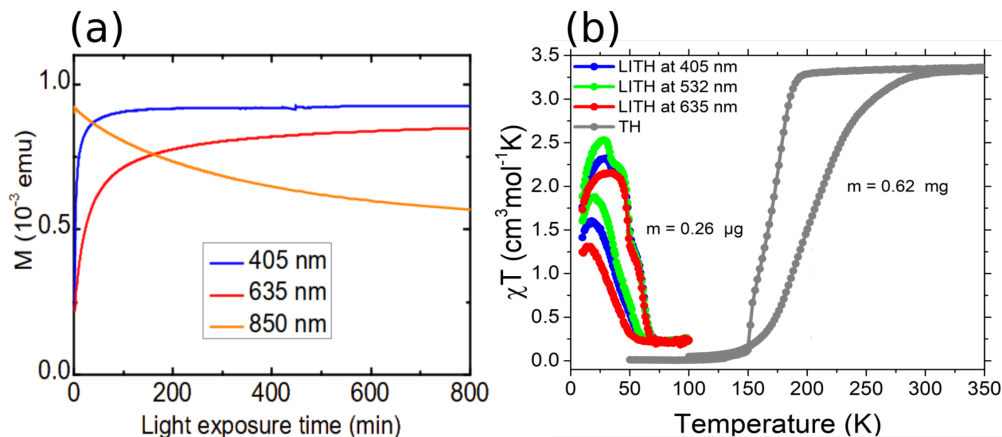


Figure 2.2: (a) Magnetization (under $\mu_0 H = 0.5$ T) measured by SQUID at 10 K on the bulk (powder, $m = 0.62$ mg) of Fe-Pyrz, as a function of the time of illumination for 405 nm (20 mW cm^{-2}), 635 nm (10 mW cm^{-2}) and 850 nm (32 mW cm^{-2}). The usual LIESST is observed for 405 nm ($^1\text{MLCT}$ excitation) and 635 nm (1A_1 to 1T_1 excitation), while the reverse LIESST is observed for 850 nm (5T_2 to 5E excitation). (b) χT as a function of temperature. blue: 405 nm; green: 532 nm; red: 635 nm ($\mu_0 H = 0.5$ T and $m = 0.26 \mu\text{g}$); gray: χT without irradiation. The LITH curves were taken under 1 K.min^{-1} while the χT were taken under 2 K.min^{-1} .

Figure 2.2-a shows the evolution of the magnetization measured by SQUID (for Superconducting QUantum Interference Device) under constant illumination with blue (405 nm, $^1A_1 \rightarrow ^1T_1$), red (635 nm, $^1A_1 \rightarrow ^1T_2$) and infrared (850 nm, $^5T_2 \rightarrow ^5E$ excitation). We observe the usual LIESST effect [29] in the UV-Visible range via the parity and spin-allowed ligand-field states and is more efficient in the blue frequency and less in the red one while conversely the reverse-LIESST process is triggered by near infrared light. In addition, reference [81] made magnetic susceptibility measurements ($\chi T(T)$, see figure 2.2-b in grey) and it was shown that the powder of SCO molecules exhibits a thermal hysteresis behavior (of 31 K width) with a transition temperature ($T_{1/2}$) equals to 189 K. Furthermore, the reported differential scanning calorimetry (DSC) measurements gives a difference of enthalpy (ΔH) between the HS state and LS state of 10.2 kJ.mol^{-1} . An estimation of the entropy value ($\Delta S = \frac{\Delta H}{T_{1/2}}$, with $T_{1/2}$ is extracted from the magnetic data) is $53.8 \text{ J.K}^{-1} \text{ mol}^{-1}$. The enthalpy and entropy values are within the range expected for Fe^{II} compounds exhibiting a spin transition. Finally, the light-induced thermal hysteresis behavior was also measured on a powder under different wavelengths, as shown in figure 2.2-b (in colour). We can make two remarks at this point. Firstly, it seems that the LITH under blue is less efficient than the green one. The reason is the following: since the molecule absorbs more in the blue range rather than the green (effective cross-section MLCT band $> d-d$ band), the light penetration is much higher with green. As a result, the deep layers of the material are more homogeneously excited. For blue, excitation gradients are formed closer to the

surface. Secondly, the signal does not drop to zero after 100 K (all LS). The reason is that those data are derived from photomagnetic measurements and are acquired on a very small amount of material (compromise between the signal which increases with the amount of material and the number of photoexcited sites which decreases) and that it could come from defects in the solid. Finally, note that the temperature sweep rate (1 K/min) are the same for both measurements. For this reason, these measurements cannot be compared with other compounds in the literature where the temperature ramps are 0.3 K/min but they can be compared with the measurements in the chapters 3 and 4.

2.2 Theoretical Aspects of X-ray Absorption Spectroscopy (XAS)

2.2.1 Introduction

X-ray Absorption Spectroscopy (XAS) is a core-level spectroscopy technique [27, 232–235] that helps to determine the electronic structure of empty states in a material (see figure 2.3-a). When an X-ray strikes an atom, it absorbs its energy ($\hbar\omega$), which allows it to pass an electron from a lower energy level (E_i) to an upper energy level (E_f) according to the law of conservation of energy:

$$E_f = E_i + \hbar\omega \quad (2.1)$$

When the process occurs, it leaves a hole in the probed core-level. After the absorption of

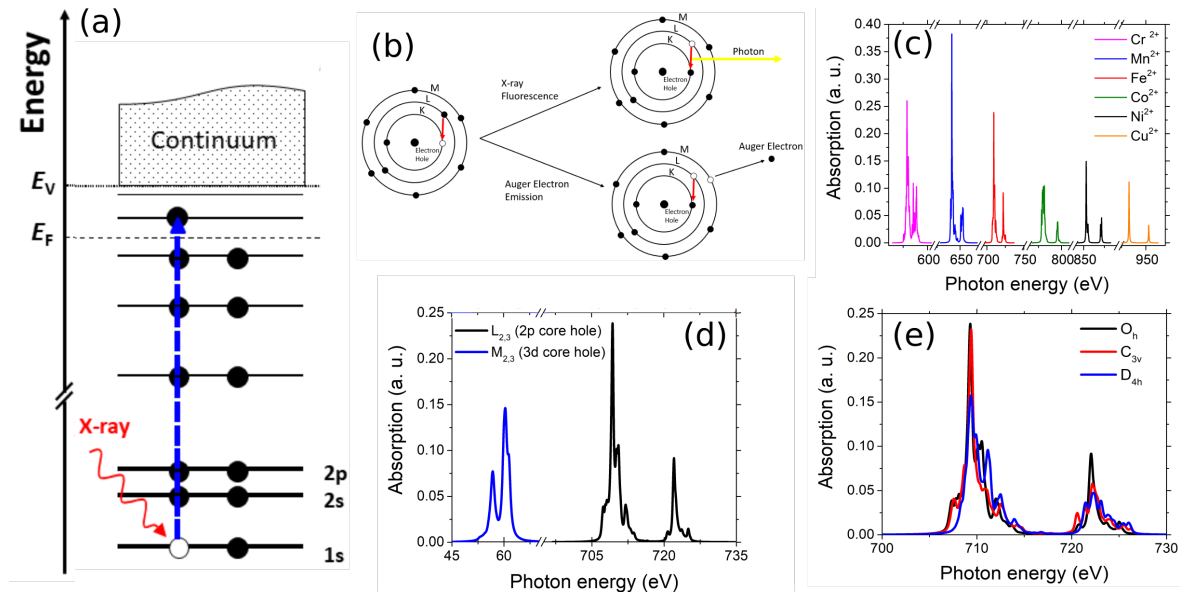


Figure 2.3: (a) Schematic representation of the XAS. (b) Scheme of the different processes (excitation and de-excitation) that take place after the absorption of a photon in XAS. (c) Chemical selectivity for different elements. (d) Orbital sensitivity for Fe^{II}. (e) Symmetry-site sensitivity for Fe^{II}. Figures (c), (d) and (e) were calculated using QUANTY [224, 225]

the X photon, the final state is described by a photo-electron in the excited (or final) level and a hole in the starting (or initial) level. The absorption edge identifies the transition

from the ground state to the lowest empty state. For example, the K edge relates to the $1s$ core-level, the $L_{2,3}$ edges relate to the $2p_{1/2}$ and $2p_{3/2}$ core-levels, the $M_{4,5}$ to the $3d_{5/2}$ and $3d_{3/2}$ core-levels, and so on. As shown in figure 2.3-b, in the excited state of the atom, two processes can occur to get back to the ground state of the system. First, a radiative process, which consists on the emission of a fluorescence photon whose energy corresponds to the difference in energy between two levels of the atom. Second, a non-radiative process by the emission of an Auger electron. Moreover, XAS is said to be selective both from the point of view of the chemical element considered as well as of the orbitals considered. Indeed, the XAS spectrum of two different elements are of course different (see figure 2.3-c) but not only. The spectrum of the same chemical element for different orbitals are different, as it can be seen for example for the Fe^{II} (figure 2.3-d). Likewise, the XAS shape is sensitive to the symmetry of the environment around the probed element as shown in figure 2.3-e.

2.2.2 Light-Matter interaction

X-rays are electromagnetic waves that are divided into *Soft X-rays*² (between 100 eV-3 keV) and *Hard X-rays* (above 3 keV). The central object to represent an electromagnetic wave is the vector potential $\hat{A}(\vec{r}, t)$ which is written in second quantization as:

$$\hat{A}(\vec{r}, t) = \sum_{\vec{k}, \lambda} A_0 \vec{e}_{\vec{k}, \lambda} b_{\vec{k}, \lambda} \exp[i(\vec{k} \cdot \vec{r} - \omega \cdot t)] + h.c \quad (2.2)$$

\vec{k} is the wave vector, λ is a set of collective variables, $\vec{e}_{\vec{k}, \lambda}$ is the polarization of the photon, $b_{\vec{k}, \lambda}$ (resp. $b_{\vec{k}, \lambda}^\dagger$) is the annihilation (resp. creation) operators which satisfy the commutation relations for bosons and $h.c$ refers to the hermitian conjugate. When X-rays interact with atomic electrons bounded by a potential $V(\vec{r})$, the overall Hamiltonian can be written as:

$$\hat{H} = \hat{H}_{ion} + \hat{H}_{photon} + \hat{H}_{int} \quad (2.3a)$$

$$\begin{aligned} \hat{H} = & \sum_{i=1}^N \left[\frac{\hat{p}_i^2}{2m} + \hat{V}(\vec{r}_i) \right] + \sum_{\tau_1, \tau_2, \tau_3, \tau_4} U_{\tau_1, \tau_2, \tau_3, \tau_4} a_{\tau_1}^\dagger a_{\tau_2}^\dagger a_{\tau_3} a_{\tau_4} + \zeta \sum_{i=1}^N \hat{l}_i \cdot \hat{s}_i + \hat{H}_{CF} \\ & + \sum_{\vec{k}, \lambda} \hbar \omega (n_{\vec{k}, \lambda} + \frac{1}{2}) + \frac{e}{mc} \sum_{i=1}^N \hat{p}_i \cdot \hat{A}(\vec{r}_i) + \frac{e}{2mc} \sum_{i=1}^N \hat{\sigma}_i \cdot \vec{\nabla} \wedge \hat{A}(\vec{r}_i) \end{aligned} \quad (2.3b)$$

The first five terms denotes the Hamiltonian of the free ion (\hat{H}_{ion}) where the first two ones describe the kinetic and potential energies respectively. The third term is the Coulomb interaction where $\tau = (n, l, m, \sigma)$ labels the spin and orbital degree of freedom, $U_{\tau_1, \tau_2, \tau_3, \tau_4}$ encodes the interactions between the electrons belonging to the same shell or different shells and a_τ (resp. a_τ^\dagger) is the annihilation (resp. creation) operators which satisfy the commutation relations for fermions. The fourth term is the spin-orbit coupling (SOC) where \hat{l}_i and \hat{s}_i are the one electron orbital and spin operators respectively and the sum is over

²We call them Soft X-rays because in this energy range X-rays do not penetrate air and it is safe enough to work with.

all electrons. The prefactor ζ ($\propto \frac{1}{r} \frac{dV}{dr}$) is the SO constant which is atom dependent and is calculated numerically in a Hartree-Fock model. The last term in (\hat{H}_{ion}) is the crystal field (CF). The last three terms in (\hat{H}_{ion}) will be discussed within the sections 2.2.3.3, 2.2.3.4 and 2.2.3.5. The sixth term is the Hamiltonian of the incoming photons (\hat{H}_{photon}). The last two terms describe the interaction (small perturbation) between photons and electrons (\hat{H}_{int}) where the first term (resp. second term) of \hat{H}_{int} describes the action of the electric field (resp. magnetic field) on the electron (resp. on its spin). The central part in the interaction of X-rays with matter is given by the Fermi Golden rule [232, 236]:

$$W_{fi} = \frac{2\pi}{\hbar} |\langle \phi_f | \hat{T} | \phi_i \rangle|^2 \delta(E_f - E_i - \hbar\omega) \quad (2.4)$$

The equation 2.4 gives the transition probability between the initial state $|\phi_i\rangle$ and final state $|\phi_f\rangle$ by the incident photon of energy $\hbar\omega$ where \hat{T} is the interaction Hamiltonian related to \hat{H}_{int} using Lippman-Schwinger equation³ [236]. The squared matrix element gives the transition rate and the delta function reflects the energy conservation. The initial state $|\phi_i\rangle$ and final state $|\phi_f\rangle$ are coupled via the dipole selection rules. In the case of 2p XAS, the allowed transitions are from $2p \rightarrow 3d$ and $2p \rightarrow 4s$ [237], but the transitions to 3d states dominate over transitions to 4s states. This is due to the fact that in the soft X-ray regime, the transition induced by the electric quadrupole coupling is significantly lower (since $\vec{k} \cdot \vec{r}$ is very small) than that induced by the electric dipole coupling. By using the Heisenberg equation one can show that the equation 2.4 has this more convenient form:

$$W_{fi} \propto |\langle \phi_f | \vec{e}_{\vec{k},\lambda} \cdot \vec{r} | \phi_i \rangle|^2 \quad (2.5)$$

Now I will remind what the electric dipole selection rules are [26, 28, 236]. Due to the SOC, the good quantum numbers are the total angular momentum J and the $2J + 1$ projections of the magnetic quantum number M_J . Since X-rays carry an angular momentum of 1, this implies that the angular momentum of the excited state differs by 1 from that of the ground state ($\Delta l_i = \pm 1$). The spin is conserved because X-rays do not carry spin ($\Delta s_i = 0$). It means that the total momentum cannot be changed by more than 1. Moreover, the condition for the magnetic quantum number changes according to the polarization of light. All this discussion is summarized in the following equations:

$$\begin{cases} \Delta J = 0, \pm 1 \\ \Delta M_J = 0, \pm 1 \\ \Delta S = 0 \end{cases} \quad (2.6)$$

³The relation between the transition operator and the interaction Hamiltonian is given by:

$$\hat{T} = \hat{H}_{int} + \hat{H}_{int} \frac{1}{E - \hat{H}_0 + i\frac{\Gamma}{2}} \hat{T}$$

2.2.3 Ligand Field Multiplet Theory (LFM) of transition metal $L_{2,3}$ edges

Up to now, we have discussed the XAS with a single particle approach. This approach breaks down in the case of the $L_{2,3}$ absorption edges for transition metal ions (strongly correlated systems). In this part, I will briefly explain effects beyond the single particle approach, and the role of the many-body effects in the $L_{2,3}$ absorption edges for transition metal ions. Finally, I will give physical reasons to show why the multiplet effects and the CF effect play a more important role in XAS spectra than the charge-transfer effect.

2.2.3.1 Single particle picture versus many-body effects in XAS

The many-body effects in XAS could be distinguished into two categories: multiplet and charge-transfer effects [232, 238–242]. There are two physical reasons for the dominance of the multiplet effects in $2p$ XAS of transition metal ions. The first effect is the so-called self-screening effect [243]. Indeed, in the $L_{2,3}$ absorption edges of transition metals, the core-hole potential is mainly screened by the photo-excited electron itself (see figure 2.4). As a consequence of the self-screening of the core-hole potential is the localization of final states due to the weak energy difference between the initial state and the final states. This implies, on one hand, that the interaction between the photo-electron and the core-hole is strong, and that on the other hand, the electrostatic repulsion between the photo-electron and the other core electrons is also strong. The second reason for the use of a multielectronic approach is the large overlap between the initial and final states. Indeed, the potential overlap between the core and valence wave functions of the ground state ($2p^6 3d^n$) is not effective since all the $2p$ orbitals are filled. But in the final state ($2p^5 3d^{n+1}$), the core states, as well as the valence states, are partially filled, it implies a strong Coulomb intra-atomic effects between the radial parts of the wave functions. So all electrons must be taken into account. Indeed, the Hamiltonian describing the ion is multielectronic and takes into account a sum over all the electrons and the eigenfunctions are multielectronic (Slater determinants). Consequently, the atomic multiplet theory (with CF effect but without charge-transfer effect), which is often called **Ligand Field Multiplet Theory (LFM)** serves as a good starting approximation, and the charge-transfer effect gives some corrections to this first approximation. In practice, the LFM is mainly used in the case of the $L_{2,3}$ [224] edges of transition metal ions, the $M_{4,5}$ [244–246] edges of lanthanide ions, the $N_{4,5}$ edges for $4d$ ions and $O_{4,5}$ [246] for $5d$ ions or more exotic elements such $M_{4,5}$ edges for actinides. In addition to what is discussed, the LFM approach is accurate in the case of a strong SOC and when the chemical bond is "more" ionic than covalent or metallic.

2.2.3.2 The basis

As discussed before, in order to have an accurate description of the $L_{2,3}$ edges of a transition metal, we need to consider the multielectronic point of view. For a basis of N spin-orbitals and n electrons there are $\binom{N}{n} = \frac{N!}{n!(N-n)!}$ possible states. The multielectronic wavefunction ($\Psi(\vec{r}_1, \vec{r}_2, \dots, \vec{r}_N)$) for N electrons is constructed as a linear combination of Slater determinant built from the monoelectronic wavefunction ($\phi_\tau(\vec{r})$) with τ is a collective quantum

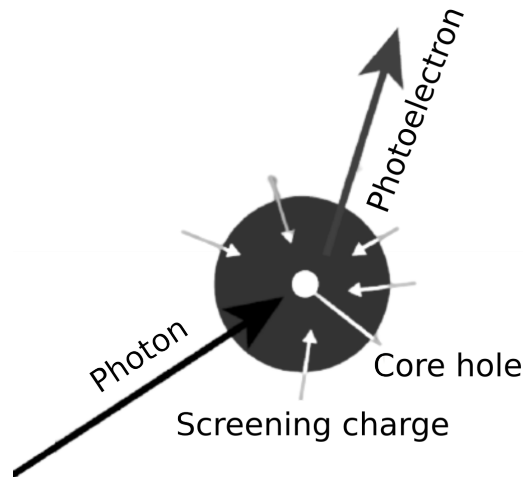


Figure 2.4: Excitation of a photoelectron by an x-ray photon creates a core hole that is screened by the surroundings. This figure was taken from [232].

number) wavefunctions and because of the Pauli exclusion, they satisfy the antisymmetry principle for fermions. The single Slater determinant basis state with more than one electron will be given by the antisymmetric product of the one particle spin-orbitals. Now, let's think about the number of states needed to have a complete description of a system. In the case of the simplest atom that we can find, the hydrogen (H) with 2 spin-orbitals and 1 electron, we need 2 states to describe properly the system. Now, if we want to describe a cluster of 18 atoms of H for example, we need 9075135300 states. Let's not even talk about the possibility of describing for example 7 atomic units of Nickel Oxide (NiO), we need the unpronounceable number of 240260199935164200 states. The calculation is obviously impossible even with the best supercomputers in the world. Hence, the description using Slater determinants is extremely time consuming. In order to counter these limitations, I introduce the language of the second quantization for fermions, such as they respect the well-known anticommutation relations for the creation a_τ^\dagger (resp. annihilation a_τ) operator which creates (resp. annihilates) an electron in the spin-orbital $\phi_\tau(\vec{r})$. For instance, the code I use (QUANTY 2.2.4) can deal with 10^{100} possible many particle states. The only reason one can do this is by never writing down those determinants.

2.2.3.3 Treatment of the electron-electron repulsion

The electron-electron interaction contains a lot of information on the multiplet splittings and the computation of its matrix elements is done in non-relativistic limit (no SOC) and therefore in the base $|\alpha, L, M_L, S, M_S\rangle$ where α is a collective quantum number which contains the other degrees of freedom of the system. The matrix elements of two-electron wavefunctions in the basis of spherical harmonics can be written as [28, 247]:

$$\begin{aligned}
 \langle \alpha, L, M_L, S, M_S | \frac{e^2}{|r_i - r_j|} | \alpha', L, M'_L, S', M'_S \rangle &= \sum_k \sum_J^{\infty \text{ shells}} f_k(l_j, l_j) F^k(l_j, l_j) \\
 + \sum_k \sum_{i,j,i \neq j}^{\infty \text{ shells}} f_k(l_i, l_j) F^k(l_i, l_j) &+ \sum_k \sum_{i,j,i \neq j}^{\infty \text{ shells}} g_k(l_i, l_j) G^k(l_i, l_j)
 \end{aligned} \tag{2.7}$$

The first term is called **direct interaction** between **equivalent** electrons belonging to the same shell, i.e $n_1 = n_2 = n_3 = n_4$ (see figure 2.5-a). This term plays a role for the ground state for L -edge in XAS ($2p^6 3d^n$). The second term is called **direct term** between **inequivalent** electrons which belong to different shells, i.e $n_1 = n_3$ and $n_2 = n_4$ (see figure 2.5-b) this means that each electron scatters in its shell. This term plays a role in the excited state for L -edge in XAS ($2p^5 3d^{n+1}$) since the $2p$ electrons interacts with the $3d$ ones. The last term is called **exchange term** between **inequivalent** electrons belonging to different shells, i.e $n_1 = n_4$ and $n_2 = n_3$ (see figure 2.5-b) which means that electrons exchange shells. The terms F^k and G^k are radial integrals and are called Slater-Condon parameters. For an (free) ion in a spherical symmetry, they are calculated from the radial part of the monoelectronic wave function and have numerical expressions calculated from the Hartree-Fock model. However, if we consider the symmetry of the environnement around the absorber, these values are reduced empirically to take into account the effect of the chemical bond which delocalizes the orbitals. This factor is called the nephelauxetic parameter (κ) and is set typically between 0.7-0.9 (resp. 0.5-0.6) for an ionic (resp. a covalent) bond. The magnitude of the multiplet splitting depends on the magnitude of the Slater-Condon integrals. Moreover, the terms f_k and g_k are angular integral terms and depend only on the orbital part and the electronic filling in the shells, they also have analytical values which are calculated using angular momentum coupling. Thus, it imposes conditions on the possible k values in the sum. For the direct term k of equivalent electrons, k is even and is running from 0 to $2l$. For a d shell the Coulomb operator is proportional to F_{dd}^0 , F_{dd}^2 and F_{dd}^4 . For the direct term of inequivalent electrons, $k \in [0, \min(2l_1, 2l_2)]$ in steps of 2. It means that for $2p \rightarrow 3d$ transition, there is two values of F_k , namely, F_{pd}^0 and F_{pd}^2 . For the exchange term, $k \in [|l_1 - l_2|, l_1 + l_2]$ in steps of 2 and is even if both l_1 and l_2 are even or odd and k is odd if one of the angular momenta involved is even and the other is odd. Thus, for $2p \rightarrow 3d$ transition, there is two values of G_k , namely, G_{pd}^1 and G_{pd}^3 .

2.2.3.4 Treatment of the spin-orbit coupling

By developping the scalar product in the spin-orbit (SO) [26, 28, 232, 247] term in equation 2.3b and using the ladder operators, one can write in the second quantized form [248]:

$$\sum_{i=1}^N \hat{l}_i \cdot \hat{s}_i = \sum_{m=-l}^{m=+l} \sum_{\sigma=\uparrow, \downarrow} m \sigma \hat{a}_{m,\sigma}^\dagger \cdot \hat{a}_{m,\sigma} + \frac{1}{2} \sum_{m=-l}^{m=l-1} \frac{1}{2} \sqrt{l+m+1} \sqrt{l+m} (\hat{a}_{m+1,\downarrow}^\dagger \cdot \hat{a}_{m,\uparrow} + \hat{a}_{m,\uparrow}^\dagger \cdot \hat{a}_{m+1,\downarrow}) \tag{2.8}$$

Where σ ($= \uparrow, \downarrow$) are the projection of the spin (up and down respectively) along the quantization axis. The first term denotes the action of the $\hat{l}_z \cdot \hat{s}_z$ operator, while the second term is the action of the ladder operators. In the case of $2p$ XAS, there are two kind of ζ

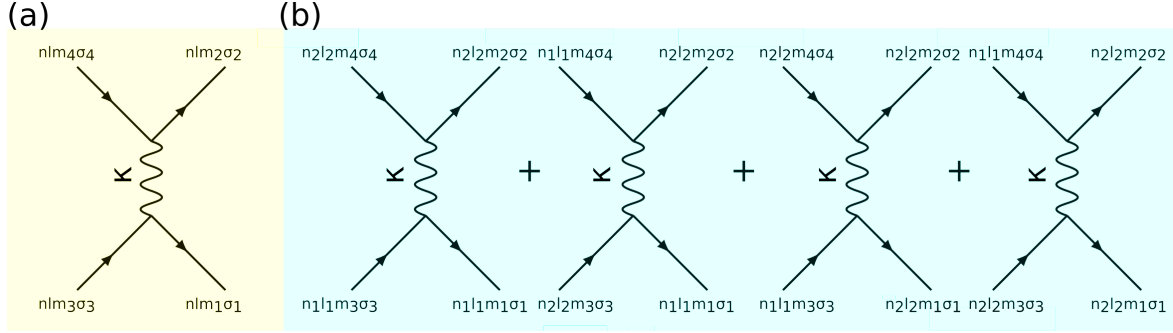


Figure 2.5: Feynmann diagrams for Coulomb interaction. (a) direct term between equivalent electrons belonging to the same shell, i.e. $n_1 = n_2 = n_3 = n_4$ and $l_1 = l_2 = l_3 = l_4$ (F_{dd}). (b) Two contributions. Firstly, direct term between inequivalent electrons belonging to different shells i.e. $n_1 = n_3$ and $n_2 = n_4$ (F_{pd}). Secondly, exchange interaction between inequivalent electrons belonging to different shells i.e. $n_1 = n_4$ and $n_2 = n_3$ (G_{pd}).

which contribute: i) ζ_{2p} which separate the $2p$ levels (the larger ζ is, the more the edges are separated). ii) ζ_{3d} in the same way plays on the internal structure of a given multiplet. From the previous equation, it is clear that the SOC mixes states with different projected orbital and spin momenta. Finally, the energy separation between the L_2 and L_3 edges is due to the SOC and is given by:

$$E_{J,L,S} = \frac{\zeta_{2p}}{2} (J(J+1) - L(L+1) - S(S+1)) \quad (2.9)$$

2.2.3.5 Treatment of the crystal field

In the case of transition metal ions, $3d$ orbitals are influenced by the CF which describes an electrostatic potential of the environment (ligands) around the ion. If the ion is isolated, then the set of $3d$ orbitals are all degenerate (see figure 2.6-a). On the contrary, different splittings of the orbitals can occur if different symmetries are applied around the $3d$ ion (see figure 2.6-b). Consequently, the symmetry of the environment around the metallic center is responsible for many physical and spectroscopic properties. Therefore, $|\alpha, J, M_J\rangle$ is no longer an adequate basis because the symmetry is no longer O_3 (spherical group or group of rotation in the space). Thus, the eigenbasis is $|\Gamma\gamma, J\rangle$ with Γ the irreducible representation (irrep.) of the symmetry group of the CF and γ is the dimension of these representations. The irrep. Γ are obviously the irrep. of the point symmetry group of the considered site. The spectroscopic states are then described by $\Gamma\gamma$. By knowing the effective potential expansion to the power of r^k on the renormalized spherical harmonics $C_{k,m}(\theta, \phi)$ ⁴ with the coefficients $A_{k,m}$, one knows the specific point group describing the CF and the general form is:

$$\hat{H}_{CF} = \sum_{\tau_1, \tau_2} \sum_k \sum_{m=-k}^{\infty} A_{k,m} \langle Y_{l,m_1} | C_{k,m} | Y_{l,m_2} \rangle \hat{a}_{\tau_1}^\dagger \hat{a}_{\tau_2} \quad (2.10)$$

⁴The normalized spherical Harmonics are written as:

$$C_{k,m}(\theta, \phi) = \sqrt{\frac{4\pi}{2k+1}} Y_{k,m}(\theta, \phi)$$

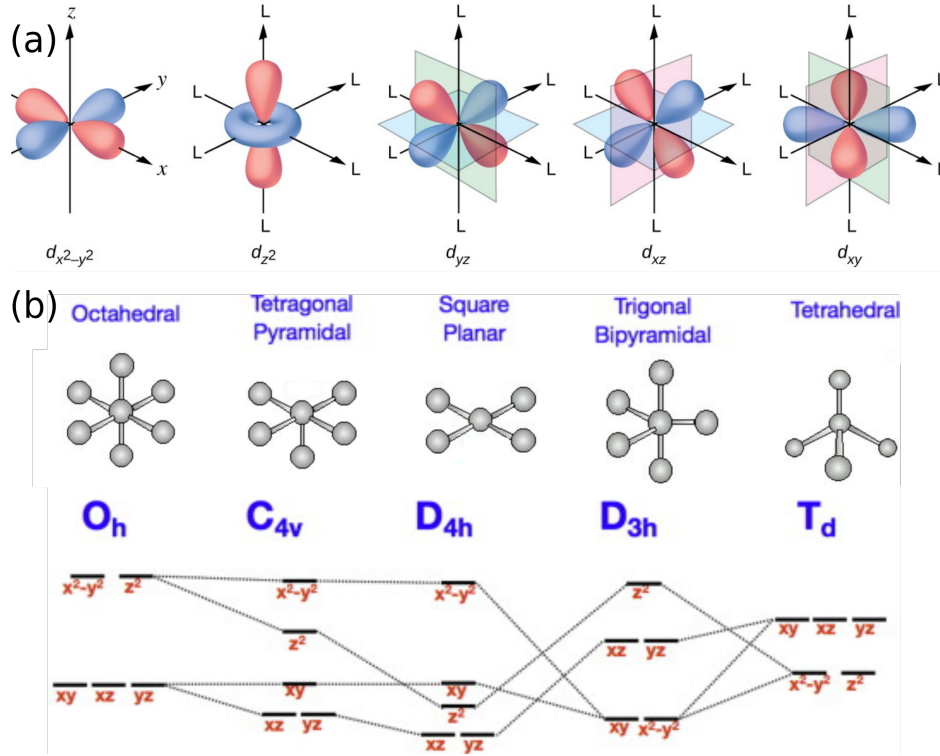


Figure 2.6: (a) Degenerate d -orbitals in spherical (O_3) symmetry. (b) Different symmetries of the crystal field induces different splittings of the molecular orbital energy levels between the t_{2g} and e_g sets.

Using the triangular relations on the $3j$ -symbols [28] of the matrix element, one can show that not all the values of k contribute to the sum and the matrix element is not zero if and only if k is even, $(2l + k)$ is even and $0 \leq k \leq 2l$. Hence, the sum over k in equation 2.10 runs from 0 to $2l$. Furthermore, the $A_{k,m}$ coefficients combine all the radial parts of the previous equation and are related to the CF parameters which are usually not known precisely. In addition, not all values of $A_{k,m}$ are allowed, many are zero due to symmetry. For all symmetry operation (O_i) of the point group, the only permitted $A_{k,m}$ are those which leaves the Hamiltonian invariant under O_i , such as:

$$O_i \hat{H}_{CF} = \hat{H}_{CF} \quad (2.11)$$

For instance in $2p$ XAS ($l = 2$), the multipole expansion of the octahedral potential reduces to $C_{0,0}$, $C_{4,0}$, $C_{4,4}$ and $C_{4,-4}$ with the adequate $A_{k,m}$ ⁵ values which encodes the CF parameter, namely, $10D_q$.

2.2.3.6 The XAS spectra

The simulation of a XAS spectrum is done via the calculation of the Green's function in the frequency domain, defined as:

$$G^{(\pm)}(\omega) = \langle \psi_i | \hat{T}^\dagger \frac{1}{\omega - \hat{H}_f \mp i\frac{\Gamma}{2}} \hat{T} | \psi_i \rangle \quad (2.12)$$

⁵All the $A_{k,m}$ coefficients are tabulated in references [28, 247, 248].

This equation is completely equivalent to the Fermi Golden rule in equation 2.4, where the finite lifetime of the excited state (Γ) is included. During a XAS process, an electron is created in the valence shell and annihilated in the core shell (or creation of hole via electron-hole symmetry), then the transition operator is the product of a creation and annihilation operator. Finally, the absorption spectrum is given by the imaginary part of the Green's function:

$$XAS(\omega) = -\frac{1}{\pi} \Im G(\omega) \quad (2.13)$$

2.2.4 The QUANTY software

The computational time required to solve the N-body problems of quantum mechanics is exponential with the size of the system, so it was necessary to write programs (in some approximations) capable of handling N-body problems of quantum mechanics and to solve them. QUANTY [224, 225]⁶ is a scripting language that allows the user to program quantum mechanical problems in second quantization and (when possible) solve them. The idea of QUANTY is that the user can focus on the model and its physical significance. The code makes it possible to calculate spectroscopic quantities (X-ray Absorption Spectra, Resonant Inelastic X-ray Scattering [249–251], etc.) for strongly correlated compounds of transition metals and rare earths. The code is written in LUA and is constantly updated by Maurits W. Haverkort and his co-workers. Finally, there are Graphical User Interface (CRISPY [252]⁷) based on QUANTY which is more "user friendly". In light of what I explained previously, the LFM approach in QUANTY is a parameterized simulation with the following parameters:

- **The Slater integrals:** $F_{dd}^0, F_{dd}^2, F_{dd}^4, F_{pd}^0, F_{pd}^2$ and G_{pd}^1 and G_{pd}^3 . They are rescaled by the nephelauxetic effect with a κ value.
- **The spin-orbit constants:** ζ_{2p} and ζ_{3d} .
- **The CF parameters:** $A_{k,m}$ which are used to reconstruct the CF splittings. In Crispy, it is possible to enter directly the CF values. For example, $10D_q$ for O_h , D_q , D_σ and D_τ for C_{3v} .
- **Experimental conditions:** The shape of a XAS spectrum is temperature-dependent. In fact, the filling of the higher electronic energy states depends on temperature via a Boltzmann-type distribution. The magnetic field also adds an additional contribution through the Zeeman energy (which I will not deal with in the context of this manuscript).
- **The experimental and life-time broadening:** Γ_{exp} , Γ_{L_2} and Γ_{L_3} . The former is a Gaussian broadening which is related to the experimental resolution. The second and third ones are the Lorentzian broadening related to the life-time of the core-hole particle. You can find all the natural width of atomic levels in reference [253].

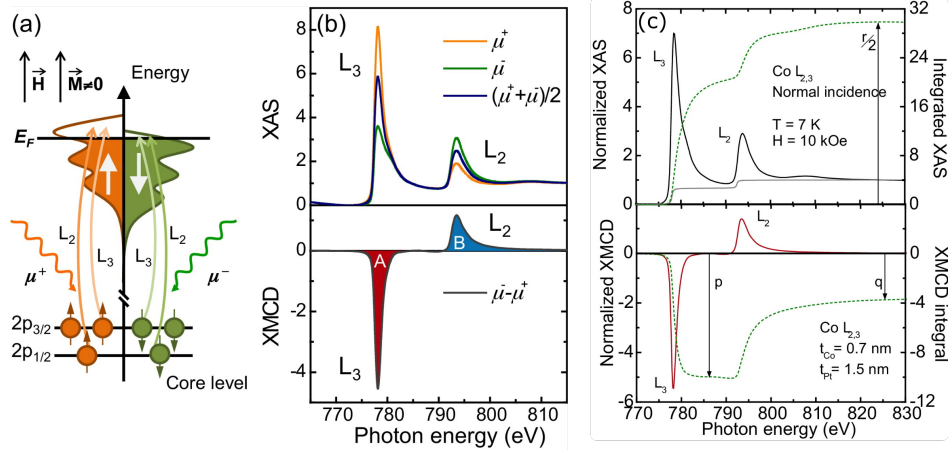


Figure 2.7: (a) Diagram of the two-step picture of XMCD for a single-electron in the resonant excitation process for a magnetic material. In the first step, a circularly polarized photon excites a spin-polarized electron from the spin-orbit split 2p level. From the 2p_{3/2} level (L₃ edge) X-rays with positive helicity (μ₊) excite 62.5% spin-up electrons and those with negative helicity (μ₋) excite 37.5% spin-up electrons, while the 2p_{1/2} level (L₂ edge) gives 25% spin-up with μ₊, and 75% spin-up with μ₋. In the second step the spin-polarized electrons have to find a place in the unoccupied 3d band, resulting in a difference if the 3d electron are spin-polarized. (b) XAS at the Co L_{2,3} for right (μ₊) and left (μ₋) circular polarization together with the difference spectrum: the XMCD. (c) Sum rule analysis for Co L_{2,3} XAS and XMCD spectra of Co-Pt nanoparticles [254]. The upper panel shows the normalized XAS spectra mean curve (black, solid), the double-step function used to represent the transitions into the continuum (solid grey line) and the integrated 'white line' after subtracting the double-step function (dashed line). The bottom panel shows the normalized XMCD spectra (solid red line) and the integrated area (dashed green line). All figures were taken from [255].

2.2.5 X-ray Magnetic Circular Dichroism (XMCD)

X-ray dichroism can be defined as the difference in the X-ray absorption cross-section measured for two orthogonal polarization states of the incident light. One of the most powerful applications of XAS to magnetic materials is the circular polarization effect [246, 255–258]. Indeed, the XAS intensity depends on the plus (μ₊) and minus (μ₋) helicities of the circularly polarized incident X-rays with respect to the direction of the magnetic field (see figures 2.7-a/b and figures 2.8-d/e) and the difference between them is called X-ray magnetic circular dichroism (XMCD). You can find in the caption of the figure 2.7-a, the description of the XMCD process. Moreover, XMCD analysis provides data on the magnetic properties of the studied atom (spin, orbital magnetic moment, anisotropy). The variation of the maximum intensity of XMCD spectrum under magnetic field is directly proportional to the magnetization *M*. In addition, XMCD is suitable for sub-monolayer coverages of magnetic molecules or magnetic atoms on surfaces. In order to understand the XMCD features and extract quantitative informations about the probed element, Thole et al. [256] and Carra et al. [257] proposed XMCD sum rules, as shown in figure 2.7-c, by which the orbital and spin

⁶You can visit the QUANTY website and download the software at <https://www.QUANTY.org/> [248].

⁷You can visit the CRISPY website and download the software at: <https://www.esrf.fr/computing/scientific/crispy/index.html>

magnetic moments can be obtained, at least approximately, from energy-integrated intensities of XAS and XMCD spectra. This method has been widely used in estimating orbital and spin magnetic moments of various materials [255]. The orbital and spin sum rules are:

$$\langle \hat{L}_z \rangle = \frac{2}{3} \frac{q}{r} n_h \quad (2.14a)$$

$$\langle \hat{S}_z \rangle + \frac{7}{2} \langle \hat{T}_z \rangle = \frac{3p - 2q}{2r} n_h \quad (2.14b)$$

Where n_h is the number of holes in the ground state and $\langle \hat{T}_z \rangle$ is the dipolar operator. The expressions of r , p and q integrals are:

$$r = \frac{1}{2} \int_{L_3+L_2} (XAS(\mu^+) + XAS(\mu^-)) dE \quad (2.14c)$$

$$p = \int_{L_3} (XAS(\mu^+) - XAS(\mu^-)) dE \quad (2.14d)$$

$$q = \int_{L_3+L_2} (XAS(\mu^+) - XAS(\mu^-)) dE, \quad (2.14e)$$

2.3 Experimental aspects of X-ray Absorption Spectroscopy and Magnetic Circular Dichroism

The synchrotron radiation comes from a special type of accelerator [27, 233–235], but it also describes the radiation emitted by charged particles moving at relativistic velocities in magnetic fields curving their trajectories. Synchrotron radiation is produced in storage rings of varying size (from 50 m to 300 m diameter) around which are tangentially installed experiments or beamlines. Storage rings are made up of complex combinations of magnetic and electric field, the former serving to produce radiation and the latter to reaccelerate particles that have lost their energy by radiating.

2.3.1 Description of the Dichroism Experimental Installation for Magneto-Optical Spectroscopy (*DEIMOS*) beamline

The use of synchrotron radiation techniques in various field of magnetism (examples : surface and interface magnetism, molecular magnets, paleomagnetism, etc.) is based on the development of circularly and linearly polarized X-ray sources. For this purpose, The *DEIMOS* (**D**ichroism **E**xperimental **I**nstallation for **M**agneto-**O**ptical **S**pectroscopy) beamline [259] was part of the second phase of development at French Synchrotron SOLEIL (Source Optimisée de Lumière à Energie Intermédiaire du LURE) and is dedicated to the study of the magnetic and electronic properties using polarized soft X-rays. It delivers polarized soft X-rays to perform XAS, XMCD, X-ray natural linear dichroism (XNLD) and X-ray magnetic linear dichroism (XMLD) in the energy range 350–2500 eV. The advantage of the magnetic dichroism techniques used on *DEIMOS*, compared to other magnetometry

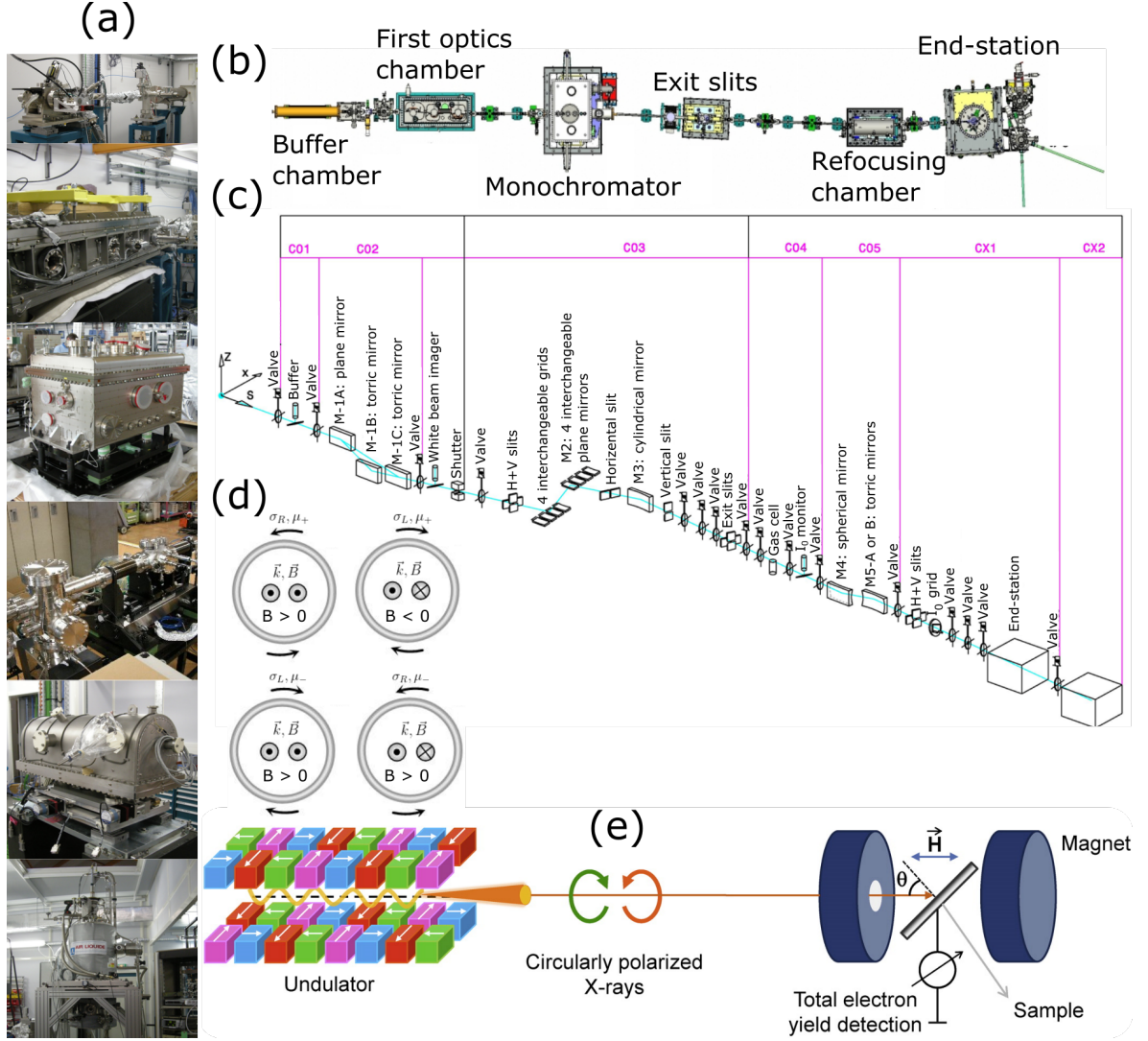


Figure 2.8: (a) Photos of the DEIMOS beamline. (b) Schematic representation of each compartment shows in (a). (c) The X-ray path between the insertion device and the experimental station. (d) Scheme representing the direction of the magnetic field, the wave vector, the circular polarization of the X-rays (σ_R, σ_L) and the helicities (μ_+, μ_-). This scheme must be seen from the point of view of the observer at the experimental station. (e) Schematic diagram of an experimental XMCD setup at a beamline, where circularly polarized X-rays are produced by an Apple-II type insertion device. The beamline optics has been omitted in the diagram. Figures (a), (b) and (c) were realized by DEIMOS beamline. Figure (e) was taken from [255].

techniques, is the ability to measure the electronic and magnetic structure of each chemical element independently. Moreover, thanks to an extremely low detection limit, these measurements can be carried out on a few atoms or molecules. The beamline is made up of three *hutches* (undulator, optical and end-station) that I will detail in the next paragraph. Photos, plans and schemes of the whole set-up is presented in figure 2.8.

In the first hutche, there are two undulators as a source of photons, namely, HU-52 (helical undulator) and EMPHU-65 (ElectroMagnet/Permanent magnet Helical Undulator) [259]. Both deliver circularly (right (CR) and left (CL)) and linearly (horizontal (LH)

and vertical (LV)) polarized X photons. The HU-52 consists on a clever arrangement of four magnetic arrays with a period of 52.4 mm. For the EMPHU-65 insertion device, it consists on an arrangement of pole orientations with a period of 65 mm and is very suitable for measuring very small XMCD signals. Then, there is the buffer chamber which is a delay line which consists of a large volume acting as a buffer for the vacuum. Afterwards, we find the first optics chamber. It is made up of 3 mirrors which divide the incident photons into two choosable optical paths and orient the selected beam onto the entrance slits of the monochromator. Moreover, this chamber aims to stop the bremsstrahlung using a water cooled tungstene block; this process producing ionizing radiations it required for the chamber to be locked inside a radiation protection hutch.

Then, we find **the monochromator**. It consists of 2 interchangeable gratings: a variable groove depth (VGD) and an alternating multilayer network (AML) [260]. The VGD (resp. AML) is optimized for the energy range 240–1500 eV (resp. 1000–2500 eV). Moreover, the energy stability (1 meV/h) is mainly limited by the temperature variations produced by the day-night cycles, although the monochromator has its own hutch with a dedicated air conditioner that keeps the temperature variations below ± 0.5 K. The X-ray beam will then enter the exit slits. The role of this latter is to cut the beam at the exit of the monochromator above and below the plane of the storage ring. The more closed they are, the less photons will travel through and the higher the energy resolution will be.

Now, we arrive to the last part, known as **the experimental hutch**. It is made up of an optical refocusing system, says Wolter, and of the end-station. The Wolter chamber associates 4 mirrors which can be switched under-vacuum to produce two different beam sizes. The first mirror set-up produces a spot size of $80 \times 80 \mu\text{m}^2$, called *the small beam*. While the second set-up produces a spot size of $800 \times 800 \mu\text{m}^2$, called *the big beam*, and also divides the photon density on the sample by 100. Regarding our experiments, we choose to work with *the big beam* because it has less flux per unit area and per unit of time and that our molecules can decompose under the effect of X-rays.

Finally, we enter to **the end-station**. It is equipped with a **superconducting magnet** providing ± 7 T along the X-ray beam or ± 2 T perpendicular to the beam. Afterwards, we have the cooling system, namely, **the variable temperature insert (VTI)** which has been developed by the beamline and suitable for temperatures between 1.5 and 370 K [261]. The last but not the least, **the detection system**. In fact, the absorption signal can be recorded in 3 different ways (transmission mode, total electronic yield, fluorescence yield). In the context of my thesis, I used the total electron yield detection that I will explain in the next section.

The XAS experiments are performed with circularly polarized X-ray with a total incoming photon flux on the samples of about $10^8 \text{ photons.s}^{-1}.\text{mm}^{-2}$. Depending on the measurements, the geometry of the experiments changes. I mainly use three geometries of measurements of the angle between the incident X-ray with respect to the normal to the surface (θ), namely, normal ($\theta = 0^\circ$) or at $\theta = 45^\circ$ (see figure 2.8-e). The temperature-dependent XAS measurements in chapter 3, as well as the magnetic measurements in chapters 5 and 6 were done in normal incidence. For the measurements under visible light illumination in chapter 4, we used 45° geometry. Indeed, the windows we use for illuminating the sample are placed at 90° with respect to the incoming direction of X-rays.

2.3.1.1 Detection technique: The Total Electron Yield (TEY) method

To measure the absorption cross section, we measure by means of electrons that escape from the superficial layers because of the decay of the core-hole; this is the so-called **total electron yield (TEY)** detection technique (see figure 2.9-b). This technique counts all escaping electrons due to the absorption of one photon. However, the energy of the outgoing electrons is not selected, the signal is dominated by secondary electrons which are created in the cascade process of the Auger decay electrons. The ease of detection and the large signal make TEY the most used technique, but the specific processes remains relatively unclear. As an estimation of the probing depth, the penetration length of X-rays (λ_{X-rays}) is of the order of 100-1000 nm while the mean free path of these electrons (λ_e) is of the order of 5 nm. As the creation and escape of secondary electrons is highly material dependent, the probing depth of TEY will certainly be material dependent too. To study the mean probing depth of TEY quantitatively, you can refer to reference [232]. All soft X-ray experiments have been performed in UHV, with a typical pressure 10^{-10} mbar. It is necessary to work under UHV conditions to assure a clean surface because the TEY detection is rather surface sensitive. During a XAS measurement the dose of soft X-rays which is impinging on the sample is relatively low because the experiments are performed with high resolution and only an extremely small proportion of the beam reaches the sample. Also charging can occur, for this reason, the samples should be grounded to prevent macroscopic charging effects. In practice, at the *DEIMOS* beamline, we measure the absorption signal as the ratio between the TEY of the probe surface (I_t) by a normalization current (I_0). I_0 is measured by a gold grid (see figure 2.8-c) that allows 50% of the incident photons to pass. Those outgoing photons hits the sample giving rise to I_t . All of these processes are proportional to the absorption of a photon, so the measured signal (in arbitrary units) is proportional to an absorption spectrum.

2.3.1.2 Let's run a spectrum !

All the end-station equipment is controlled using a computer. After putting the sample in the cryostat (called Cromag, see figure 2.9-a), adjusting the exit slits to 80 μm to have an energy resolution of 150 meV, the energy offset of the monochromator with respect to the undulator and aligning the sample with the X-ray beam (according to the experiment as discussed before), we are finally ready to get a spectrum which is typically measured within 2 minutes. For more details about the acquisition of XAS spectrum, I suggest you to read the paper published by the beamline [259]. In the following, I will explain the processing of the most important spectrum of my thesis, namely, the $L_{2,3}$ edges of Fe^{II} as shown in figure 2.9-c. In black, is shown the raw XAS spectrum as measured where the dotted line represent the background. The first step consists on calculating, on the raw data, the edge-jump in percentage of the jump at the L_3 edge at 707.9 eV (7.6 % for example). The last step consists on subtracting the linear background to get the red spectra and then we normalize to the background value at 707.9 eV so that the jump at the L_3 edge can therefore be read as a percentage of the background signal as shown in the blue spectra. Another essential point is the energy normalization of the $L_{2,3}$ edges of Fe^{II} . Indeed, the absolute energy value of the L_3 peak may change from one beamtime to the other while the energy difference between the L_2 and L_3 edges remains the same because it is proportional to ζ_{2p} (see equation 2.9).

Therefore, we have done the energy calibration of the L_3 edge of the Fe^{II} ion based on tabulated measurements of the L_3 edge of a cobalt metal [262, 263] which is at 778.1 eV. We shift the energies of the XAS spectra of Fe^{II} with an amount of $\Delta E = |E_{\text{max}}^{\text{Co}} - E_{\text{max}}^{\text{Fe}^{\text{II}}}|$. However, the calibration of the L_3 -edge of Fe^{II} in Chapter 4 was taken at 708.7 eV for the HS state and 710 eV in the LS state. The reason is that at this time, we took as reference the L_3 -edge of Co at 779 eV according to reference [264].

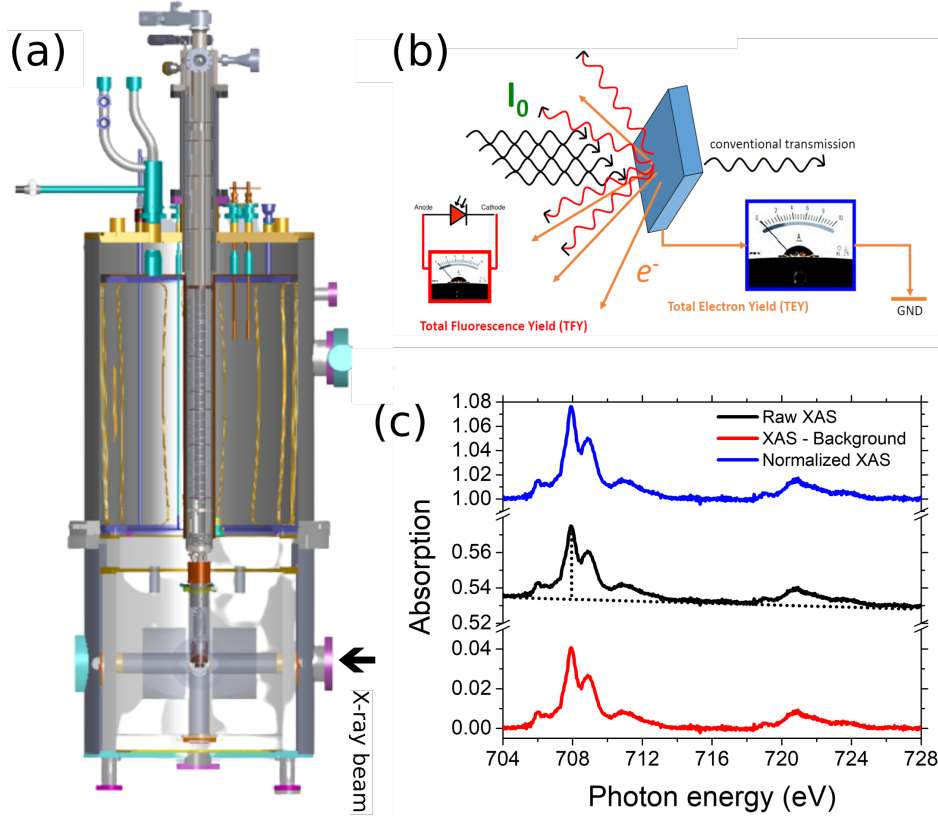


Figure 2.9: (a) Scheme of the Cromag installation (courtesy of the DEIMOS beamline). (b) The different detection techniques. I_0 is the intensity of the incident X-rays. (c) The different stages of processing an XAS spectrum. black: (in full lines) raw XAS data at the $L_{2,3}$ edge of Fe^{II} and the dashed lines represents the baseline; red: raw XAS data after background subtraction; blue: XAS after normalization by the background value at 707.9 eV

2.4 Scanning Tunneling Microscopy (STM)

The Scanning Tunneling Microscope (STM) was invented by G. Binnig and H. Rohrer at IBM Zürich [265, 266], who received the Nobel Prize in Physics for this invention, in 1986. The STM is a near-field microscopy technique that measures the properties of matter down to the atomic scale. This opened up the possibility of studying the structural and electronic properties of matter (atomic adsorbates, molecules on surfaces, etc.) in real space [179]. Indeed, the topography is measured through the integration in an energy window, from the Fermi energy (E_F) to $E_F + eV$ (with V , the bias voltage) of the local density of states (LDOS) of the sample surface. Its operating principle is based on the quantum tunnel effect of electrons which is a direct consequence of the wave-particle duality. Indeed, it expresses

the fact that a particle, described by a wave function has a non-zero transmission probability of crossing a potential barrier with an energy higher than its own.

2.4.1 Theoretical models for STM

In this part, I will briefly describe the theoretical ingredients to understand the tunnel effect. Indeed, many models have been proposed to understand this effect. For example, a basic exercise in quantum mechanics is the 1D tunnel barrier [236]. Indeed, if we have a rectangular potential of height Φ (work function) in between the metallic probing tip and the metallic sample surface separated by a distance z_0 , the solution of the time-independent Schrodinger equation shows that there is a non-zero probability that the electrons cross the potential barrier. In the approximation $\kappa z_0 \gg 1$, this probability is given by an evanescent wave:

$$\Gamma(z_0) \propto \exp(-2\kappa z_0) \quad (2.15)$$

Where $\kappa = \sqrt{\frac{2m^*\Phi}{\hbar^2}}$ is the wave number, m^* is the effective mass of the electron. This exponential dependence is at the origin of picometric vertical resolution in STM. Then a more improved model have been proposed for metal-insulator-metal (MIM) junctions by Bardeen [267] with the difference that it was treated in the many particle point of view in the time-dependent perturbation theory. At thermal equilibrium, the tunneling current (I) has the following expression:

$$I = \frac{2\pi e}{\hbar} \sum_{\mu,\nu} [f(E_\mu)(1 - f(E_\nu)) - f(E_\nu)(1 - f(E_\mu))] |M_{\mu\nu}|^2 \delta(E_\mu - E_\nu) \quad (2.16)$$

Where e the electron charge, μ and ν refers to the left and right metallic electrodes respectively, the $\sum_{\mu,\nu}$ described the fact the electrodes are a continuum of states, $f(E)$ (resp. $1 - f(E)$) is the Fermi-Dirac distribution which describes the occupied states (resp. unoccupied states), $M_{\mu\nu} = \langle \psi_\mu | \hat{H}_{tunneling} | \Phi_\nu \rangle$ is the matrix element in the first order perturbation theory and describes the transition rate for tunneling from the left to the right electrode and the delta function ensures the energy conservation. Later and based on the Bardeen model, Tersoff and Hamann [268] proposed a model which is the best to describe the STM with some more new ingredients. Firstly, we assume an energy dependence of the tunneling matrix element. Secondly, explicit expressions of the wave functions $|\psi_\mu\rangle$ and $|\Phi_\nu\rangle$ have been proposed. The tip state could be described by the state of its last atom (because of the exponential decay of the tunneling probability) at position $\vec{r}_0 = (\vec{r}_\parallel, z_0)$ and approximated by a s -wave function. Finally, the wave function of the surface can be written in the reciprocal space using a Fourier decomposition in the basis of Bloch function parallel to the sample surface and which is modulated by the evanescent wave perpendicular to the sample surface. Then, in this model using the Wentzel-Kramers-Brillouin (WKB) approximation⁸ of the trapezoidal tunnel barrier, the tunneling current could be written at low temperature

⁸WKB approximation is a method for finding approximate solutions to linear differential equations with spatially varying coefficients.

as:

$$I(\vec{r}_0, V) \propto \int_{E_F}^{E_F+eV} \rho_s(\vec{r}_{||}, E) \rho_t(E - eV) \Gamma(E, z_0, V) dE \quad (2.17)$$

$$\Gamma(E, z_0, V) = \exp(-2z_0 \sqrt{\frac{2m^*(\Phi + \frac{eV}{2} - E)}{\hbar^2}})$$

Where $\rho_s(\vec{r}_{||}, E)$ (resp. $\rho_t(E - eV)$) is the LDOS of the surface (resp. DOS of the tip). Here, Φ is the average work function of the tip and the surface and $\Phi + \frac{eV}{2}$ gives the effective height of the barrier for the applied voltage V . An other thing which is interesting in the expression of the transition probability is the fact that not all the electrons have the same probability to tunnel. Indeed, the electrons close to the Fermi level have higher probability to tunnel.

2.4.2 Principle of operation

At this stage we are going to make an additional approximation: within the limit of low voltages ($eV \ll \Phi$), we can consider that the transmission coefficient varies slowly in the energy range considered. As stated before, the wave function describing the tip is of spherical symmetry and is independent of energy. Thus, STM images can be interpreted as isodensity profiles of integrated states of the sample. The probed states could be distinguished according to the voltage polarity. Indeed, the direction of tunneling electrons depends on the polarity, so it is possible to have access to the empty states (resp. occupied states) of the sample for $V > 0$ (resp. $V < 0$). If a positive (resp. negative) bias voltage is applied on the sample side then the Fermi level of the sample side goes below (resp. above) the Fermi level of the tip side by an energy $|eV|$, then the electrons tunnel from the tip (resp. sample) side to the empty (resp. occupied) states of the sample and thereby probes the empty (resp. occupied) density of states of the sample. The discussion is sketched in figure 2.10-a.

2.4.3 Modes of operation

The STM operates at tip-to-surface distances (width of the tunnel barrier) which are of the order of few angstroms. Therefore, we want to have extremely precise tip movements. The tip can be controlled using a sensitive electronics that drives a piezoelectric crystal which can control the motion of the tip in all three directions (x, y, z) as shown in figure 2.10-b/e/f. To make the initial approach of the tip to the sample, we go there in two stages: first, the approach by a coarse motor which allows a macroscopic step (200 nm). Then, the piezoelectric crystal holding the tip, and which is connected to a feedback loop electronic, will make very precise motor steps (pm) until reaching a given set-point for the tunneling current. The whole electronics is interfaced with a computer. Depending on the operation of the feedback loop, the instrument can operate mainly in 2 modes: **measuring at constant tunneling current** or at constant height. The first mode is the only mode I used during my doctoral work and the most common one used on a STM set-up. In this method, the feedback loop is active and thus the intensity of the tunneling current is maintained at a determined value. We measure the "*topography*", corresponding to the tip-surface distance variations to keep a constant integrated LDOS over the energy range determined by the applied electrochemical potential.

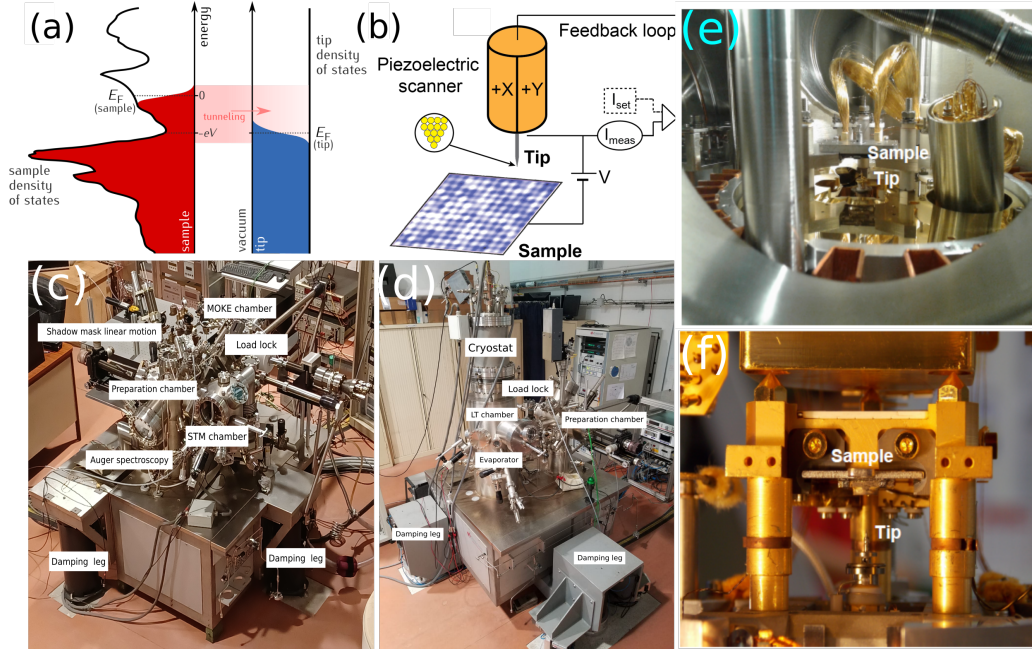


Figure 2.10: (a) Schematic diagram of a tunneling barrier between two electrodes. (b) Typical STM experiment. The tip (or sample) is directly mounted on piezoelectric elements that control the gap size and the lateral position of the junction, down to picometer. An electronic feedback loop can keep constant the value of the tunneling current when scanning the sample, which is the basic operation mode of imaging (constant current image). Presentation of (c) variable temperature (VT) and its tip (e) and (d) low temperature (LT) STM set-up and its tip (f).

2.5 Experiment under ultrahigh vacuum (UHV)

Exposing a sample to air, even for a few μs , contaminates its surface with several types of adsorbates typically: water, hydrocarbons, etc. In general, under a pressure of 1 bar, the time for the formation of a monolayer of adsorbents is $6 \cdot 10^{-9}$ s. The preparation and analysis of the sample are therefore carried out under ultrahigh vacuum conditions (UHV - very low pressure down to 10^{-11} mbar) in order to avoid any reaction with unexpected species, over a reasonable time scale (few days). UHV is obtained using four types of pumps. First, using primary pumps, the vacuum obtained is 10^{-2} mbar. Secondly, with turbomolecular pumps, the vacuum obtained is in the order of 10^{-9} mbar after heating the system to more than 130°C . Finally, with the ionic and titanium sublimation pumps the obtained vacuum is in the range of 10^{-11} mbar.

2.5.1 Substrate preparation

All the substrates used in the context of my thesis are single crystals (Cu(111), Au(111) and Ag(111)). The surface preparation is carried out in three steps. The first step consists in degassing the sample after its introduction into the UHV chamber, by heating it using a Pyrolytic Boron Nitride (PBN) oven. It is a resistive heating that consists on an electric current which is locally sent to the filament and heats the sample by Joule effect and allows

us to have temperatures up to 350°C for copper for example. All the molecules are desorbed, mainly water. The second step is the ion sputtering. After having introduced an argon (Ar) gas into the preparation chamber (up to a pressure of 2×10^{-6} mbar), it will get ionized by a electron beam of 10 mA, generated by a hot filament hold at a high negative potential. The Ar^+ ions will then be accelerated via a potential difference and will bombard the sample surface to remove the surface contaminants. For the metals used, the energy of Ar^+ ions used for sputtering are typically 600 eV for Cu(111), 900 eV for Au(111) and Ag(111). Finally, the sample is annealed thanks to the PBN oven. It consists of a step of gradual temperature rise followed by controlled cooling, which allows the desorption of remaining Ar atoms and recrystallization of the surface. Also, to check the quality of the substrates, we characterize them chemically using Auger spectroscopy and we also look at them using the STM to see if the terraces are well recrystallized, perfectly flat and clean. In the context of my thesis, there is only the surface of Highly Oriented Pyrolytic Graphite (HOPG) which is prepared differently. Indeed, the surface of the HOPG is cleaved using a UHV scotch carbon tape before its introduction into the pumping load-lock and subsequently annealing at 200°C for 60 min in UHV. Photos of the samples used in this manuscript are shown in figure 2.11 and STM images of the bare substrates are shown in figures 2.13-a/b/c/d/e.

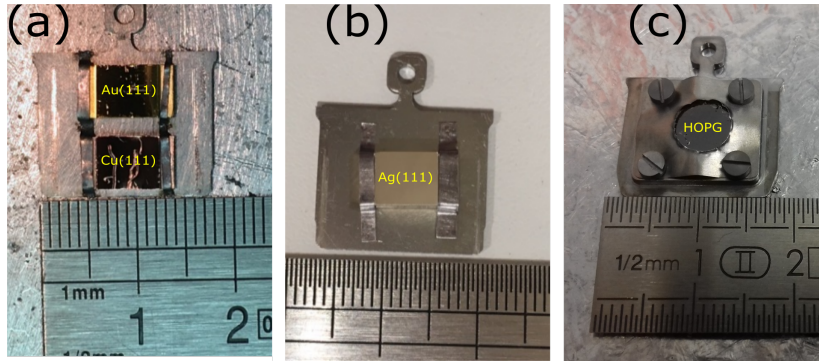


Figure 2.11: Photos of the samples used (a) Au(111), Cu(111); (b) Ag(111) and (c) HOPG.

2.5.2 Metal deposition

In our experiments, we deposited two types of metals on the clean single crystal substrates. A noble metal which is copper and a ferromagnetic metal which is cobalt. The two metal rods are of very extrem high level of purity (99.999% pure). The deposition was realized by Electron-Beam Physical Vapor Deposition (EBPVD) using a standard commercial electron beam evaporators (EFM3, *FOCUS company*). It consists on a filament (I_{fil}) which delivers a thermoionic emission current (I_e). The electron are accelerated to the evaporant material with a high voltage (U). Upon striking the metal, the electrons will convert their kinetic energy into thermal energy and will therefore sublimate the evaporant into atomic or ionic species of the evaporant (Co/Co^+ or Cu/Cu^+). The atoms and ions flux are then collimated directly on the target substrates via a collimation tube. In addition, to keep a good vacuum during the deposition, the surrounding of the evaporant is cooled by a water circuit. The flux of the evaporation (I_{flux}) is measured by the ionic current in the collimation tube and can be controlled precisely by the embedded electronic controller to have depositions from

sub-monolayer coverage to multilayers. This type of evaporation is extremely clean and the partial pressure increases only by a small amount during the experiment under UHV. The typical values for cobalt (resp. copper) evaporation are the following: $I_{fil} = 1.83$ A (resp. 1.25 A), $I_e = 13.3$ mA (resp. 14 mA), $I_{flux} = 19.8$ nA (resp. 4.1 nA), $U = 900$ V (resp. 995 V). A picture of the EFM3 evaporator is presented in figure 2.12 and STM images of Co/Au(111) and Cu/Au(111) are shown in figure 2.13-f/g. Finally, in many of the samples that I will present in my present work, some have different metallic or molecular thicknesses (see next section) on the same substrate. Indeed, to get different thicknesses on the same sample, prior to the deposition, a movable shadow mask made by a tantalum foil was placed a few millimeters from the sample surface, allowing the definition of different areas on one sample, as shown in figures 2.12-b/c/d. We therefore made samples with three regions (2 mm wide each) or two regions (3 mm wide each) which is a monumental time saver for synchrotron beamtime. Moreover, for given experimental conditions (temperature ramp in chapters 3 and 4, light exposure in chapter 4 and magnetic field in chapter 6) and for a given sample, this allows us a direct comparison of the results.

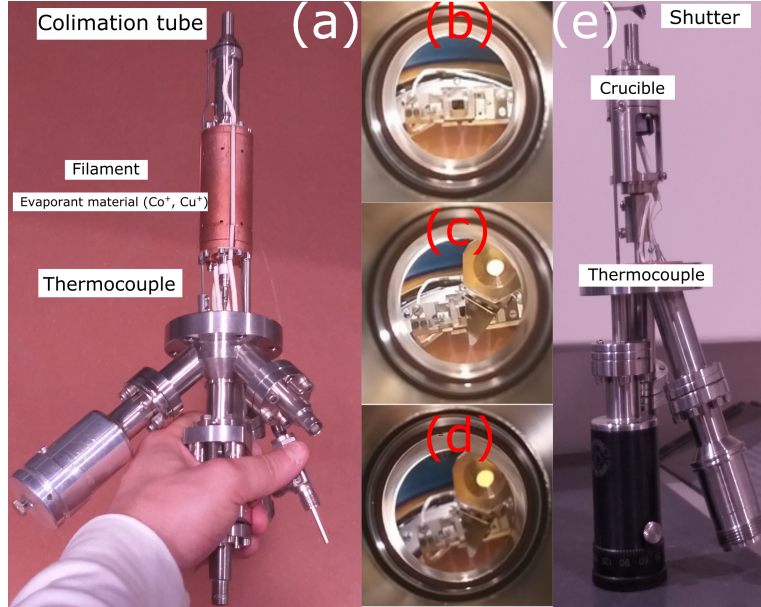


Figure 2.12: (a) Photo of the copper and cobalt evaporator. (b)-(c)-(d) Photos for different positions of the shadow mask. (top) evaporation over the whole sample; (middle) evaporation over half of the sample; (bottom) the whole sample is hidden. (e) Photo of the Fe-Pyrz evaporator.

2.5.3 Calibration of the Co thickness

In the Co evaporation chamber, we have an *in-situ* magnetometry equipment which is the Magneto-Optical Kerr Effect (MOKE) (see figure 2.10-c). It helps us to know in real time the evolution of the thickness. Indeed, the Co/Au(111) system has what is called a spin reorientation transition (SRT) [196, 269–276]. Below a certain thickness, the Co atoms form small separate islands and the system is superparamagnetic (as shown in figure 2.13-f). From a certain thickness, the Co islands coalesce and adopt a ferromagnetic behavior. Thus, the Co magnetization is out-of-plane (the cycles are square). Above a certain thickness (4.23 ML for Au(111), ML is monolayer), which is called the critical thickness of the SRT, the Co

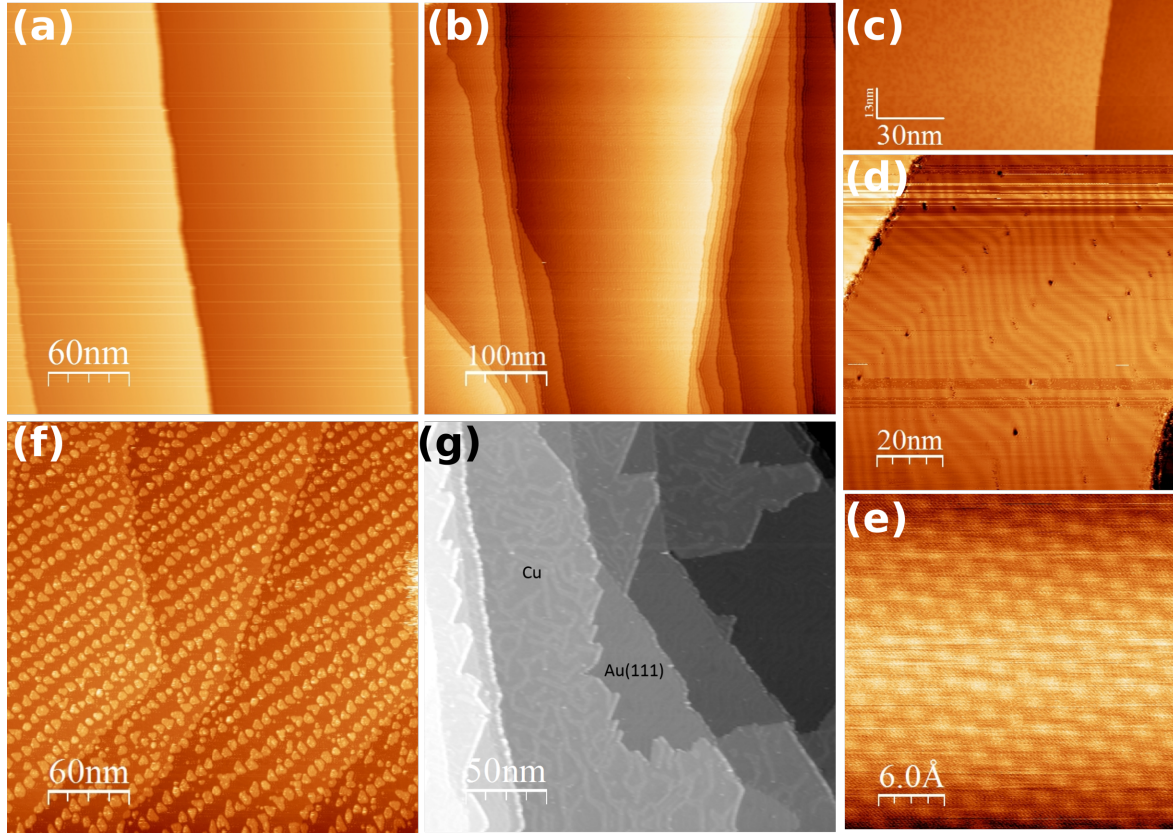


Figure 2.13: STM images of (a) Cu(111); (b) Au(111); (c) Ag(111); (d) Surface reconstruction on Au(111); (e) HOPG; (f) Co/Au(111); (g) 0.5 ± 0.1 ML of Cu on Au(111).

magnetic hysteresis cycle switches and starts to close until adopting a magnetic behavior which is completely in-plane. This SRT has been extensively studied and serves us to calibrate the Co thickness. At the end, we can plot the remanence magnetization normalized to the saturation magnetization ($\frac{M_R}{M_S}$), called the squareness, and it tells us directly about the thickness of Co. All this discussion is summarized in figure 2.14.

2.5.4 Molecule deposition

The powder deposition of Fe-Pyrz is achieved under UHV ($P = 5 \cdot 10^{-10}$ mbar) from a homemade Knudsen cell with a 0.5 cm^3 crucible heated by a tantalum filament at around 358 K [223]. The temperature is measured via a thermocouple in contact with the bottom of the crucible. Moreover, for each presented sample, the thickness calibration procedure will be discussed but in general, the thicknesses determination is based on a quantitative correspondence between coverage in several submonolayer STM images and XAS jump-to-edge intensity at room temperature as a reference to deduce the thicknesses. This will be detailed in the different chapters when necessary. Finally, when the samples are ready, they are transferred in a homemade vacuum suitcase with pressure in the low 10^{-10} mbar and transported within few hours to the DEIMOS beamline.

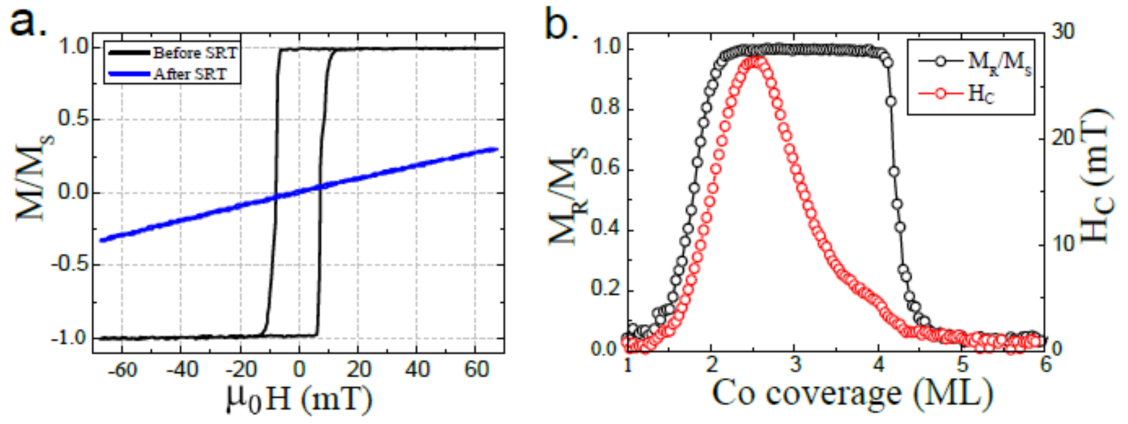


Figure 2.14: Magnetic hysteresis and spin reorientation transition. (a) Raw hysteresis cycles showing change in magnetization (M) normalized over saturation magnetization (M_S) before and after spin re-orientation transition (SRT) of Co on Au(111). (b) Remnant magnetization (M_R) normalized over saturation magnetization (M_S) is plotted along with coercive field (H_C) as a function of Co coverage. SRT in Co occurs when the M_R/M_S ratio drops from 1 to 0.5. The SRT thickness of Co on Au(111) is 4.2 ML. This figure was taken from [277].

THERMAL SWITCHING OF SURFACE-SUPPORTED FE-PYRZ ULTRATHIN LAYERS

Spin-crossover (SCO) molecules are promising systems for the development of molecular spintronics [1, 16–20, 22, 181], as they present two electronic spin states that can be controlled by external stimuli such as light, pressure or temperature [3, 5, 9]. The thermal-induced switching process between HS and LS is well documented for bulk materials [4]. This property mediated by phonon and electron-phonon coupling can be accompanied by the observation of a thermal hysteresis loop which is a manifestation of bistability or the so called 'memory-effect'. In the hysteresis range, the two spin states can be considered as being associated with binary code (ON/OFF) and this can be used for example for the conception of molecular memory devices [12, 24, 171]. However, it remains relatively uncommon and unpredictable to get an hysteresis of more than a few Kelvin [4]. Inserting them in spintronic devices remains a big challenge for future applications [13, 14, 278, 279] and requires a deep understanding of their properties in the form of nanoparticles [4, 9, 150, 151, 165–171], ultrathin films [192, 200, 201, 222] and down to a single layer on various substrates [147, 162, 175, 177, 201–203]. In addition, the structural distortions that accompany the volume change in the spin state switching produce elastic strains [48–50] manifested by short and long-range interactions and cooperative transformations [95]. The cooperativity is a key parameter to understand the thermal spin-transition behavior (transition temperature, shape and width of the thermal bistability, residual high spin fraction at low temperature). It was unveiled that the shape of the thermal transition is size-dependant [80] and can significantly differ from the bulk one in thin films or nanoparticles [154, 170, 173, 207]. Moreover, the molecule-substrate interaction is generally responsible for an incomplete transition, with a residual proportion of HS molecules at low temperature that can be ascribed to epitaxial strain and a related loss of cooperativity [162, 202, 203, 226]. In order to have a qualitative and quantitative description of the effect of cooperativity, Monte Carlo Arrhenius simulations based on a 3D mechanoelastic model enable to capture finer details of the SCO system. This theoretical tool has been applied successfully to describe the thermal bistability in macroscopic crystals and also loss of cooperativity for SCO nanoparticles adsorbed on substrates. [280].

In this chapter, using X-ray absorption spectroscopy (XAS) and mechanoelastic model, we investigate the thermal transition of ultrathin films of Fe-Pyrz on Cu(111) and Highly Oriented Pyrolytic Graphite (HOPG) surfaces. We will first describe the principle of the Monte Carlo Arrhenius simulations in the framework of the mechanoelastic model. We will then show the temperature-dependant XAS results on Cu(111), before presenting the simulation of XA spectra in the framework of LFM calculations to fit the experimental XA spectra. In order to better understand the role played by the substrate and the dimensionality on the thermal bistability, using mechanoelastic simulations that include a molecule-substrate interaction, we will discuss the obtained experimental thermal spin-crossover curves and especially the evolution of the thermal bistability range and the temperature of switching as a function on the layer thickness and the substrate interaction. Finally, by XAS measurements, we will show the modification of the thermal transition properties of Fe-Pyrz ultrathin layers on HOPG compared to Cu(111).

3.1 Monte Carlo Arrhenius simulations in the framework of the mechanoelastic model

Macroscopically, we could characterize the spin transition by the evolution of the HS population ($x_{HS}(T)$) as a function of the temperature. This macroscopic characterization was at the origin of several theoretical developments such as the mean field models [1, 33, 42, 51, 104, 114, 133] or Ising-like models [49, 53–64] which were widely used but failed to describe certain experimental observations of the transition such as nucleation-propagation of like-spin domains [54, 63, 64, 66, 68, 83–86]. In order to adequately reflect the experimental observations, a new model has been proposed, the so-called mechanoelastic model [49, 65, 67, 70, 73, 95, 226]. This latter belongs to the family of elastic models and is capable of calculating and simulating relaxation curves LS→HS, thermal hysteresis and of accounting for the evolution of clusters and distortions during the thermal transition. More specifically, in this chapter we shall use the mechanoelastic model to describe the thermal spin-crossover [281–283].

3.1.1 Description of the model

The interactions between SCO complexes are not of magnetic origin but of elastic origin [30, 42, 48–51]. The main idea of the model is as follows: the change in volume between the two HS and LS states introduces distortions of the network during the transition as shown in figure 3.1. These distortions of the molecular network are at the origin of intermolecular interactions of elastic type and are treated as connected springs with an elastic constant k_{mol} and which can be either compress or extend. Compression or elongation is related to their length at equilibrium according to the relative positions of neighboring molecules. During the transition, there is a reorganization of the positions of the molecules. As stated before and schematize in figure 3.1, the mechanoelastic model belongs to the family of so-called *Ball and spring* models which describes a system of individual molecules distributed in a two-dimensional hexagonal network connected by springs with open boundary conditions. The open boundary conditions are a big difference from historical mean-field or Ising-like

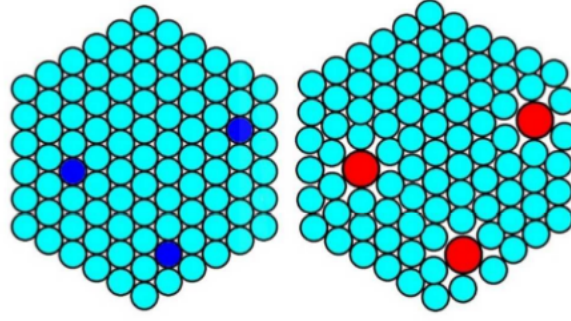


Figure 3.1: Basic representation of the elastic model for a hexagonal network of molecules. In the initial state all the molecules are in the LS state (blue circles). When some molecules (dark blue circles) switch their state to HS (red big circle), all the other molecules (small blue circles) change their positions. The hexagon becomes then distorted: the distortions are bigger in the vicinity of switched molecule (short-range effect), but they are present even in remote parts of the system (long-range effect). This figure is taken from reference [68].

models. This makes it possible to account for finite size effects and thus to account for the fact that nucleation begins at the edges, which is in accordance with experimental observations. When a molecule switches, its volume change is encoded in the radius variation of the ball (of the order of 0.2 Å for Fe(II) complexes [31, 32]). The change in volume first induces a force in the springs connecting the SCO molecules to each other (closest neighbors). This force changes the position of all molecules in the system. This switch of a SCO entity will gradually propagate throughout the system. As a result, the intermolecular interaction constructed in this way as short-range interactions, affects not only the nearest neighbors but also all molecules located at long range, so it has the information of short-range and long-range interactions (opposite of Ising-type models where interactions generally affect the closest molecules). Of course, the effect will be larger for molecules closer to the one with the switch.

After each molecular switch, all molecules in the system begin an oscillatory motion, which in the absence of any damping would continue forever. As we are interested in the new state of mechanical equilibrium, we consider that each molecule has a damped oscillator motion and the new position of the molecules is given by the following differential equations:

$$m \frac{d^2 u_i}{dt^2} = F_{u,i} - \mu \frac{du_i}{dt} \quad (3.1)$$

Where m is the mass of the molecule, μ is the damping constant, $u = x, y$ are the cartesian coordinates of molecule i and $F_{u,i}$ is the projection of the force \vec{F} on the x and y axes of the molecule i . The criterion of convergence of the calculation is when the change in position between two consecutive iterations is less than a given threshold value. The expression of the forces intervening in the equation 3.1 is:

$$F_{u,i} = \sum_{\text{neighbor springs } j} k_{mol} \delta r_{ij,u} \quad (3.2)$$

Where k_{mol} is the intermolecular interaction and $\sum_{\text{neighbor springs } j} \delta r_{ij}$ describes the algebraic sum at mechanical equilibrium of the elongations of neighboring springs. This latter is

positive (resp. negative) when the spring stretches (resp. compresses). The mechanical equilibrium is reached when the sum of all the forces applied to the molecule in all directions is zero. It is given by:

$$\sum_j k_{mol} \delta \vec{r}_{ij} = \vec{0} \quad (3.3)$$

If one molecule is switched to the HS state, the larger volume compress the neighbour springs which will apply an internal pressure on the switched molecule to relax to the LS state. The local pressure is written as:

$$p_i = \sum_j \frac{k_{mol}}{A} \delta r_{ij} \quad (3.4)$$

Where A is the molecular cross section. Furthermore, the local pressure will only be the same for all the molecules of the system for a perfectly hexagonal system ($x_{HS} = 0$ or 1), otherwise the local pressure will be different for each molecule of the system. Thus, the local pressure difference favors the formation of clusters and can lead to an avalanche phenomenon [66, 68, 284]. In figure 3.2 is presented an example of the evolution of the thermal transition for different values of intermolecular interaction. Indeed, k_{mol} is an important parameter to adjust properly in order to describe the experimental observations. We observe from the figure 3.2 that the more k_{mol} increases, the more abrupt the transition becomes until the opening of a thermal hysteresis loop. This feature is similar to the experimental situations where compounds with stronger interaction between the complexes via hydrogen bonding or $\pi - \pi$ interactions present wider hysteresis [67].

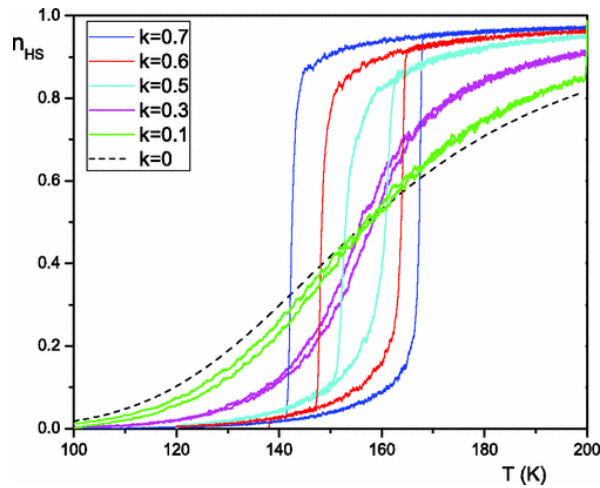


Figure 3.2: Thermal transition for various spring constant interactions. If the spring constant k_{mol} is higher than a threshold value (0.3 N/m), then the transition is accompanied by a hysteresis. This figure is taken from reference [67].

3.1.2 Implementation of the model

Initially, all the molecules are in the same spin state (HS at high temperature or LS at low temperature) and are organized in a perfectly hexagonal configuration. The sum of the

initial forces is therefore zero (no elongation or compression of the molecules). To be able to determine which molecule changes state, the mechanoelastic model uses the Monte Carlo algorithm. For this, we calculate the probability of passing from one state to the other which is compared to a number generated randomly. If the probability of passing is greater than this random number, the algorithm decides to pass the molecule from the HS to LS state or vice versa. The program calculates the equilibrium positions of molecules for a certain spin state configuration by solving the system of $2N$ coupled equations in 3.1, with $i = 1 \dots N$. The system of equations is solved using the DIVPAG routine for stiff ordinal differential equations from the IMSL Math Library based on the Gear's BDF (Backward Differentiation Formulas) method [285].

When molecules switch, the system is distorted and stores elastic energy. The canonical state will be the result of the competition between the free enthalpy of the system without distortion ($\Delta G = \Delta H - T\Delta S$) and the stored elastic energy (V_{ij}^{inter}). The Hamiltonian of the system is as follows:

$$H_{mechanoelastic} = \frac{1}{2} \sum_i (\Delta H - k_B T \ln g) S_i + W \quad (3.5a)$$

with :

$$W = \sum_{\langle i,j \rangle} V_{ij}^{inter} \quad (3.5b)$$

In equation 3.5a, ΔH represents the enthalpy difference between the HS and LS states, $\ln g$ is the ratio of the degeneracies of the electronic states for HS and LS molecules ($\propto \Delta S$, the entropy difference between the two states). Note that ΔH and g are internal properties of the molecule and can be measured experimentally by differential scanning calorimetry measurements [81, 108]. S_i is the spin state of molecule i and is "+1" when HS and "-1" when LS. The term V_{ij}^{inter} represents the intermolecular potential where W is the elastic potential energy stored by the system during the distortion. In the following, V_{ij}^{inter} is treated harmonically, and takes into account small changes in spring size, which is realistic, given that the change in radius between the two states is of the order of 0.2 Å [31, 32]. This allows us to write that:

$$V_{ij}^{inter} = \frac{1}{2} \sum_{\langle i,j \rangle} k_{mol} \delta r_{i,j}^2 \quad (3.6)$$

Several procedures have been considered for molecular switching by using various Monte Carlo techniques such as Metropolis [286]¹ or Arrhenius approaches. The Monte Carlo Arrhenius procedure is the most frequent used algorithm. Indeed, it permits the investigation of the *the dynamic properties* of SCOs and it considers that the transition rates are influenced by the energy barrier between the states. The probabilities to switch from HS to LS and vice versa are given by the following equations:

$$P_{HS \rightarrow LS}^i = \frac{1}{\tau} \exp\left(\frac{\Delta H - k_B T \ln g}{2k_B T}\right) \exp\left(-\frac{E_a - \kappa p_i}{k_B T}\right) \quad (3.7a)$$

¹Thanks to the Monte Carlo Metropolis algorithm, we have access to the *static properties* of the spin transition, i.e. the equilibrium properties of the system. It is based on a procedure of minimization of the elastic energy at each iteration. Moreover, the expression of the transition probability does not include the energy barrier between the HS and LS states and is given by reference [286].

$$P_{LS \rightarrow HS}^i = \frac{1}{\tau} \exp\left(-\frac{\Delta H - k_B T \ln g}{2k_B T}\right) \exp\left(-\frac{E_a + \kappa p_i}{k_B T}\right) \quad (3.7b)$$

Where E_a is the activation energy and τ is a scale constant which ensures that the probabilities are always less than 1 at any temperature and finally κ is a scale constant between the activation energy and the local pressure. The equations 3.7a) and 3.7b show that the switching probability depends on intrinsic properties of the molecule (the difference in enthalpy and entropy between states), as well as the extrinsic properties (the intermolecular interaction encoded by the stiffness constant k_{mol}), of the local pressure (determined by the elongation or compression of the springs), and of the temperature. It also involves the energy of the barrier between the HS and LS states as well as the parameter κ , which determines to what extent the local pressure influences the relaxation which induces a distribution of activation energies in the system depending to the local pressures. A whole discussion on the κ value is given in reference [68].

To summarize, the algorithm of the simulation is the following:

- At first all molecules are in the same spin state.
- We calculate the Arrhenius probability that a molecule i has of passing from the HS state to LS (on the other hand) given by the equations 3.7b and 3.7b.
- The algorithm generates a random number $r \in [0;1]$ and if r is lower than the probability of switching P (resp. $r \geq P$), the molecule switch (does not switch).
- The program queries all molecules in the system once.
- After an iteration and by this change of state of the molecule, a local pressure will be exerted (equation 3.4) and will reorganize the molecular network, it is therefore necessary to calculate at each iteration the new positions. In the Nose-Hoover formalism [49, 69], these positions are calculated deterministically using the $2N$ coupled equations given in equation 3.1.
- Redo the procedure until the condition given by the equation 3.3 is satisfied.

3.1.3 Implementation of the model on surfaces

The challenging novelty in these simulations is to take into account the effect of the surface. The surface is formed by 'inert' molecules with a fixed radius organized in a hexagonal network. Each SCO molecule, except those on the first layer which is in contact with the surface, is linked to its closest six neighbouring molecules on the same layer (plane), to three molecules in the plane below and to other three in the plane above by springs with an elastic constant k_{mol} , which modulates the cooperativity of the system. In addition, each SCO molecule on the first layer is linked to three substrate sites by springs with an elastic constant k_s , as simply shown in figure 3.3-a. Because of the surface effect, there are now two parameters to adjust simultaneously: k_s and k_{mol} . Moreover, to ensure that all SCO molecules, including those on the edges are linked with three surface sites, the number of sites on the substrate is larger than the number of molecules in the upper layers. Figure 3.3-b shows the evolution of HS fraction at 60 K as a function of the ratio $\frac{k_s}{k_{mol}}$ of

Fe-Pyrz on Au(111) [226]. These results were obtained for $k_{mol} = 4 \text{ N.m}^{-1}$ and we see that for low values of the ratio $\frac{k_s}{k_{mol}}$, the transition is complete, while for higher $\frac{k_s}{k_{mol}}$ ratios the transition becomes incomplete. This is explained by the fact that the associated cost of substrate-molecule elastic energy induces an incomplete switching of the layer, with remaining molecules in HS, as shown in the bottom of figure 3.3-a). In the rest of the chapter, we perform simulations of hysteresis curves and low temperature relaxations for different Fe-Pyrz thicknesses on Cu(111).

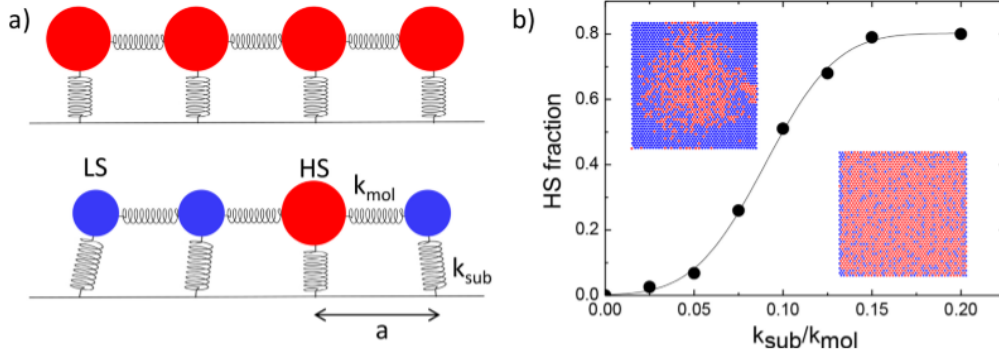


Figure 3.3: (a) Schematics of the mechanoelastic model including interactions with a substrate. Top: equilibrium configuration at high temperature where all of the molecules are HS and the springs are relaxed. Bottom: final configuration at low temperature where a part of the molecules have switched to LS, inducing a contraction of the springs. (b) Calculated fraction of HS molecules as a function of the ratio $\frac{k_s}{k_{mol}}$, obtained at 60 K by Monte Carlo on the model schematized in (a). The solid line is a guide to the eye using an error function. The insets are snapshots of the steady states for HS fractions of 25 (left) and 80% (right). Red (blue) dots correspond to HS (LS) molecules. Figure from [226].

3.2 Thermal bistability of an ultrathin film of Fe-Pyrz on Cu(111) surface

We investigated the thermal transition from submonolayers to few monolayers on Cu(111) by XAS and mechanoelastic simulations.

3.2.1 Preparation of the sample and determination of molecular coverage on Cu(111)

The preparation of Cu(111) single crystal substrate with dimensions of $6.5 \times 5.5 \text{ mm}^2$ is cleaned as described in chapter 2. The STM images show a perfectly clean surface prior to deposition with terrace sizes up to 150 nm. The powder deposition of different thicknesses of Fe-Pyrz is achieved as described in chapter 2. In this part, I will describe the results obtained by XAS on two samples of Fe-Pyrz on Cu(111) with different thicknesses on each sample: i) one sample with three regions of around 2 mm wide each; ii) an other one with 2 areas of around 3 mm and 2 mm wide respectively. The calibration of the thickness of

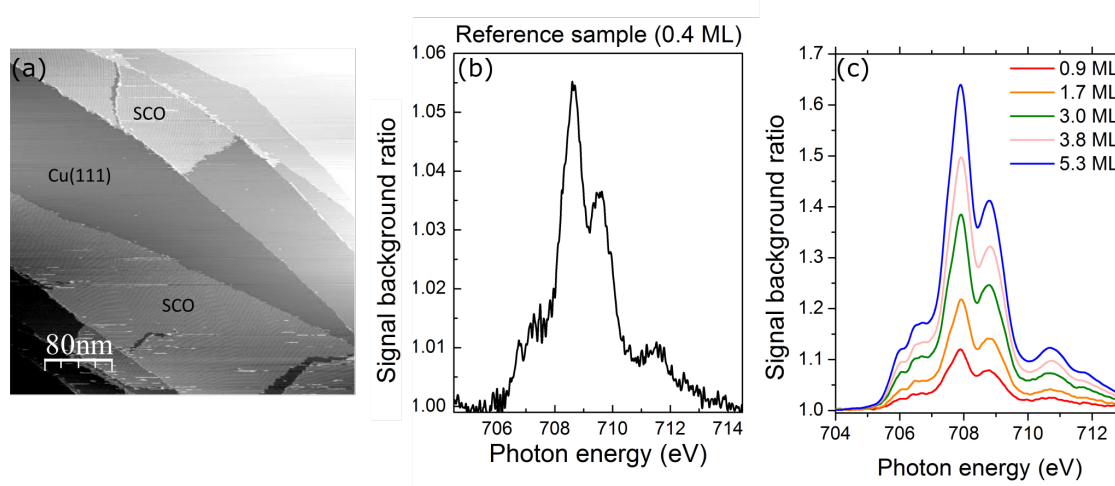


Figure 3.4: (a): $400 \times 400 \text{ nm}^2$ STM image of $0.4 \pm 0.1 \text{ ML}$ of Fe-Pyrz on Cu(111) used for calibration. $T = 200 \text{ K}$, $I = 100 \text{ pA}$ and $V = -1.5 \text{ V}$; (b): XA spectrum at the L_3 edge of Fe^{II} recorded at room temperature; (c): XA spectra for the different coverages on both samples. Red: $0.9 \pm 0.2 \text{ ML}$; Orange: $1.7 \pm 0.4 \text{ ML}$; Green: $3.0 \pm 0.7 \text{ ML}$; Pink: $3.8 \pm 1.0 \text{ ML}$; Blue: $5.3 \pm 1.3 \text{ ML}$. A linear background has been subtracted for all the spectra and the signal is normalized to the background value at 707.9 eV .

the molecules is based on a quantitative correspondence between coverage in several sub-monolayer STM images (such as figure 3.4-a) and XAS jump-to-edge intensity at room temperature (figure 3.4-b) as a reference to deduce the thicknesses. Indeed, the XAS signal is proportional to the amount of absorbing centres (i.e. molecules) and the STM is a direct observation technique that allows us to extract the coverage as well. We have directly calibrated the molecular coverage of Fe-Pyrz by a statistical analysis of 8 images on Cu(111) recorded at different places, the error bar giving the standard deviation of the average value. Unfortunately, this procedure was not possible for all the measured samples especially since it is impossible to measure by STM molecular coverages of more than 1 ML. By XAS, we have measured the normalized jumps at L_3 edge of Fe^{II} peak at 707.9 eV , for spectra recorded at room temperature where all the molecules are in a HS state. We have found a jump at the edge of 5.4% for the sample for which STM determined a $0.4 \pm 0.1 \text{ ML}$ coverage. Figure 3.4-c shows the L_3 edge of Fe^{II} on the different areas of the 2 samples. For the first (resp. second) sample, a measurement of the L_3 edge-jump of Fe^{II} gives 12 %, 21.8 % and 38.5 % (resp. 49.8 % and 69.3 %), thus the coverage rates in terms of number of layers are: $0.9 \pm 0.2 \text{ ML}$, $1.7 \pm 0.4 \text{ ML}$ and $3.0 \pm 0.7 \text{ ML}$ (resp. $3.8 \pm 1.0 \text{ ML}$ and $5.3 \pm 1.3 \text{ ML}$). Please note that the linear relation between the edge-jump and the coverage is rather reasonable in our range of thickness, since the escape length for secondary electrons at this energy is of the order of 10 nm (cf. chapter 2).

A direct check of the integrity of the molecular layer is given by the STM image in figure 3.4-a. It shows that the molecular deposition on Cu(111) leads to islands of a densely packed single molecular layer, what would not be possible if a significant percentage of the molecules were decomposed [201, 287]. Furthermore, the shape of the XAS signal in figure 3.4-b is very typical of a Fe^{II} ion in C_{3v} symmetry, as observed in the literature and demonstrated by comparison with LFM calculations in the section 3.2.2.2. A partial decomposition, modifying for example the number of ligands and therefore the symmetry, would

change significantly the spectrum [162, 201], both in the LS and HS states, as already shown on other SCO molecules on metals. Another typical product of decomposition could be the presence of Fe^{III} ions, which also display a very different XAS shape, with for example an intense peak close to 707 eV that we do not observe, even after long X-rays irradiation time [144, 145, 288, 289].

3.2.2 Temperature-dependant XAS measurements and determination of the high-spin fraction as a function of temperature

3.2.2.1 Temperature-dependant XAS measurements at different coverages

Figure 3.5 shows XA spectra taken at high temperature (grey) and low temperature (colored) for five different coverages of Fe-Pyrz on a Cu(111) surface. At high temperature, the spectra measured for all coverages are typical of a full HS with the main characteristic peak at 707.9 eV, as expected for a bulk material at 300 K. As the temperature decreases, the HS peak decreases and the characteristic LS peak at 709.2 eV increases [290]. At low temperature, two striking observations can be done from those spectra. Firstly, the HS to LS conversion is more efficient for higher thicknesses. Secondly, the molecular layer never shows a pure LS phase at low temperature, in contrast to what is observed in bulk [81, 154], but a mixture of HS and LS. Such a spin-state mixing has already been observed for Fe-Pyrz on Au(111)[222, 223, 226] or for other surface-supported molecules[147, 162, 174, 206, 211]. In the following, I will explain why the incomplete transition originates from the epitaxial relationship between the substrate and the molecular layer as it was previously reported on Au(111) by reference [226].

3.2.2.2 Determination of the high-spin fraction as a function of temperature and calculation of temperature-dependant XAS spectra

To extract the HS population as a function of the temperature, a linear combination of the HS and LS reference spectra must be made at each measurement temperature:

$$XAS^{exp}(T) = a.XAS_{HS}^{ref}(T) + b.XAS_{LS}^{ref}(T) \quad (3.8a)$$

$$x_{HS} = \frac{a}{a + b} \quad (3.8b)$$

The equation 3.8a supposes to use reference spectra for the LS and HS at each temperature. A HS reference at 300 K and a LS reference at 80 K have been recorded on a 130 nm thick film on SiO_2 that showed a complete spin transition (cf. Fig. 3.6-a/c). Since at 4 K (below 100 K) we have a fully LS spectrum as shown in figure 3.6-c, the HS spectrum at 4 K (figure 3.6-b) was obtained on an analogous compound $\text{Fe}^{\text{II}}((3-(\text{Ph})\text{Pz})_3\text{BH})_2$ (cf. chapter 2) which is a pure HS at all temperatures [229]. The spectra (full lines in black) in figures 3.6-a, 3.6-b and 3.6-c are the best simulations of the experimental spectra shown in dotted lines. The details of the simulation are in the following.

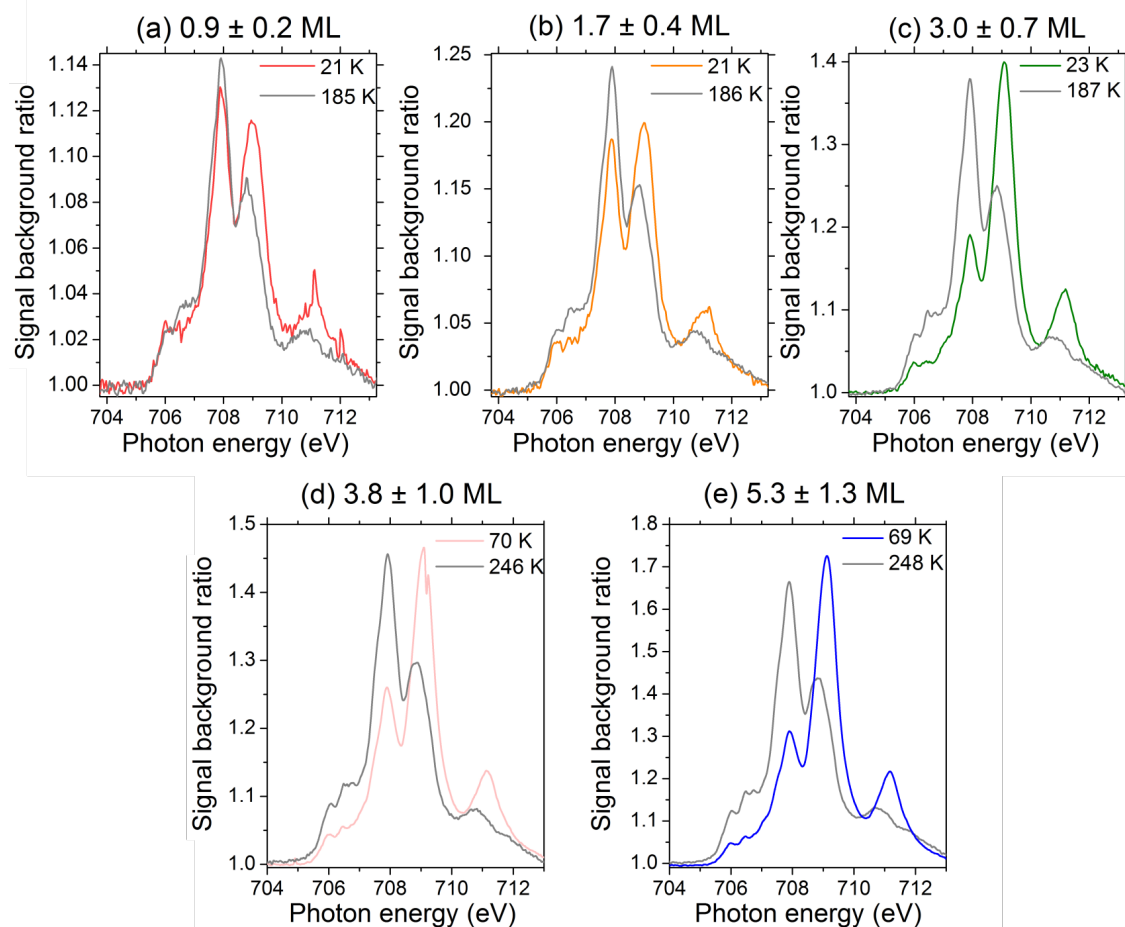


Figure 3.5: Normalized XAS signal at L_3 edge of Fe^{II} of Fe-Pyrz on Cu(111) recorded at low temperature (colored) and high temperature (grey). (a): 0.9 ± 0.2 ML; (b): 1.7 ± 0.4 ML; (c): 3.0 ± 0.7 ML; (d): 3.8 ± 1.0 ML; (e): 5.3 ± 1.3 ML. A linear background has been subtracted for all the spectra and the signal is normalized to the background value at 707.9 eV. The jump at the L_3 edge can therefore be read as a percentage of the background signal.

To determine the shape evolution of the HS spectra with the temperature, we carried out LFM calculations. The multielectronic ground state is 210 degenerated and the excited state is 120 degenerated, so there are many thermally accessible states described by a Boltzmann distribution. The shape of a XAS spectrum is of course given by the symmetry of the environment around the metal center but also by the modifications in temperature of the various multiplets on an edge which reflects the electronic occupation on the energy levels, as depicted in figures 3.7-b, 3.7-e and 3.7-f. From *ab-initio* calculations², we compute the multielectronic energy levels of the molecule in HS state (see figures 3.7-a), where the numbers 1 or 2 refer to the degeneracy of the energy levels. We then performed LFM to reproduce the energy levels. We get the right energy splitting between the different multi-

²All calculations were done with the Orca 4.2 package. A state average CASSCF (complete active space self consistent field) was performed; then, the dynamical correlation was added by the NEVPT2 method in its strongly contracted scheme, without a frozen core. Finally, the Spin-Orbit (SO) coupling was accounted for by quasi-degenerate perturbation theory with the SOMF Hamiltonian [231, 291]. The calculations were done thanks to our collaborators T. Mallah and M. Atanasov.

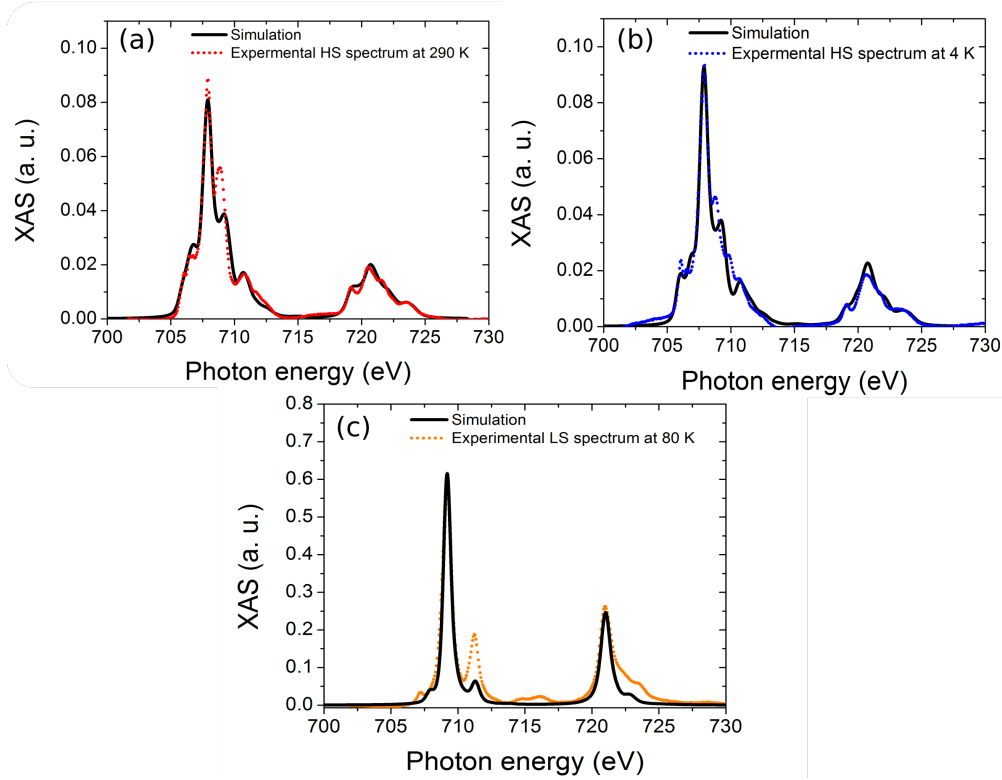


Figure 3.6: (a) The red dotted curve is the experimental HS spectrum of 130 nm of Fe-Pyrz deposited on a SiO_2 substrate annealed at 400 K and recorded at 290 K [81]. In black full lines is represented the LFM calculation of the $L_{2,3}$ edges for a HS Fe^{II} at 290 K. (b) The blue dotted curve is the experimental HS spectrum of powder of $\text{Fe}^{\text{II}}((3\text{-(Ph)Pz})_3\text{BH})_2$ on glass recorded at 4 K. In black full lines is represented the LFM calculation of the $L_{2,3}$ edges for a HS Fe^{II} at 4 K. (c) The orange dotted curve is the experimental LS spectrum of powder of Fe-Pyrz on a SiO_2 substrate recorded at 80 K [81]. In black full lines is represented the LFM calculation of the $L_{2,3}$ edges for a LS Fe^{II} at 80 K.

electronic states using a C_{3v} symmetry point group with the following crystal field parameters $D_q = 0.117$ eV, $D_s = 0.02$ eV, $D_t = 0.04$ eV. The SO constants were set to $\zeta_{3d} = 0.052$ (for the ground state and excited state) and the $\zeta_{2p} = 8.201$ for the excited state. The Slater integrals for the ground state are set to $F_2^{dd} = 10.966$ and $F_4^{dd} = 6.815$. For the excited state they are set to $F_2^{pd} = 11.780$, $F_4^{pd} = 7.328$, $F_2^{pd} = 6.793$, $G_1^{pd} = 5.001$ and $G_3^{pd} = 2.844$. All these integrals are reduced from their Hartree-Fock values by the nephelauxetic coefficient to 0.75. The instrumental Gaussian broadening has been set to 0.4 eV and $\Gamma_{L_3} = 0.32$ eV and $\Gamma_{L_2} = 0.64$ eV [253]. However, I will make some comments to point out the differences between the two results. According to the *ab-initio* calculations, the degeneracy of the lowest levels is lifted by the SO coupling in contrast to our calculations. On the other hand, for the LFM calculation, a strictly C_{3v} symmetry was considered. For this reason, the second and third levels remain degenerate (as for the higher energy levels) in the LFM calculation. Nevertheless, the energies of the two calculations are (incredibly) close.

We can then correctly simulate the good temperature dependencies of the XAS spectra especially the evolution of the two main peaks at 707.9 eV and 708.75 eV which contribute the most to the HS population (see figure 3.7-b and 3.7-c). Their ratio is fitted by a double

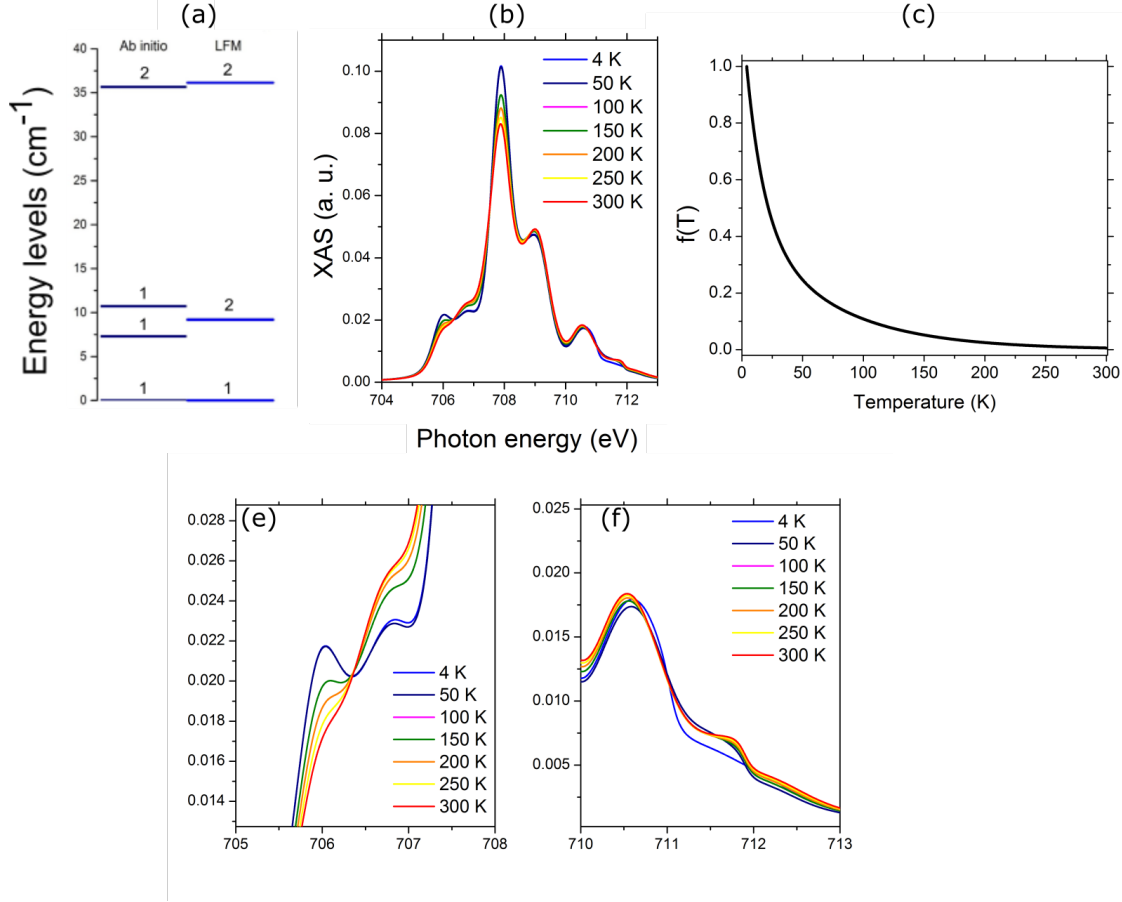


Figure 3.7: (a) The energy levels calculated in *ab-initio* and compared with LFM calculations (C_{3v} symmetry point group). The numbers 1 and 2 represent the degeneracy of the levels. (b): Calculated HS XA spectra at the L_3 edge of Fe^{II} for different temperatures. (c): The evolution of the ratio between the main peaks at 707.9 eV and 708.75 eV as a function of temperature that is used to reconstruct the HS references. (d): The modification of the L_3 pre-edge as a function of temperature. (e): The modification of the multiplet above the L_3 edge as a function of temperature.

exponential function (see equation 3.9b and figure 3.7-c). Finally, in order to reconstruct an "experimental" HS reference at any temperature, we use the following equation:

$$XAS_{HS}^{ref}(T) = f(T).XAS_{HS}^{ref}(T = 4K) + (1 - f(T)).XAS_{HS}^{ref}(T = 280K) \quad (3.9a)$$

with :

$$f(T) = 0.56. \exp\left(-\frac{T-4}{14.3}\right) + 0.44. \exp\left(-\frac{T-4}{68.2}\right) \quad (3.9b)$$

On the contrary, LS spectrum is the same whatever the temperature, since the multi-electronic ground state is not degenerated. To avoid SOXIESST effect that switches LS to HS at low temperature, we have recorded the LS spectrum at 80 K for which the thermal HS-to-LS relaxation is fast enough to neglect the SOXIESST. The figure 3.6-c in full lines is obtained by LFM calculations and confirm that the LS spectrum is very insensitive to temperature, and we can therefore use this reference to fit our datas for all temperatures. The parameters for the calculations are very similar to the HS spectrum with the difference in the value of D_q which is sets to 0.23 eV and also the reduction coefficient which is

now equals to 0.55. The difference in the nephelauxetic parameter values between HS to LS comes from the fact that the distances between the iron and nitrogen atoms are different. Indeed, in the HS (resp. LS) state, the Fe-N distances are larger (resp. smaller) and therefore the hybridizations are weaker (resp. larger), so the type of bond has an ionic (resp. covalent) character.

3.2.2.3 Thermal diffusion model for temperature correction

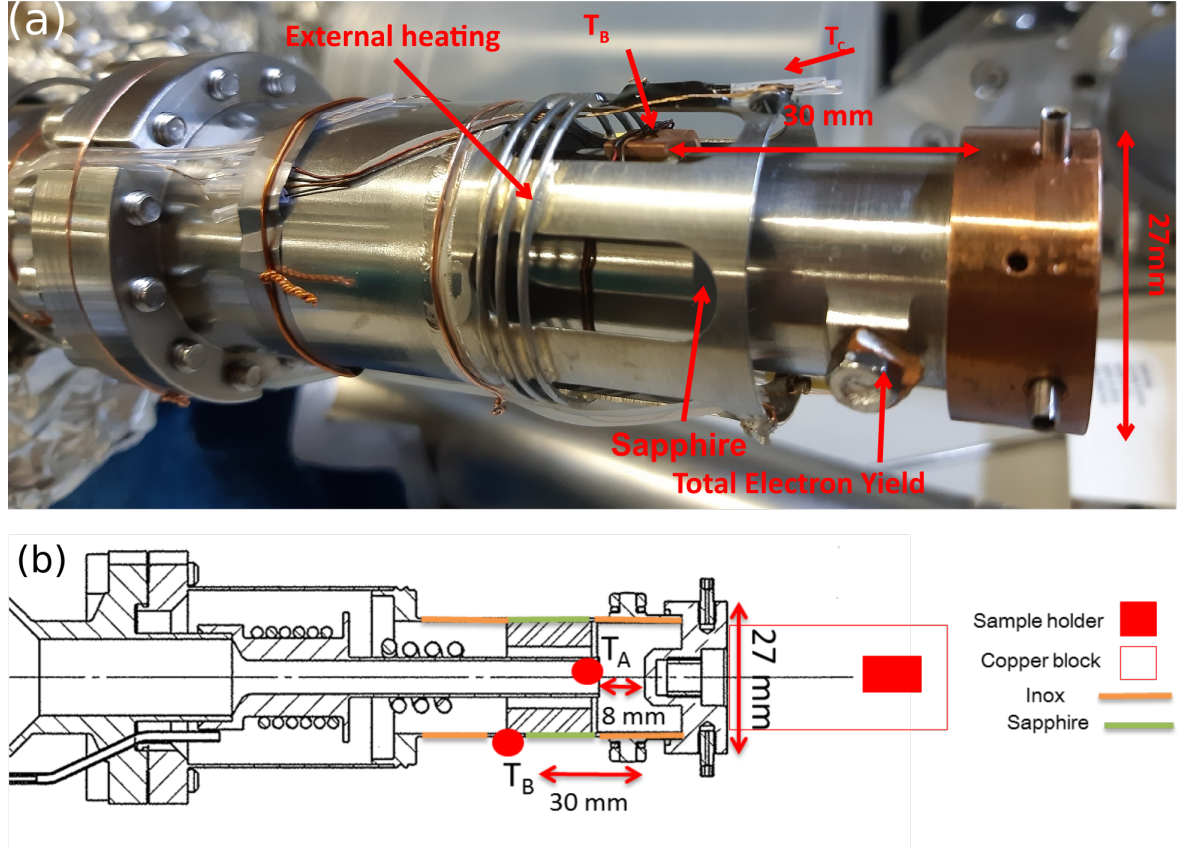


Figure 3.8: (a): The 2 K insert. (b): Horizontal cut of a scheme of figure (a). In red is added the copper block which is not shown in (a).

At the DEIMOS beamline, a 2 K insert allows to measure the TEY of a sample fixed on an electrically isolated copper block, at various temperature between 2 and 300 K [259, 261]. In order to keep a good signal to noise of the total electron yield, the temperature measurement cannot be installed directly on this block, as shown in figure 3.8-a. Thus, it can induce a shift between the *real* temperature of the sample and the measured temperature. Figure 3.8-b shows a horizontal section of figure 3.8-a in which the temperature T_A is a probe of the temperature in the exchanger and is isolated from the sample holder (8 mm gap) by an exchange gas. The temperature measurement, T_B , is located at 3 cm of the sample holder and is separated by sapphire and stainless steel. Therefore, we decided not to take this temperature as the sample temperature, especially during the temperature ramp of around $1 \text{ K} \cdot \text{min}^{-1}$ that has been applied for the measurements of figure 3.10. Consequently, we have taken great care to correct accurately the measured temperature using a calibration

procedure based on one-dimensional thermal diffusion in order to estimate the *real* sample temperature (T_A). The solution of the 1D thermal diffusion model for a step of temperature between T_1 and T_2 starting at $t = 0$ is:

$$T(x, t) = T_1 + (T_2 - T_1) \left(1 - \operatorname{erf}\left(\frac{x}{\sqrt{4D_{th}t}}\right) \right) \quad (3.10)$$

Where x and t are the sample position and time respectively, $\operatorname{erf}(x)$ is the error function and D_{th} is *ad-hoc* thermal diffusivity coefficient that we have decided to keep independent of temperature. We have simulated the temperature ramp by integrating numerically equation 3.10, reproducing perfectly the experimental temperature ramp, done by successive steps of 5 K on the thermal exchanger temperature T_A . The best agreement is obtained with a thermal diffusivity coefficient of $D_{th} = 5 \pm 3.10^{-3} \text{ cm}^2 \cdot \text{s}^{-1}$ and which reproduces previous calibration measurements done with a thermometer at the sample position. Furthermore, as shown in figure 3.9-a, with this parameter and the thermal diffusion model, we have simulated the expected sample temperature (red) from the experimental temperature measured (black). The error bar on the temperature is calculated from the uncertainty on D_{th} . With this temperature correction, the width of the thermal hysteresis is reduced, as shown for the 0.9 ML case in figure 3.9-b. It means that for this thickness, we cannot unambiguously conclude, within the error bars, on the SCO bistability. Typically, this correction reduces the hysteresis for the 0.9 ML thickness from 20 K for the uncorrected data to 11 ± 9 K for the corrected data. Finally, we are aware that this model has disadvantages in two aspects. The first one is the fact that the thermal diffusivity coefficient can depend on temperature and probably on the pressure of the exchange gas. The second is the fact that for a rigorous study, it would have been necessary to take into account the 3D spatial structure of the insert. To conclude, all curves presented afterward are obtained using reconstructed HS references and the corrected temperature.

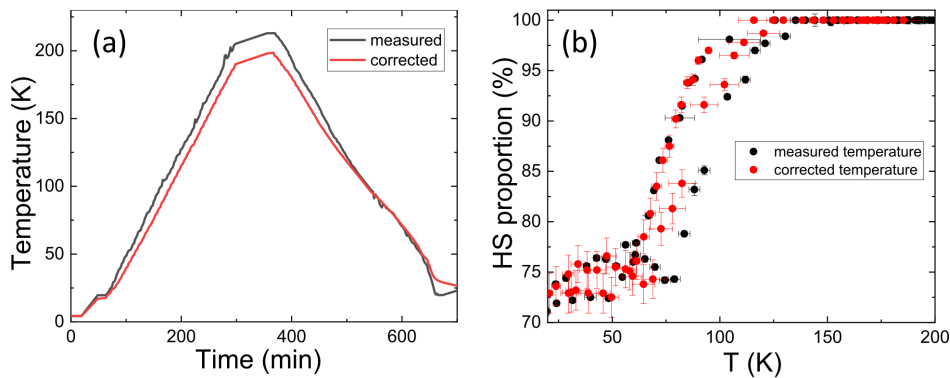


Figure 3.9: (a): Measured T_A and corrected temperatures as function of time. (b): HS fraction versus temperature with measured and corrected temperatures for the 0.9 ML sample.

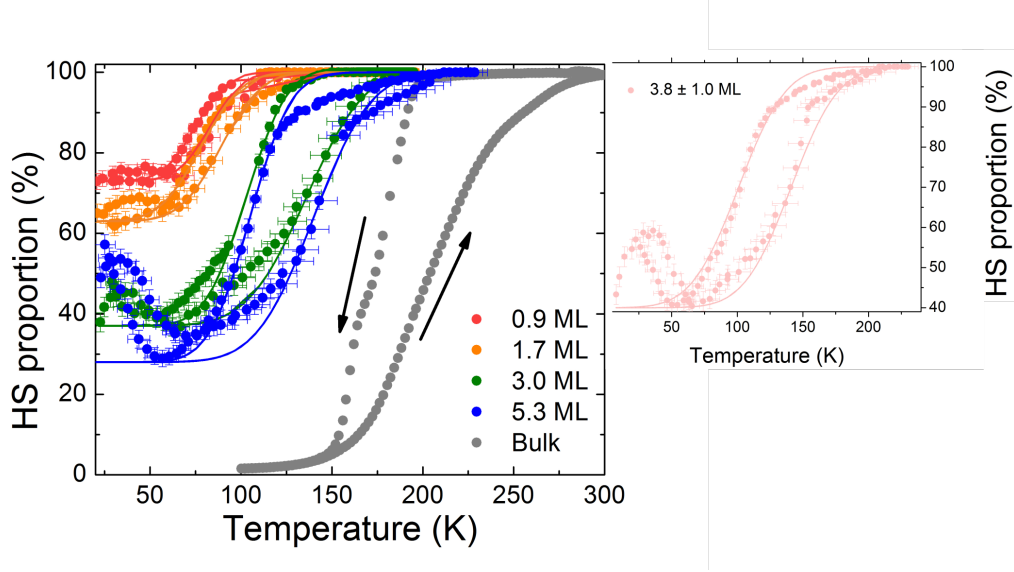


Figure 3.10: HS proportion as function of temperature from XAS measurements. Red: 0.9 ± 0.2 ML; Orange: 1.7 ± 0.4 ML; Green: 3.0 ± 0.7 ML; Pink: 3.8 ± 1.0 ML; Blue: 5.3 ± 1.3 ML; Grey: bulk extracted from a susceptibility measurement. The pink curve has been shown separately so as not to encumber the main figure. The solid lines are guides to the eye using an error function.

3.2.3 The thermal hysteresis cycles

Figure 3.10 presents the evolution of the HS proportion in percentage (x_{HS}) as a function of the temperature for different thicknesses (colored), and are compared to the bulk behavior (grey), extracted from a magnetic susceptibility measurement [81]. A thermal ramp of $1 \text{ K} \cdot \text{min}^{-1}$ is imposed by first raising and then lowering the temperature. For all these curves, the left branch (resp. right) of the hysteresis curve corresponds to the descending (resp. ascending) branch in temperature as it is shown for the bulk. To ensure that the opening of a thermal hysteresis was not due to a systematic error on the sample temperature, we have first decided to realize three different molecular thicknesses (0.9 ML, 1.7 ML and 3.0 ML) on the same Cu(111) single crystal. Similarly, the 3.8 ML and 5.3 ML thicknesses have been recorded concomitantly. Thus, on the same sample, the differences in the switching properties can be directly ascribed to the different thicknesses and not to possible differences in the thermal contact of the samples, or different temperature ramps. We have extracted three important quantities from those curves: the residual fraction of HS molecules at low temperature (x_{HS}^{res}), the transition temperature (T_{tr} called $T_{1/2}$ in chapter 1)³ and the width of bistability (ΔT). The last two quantities are defined by looking at the intersection of the horizontal line $y = \frac{1 + x_{HS}^{res}}{2}$ with the hysteresis branches. We obtain two temperatures, namely T_{up} and T_{down} , with T_{tr} the average and ΔT the difference. All these quantities are summarized in table 3.1. One can directly observe that the thicker the film is, the lower x_{HS}^{res} and the higher T_{tr} are. Moreover, we observe the opening of a hysteresis while the number of layers increases. The most striking is the clear opening of a thermal hysteresis of $35 \pm 9 \text{ K}$ for a 3 ML film. To the best of our knowledge, this is the

³Note that I use the denomination $T_{1/2}$ in the case of complete thermal transition while T_{tr} is used in the case of incomplete thermal transition.

first time that a so-wide bistability is achieved for such a thin SCO molecular layer. The bistability range becomes even larger as we increase the molecular coverage. Finally, for the temperature range below 50 K, the rising of HS proportion is certainly due to SOXIESST effects and which is hysteretic - especially for higher thicknesses - even though the X-ray flux is reduced to minimize this effect. The appearance of this bistability [108, 113, 114, 125] due to X-rays can be called (by analogy to the same effect under light), Soft X-ray Induced Thermal Hysteresis (SOXITH). Note that a similar effect has already been observed in the hard X-ray range by reference [292] on $\text{Fe}(\text{phen})_2(\text{NCS})_2$ complex.

Sample (ML)	x_{HS}^{res} (%)	T_{tr} (K)	ΔT (K)
0.9±0.2 ML	73±2	81±4	11±9
1.7±0.4 ML	62±2	82±4	13±8
3.0±0.7 ML	39±2	119±5	35±9
3.8±1.0 ML	41±2	121±6	39±13
5.3±1.3 ML	29±2	122±7	37±13

Table 3.1: Values of x_{HS}^{res} , T_{tr} and ΔT determined for the different thicknesses from the thermal hysteresis.

3.2.4 Mechanoelastic simulations

To understand why the residual HS fraction at low temperature decreases, the influence of the size of the system that leads to the opening of a hysteresis cycle and the influence of the substrate, we did simulations in the framework of the mechanoelastic model with a substrate, as shown in figure 3.3. We prepared different systems of 1, 2, 3, 4, 5, 6 ML for the simulations including the surface and 11 ML without a surface for the bulk, with 3030 molecules in each layer. Initially all of the molecules are in the HS state and are organized in an hexagonal lattice such that the SCO molecules in their HS state and the surface molecules have a radius of 0.22 nm, while the molecules in the LS state have a radius of 0.20 nm. The distance between the centers of the molecules is 1 nm in the LS state (1.04 nm in the HS state), resulting in an uncompressed spring length of 0.6 nm. The intrinsic parameters of the system are: $\Delta H = 1698 \times 10^{-23}$ J and $\Delta S = 8.86 \times 10^{-23}$ J. K⁻¹ (or $g = 1096$), which gives a thermal transition temperature $T_{1/2} = \frac{\Delta H}{k_B \ln g}$ of about 189.5 K and $E_a = 600$ K.

3.2.4.1 Determination of the molecule-molecule interaction and Monte Carlo time

To find a realistic set of parameters k_{mol} and Monte Carlo time (MC time) which determine ΔT , T_{tr} and x_{HS}^{res} , we have done a series of tests. We first simulated the thermal behavior of the bulk. Depending on the strength of the intermolecular interactions, the transition could be gradual or accompanied by hysteresis. In the mechanoelastic model, in the absence of interactions or for a very weak interaction, the thermal transition is regular and smooth

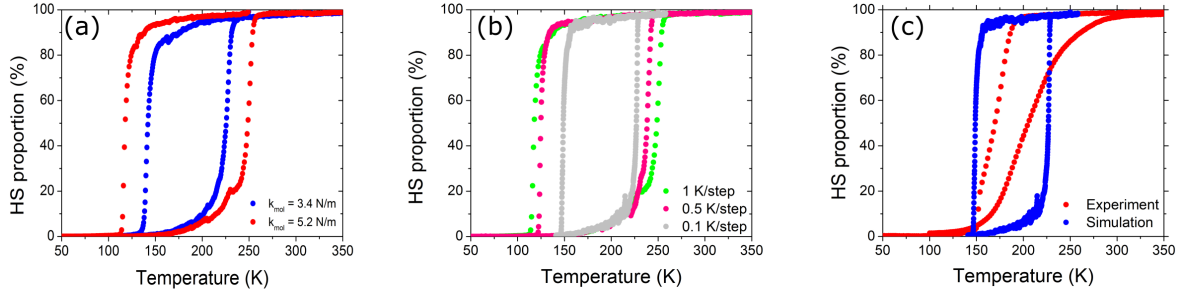


Figure 3.11: (a): Effect of the molecule-molecule interaction on the thermal transition at a constant MC time. (b): Effect of MC time on the thermal transition at a constant spring constant. (c): Comparison between experiment (red) and simulation (blue) for $k_{mol} = 5.2 \text{ N.m}^{-1}$ and 11 ML.

without hysteresis (as shown in figure 3.2). When the strength of the intermolecular interaction is large enough, we have a hysteresis such that its width and shape depend on the strength. Figure 3.11-a shows that by increasing the value of k_{mol} and thus the strength of the interaction (3.4 N.m^{-1} and 5.2 N.m^{-1}) at constant MC time (1 K/step) and the same number of layers (11 layers), the width of the hysteresis increases.

Effect of the MC time: The effect of the temperature ramp is as important for experiments as for simulations. From the point of view of simulation, due to the finite computation time to find the exact thermodynamics at a given temperature (the fraction $x_{HS}(T)$), the result obtained by the Monte Carlo method may be affected by kinetic effects. The figure 3.11-b shows that the temperature sweep rate influences the width and T_{tr} (and could also affect the shape) of the hysteresis. A fast temperature sweep rate results in a kinetic effect in the form of an extrabroadening of the thermal hysteresis, visible especially for the downward branch (as the probabilities are temperature dependent). This effect is attenuated for lower sweep rates. Therefore, in order to establish the transition temperature ramp for which the hysteresis width appears to stabilise, it is necessary to determine the MC time for which the upper and lower hysteresis loop temperatures approach constant values[293, 294].

Finally, we approximated the bulk here as a free system composed of eleven layers (without substrate). As shown in figure 3.11-c in blue, the simulated curve in blue with fixed values of MC time = 0.1 K/step and $k_{mol} = 5.2 \text{ N.m}^{-1}$ which gives a good estimation of T_{tr} and ΔT . These quantities are kept fixed for all following simulations. Note that the shape of the transition curves between experiment and simulation are different. The shape of $\chi T(T)$ of Fe-Pyrz is probably due to structural phase transition which accompanies the spin transition and can give rise to steps or asymmetries in the curves describing the thermal transition [40, 47, 74–79, 82]. All these cases are very well explained from the Landau theory of phase transitions made by reference [46].

3.2.4.2 Effect of the molecule-substrate interaction

We have then determined a value of k_s that reproduces, at least qualitatively, the experimental measurements. Figure 3.12-a presents the hysteresis cycles obtained for $k_{mol} = 5.2 \text{ N.m}^{-1}$,

$k_s = 0.5 \text{ N}\cdot\text{m}^{-1}$ for which the best qualitative agreement with experimental data is obtained⁴. Indeed, it reproduces well that the thicker the molecular layer, the lower x_{HS}^{res} and the higher T_{tr} and ΔT .

A careful analysis of simulation results reveals the existence of two main competitions between the parameters in the system. On one side, there is a competition between the HS-LS relaxation and the stresses induced by the layers with the tendency to maintain the system in the HS state. This is somewhat similar to the competition between relaxation and photoexcitation during light-induced thermal hysteresis (with the notable exception that the photoexcitation rate is constant, while the stresses increase with decreasing HS). With regard to this competition, it is evident that a larger k_s induces a larger residual HS fraction, as depicted in figure 3.12-b for three different k_s . On the other side, the same figure shows the competition between the size (i.e., the number of layers), which normally plays towards the increase of the hysteresis width and the average values of stresses due to the substrate felt by all the SCO molecules, which decrease with the size. Due to this second competition, T_{tr} tends to increase for a larger number of layers (because the descending branch decreases faster due to less constraints, while the ascending branch goes up slower due to the larger size). The residual fraction depends mainly on the $\frac{k_s}{k_{mol}}$ ratio, but also on the temperature sweep rate and on E_a . A larger temperature sweep rate will lead to the increase of the residual fraction, but also to a larger hysteresis width. Finally, E_a modulates the relaxation rate and due to the above-mentioned relaxation-stress competition, may dramatically affect the equilibrium fractions. The smaller the E_a is, the smaller the residual fraction will be.

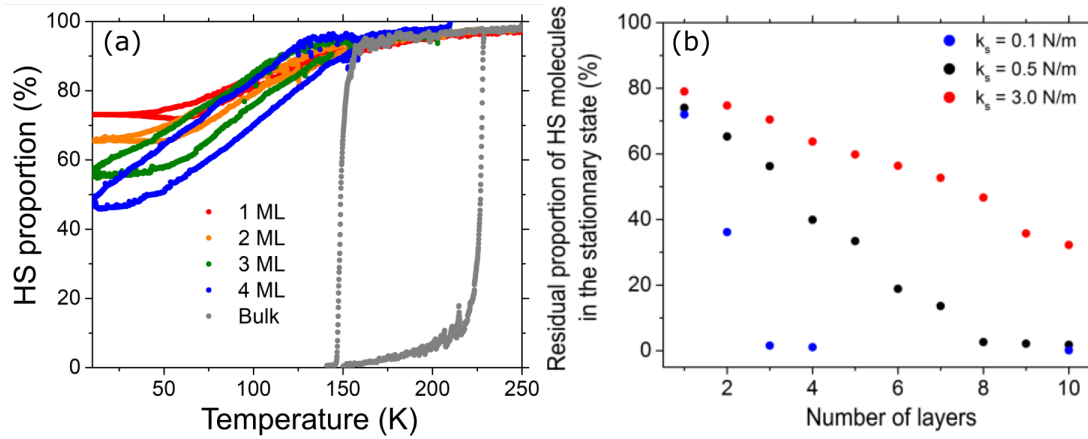


Figure 3.12: (a): Calculated fraction of HS molecules as a function of temperature for $k_{mol} = 5.2 \text{ N}\cdot\text{m}^{-1}$, $k_s = 0.5 \text{ N}\cdot\text{m}^{-1}$, MC time = 0.1 K/step. Red, 1 ML; orange, 2 ML; green, 3 ML; blue, 4 ML; gray, bulk ($k_s = 0 \text{ N}\cdot\text{m}^{-1}$). (b): Residual fraction of HS molecules as a function of the number of layers for $k_{mol} = 5.2 \text{ N}\cdot\text{m}^{-1}$ and obtained from relaxation calculations at 10 K. Black, $k_s = 0.5 \text{ N}\cdot\text{m}^{-1}$; blue, $k_s = 0.1 \text{ N}\cdot\text{m}^{-1}$, red, $k_s = 3.0 \text{ N}\cdot\text{m}^{-1}$.

⁴The values of ΔH , ΔS , E_a , MC time and $\tau = 1000$ are kept constant for the rest of our simulations, if not stated otherwise.

3.2.4.3 Effect of the number of layers on the switching properties

To better understand the role of the substrate and the thickness on x_{HS}^{res} , we have performed simulations of the relaxed state at low temperature. Figure 3.12-b shows the evolution of x_{HS}^{res} as we increase the number of layers for k_s equals to 0.1 N.m^{-1} , 0.5 N.m^{-1} and 3.0 N.m^{-1} . For $k_s = 0.5 \text{ N.m}^{-1}$ and as discussed for figure 3.12-a, the increase of the number of molecular layer leads to a decrease of the final HS proportion. For this (k_{mol} , k_s) set, the complete thermal transition to the LS state is expected for a thickness superior to that of 8 ML. In addition and discussed before, the lower the molecule-substrate constant relative to the intermolecular interaction, the more the system behaves like a free system with a low average of residual HS over the layers. Conversely, the more the molecule-substrate constant is increased, the more the system becomes constrained by the substrate and thus the average residual HS becomes important.

3.2.4.4 Distribution of the high spin fraction inside the layers

At this point, it is important to note that x_{HS}^{res} as measured in experiments is an average quantity over the different molecular layers and the x_{HS}^{res} obtained from the simulation are comparable to the experiments. To understand how the x_{HS}^{res} is distributed from one layer to the other, the proportion of HS molecules can be decomposed in the different layers of the film, as it is represented in figure 3.13-a/b/c for $k_s = 0.5$, 3.0 and 0.1 N.m^{-1} , respectively. Interestingly, we find that the proportion of HS molecules is higher close to the metallic surface, what is explained by the substrate constraint imposed by k_s . For $k_s = 0.5 \text{ N.m}^{-1}$ (figure 3.13-a), whatever the size of the system, the first layer always has a HS residual at low temperature but with a complete transition of the upper layers for a 10 ML system. For $k_s = 3.0 \text{ N.m}^{-1}$ (figure 3.13-b), whatever the number of layers is, the HS proportion of the first layer does not vary much (between 60 % and 80 %) and the transition inside each layer is incomplete even for the thickest system. Whereas for $k_s = 0.1 \text{ N.m}^{-1}$ (figure 3.13-c), the proportion of HS molecules in the first layer varies greatly depending on the size of the system and the transition is almost complete over all the layers above 2 ML (see zoom in the figure). From this analysis, we can conclude that the lower the k_s is, the more efficient the cooperativity induced by the topmost layers will be. Furthermore, the interface HS proportion decreases when the number of topmost layers increases, what shows that the overall HS fraction is a delicate balance between the interface constraint and the cooperativity imposed by the other layers.

3.2.4.5 Role of the interface layer

In the light of what we have just explained, figure 3.14-a presents the fraction of HS molecules in the interface layer as a function of the film thickness and for different k_s values. As discussed previously, for all the values of tested k_s , the proportion of HS molecules in the interface layer decreases when the total number of layers increases due to the competition between the forces generated by the substrate and those coming from the topmost layers. For $k_s = 0.5 \text{ N.m}^{-1}$, we see that the HS proportion of the interface layer decreases as we increase the number of layers but this interface layer never converts to 100 % the molecules

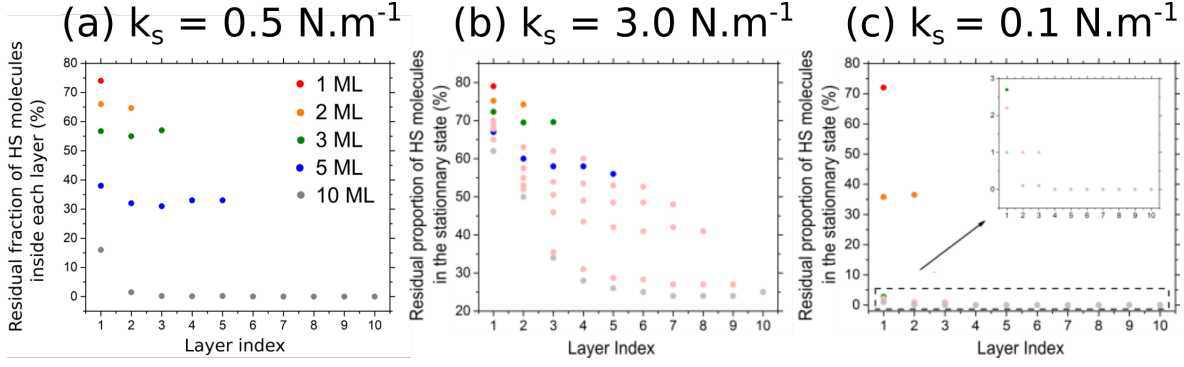


Figure 3.13: Decomposition of the residual fraction of HS molecules (obtained from figure 3.12-b) inside each layer for Red, 1 ML; orange, 2 ML; green, 3 ML; blue, 5 ML; gray, 10 ML; Pink: 4, 6, 7, 8 and 9 ML. (a): $k_s = 0.5 \text{ N}\cdot\text{m}^{-1}$; (b): $k_s = 3.0 \text{ N}\cdot\text{m}^{-1}$; (c): $k_s = 0.1 \text{ N}\cdot\text{m}^{-1}$. All the relaxation curves are done for $k_{mol} = 5.2 \text{ N}\cdot\text{m}^{-1}$.

in the LS state. For a very low k_s value ($= 0.1 \text{ N}\cdot\text{m}^{-1}$) as compared to k_{mol} , we can observe a complete transition of the interface layer for a 3 ML thickness. On the contrary, for a large k_s value ($= 3.0 \text{ N}\cdot\text{m}^{-1}$) which is of the same order of magnitude as k_{mol} , the residual fraction on the first layer does not decrease significantly with the thickness because the molecule-substrate interaction overcomes the molecular interlayer interaction. From these analysis, we expect a strong gradient of HS proportion with the thickness, what can have important consequences on the charge and spin transport properties of such ultrathin films [13, 14, 25, 159, 279]. Figure 3.14-b presents snapshots of the interface layer in which we see that the nucleation-propagation of like-spin molecules begins at the corners, as observed in the bulk experiments [54, 63, 64, 66, 68, 83–86].

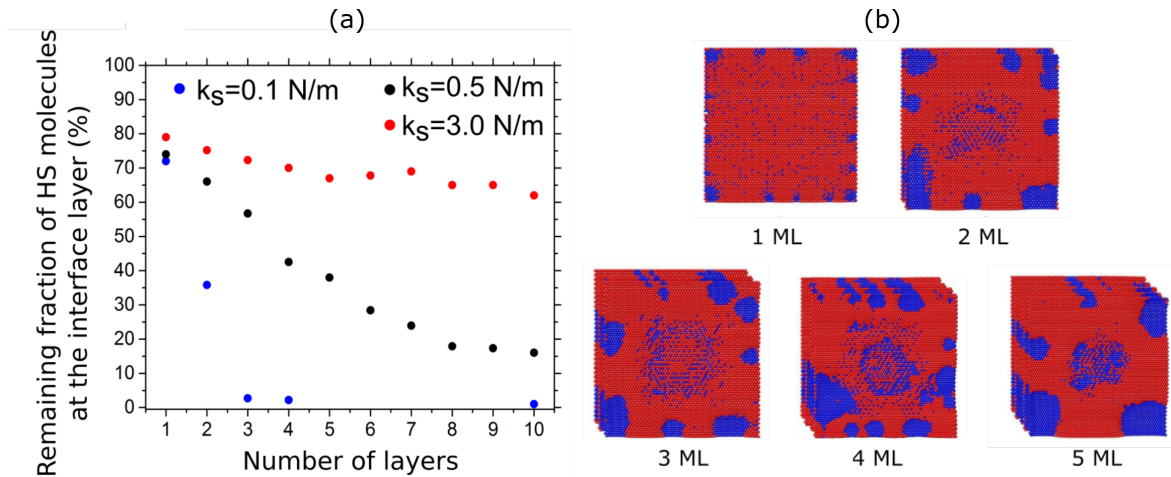


Figure 3.14: (a): Evolution of the remaining fraction of HS molecules in the interface layer as a function of the total number of layers. Blue, $k_s = 0.1 \text{ N}\cdot\text{m}^{-1}$; black, $k_s = 0.5 \text{ N}\cdot\text{m}^{-1}$; red, $k_s = 3.0 \text{ N}\cdot\text{m}^{-1}$. (b): Snapshots of the relaxed states for the first layer for 1 ML, 2 ML, 3 ML, 4 ML and 5 ML. The parameters used are $k_s = 0.5 \text{ N}\cdot\text{m}^{-1}$ and $k_{mol} = 5.2 \text{ N}\cdot\text{m}^{-1}$. In red (resp. blue) are molecules in the HS (resp. LS) state.

3.3 Thermal bistability of an ultrathin film of Fe-Pyrz a Highly Oriented Pyrolytic Graphite (HOPG) surface

3.3.1 Preparation of the sample and determination of molecular coverage on HOPG

The HOPG sample (ZYA grade), with dimensions $7 \times 7 \times 1 \text{ mm}^3$, was purchased from Neyco. The sample was cleaved at atmospheric pressure conditions using a carbon tape just before entering in the vacuum chamber. It was then degassed for at least one hour at 200°C . Then the deposition of different thicknesses of molecules was done as described in chapter 2. Figure 3.15-a shows an island of molecules which are organized in a rectangular array as shown in figures 3.15-b (small scale image) and 3.15-c (Fourier transform of 3.15-b). The analysis of 80 STM images has allowed to extract the following unit cell parameters: $a = 1.05 \pm 0.03 \text{ nm}$, $b = 0.88 \pm 0.02 \text{ nm}$, $\gamma = 90.8 \pm 2.1^\circ$. The two-dimensional network would not be possible if some of the molecules were decomposed on the HOPG surface, as expected for the class of surface-supported SCO molecules on semi-metals. In addition, the XA spectra shown in figure 3.15-d are typical of a Fe^{II} ion in C_{3v} environment.

In Figure 3.15-d is shown the XAS spectra recorded at room temperature for a thin molecular layer (blue with 6.2% edge-jump) and a thick layer (pink with 29.7% edge-jump), of which we will determine the thickness. Unlike the Cu(111) case, we did not perform a calibration study between XAS edge-jump intensity and STM at room temperature. Therefore, we do not know what the edge-jump percentages correspond to in terms of the number of layers. Nevertheless, we will determine a calibration using three different methods:

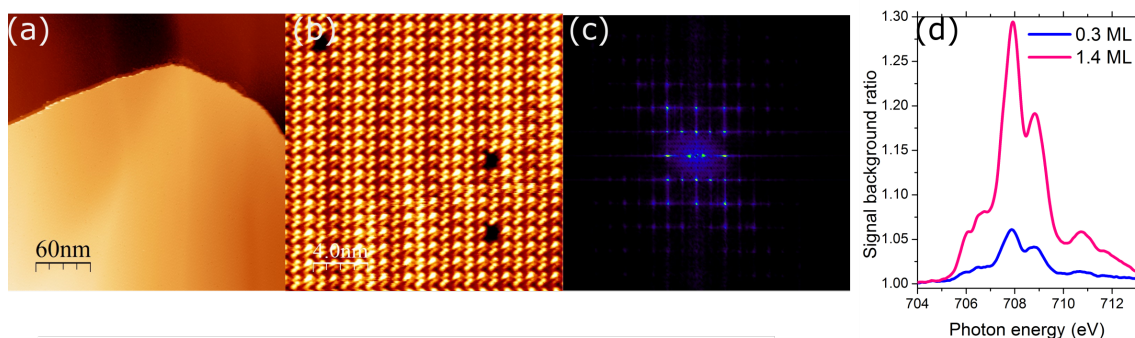


Figure 3.15: (a): $300 \times 300 \text{ nm}^2$ STM image of a molecular island of Fe-Pyrz on HOPG. $T = 4.7 \text{ K}$, $I = 30 \text{ pA}$ and $V = -1.5 \text{ V}$; (b): $20 \times 20 \text{ nm}^2$ STM image of a network of Fe-Pyrz on HOPG. $T = 4.7 \text{ K}$, $I = 10 \text{ pA}$ and $V = -2.0 \text{ V}$; (c): Fast Fourier Transform of (b); (d): XA spectra for the different coverages on HOPG at room temperature. Blue: $0.3 \pm 0.1 \text{ ML}$; Pink: $1.4 \pm 0.3 \text{ ML}$. A linear background has been subtracted for all the spectra and the signal is normalized to the background value at 707.9 eV .

Method 1: The first method consists in taking as a reference for the calibration the study carried out by reference [200] on the $[\text{Fe}(\text{bpz})_2\text{phen}]$ molecule on HOPG. The edge-jump determined by the authors at 300 K is 6.3% for a molecular coverage (θ) of 0.4 ML . Another important information is the Fe ion density per nm^2 in the $[\text{Fe}(\text{bpz})_2\text{phen}]$ molecular lattice

(d_{Fe-bpz}) which is equal to $0.82 \text{ Fe ions.nm}^{-2}$ (for a monolayer). Thus, we can determine the density of Iron ions that are scattered by X-rays and that I will call x_{bpz} ($= \theta_{bpz} d_{Fe-bpz}$) for an edge-jump of 6.3 %. By doing the same reasoning for our molecule, we can determine the density of Iron ions that are scattered by X-rays which is $x_{Fe-pyrz} = x_{Fe-bpz} \frac{6.2\%}{6.3\%} = 0.3$. Despite the fact that the edge-jumps are roughly similar, the difference in the density of Iron ions in the molecular network has to be taken into account. Thus, the density of Iron ions has been determined from the analysis of 80 STM images and we find that is equal to $d_{Fe-Pyrz} = 1.08 \text{ Fe ions.nm}^{-2}$. We therefore obtain a molecular coverage which is: $\theta_{Fe-Pyrz} = \frac{x_{Fe-Pyrz}}{d_{Fe-Pyrz}} = 0.3 \text{ ML of Fe-Pyrz for } 6.2\% \text{ on HOPG}$.

Method 2: In this method, we have calculated, using the X-ray database of the Center for X-ray optics (CXRO) of the Lawrence Berkeley Laboratory⁵, the absorption of 10 nm thick Cu and C at 712 eV in order to have an estimate of the relative total electron yield backgrounds. We find respectively absorption values of 0.028 and 0.01239. On Cu(111), 5.4 % of jump corresponds to $0.4 \pm 0.1 \text{ ML}$. On HOPG, we measure a jump of 6.2 %, what leads to $6.2 \times \frac{0.01239}{0.028} = 2.8 \%$ when normalized to the Cu background, giving finally a coverage 0.2 ML .

Method 3: The last method consists in calculating the ratio of the Fe-Pyrz/Cu(111) and Fe-Pyrz/HOPG edge-jumps (in absolute value) that were measured during the same experimental campaign at DEIMOS. The interest is that we have exactly the same beamline settings. I take as reference the thinnest sample on Cu(111) (the $3.8 \pm 1.0 \text{ ML}$ of figure 3.4-c) and the thin sample on HOPG. The ratio of absolute edge-jumps is about 10. Therefore, we obtain a thickness equal to 0.38 ML .

Finally, the average value over the three methods gives a molecular coverage for the thin sample equal to $0.3 \pm 0.1 \text{ ML}$ for 6.2% edge-jump on HOPG. For the thick sample, the ratio of the absolute edge-jumps is approximately 4.7, so we have a molecular coverage of $1.4 \pm 0.3 \text{ ML}$ for 29.7% edge-jump.

3.3.2 Temperature-dependant XAS measurements and determination of the high-spin fraction as a function of temperature

Figure 3.16-a/b represents the XAS spectra taken at high temperature (grey) and low temperature (colored) for the thin and thick film respectively. From these two spectra, it is clear that the thicker the sample, the more LS molecules there are at low temperature. Similarly to what is discussed before, the HS fraction as function of temperature was determined using the equation 3.9a as it is represented in Figure 3.16-c. All the discussion made on Cu(111) remains valid on the HOPG. The major and most spectacular difference is the drastic change in the residual fraction of HS molecules at low temperature between 0.3 ML and the 1.4 ML coverage. Indeed, there are very few molecules in the LS state at low temperature for the submonolayer sample, whereas half of the molecules converts to the LS state at low temperature for the 1.4 ML one. This is due to the fact that changing the nature of the substrate changes the molecule-substrate interactions that have a significant effect on the surface properties of SCO layers. Surprisingly, one would have thought that

⁵You can consult the database on <https://cxro.lbl.gov/>

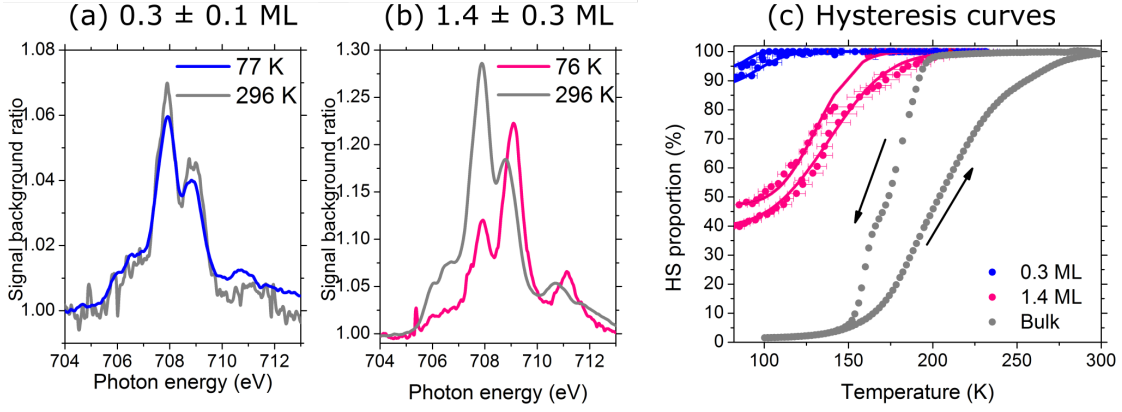


Figure 3.16: Normalized XAS signal at L_3 edge of Fe^{II} of Fe-Pyrz on HOPG recorded at low temperature (colored) and high temperature (grey). (a): 0.3 ± 0.1 ML; (b): 1.4 ± 0.3 ML. A linear background has been subtracted for all the spectra and the signal is normalized to the background value at 707.9 eV. (c): HS proportion as function of temperature. Blue: 0.3 ± 0.1 ML; Pink: 1.4 ± 0.3 ML; Grey: bulk extracted from a susceptibility measurement. The solid lines are guides to the eye using an error function.

more molecules would be switched on HOPG (as shown for this class of molecules on this substrate) than on Cu(111) [162, 200, 202, 207]. We suspect that this difference comes from a non-negligible interaction between the methyl groups and the π states of the HOPG surface, that is sufficient to hinder the thermal transition on this substrate [203]. Moreover, we can clearly see that the HS proportion as a function of the number of layers decreases much more on HOPG than on Cu(111). Indeed, the value of the residual HS fraction on HOPG for the 1.4 ML sample is comparable to that expected for 4 ML on Cu(111). This scenario, where the first layer remains very blocked while the bilayer system is much less blocked, is qualitatively captured by the numerical investigations via the mechanoelastic model that we have done with a low k_s ($= 0.1 \text{ N.m}^{-1}$) value (cf. Figure 3.13-c). Finally, it is worth to note that at this stage, we have not done any link between k_s values and the structure of the interface, as observed by STM. An interesting perspective would be to perform Grazing Incident X-ray Diffraction (GIXD) experiments at each temperature, in order to link the spin transition to the interface structure, possibly with the help of state-of-the-art *ab-initio* calculations to determine the energetic parameters to introduce in the mechanoelastic model.

3.4 Conclusions

As a conclusion, we have shown by means of X-ray absorption spectroscopy that spin-crossover molecular films of $\text{Fe}^{\text{II}}((3,5-(\text{CH}_3)_2\text{Pz})_3\text{BH})_2$ display a clear thermal bistability for thicknesses above 3 ML when grown on Cu(111). We also found that the transition temperature is rapidly increasing with the thickness whereas the fraction of residual HS molecules at low temperature is decreasing.

All the experimental XAS data obtained have been adjusted thanks to the work done on the simulation and the reconstruction of HS reference spectra at all temperatures using the QUANTY [224, 225] program in the LFM approach. All those obtained results can be

well reproduced by a mechanoelastic model that includes a specific interaction with the substrate. A detailed analysis of such simulations shows that for a strong enough interaction with the substrate, the HS proportion is more important. More interestingly, the distribution of HS molecules is not homogeneous over the film thickness. More specifically, the investigation of the role of interface layer for different system sizes shows that the proportion of HS molecules decreases when the total number of layers increases due to the competition between the forces generated by the substrate and those coming from the topmost layers. These results highlight the importance of the size of the system and the nature of the substrate on the thermal transition; it may be important for the electronic transport properties through such molecular layers. Finally, the same measurements on HOPG show that we can modulate the thermal transition properties by changing the nature of the substrate, which in turn changes the molecule-substrate interaction and have a strong influence on the thermal SCO transition curve.

As a perspective, since the epitaxial relationships seem to be different, it would be fundamental to link the interface structure with the spin transition properties.

EFFECT OF THE SUBSTRATE ON THE TRANSITION UNDER LIGHT

Light-induced spin-state switching is one of the most attractive properties of spin-crossover materials. In bulk, the low-spin (LS) to high-spin (HS) conversion via the light-induced excited spin-state trapping (LIESST) effect may be achieved with a visible light, while the HS-to-LS one (reverse-LIESST) requires an excitation in the near-infrared range. However, due to the fragmentation of SCO molecules on metal surfaces [147, 162, 174, 175, 201, 206], little is known about the behavior of spin transition molecules as a submonolayer on metal substrates.

In this chapter we present the studies done on $[\text{Fe}^{\text{II}}((3,5-(\text{CH}_3)_2\text{Pz})_3\text{BH})_2]$ in direct contact with metallic (111) single-crystal surfaces (copper, silver, and gold) and on a semimetal (HOPG). In a first step, we will investigate, by X-ray absorption spectroscopy and STM, the effect of the modification of the spin transition properties for submonolayer samples on the different metallic substrates and under the effect of different wavelengths. Then, in the specific case of Cu(111), we will see how the thickness of the molecular layers modifies these transition properties. To interpret our observations, a new mechanism is proposed for the spin conversion mediated by the metallic substrates. Then, we will see the effect of the transition on a Highly Oriented Polygraphite (HOPG) substrate, and we will study its transition behavior under light for two thicknesses, one submonolayer and more than one layer of molecules. Finally, we will finish this section with Light-Induced Thermal Hysteresis (LITH) measurements on submonolayer and multilayer samples of molecules on Cu(111) and HOPG.

4.1 Effect of light on submonolayer to monolayers of Fe-Pyrz on Cu(111), Au(111) and Ag(111)

We investigated the light-induced transition of ultrathin films of Fe-Pyrz on three metallic substrates: Cu(111), Au(111) and Ag(111).

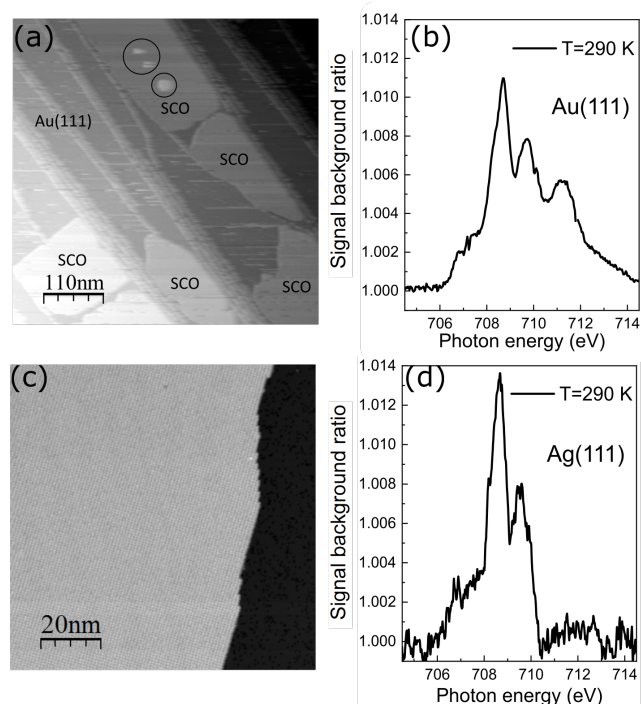


Figure 4.1: (a) STM image of 0.5 ± 0.1 ML of Fe-Pyrz on Au(111). $530 \times 530 \text{ nm}^2$. $T = 4.7 \text{ K}$. $I = 50 \text{ pA}$ $V = -2 \text{ V}$. Black circles underline small islands of a second molecular layer. (b) Normalized XAS signal at L_3 edge of Fe^{II} of 0.5 ± 0.1 ML of Fe-Pyrz on Au(111) recorded at room temperature. (c) STM image of a submonolayer of Fe-Pyrz on Ag(111). $100 \times 90 \text{ nm}^2$. $T = 4.7 \text{ K}$. $I = 10 \text{ pA}$ $V = -1.5 \text{ V}$. (d) Normalized XAS signal at L_3 edge of Fe^{II} of 0.5 ± 0.1 ML of Fe-Pyrz on Ag(111) recorded at room temperature.

4.1.1 Sample preparation of submonolayer of Fe-Pyrz and determination of molecular coverage

On Au(111), the deposition is done with the substrate at 4.7 K followed by an annealing at room temperature or a direct deposition on the substrate at room temperature. We have checked by STM that the two deposition techniques give the overall same morphology of the molecular layer (see figure 4.1-a). The coverage is estimated by the analysis of several large scale (typically $1 \mu\text{m}$) STM images and gives 0.5 ± 0.1 ML. The uncertainty reflects the coverage fluctuations from image to image. Figure 4.1-b shows the corresponding XA spectrum at the L_3 -edge measured at room temperature where all the molecules are in the HS state. We measure a jump of 1.1% on Au(111) which corresponds to 0.5 ± 0.1 ML. Note that the Au(111) and Cu(111) samples have been prepared and measured by STM in a separate UHV chamber, before being transported within few hours to the DEIMOS UHV setup, in a home-made vacuum suitcase with a pressure below 10^{-9} mbar.

The Ag(111) has been directly prepared in the DEIMOS preparation chamber. Then, the determination is a bit more delicate as we do not measure the same sample by STM (figure 4.1-c) and XAS (figure 4.1-d). Indeed, edge-jumps on different samples have therefore to be normalized by those absorption values for a proper calibration. We have then calculated, using the X-ray database of CXRO (as in chapter 3 on HOPG), the absorption of 10 nm on Ag at 712 eV (0.138), in order to have an estimate of the relative total electron

yield backgrounds compared to Cu (0.028). We measure a jump of 1.3% on Ag(111), what leads to $1.3 \times \frac{0.138}{0.028} = 6.4\%$ when normalized to the Cu background, giving finally a coverage 0.5 ± 0.1 ML. This calibration on silver is very close to the one on gold and this is explained by the fact that the absorption of 10 nm thick film at 710 eV are almost the same, namely, 0.158 for Au and 0.138 for Ag.

On Cu(111), we prepared four different samples. The first one, that is presented in figure 4.3-a has a molecular coverage of 0.4 ± 0.1 ML and corresponds to the sample on which we showed the calibration in chapter 3, and for which 5.4 % edge-jump corresponds to 0.4 ± 0.1 ML of Fe-Pyrz on Cu(111). The second one, in figure 4.4-a/b and 4.5, have a molecular coverage of 0.6 ± 0.2 ML and finally, the figure 4.8 shows the two samples presented in chapter 3, namely, 0.9 ± 0.2 ML, 1.7 ± 0.4 ML, 3.0 ± 0.7 ML, on one sample, and 3.8 ± 1.0 ML, 5.3 ± 1.3 ML, on an other sample.

4.1.2 Anomalous LIESST of submonolayer of Fe-Pyrz on Cu(111), Au(111) and Ag(111)

4.1.2.1 XAS measurements

As shown in figure 4.2, the sample is placed with the X-ray incident direction at 45° to the surface normal for purpose of light exposure through a window perpendicular to the incoming X-rays. The blue and red lights are produced by laser diodes with wavelengths of 405 nm and 635 nm respectively. An *ex-situ* measurement of the fluences taking care of the various geometric factors gives an estimate of 0.5 mW.cm^{-2} for both wavelengths. Unfortunately, we did not measure the green light fluence. Finally, to reduce the time of exposure to the X-ray of the sample, in most of the experiments we have measured only the L_3 edge with a 74 s duration for one spectrum.

Figure 4.3 shows XA spectra around the $\text{Fe}^{\text{II}} L_3$ edge, recorded at 4 K for 0.5 ± 0.1 ML, 0.4 ± 0.1 ML and 0.4 ± 0.1 ML coverage of Fe-Pyrz on Cu(111) (figure 4.3-a), Au(111) (figure 4.3-b) and Ag(111) (figure 4.3-c) respectively. The bulk sample (130 nm of Fe-Pyrz on SiO_2) is presented in figure 4.3-d. The spectra before (red curves) and in the stationary photoinduced state (blue curves) under blue light exposure during 20 minutes (with X-rays off) are compared. In such 4 K XA spectra, the peak at 708.7 eV is characteristic of a HS state while the peak at 710 eV is characteristic of a LS state [290]. Two observations can be done from those spectra. Firstly, as explained in chapter 3, at this coverage, the molecular layer shows a mixed spin-state [81, 154, 211] at low temperature because of the epitaxial relationship with the substrate (red curves) [222, 223, 226].

Secondly and very surprisingly, the molecular layer switches partially under a blue light illumination but very differently from what is known so far for the bulk and for thin films. Indeed, we clearly observe for the samples on Cu(111) and Au(111), that the LS proportion increases after light illumination, in contradiction with the bulk optical properties of both spin-states and the so far proposed LIESST mechanism, where blue light only switches the LS ground state into the HS state ($^1\text{MLCT}$ excitation). For its part, no significant evolution is observed on Ag(111).

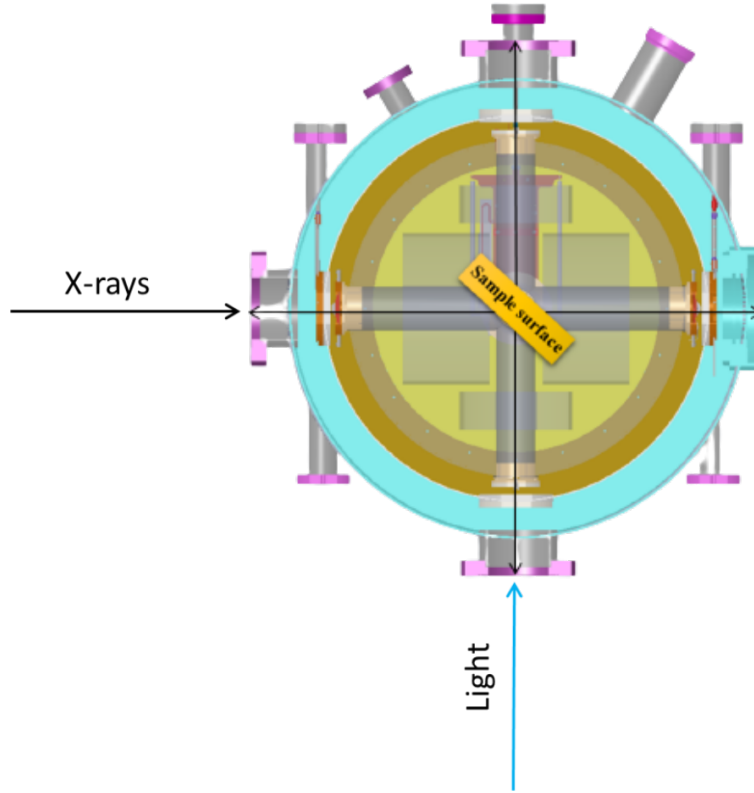


Figure 4.2: Top view of the CroMag showing the sample at 45°, measured by X-ray and irradiated by light, at the same time. Courtesy of the DEIMOS beamline.

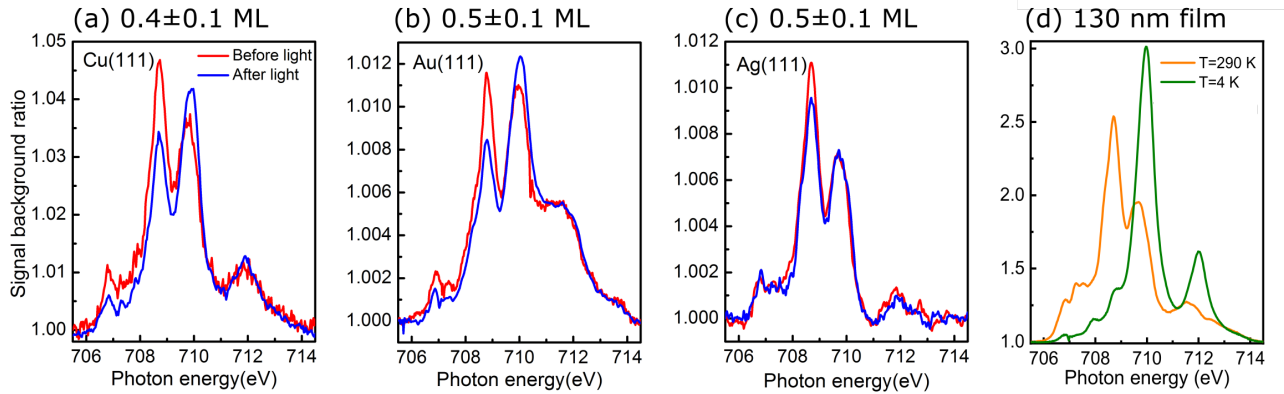


Figure 4.3: 4 K X-ray absorption spectra of the $\text{Fe}^{\text{II}} L_3$ edge of Fe-Pyrz before and under illumination of the sample with a blue light (405 nm) for 20 minutes for: (a) 0.4 ± 0.1 ML on Cu(111). (b) 0.5 ± 0.1 ML of on Ag(111). Average over 11 spectra before light and 10 spectra under light in steady state conditions. (c) 0.5 ± 0.1 ML of on Au(111). Average over 6 spectra before light and 13 spectra under light in steady state conditions. (d) Reference spectra recorded at 4 K and 290 K on a 130 nm thick film of Fe-Pyrz on a SiO_2 substrate.

Afterwards, to have a quantitative estimation of the HS proportion in the molecular layer, we fit our data by a linear combination of the two reference spectra at 4 K. We find that on Cu(111), the HS proportion is $75.0 \pm 0.7\%$ before light and $54.9 \pm 0.6\%$ after light. On Ag(111), it is $78.6 \pm 1.3\%$ before light and $73.8 \pm 1.6\%$ after light. On Au(111), we find

$65.6 \pm 1.3\%$ before light and $49.7 \pm 1.2\%$ after light. Therefore, it appears that the spin-state switching with blue light strongly depends on the substrate nature. In addition, the anomalous HS-to-LS switching under blue light illumination has been reproduced on four samples on different Au(111) substrates and on two different Cu(111) substrates. In all cases, the coverage was in the submonolayer range.

Finally, a last subsidiary and important remark must be made concerning the shape of the XAS spectra which is different depending on the substrate. We manage to perfectly match the spectra on Cu(111) which are very reminiscent of spectra in C_{3v} symmetry but the "deep" that we observe at 711 eV on silver and the "bump" at 712 eV on gold remain not yet understood. That might be due to: i) change of the symmetry in the coordination sphere due to different orientations of the molecules on different substrates; ii) a charge transfer mechanism [232, 238–242] between the central ion and the neighbouring ligands that was not included in the simulations. Several attempts were made to include charge transfer in a C_{3v} symmetry but the number of parameters to handle was too large and unfortunately we did not manage to reproduce these features on the spectra.

4.1.2.2 Dynamics of the anomalous switching under light

Figure 4.4 shows the time evolution of the anomalous light induced HS to LS switch for 0.6 ± 0.2 ML of Fe-Pyrz on Cu(111) (Figure 4.4-a/b) and 0.4 ± 0.1 ML on Au(111) (Figures 4.4-c/d) samples, using both blue in figures 4.4-a/b/c/d (405 nm) and red light in figures 4.4-b/d (635 nm) with a fluence of 0.5 mW.cm^{-2} . As detailed in chapter 2, in the bulk, the LIESST effect is observed in the UV-Visible range and is more efficient in the blue frequency ($^1\text{MLCT}$ excitation in bulk) and less in the red one ($^1\text{A}_1$ to $^1\text{T}_1$ excitation in bulk). Conversely the reverse-LIESST process is triggered by near infrared light ($^5\text{T}_2$ to ^5E excitation). Note also that for thicker films of the same spin-crossover compound it has been demonstrated using the same XAS technique that illumination with a Ti:sapphire laser was inducing a partial LS-to-HS transition [154], i.e. a normal light-induced switching behaviour.

In contrast, on both Cu(111) and Au(111) surfaces, we observe that a red light has a very small influence on the proportion of HS molecules and blue light switches efficiently HS molecules into LS ones. On the Ag(111) surface, no significant evolution of the HS proportion is measured, whatever the used wavelength is. From the fitted data of figures 4.4-a/c related to blue light irradiation, we can extract, using a single-exponential fit (solid lines in figures 4.4-b/d), both the amplitude in HS proportion of this light-induced effect and the typical switching time scale τ for the given fluence of 0.5 mW.cm^{-2} . On the Cu(111) surface, 20 % of HS molecules are switched and $\tau = 226 \text{ s}$. On the Au(111) surface, 13 % of HS molecules are switched and $\tau = 403 \text{ s}$. Green light (532 nm, not shown here) has an effect rather similar to blue light. We therefore conclude that the observed anomalous HS-to-LS switching under blue light is specific to the metal-molecule interface.

It is worth to notice that those measurements are done using X-rays that have also an influence on the spin-state proportion (SOXIESST effect). Indeed, we have taken great care to reduce this effect to its minimum by using a low X-rays fluence. In figure 4.5, we show on 0.6 ± 0.2 ML of Fe-Pyrz deposited on Cu(111) that using the switching from HS to LS state

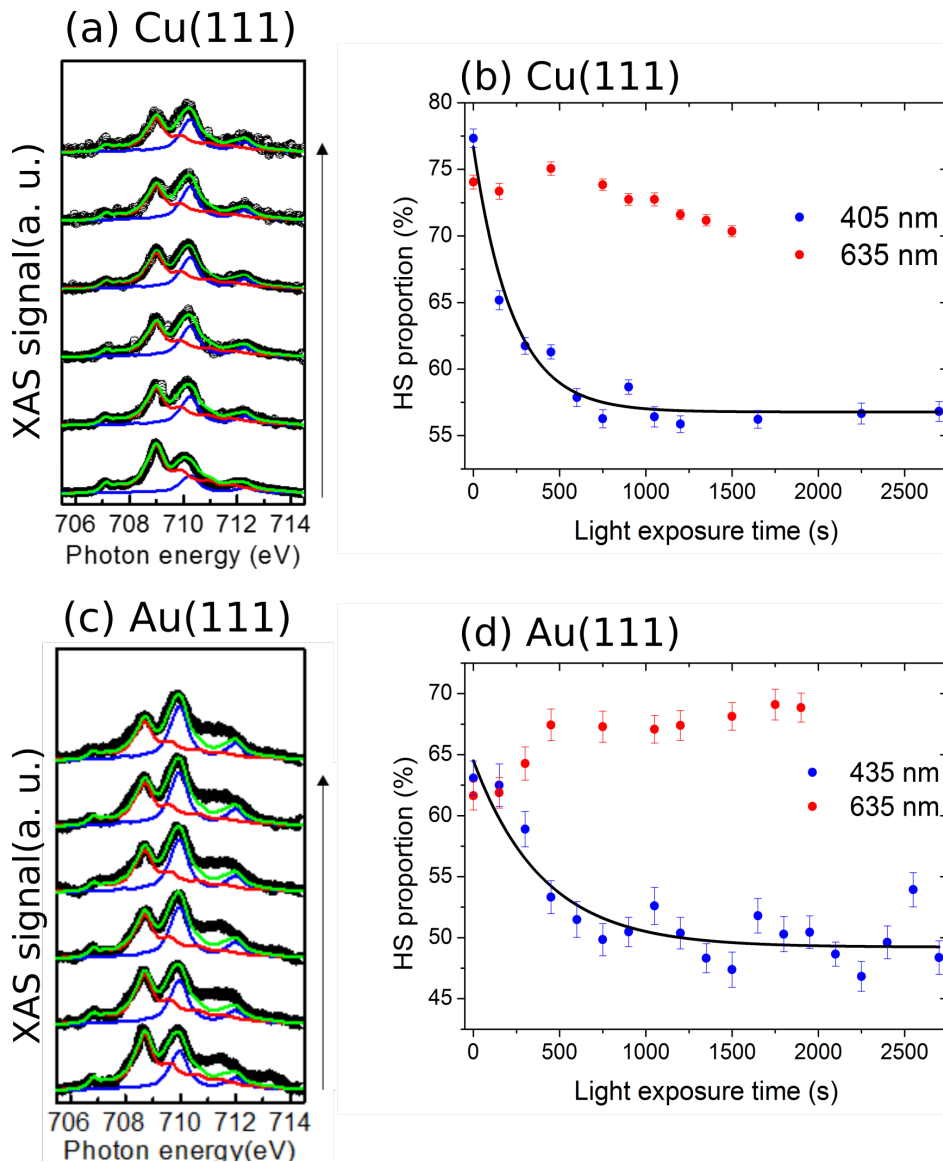


Figure 4.4: Raw XAS data after background subtraction (open symbols) fitted by a linear combination (green lines) of the HS and LS references (red and blue lines). In each figure, the time is indicated by the arrows, i.e. from bottom to top (for figures (a) and (c)). (a) 0.6 ± 0.2 ML of Fe-Pyrz on Cu(111), showing the anomalous evolution towards LS under blue light with time. (b) 0.6 ± 0.2 ML of Fe-Pyrz on Cu(111). Time evolution of the HS proportion, measured at 4 K, extracted from the XAS spectra, as function of the time of illumination for a blue (405 nm) or a red (635 nm) light. The black lines are exponential fits. (c) 0.5 ± 0.1 ML of Fe-Pyrz on Au(111), showing the anomalous evolution towards LS under blue light with time. (d) Same as (b) for 0.5 ± 0.1 ML of Fe-Pyrz on Au(111).

with blue light (figures 4.4-a/b and figure 4.5-b) and from LS to HS with X-rays (SOXIESST in figure 4.5-a/B) we can perform almost reversible switching cycles at 4 K. Qualitatively, this behavior is rather similar to what can be obtained on bulk materials via LIESST and r-LIESST effects but using very different wavelengths and with a reduced amplitude in the HS fraction. According to the above findings, the substrate plays a decisive role in the photoconversion mechanism. In this section, we discuss the relationship between the nature of the substrate and the observed HS to LS switching that occurs with blue light

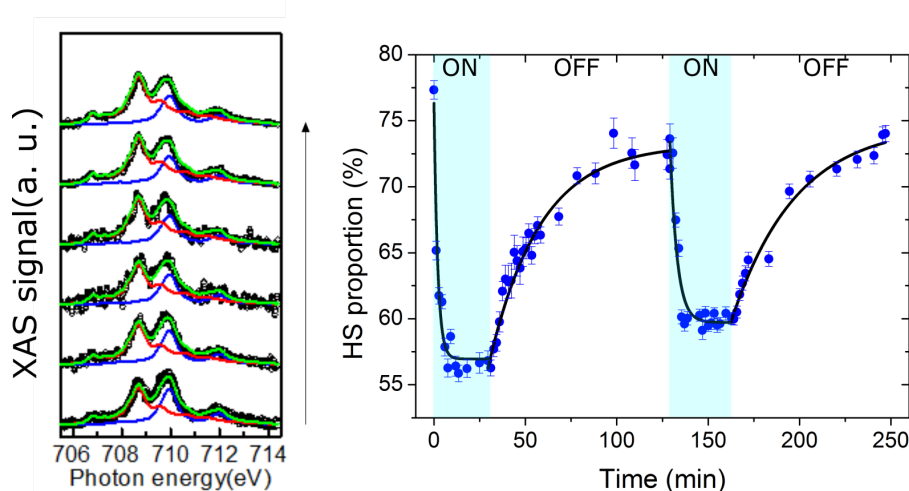


Figure 4.5: (a) Raw XAS data after background subtraction (open symbols) fitted by a linear combination (green lines) of the HS and LS references (red and blue lines). The exposure time to X-rays is indicated by the arrows, i.e. from bottom to top. 0.6 ± 0.2 ML of Fe-Pyrz on Cu(111), showing the usual evolution towards HS under X-rays with time. (b) Reversible switching of 0.6 ± 0.2 ML of Fe-Pyrz on the Cu(111) surface using blue light on and off irradiations series under X-rays. Blue circles are data points extracted from the XAS spectra. The black line are fits using single-exponential functions.

irradiation for submonolayer coverages on surfaces rather than with near infrared light for the bulk compound.

4.1.3 STM study of the anomalous switching

In this section, we investigate by means of STM experiments at 4.7 K, the light-induced transition to demonstrate further the incomplete thermal conversion and the anomalous light-induced spin-state switching observed by XAS, before and after blue light illumination ($\lambda = 405 \pm 5$ (BW) nm, BW refers to bandwidth). At a negative gap voltage shown in figures 4.6-a/d/g, we see only bright molecules with no contrast between HS and LS states. At a gap voltage of 0.3 V, we observe a clear contrast between molecules that we ascribe to the different electronic conductances of the LS and HS states [295]. However, at this stage we cannot deduce which the HS and LS molecules are. In addition, it is important to note that there is no relationship between the observed contrast and defects in the molecular array. Figures 4.6-b/e/h show the thermal states at 4.7 K, obtained by cooling the sample in dark conditions, for respectively Cu(111), Ag(111) and Au(111). From a statistical analysis of the images, it is possible to extract the proportion of black molecules which is 75%, 80% and 76% [223] respectively, in rather good agreement with the proportion of HS molecules determined by XAS. By this quantitative comparison between STM and XAS, we can deduce that the dark (resp. bright) molecules are the molecules in the HS (resp. LS) state [295]. More interestingly, we have also scanned the same area after blue light irradiation emitted by a supercontinuum source (typically around 1 mW for 20 min)¹. Figures 4.6-c/f/i show

¹we have recently measured that our supercontinuum was emitting a non-negligible infrared radiation around 800 nm when set in the range 400-420 nm, which was the case for this experiment. As we have not

the STM images after light illumination recorded at the exact same location that figure 4.6-b/e/h (before light illumination). We observe more bright molecules (with no destruction of the molecular lattice) which is the signature of a clear switching of some molecules from HS \rightarrow LS, at random positions. However, the switching is found to be far less efficient on Ag(111) than for the two other substrates. A quantitative analysis gives a proportion of dark molecules of around 50%, 75% and 50% on Cu, Ag and Au respectively. Once again in reasonable agreement with the proportion of HS molecules measured by XAS under a blue light irradiation. Finally, we can conclude from the STM experiments conducted under light illumination that we have a good agreement with the anomalous transition measured by XAS, showing once again that the X-rays can be considered only as a slight perturbation and not at the origin of this peculiar effect.

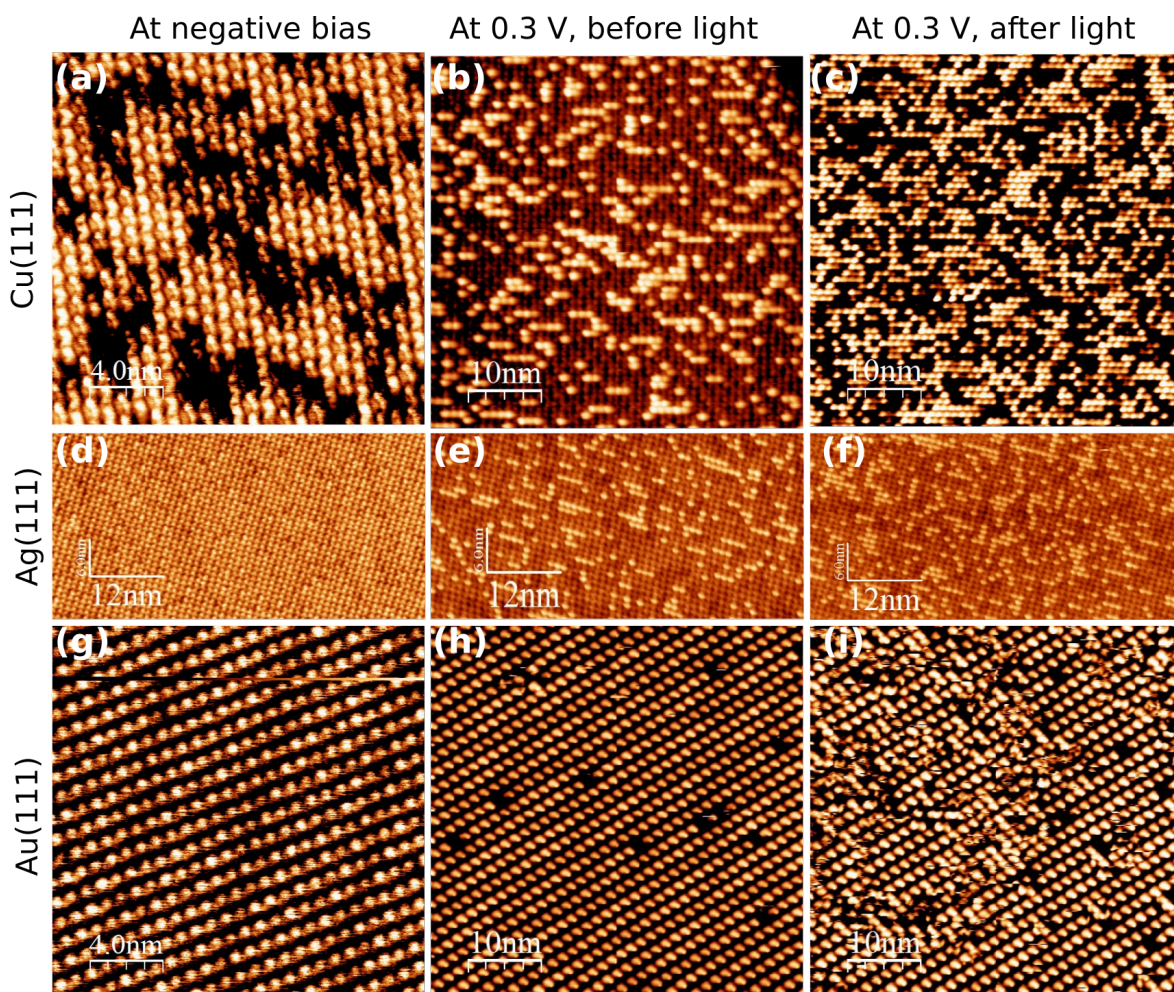


Figure 4.6: STM images of Fe-Pyrz on different metallic substrates recorded at 4.7 K at different bias voltages and a typical tunneling current of 10 pA. On Cu(111), $10 \times 10 \text{ nm}^2$: (g) before light at $V = -2.0 \text{ V}$; $20 \times 20 \text{ nm}^2$: (h) before light (i) after light at $V = 0.3 \text{ V}$. On Ag(111), $60 \times 25 \text{ nm}^2$: (d) before light at $V = -1.5 \text{ V}$; (e) before light (f) after light at $V = 0.3 \text{ V}$. On Au(111), $10 \times 10 \text{ nm}^2$: (g) before light at $V = -1.5 \text{ V}$; $20 \times 20 \text{ nm}^2$: (h) before light (i) after light at $V = 0.3 \text{ V}$.

carried out infrared illumination in XAS, we don't know the importance of this spurious illumination on our conclusions. However, we have found similar STM results with green light, where no infrared spurious is observed.

4.1.4 Model for the light anomalous switching: substrate-mediated switching

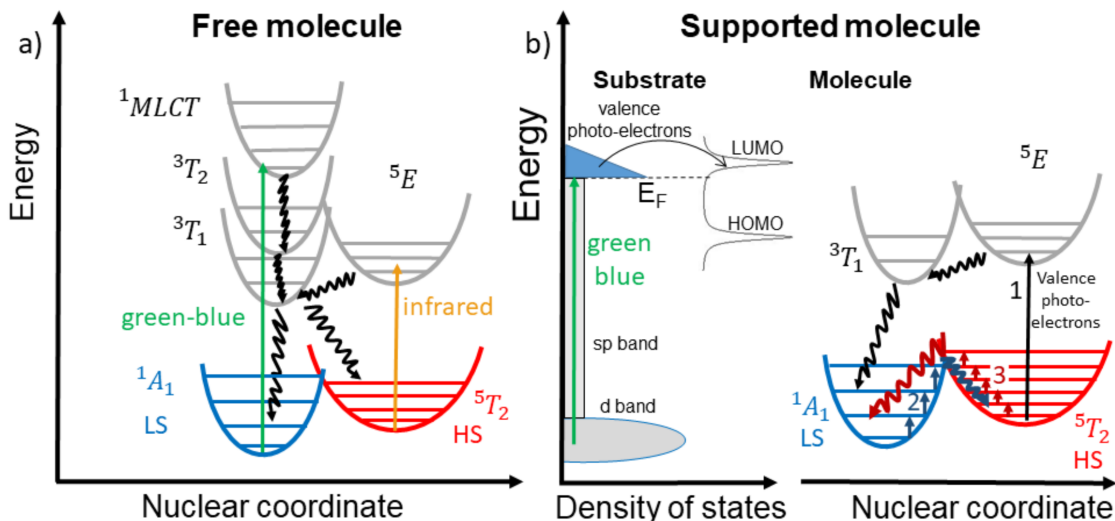


Figure 4.7: (a) Schematic drawing of the usual LIESST (green arrow) and r-LIESST (orange arrow) mechanisms through excited states. (b) Schematic drawing of the interband light absorption by the substrate and the induced low-energy valence photo-electrons HS to LS switching through the transition by excited molecular states (path labeled 1) or through vibrational heating (path labeled 2 from LS to HS and labeled 3 from HS to LS). For simplicity, we have skipped the parity index for all the irreducible representations since they are all even.

For LIESST, r-LIESST (or SOXIESST) phenomena, it has been proposed and demonstrated that the spin-state switching occurred through transitions, driven either by direct light excitation or secondary photo-electrons excitation or injection (cf. figure 4.7), from the lowest energy states ($^1A_{1g}$ for LS and $^5T_{2g}$ for HS) to excited states (1MLCT , $^1T_{2g}$ or $^1T_{1g}$ levels for LS and 5E_g for HS), eventually decaying through intermediate states ($^3T_{2g}$ and $^3T_{1g}$) [29, 88, 92]. Concerning the outcome of the anomalous light-induced spin-state switching from HS to LS, we can rule out the direct photon absorption by the molecules in the HS state as thin films of Fe-Pyrz show no absorption in the blue or green light range [81]. Thus the usual mechanism for r-LIESST involving the transition through HS excited states can be ruled out, or has a relatively small efficiency, as the spin-state switching is observed out of the absorption band. Moreover, it would not explain why the effect is more pronounced on Cu(111) and Au(111) than on Ag(111) surfaces. Therefore we propose an alternative competitive mechanism involving the absorption of light by the metallic substrate and a spin-state switching driven by low-energy valence photo-electrons.

The absorption cross sections by the metallic substrates are well-known [296]. In the case of Ag, it is due to conduction electrons and can be well interpreted by a simple Drude model, giving rise to a very small absorption in the whole visible range (giving rise to an almost perfect optical mirror surface). For Cu and Au, it is rather different, due to d - sp interband optical transitions that occur typically for green and blue lights (giving rise to their reddish and yellowish colors). Using data from reflectance measurements, the absorption coefficients ($\alpha = \frac{2nk}{\lambda}$) can be estimated for Cu to 14 and 3 μm^{-1} , for Au to 14 and 2 μm^{-1}

and for Ag to 0.8 and 0.5 μm^{-1} at 3 eV (410 nm) and 2 eV (620 nm) respectively [296]. As a consequence of this rather strong interband absorption in the blue for Cu and Au, transient low energy valence photo-electrons, typically between 0 and 1 eV with a typical lifetime of 100 fs [297, 298], are excited at the interface between the substrate and the molecular layer. We propose that those electrons, by a hopping, tunneling or energy transfer process [299], can either populate directly the 5E_g excited state (path labeled 1 in Fig. 4.7), for the most energetic of them or, most probably, the vibrational states of the Fe^{II} ion for lower energy electrons (paths labeled 2 and 3 in Fig. 4.7), allowing finally the switching from HS to LS [185]. In this second mechanism, both HS and LS molecules are *a priori* excited by the photo-electrons but it is known that the vibrational energy spacing of LS molecules is higher than for HS molecules, in a ratio close to 1.8 [300] (the spacing between energy levels being typically 30 meV for HS and 50 meV for LS). The larger density of vibrational states for HS therefore induces a more efficient vibrational heating of HS molecules as compared to LS ones. Moreover, considering that the HS state is higher in energy than the LS one, the energy barrier to switch from HS to LS is smaller than the one to switch from LS to HS. Accordingly, the rate of switching from HS to LS by this mechanism is expected to be larger than the rate of switching from LS to HS, leading to an anomalous spin-state switching. It is worth noting that this mechanism is in competition with the direct photon absorption by the LS molecules, that leads to the usual LIESST and/or SOXIESST effects, switching from LS to HS. This can explain why for the case of red light, where a very small density of inter-band photo-electrons are excited on Au, we observe a slight increase of the HS proportion under illumination, as expected from the LIESST and/or SOXIESST effects (Fig. 4.4-d). In contrast, for blue light, the density of valence photo-electrons is much larger and their contribution to the switching, from HS to LS, dominates over the usual LIESST mechanism. Finally, it seems that the influence of substrate induced low-energy valence photo-electrons on the switching should be inherently limited to the first molecular layers. As an example, a dominant LIESST effect is already measured for the second molecular layer on Au(111) with blue light [222, 223]. It is worth noting that this whole mechanism is very close to what has been proposed recently for the photo-induced tautomerization of porphycene molecules on Cu(111) [301, 302].

4.2 Effect of light on submonolayer to monolayers of Fe-Pyrz on Cu(111) and HOPG

After the investigations of the effect of several metallic substrates on the switching properties under light of submonolayers Fe-Pyrz, we will see in this section the effect of the number of layers on the anomalous switching on Cu(111) to confirm if this effect is only confined on the interface. Besides that, toward the reduction of molecule-substrate interaction, we propose to study the Fe-Pyrz molecules on HOPG. As shown in the previous chapter, HOPG is expected to have a lower molecule-substrate interaction than metals and it has been shown that complete transitions under light are possible for other molecules on this substrate [200, 207].

4.2.1 On Cu(111)

Figure 4.8 shows the evolution of HS proportion as a function of light exposure time on the samples studied for the thermal transition in chapter 3. On Cu(111), we recall that the three (resp. two) thinnest (resp. thickest) areas, namely 0.9 ± 0.2 ML, 1.7 ± 0.4 ML and 3.0 ± 0.6 ML (resp. 3.8 ± 1.0 ML and 5.3 ± 1.3 ML), have been measured concomitantly on the same sample. At $t = 0$ s (light blue off), the residual fraction of HS molecules before light irradiation at 4 K decreases as the molecular coverage is increased and this is, quantitatively, very consistent with the reported values in chapter 3. At $t > 0$ s (light blue on), the effect of the molecular coverage on the transition under light is impressive. Indeed, we observe an anomalous switching under blue light from HS to LS for the 0.9 ± 0.2 ML and 1.7 ± 0.4 ML on Cu(111) samples with a return to the expected bulk behaviour, i.e. from LS to HS, for 3.0 ± 0.7 ML. We remark that the 0.9 and 1.7 ± 0.4 ML samples have the same HS population values at saturation. Moreover, for thicknesses superior to 3 ML, the greater the thickness is, the more efficient the conversion from LS to HS becomes. The effect is even more spectacular for the thicker sample. Indeed, the increase in the number of layers is accompanied by an increase in the cooperativity of the system which results in a reduction of the molecule-substrate interaction. Since the molecules are less constrained by the substrate to maintain their spin-state, the switching is more efficient on the thick samples. More importantly, this measurement suggests that the previously observed anomalous light transition is confined to the first layers only, thus the interface effect is indisputable. Finally, as the measurements are averaged values over the number of layers, we can assume that the transition is always incomplete on the interface layer and almost complete on the others, especially for the top most layers. We expect a complete light-induced transition under blue light from 0 % HS to 100 % HS for larger thicknesses.

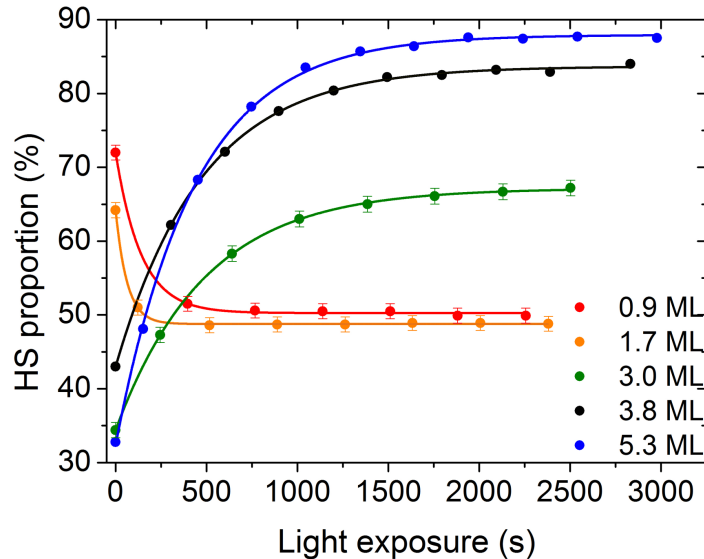


Figure 4.8: HS conversion curve as function of blue light exposure time at 405 nm at fluence of 0.5 mW/cm^2 on Cu(111). (red): 0.9 ± 0.2 ML; (orange): 1.7 ± 0.4 ML; (green): 3.0 ± 0.7 ML; (black) 3.8 ± 1.0 ML; (blue): 5.3 ± 1.3 ML. The scatters are data points extracted from the XAS spectra. The full line is a fit using single-exponential functions.

4.2.2 On HOPG

Figure 4.9 shows the HS fraction as a function of light exposure time for 0.3 ± 0.1 ML and 1.4 ± 0.3 ML of Fe-Pyrz on HOPG. Qualitatively, the story is very similar with what has been found on the Cu(111). For the submonolayer system, the transition from HS to LS (40 % conversion) is achieved under blue light while green light does not switch the molecules, what is rather surprising as the absorption band of HOPG is rather flat at optical wavelengths. At 1.4 ± 0.3 ML, we find the usual behavior of LS to HS under blue light (50 % conversion) and green light (40 % conversion). Quantitatively, we have more molecular switching on HOPG than on Cu(111) and this for smaller thicknesses. Indeed, the 1.4 ± 0.3 ML system on HOPG behaves almost similarly as the 5.3 ± 1.3 ML on Cu(111) (in figure 4.8-blue), we thus have a more efficient switching on HOPG. The reason for this is probably that the epitaxial stress on HOPG is lower than on Cu(111) which results in the molecules being more cooperative on HOPG and thus induce a recover of the bulk properties for a lower coverage.

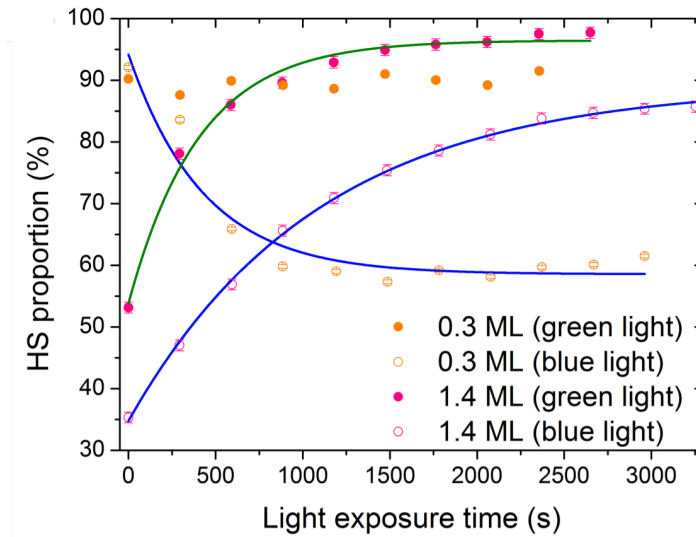


Figure 4.9: HS conversion curve as function of light exposure time at 405 nm (open circles) and 532 nm (filled circles) on HOPG. (orange): 0.3 ± 0.1 ML; (pink): $1.4 \pm 0.3 \pm 0.1$ ML. The scatters are data points extracted from the XAS spectra. The full line are fits using single-exponential functions.

Moreover, HOPG is a semimetal and as shown by the paper in the reference [162], there is an effect of the electronic properties of the substrate near the Fermi level on the spin transition properties. Since HOPG has an anisotropic band structure, its optical properties (given by its dielectric constant tensor) depend greatly on the polarization and angle of the incident light. Thus, the absorption of light by HOPG and the creation of valence photoelectrons due to the interband transition in the material should also depend on it. This was confirmed by reflectivity measurement (ratio between reflected and incident powers) at different incidence angles and for LV (s) and LH (p) polarizations, as shown in figure 4.10-a. At a given angle and polarization, the HOPG absorbs as similarly blue, red or green lights. In addition, the absorption is more important when the light is incident in LH than in LV polarization. Finally, we see that this difference in absorption due to polarization becomes more important, as the incident angle is large [303].

Figure 4.10-b/c shows preliminary results of the evolution of the photoconversion as a

function of blue light exposure time and by polarizing the incident blue light at an incidence angle of 70° with respect to the surface normal, for the 0.3 ± 0.1 ML (a) and 1.4 ± 0.3 ML (b). From the figure 4.10-b, we observe almost no difference in the HS to LS conversion for LH and LV polarization although the absorption is very different, what seems in contradiction with the model based on switching induced by valence photo-electrons. In the contrary, Figure 4.10-c shows for a thicker molecular film, with a standard LS to HS transition, a measurable effect of the polarization, whereas a direct absorption by the molecule should not be very sensitive to the polarization direction. Those results, that we had not time to reproduce, raise some questions and it will be interesting in the future to confirm such results and understand such a behavior.

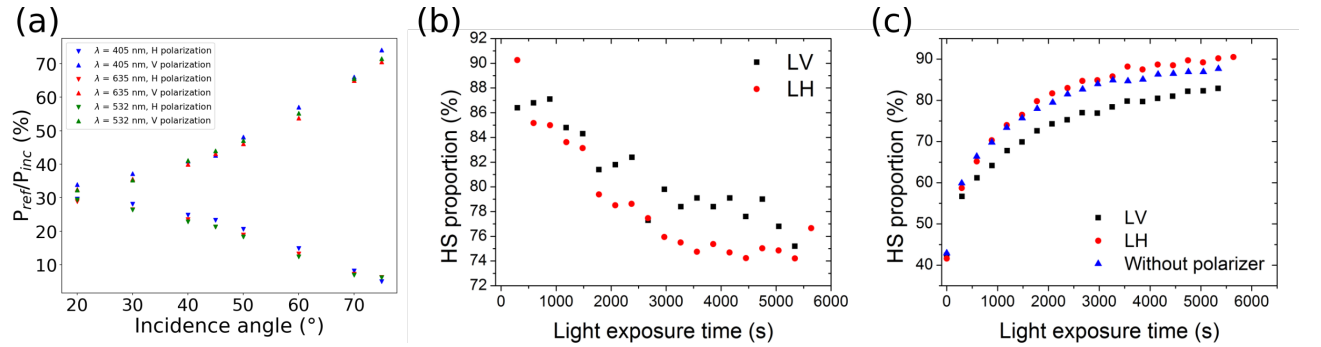


Figure 4.10: HS proportion as a function of blue light exposure time at a fluence of 0.21 mW/cm^2 . The light incidence angle is 70° with LV polarization (black) LH (red) and without polarizer (blue) for 0.3 ± 0.1 ML (a) and 1.4 ± 0.3 ML (b). (c) Reflectivity measurements as a function of the angle of incidence for HOPG under blue (405 nm), green (532 nm) and red (635 nm). The up triangles represent the linear horizontal polarization (LH) and the down triangles represent the vertical polarization (LV).

4.3 Light Induced Thermal Hysteresis (LITH) measurements on Cu(111) and HOPG

In this section, we will first investigate the relaxation (or T_{LIESST}) of the transition under light on Cu(111). Then, we will show the measurements of light-induced thermal hysteresis (LITH) on Cu(111) and also on HOPG.

4.3.1 T_{LIESST} measurements on Cu(111)

Figure 4.11-a shows the evolution of the photoinduced HS proportion (after 20 min under blue irradiation at low temperature) as function of temperature, in dark conditions at 1 K/min ramp, or the so-called T_{LIESST} measurement. We recall that the T_{LIESST} is not an intrinsic parameter of the molecule and is therefore a dynamic measurement that depends on the temperature ramp rate. It is usually fixed at 0.3 K/min to be able to compare with other bulk compounds in the literature [39]. The goal here is to rationalize the LITH measurements that we will see later by trying to deduce the temperature at which the LIESST is no longer effective and the thermal effects become more important.

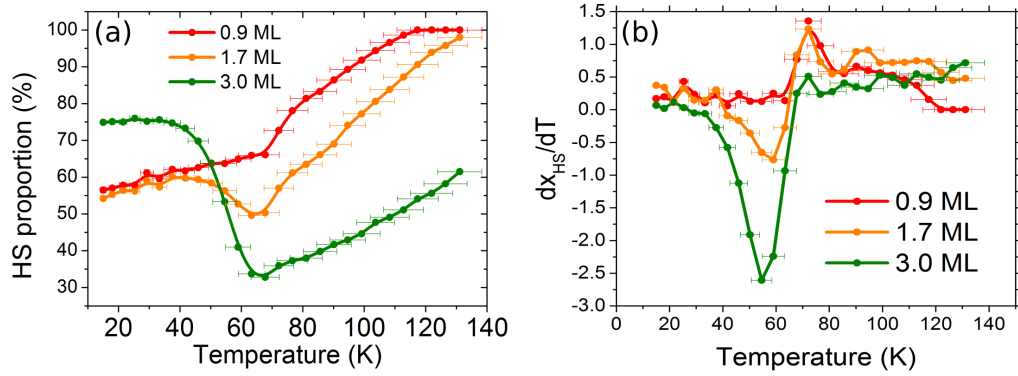


Figure 4.11: (a) Evolution of the photoexcited HS state ($x_{HS}(T)$) as a function of temperature for 0.9 ± 0.2 ML (red), 1.7 ± 0.4 ML (orange) and 3.0 ± 0.7 ML (green). (b) Derivative of the photoexcited HS population ($\frac{\partial x_{HS}(T)}{\partial T}$) with respect to temperature.

To obtain the T_{LIESST} , we simply derive the HS(T) conversion curve (figure 4.11-a) with respect to temperature and we obtain figure 4.11-b. The T_{LIESST} corresponds to the temperature for which the derivative (in absolute value) is maximum. For the 0.9 ± 0.2 ML, there is no relaxation towards the LS state since the system is saturated in the LS state with blue light. Therefore, we should better call $T_{r-LIESST}$ the relaxation temperature. This $T_{r-LIESST}$ is ascribed to the maximum of the derivative at 72 ± 5 K (see figure 4.11-b in red) but is rather peculiar as it corresponds to a temperature where the thermal conversion has already started. For the 3 ML the curve is much more usual and we find $T_{LIESST} = 55 \pm 4$ K (cf. Fig 4.11-b in green). For the 1.7 ML, we find two maxima, one corresponding to T_{LIESST} (59 ± 4 K) and an other one to $T_{r-LIESST}$ (72 ± 5 K), what seems to demonstrate that at this coverage, two antagonist effects occur for the interface and the topmost layer, with different relaxation energy barriers. However, as shown in figure 4.8 in red and orange, the dominant effect is the transition from HS to LS. In addition, as seen in chapter 3, the transition temperature decreases as we decrease the molecular coverage and this favors the overlap with the T_{LIESST} region [39, 121, 304]. This is the first time that this situation has been observed for ultrathin films of SCO on surfaces.

4.3.2 LITH measurements on Cu(111) and HOPG

Figure 4.12 shows the LITH results on Cu(111) (a) and HOPG (b). The star symbols in the figures represent the thermal state at low temperature (in the dark). Then, we turn on the blue light (405 nm) for 20 min without measuring with X-rays to avoid SOXIESST effects. As expected from the results of the previous sections, blue light induces a transition from HS to LS for the lower thicknesses (0.9 ± 0.2 ML, 1.7 ± 0.4 ML on Cu(111) and 0.3 ± 0.1 ML on HOPG) and LS to HS for the thicker ones (3.0 ± 0.7 ML, 3.8 ± 1.0 ML and 5.3 ± 1.3 ML on Cu(111) and 1.4 ± 0.3 ML on HOPG). After reaching the photostationary state, we start measuring continuously with the light on and with a temperature ramp of 1 K/min. We will first discuss the case of Cu(111) and then HOPG.

On Cu(111), no LITH is observed for 0.9 ± 0.2 ML and 1.7 ± 0.4 ML in which we have a HS to LS conversion. For thicker samples, where we have a transition from LS to HS, there is a

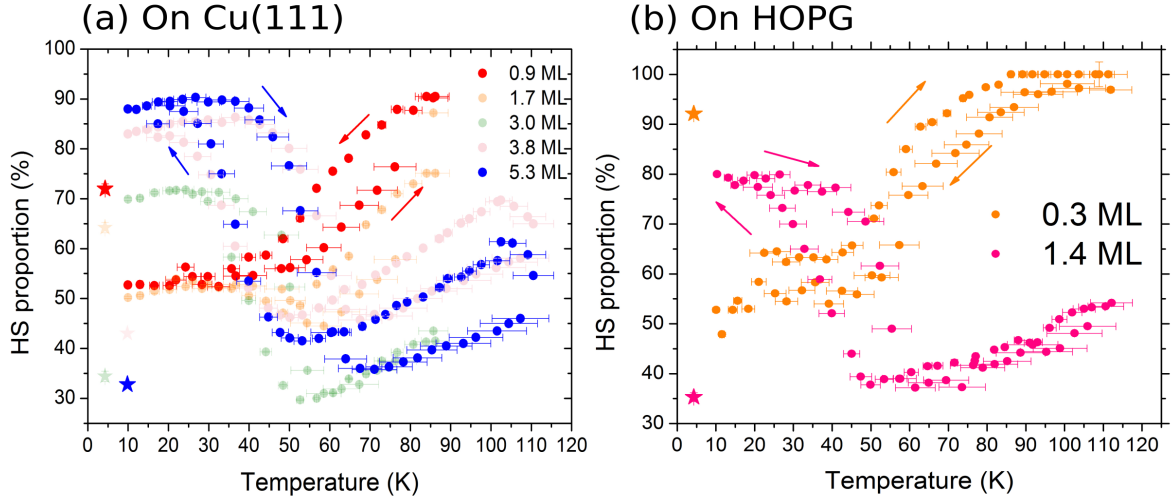


Figure 4.12: Evolution of the photoexcited HS state as a function of temperature under constant irradiation at 405 nm with 1 K/min temperature ramp and at a fluence of 0.5 mW/cm^2 . (a) Cu(111), $0.9 \pm 0.2 \text{ ML}$ (red), $1.7 \pm 0.4 \text{ ML}$ (orange), $3.0 \pm 0.7 \text{ ML}$ (green), $3.8 \pm 1.0 \text{ ML}$ (pink) and (blue) $5.3 \pm 1.3 \text{ ML}$; (b) HOPG: $0.3 \pm 0.1 \text{ ML}$ (orange) and $1.4 \pm 0.3 \text{ ML}$ (pink). The star symbols in both figures shows the thermal state before illumination.

light-induced thermal hysteresis cycle opening (in the vicinity of T_{LIESST}). Secondly, two quantities can be derived from these figures, namely the width of the LITH cycle and its centre. The widths are $10 \pm 3 \text{ K}$ for $3.0 \pm 0.7 \text{ ML}$ and $20 \pm 3 \text{ K}$ for $3.8 \pm 1.0 \text{ ML}$ and $5.3 \pm 1.3 \text{ ML}$. Moreover, all the LITH cycles are centred to nearly the same values which are $45 \pm 3 \text{ K}$ for $3.0 \pm 0.7 \text{ ML}$ and $47 \pm 3 \text{ K}$ for $3.8 \pm 1.0 \text{ ML}$ and $5.3 \pm 1.3 \text{ ML}$ on Cu(111). As explained in chapter 1, the temperature ramp is important because the thermal transition as well as the lifetime of the metastable state are dynamical effects. For this reason, these measurements were acquired under exactly the same experimental conditions as the thermal transition curves (1 K/min) in chapter 3. We observe that the thermal transition and LITH curves become hysteretic at the same thickness. As the thermal transitions are not shifting and we have used the same temperature ramp and the same fluence of blue light, we can therefore deduce that the LITH we observe is an effect exclusively due to the cooperativity [86, 106, 108, 111, 125] of the top most layers which increases as the number of layers increases.

On HOPG, we observe an opening of the LITH cycle for a smaller thickness than on Cu(111) (1.4 ML) with a width that is $16 \pm 4 \text{ K}$ and its center positioned at $48 \pm 5 \text{ K}$. The behavior of this system at 1.4 ML on HOPG is very similar to the 5.3 ML on Cu(111). Indeed, on HOPG, the fact that we observe the LITH for a smaller coverage than on Cu(111) indicates that the molecule-substrate interaction is weaker on HOPG than on Cu(111). This results in a stronger cooperativity on HOPG, for lower thicknesses compared to Cu(111). As far as we know, this is the thinnest system that exhibits a LITH.

Figure 4.13 shows the superposition in the same graph of the LITH (under constant blue irradiation, full lines), the thermal transition (black scatters) and the relaxation temperature measurement (in the dark, colored scatters) for $0.9 \pm 0.2 \text{ ML}$ (a), $1.7 \pm 0.4 \text{ ML}$ (b) and

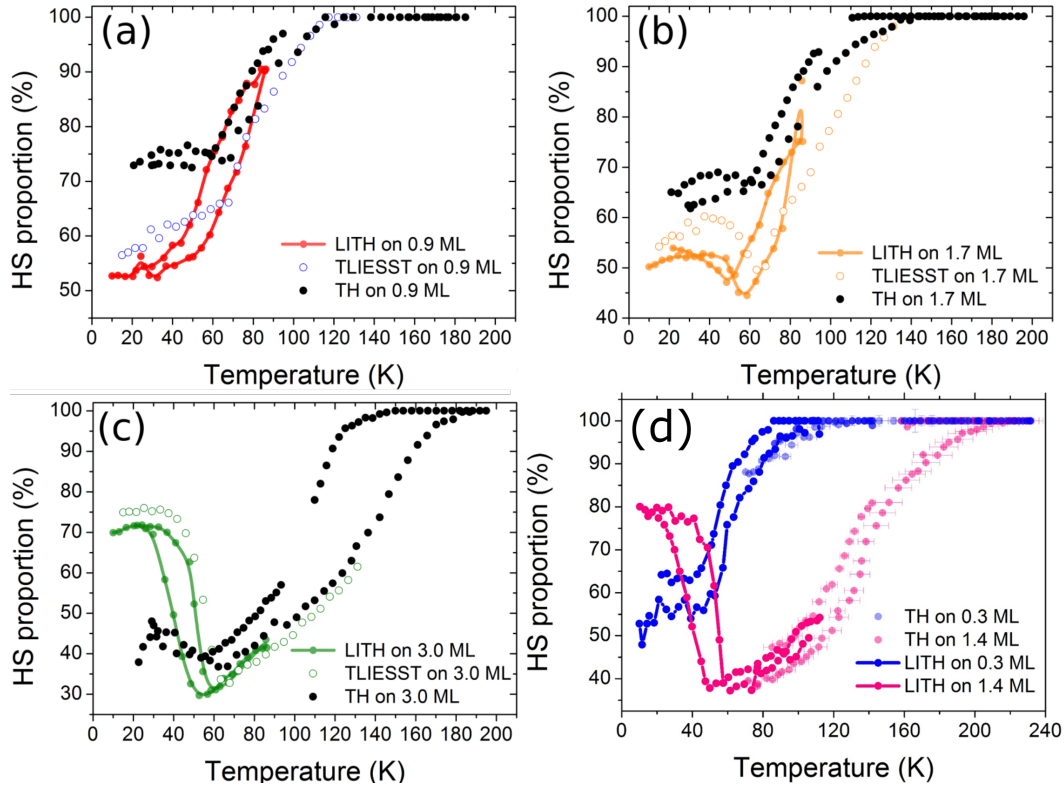


Figure 4.13: HS proportion as function of temperature on Cu(111). Superposition of the LITH curve (colored), the thermal hysteresis curve (TH in black) and the T_{LIESST} curve (open symbols) for (a) 0.9 ± 0.2 ML; (b) 1.7 ± 0.4 ML and (c) 3.0 ± 0.7 ML on Cu(111). (d) Thermal hysteresis (scatter) and LITH (full line) curves for 0.3 ± 0.1 ML (blue) and 1.4 ± 0.3 ML (pink) on HOPG.

3.0 ± 0.7 ML (c) on Cu(111) and for both presented coverages on HOPG (d). We observe that above T_{LIESST} for which the thermal relaxation effects are too fast, then we catch up with the thermal hysteresis curve. In the LITH curves, the increase of the HS proportion, observed at 100 K, is due to the waiting time between the measurements of the ascending and descending branches. Indeed, during this time, the system evolves to the HS state. For 0.9 ± 0.2 ML, 1.7 ± 0.4 ML on Cu(111) (Fig. 4.13-a/b), we observe the catching up of the thermal hysteresis curves (in black scatters) around $T_{r-LIESST}$ with the only difference that we start with a lower HS proportion compared to the thermal hysteresis, so the light "extends" the thermal-induced SCO. This effect is even more spectacular for the submonolayer on HOPG. The reason for the "extension" of the thermal hysteresis may be due to the fact that thanks to the light, we observe a hidden phase transition [39, 121]. Indeed, the thermal relaxation and the light-induced phenomena occur in the same temperature range and this overlap of the SCO phenomenon inhibits the system which remains almost fully HS over the whole temperature range. However, it leads to an interesting situation where the thermal hysteresis is hidden under the quenching of the HS state. Thus, light irradiation permits to access to a macroscopic state with more LS species and this would be normally hidden by temperature as it was already demonstrated for SCO compounds in bulk [75, 129, 138, 305, 306] or for the Prussian blue analogs $(Rb_xMn[Fe(CN)_6]_{x+2})/3 \cdot (zH_2O)$ in solid solutions [307]. Moreover, it seems that the LITH loop for 1.7 ± 0.4 ML (figure 4.13-b) is shifted toward higher temperature compared to the one obtained without irradiation. This shift of the transition under the effect of light has already been seen by reference [143] and has

been named "Light-Induced Perturbed Hysteresis (LiPTH)" but no explanation for this phenomenon has been given. Finally, for the 3.0 ± 0.7 ML coverage on Cu(111) and 1.4 ± 0.3 ML on HOPG, the transition under light is from LS to HS, then we measure two well separated cycles: the LITH for temperatures below 60 K and the thermal transition curve above 60 K. These findings open new potentialities to design information storage devices at the nanoscale: write information with light ON and then erase it with temperature.

4.4 Conclusions

In this chapter, we have **first** measured, by means of XAS and STM, the light-induced behavior of a single molecular layer of $\text{Fe}^{\text{II}}((3,5-(\text{CH}_3)_2\text{Pz})_3\text{BH})_2$ molecules adsorbed on three noble metal surfaces, namely Cu(111), Ag(111) and Au(111). We find that the molecules keep their integrity on the three substrates, leading to well-ordered two-dimensional molecular arrays. We also find that their switching properties are strongly affected by the contact with metal surfaces. Indeed, at low temperature, only a fraction of the molecules are in a LS state because of the epitaxial constraint imposed by the substrate. Moreover, illumination with a blue light induces a switching from HS to LS despite the absence of a HS absorption band, in contrast with the bulk behavior. By comparing the efficiency of this anomalous light induced HS to LS switching on the different substrates and at different wavelengths, we propose a possible mechanism involving the light absorption by the substrate.

Secondly, the effect of the number of layers on the anomalous switching on Cu(111) confirms that the HS \rightarrow LS transition is only confined below a critical thickness of 1.7 ± 0.4 ML. Moreover, T_{LIESST} measurements show the existence of a HS metastable state which suggests the existence of two populations of HS molecules: the ones on the interface (resp. top layers) with the tendency to switch to LS (resp. HS).

Thirdly, to check if this specific interfacial effect between metals and spin-crossover molecules is rather general or more particular to these metals, we proposed to study submonolayer and a monolayer of $\text{Fe}^{\text{II}}((3,5-(\text{CH}_3)_2\text{Pz})_3\text{BH})_2$ molecules on HOPG. We have also demonstrated the existence of the anomalous light-induced effect which is confined only on the first molecular layer.

Finally, we have measured light-induced thermal hysteresis curves for submonolayers to multilayers of $\text{Fe}^{\text{II}}((3,5-(\text{CH}_3)_2\text{Pz})_3\text{BH})_2$ on Cu(111) and HOPG. On submonolayers on Cu(111) and HOPG, where the HS to LS transition is dominant, we demonstrate the shift of the thermal hysteresis loop toward a macroscopic scale with lower HS species. This is somehow similar to hidden phase transitions observed for other spin-crossover compounds. Further experiments, such as grazing-incidence X-ray diffraction, can be a good way to elucidate if it is indeed a hidden phase transition. For multilayers, for the first time, a light-induced thermal hysteresis was measured (3.0 ± 0.7 ML on Cu(111) and resp. $1.4 \pm 0.3 \pm 0.1$ ML on HOPG). This is the direct consequence of the cooperativity of the metastable HS state which leads to light-induced bistability which can lead to the formation of like-spin domains under blue illumination. Mechanoelastic simulations should be carried out, to investigate in more detailed how the balance between molecule-substrate interaction and the cooperativity influence the light transition (LIESST or LITH).

ROBUST MAGNETIC ANISOTROPY OF AN ULTRATHIN FILM OF Fe-PYRZ ASSEMBLED ON Cu(111)

Since the 1970s [308], molecular magnetism [1, 309, 310] has been of increasing interest within the physicist and chemist communities. These molecular magnets arouse immense interest from a practical point of view, because they offer the possibility of considering storing information on a single molecule, thus making it possible to achieve storage densities of the order of 1000 Tbits/in² [16, 20, 22, 178]. Such a storage density associated with the dynamic magnetic behavior of these molecules also makes it possible to envision a quantum computer operating at clock speeds inaccessible today (of the order of 10 GHz) [311]. On the fundamental point of view, one of the important objectives is to be able to open magnetic hysteresis cycles at room temperature. In 1993, the pioneering work done by reference [312] shows the first opening of a hysteresis cycle on an inorganic compound containing 12 manganese atoms ([Mn₁₂O₁₂(CH₃COO)₁₆(H₂O)₄] or Mn₁₂) at a temperature of 3 K. Today, the world record temperature of the opening of a cycle is at 500 K, to be credited to a 2D coordination networks, namely Li_{0.7}[Cr(py_z)₂]Cl_{0.7}·0.25(THF) (py_z pyrazine) [313] and is shown in figure 5.1-a.

Now, a major objective of the community is to be able to measure and address these molecules by depositing them on surfaces. That is why the study of how the magnetic properties of molecular magnets are modified when supported on a substrate [316] is of great importance for their practical integration in solid state devices. Up to now, most of the molecular magnets studied in their bulk form are extremely sensitive to small deformations and it took some years to establish, by means of XAS and XMCD, the quantum magnetization reversal [317] for a monolayer of specially designed Fe₄C₅ molecules grafted on Au(111) surface [314, 318], as shown in figure 5.1-b/c. This previous complex was the first example to exhibit a magnetic hysteresis at 0.5 K once adsorbed on a surface. However, regarding the change of magnetic anisotropy of such molecules when adsorbed on a surface [319], little is known. It has been shown recently that for planar molecules such as Fe(II)-phtalocyanin or Fe(II)-porphyrin, not only the magnetic anisotropy but also the spin state can be strongly modified on the surface, depending on the adsorption geome-

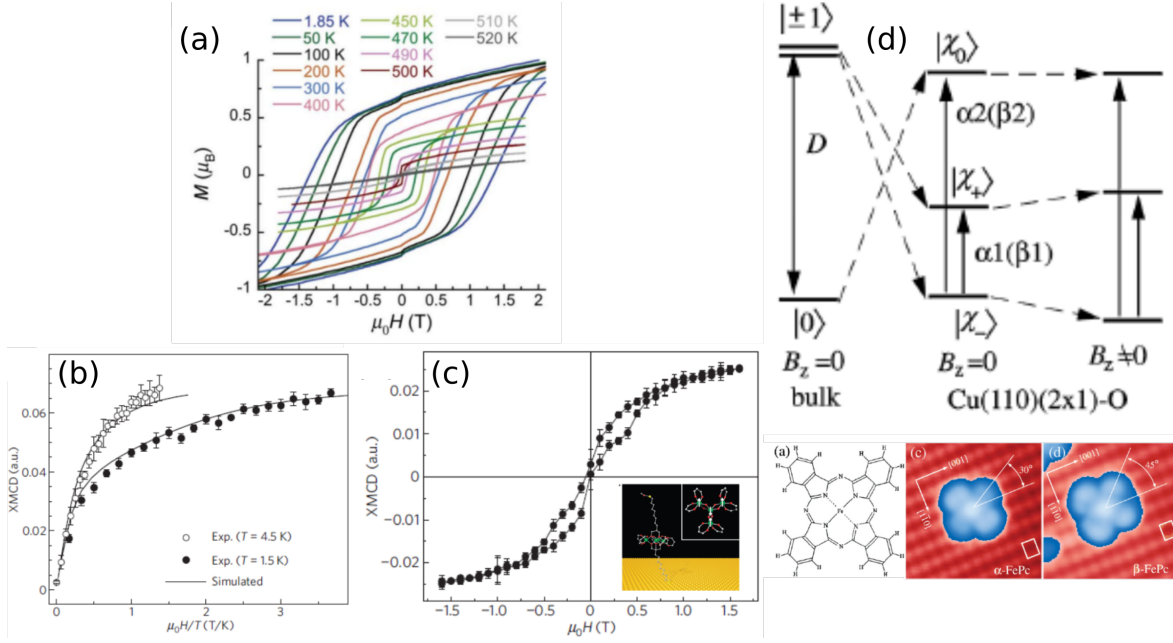


Figure 5.1: (a) Magnetization versus applied dc magnetic field data (at 7.10^{-4} T/s) in the 2.1 to 2.1 T field range and in the 1.85 and 500 K temperature range. (b) Variation of the XMCD signal at 709.2 eV as a function of the ratio between the applied magnetic field and temperature B/T , recorded on the Fe_4 monolayer. The data have been taken by scanning the field up to 5.5 T at two different temperatures. The lines correspond to the calculated magnetization by using the Spin Hamiltonian (see section 5.2). (c) Magnetic hysteresis at 0.5 K for the Fe_4 monolayer, monitored through the XMCD intensity at 709.2 eV obtained from XAS signals normalized to the pre-edge intensity (704.0 eV) under a magnetic field sweeping rate of 2 mT/s, showing a magnetic hysteresis loop. Inset: Schematic diagram of the anchoring on a gold surface of the Fe_4 . These figures were taken from [314]. (d) The energy diagram of the zero-field splitting (ZFS) for bulk Fe-phthalocyanine and a single Fe-phthalocyanine molecule on $\text{Cu}(110)(2 \times 1)\text{-O}$ surface. In bottom: Schematic model of the molecule (left); Topographic STM taken at 0.4 K ($4 \times 4 \text{ nm}^2$, $I = 100 \text{ pA}$, and $V = 0.5 \text{ V}$) showing the two orientations of Fe-Phthalocyanine on $\text{Cu}(110)(2 \times 1)\text{-O}$. These figures were taken from [315].

try [320], local distortions, and intermolecular interactions [321]. As shown in figure 5.1-d from reference [315], upon adsorption on a $\text{Cu}(110)$ surface, the energy diagram of zero-field splitting, encoded by D (zero-field splitting energy), is different for bulk Fe-phthalocyanine and a single Fe-phthalocyanine molecule. Moreover, the molecule shows two different orientations on the surface and their magnetic anisotropy are slightly different. The origin of this large change in the spin electronic structure of this type of molecules is the relatively flexible and unsaturated coordination sphere of Fe(II) . They possess, however, high thermodynamic stability that allows maintaining their integrity when sublimed under vacuum and assembled on metallic substrates. For non-planar molecular magnets, with a metallic ion in the most common hexacoordinate coordination sphere (distorted octahedral geometry), specially designed complexes have also shown a substrate-induced modification of their magnetic anisotropy because they were chemically grafted on oxide surfaces [316]. To ensure some robustness of magnetic anisotropy, a possible approach consists of using organic ligands that impose a relative rigidity on the metal ion coordination sphere so that major structural deformations are precluded when the molecules are present at the sub-

strate/vacuum interface.

SCO molecules are an other class of interesting molecules for magnetism, due to their ability to switch between two spin states. In their non zero spin-state, they also possess a magnetic anisotropy, and one can imagine to combine both properties, *i.e* spin-state switching and opening of a magnetic hysteresis cycle. The difficulty comes from the fact that most SCO molecules are Fe^{II} , which inherently shows small spin-orbit coupling and therefore small magnetic anisotropy. However, the magnetic anisotropy of SCO molecules is not very well-known and even less for molecules deposited on a substrate. In this chapter, we ask the question that has not yet been addressed is: **how is modified the magnetic anisotropy of Fe-Pyrz molecule when adsorbed onto a Cu(111) surface ?** The organization of the chapter is as follows: first, we will see some generalities about molecular magnets as well as the theoretical ingredients *i. e.* the Spin Hamiltonian formalism, that will help us to analyze the experimental results. Then, I will present the *PHI* software with which we analyze the data and we will confront the results obtained by *PHI* with analytical expressions obtained from the Spin Hamiltonian formalism. Then, we will move to the experimental results. First, we will show the magnetic susceptibility results for Fe-Phen which we will discuss comparatively with XAS and XMCD data of a Fe-Pyrz submonolayer on Cu(111). From these measurements, we extract the magnetic anisotropy parameters as well as the orientation of the C_3 axis of the Fe-Pyrz molecule on Cu(111). Finally, by *ab-initio* calculations made by our collaborators, we will rationalize the obtained results on the basis of structural arguments of the molecule.

5.1 What is the difference between single molecular magnets and paramagnetic molecules ?

Among molecular magnets, there is a family of paramagnetic compound called single molecular magnets (SMM). To illustrate this concept, I will take the *historical* example of Mn_{12} [312]. This molecule was the first to exhibit SMM behavior and is made up of several metal centers $\text{Mn}(\text{III})$ (of spin $S = 2$) and $\text{Mn}(\text{IV})$ (of spin $S = 3/2$), interacting via magnetic exchange interactions, giving rise to a total spin of 10. In addition, this molecule has a D_{2d} symmetry and therefore an easy magnetization axis along its S_4 symmetry axis. The presence of this easy axis confers a zero-field splitting (which we will call D in the following) of the state $S = 10$, with two projections, $M_S = \pm 10$ which have the lowest energies. Figure 5.2 shows a general scheme of the double potential well of any SMM with a total spin S and with its projection M_S . As previously mentioned, the observation of the magnetic hysteresis cycle of this molecule was observed at less than 3 K. The reason is that this molecule has a so-called superparamagnetic behavior. Indeed, for any cluster of magnetic atoms, when the cluster forms a monodomain, then above a so-called blocking temperature (T_B) the particle behaves in the presence of a magnetic field like a paramagnet but with a very high susceptibility resulting from the large number of interacting spins. Below T_B , the dynamic behavior (in the presence for example of an oscillating magnetic field) is on the other hand different from that of a "simple" paramagnetic. The presence of a magnetic anisotropy associated with the relatively high spin-orbit coupling of the ground state leads to a long magnetization relaxation time compared to the time characteristic of the measurement technique. Below this blocking temperature, the application of a magnetic field

leads to saturation of the magnetization which remains constant when the magnetic field is canceled and thus a magnetic hysteresis cycle is observed. It is important to emphasize that this magnetic hysteresis is due to the presence of magnetic anisotropy energy (DS_z^2) greater than thermal energy. Another important feature is the fact that the relaxation of the magnetization can either be due to the interaction of the spin with the modes of vibrations of the network (spin-phonon interaction) or by tunneling. Indeed, there can be a direct process (from an M_S state to a $M_S \pm 1$ state) via the absorption or emission of a phonon (Orbach process) [322]. The Quantum Tunneling of the Magnetization (QTM) does not require absorption or emission of phonons but directly of a direct passage from the state M_S to $-M_S$. There can be also a two-phonon process via a virtual state, called the Raman interaction. Regarding the Mn_{12} molecule, it was shown that there was a direct sequential spin-phonon transitions that was involved. To sum up, a SMM is a molecule which has an easy magnetization axis and which below a certain so-called blocking temperature, then finds the projection of the spin moment blocked along the direction of the magnetic field, and then magnetic relaxation may take (long) time.

For the molecules that we will study in this chapter (Fe-Pyrz and Fe-Phen, both of spin $S = 2$), we will show, in next sections, that these molecules have a hard axis of magnetization ($D > 0$) and therefore an easy plane of magnetization. This means that, unlike the case of SMMs where we have a potential barrier, here we have an energy potential well with a minimum of energy for $M_S = 0$ (reverse of the figure 5.2). Since the magnetization is always blocked in the direction of easy axis of magnetization, it means that these molecules can orient themselves as they want according to an easy plane of magnetization and therefore cannot block their magnetization. However, whether in the case of SMMs or paramagnetic compounds, the theoretical formalism is the same and is called "Spin Hamiltonian" that we are going to develop in the next section. Finally, I would also like to mention important

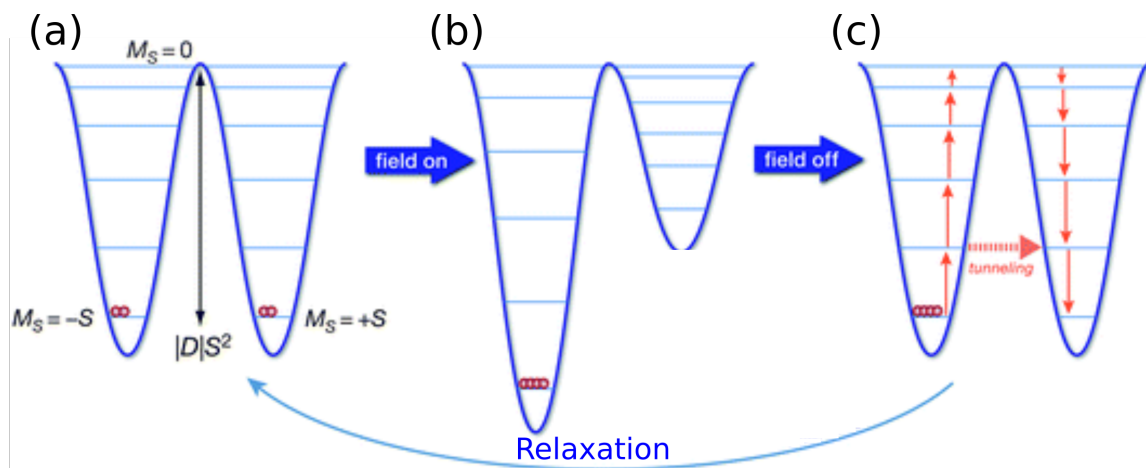


Figure 5.2: Schematic of the zero-field degeneracy of the ground state for a single molecular magnet with a total spin S . Energy levels for a spin state S with easy axis magnetic anisotropy. The $-M_S$ sub-levels are localized in the left well and the $+M_S$ levels in the right well, separated by an energy barrier (DS_z^2). In zero field the two wells are equally populated; b) the application of a magnetic field selectively populates the left well; c) after removing the field the return to equilibrium occurs through a series of steps. These figures were taken from [323].

characteristics of paramagnetic systems. In fact, the magnetic susceptibility as a function

of temperature follows the Curie's law, as shown in the black curve in figure 5.3-b:

$$\chi = \frac{C}{T} \quad (5.1a)$$

Where C is a constant. The low temperature deviation from the Curie law is a direct consequence of the presence of a magnetic anisotropy as shown in figure 5.3-b. Moreover, the measurement of the magnetization of a paramagnetic system as a function of the magnetic field and for different temperature ($M(\frac{B}{T})$ where B is the magnetic field and T is the temperature), immediately informs us whether the system has a magnetic anisotropy or not. Indeed, for a quantum paramagnet, the magnetization is described by a universal curve, the Brillouin function ($B_J(x)$):

$$B_J(x) = \frac{2J+1}{2J} \coth(\frac{2J+1}{2J}x) - \frac{1}{2J} \coth(\frac{x}{2J}) \quad (5.1b)$$

With $x = \frac{\mu_B B}{k_B T}$. If there is no anisotropy, then all the measures of $M(B/T)$ should merge with the same curve as shown in the inset of figure 5.3-a. In an anisotropic system, the magnetization curves are different depending on the temperature and deviate from the Brillouin function, as shown in figure 5.3-a. In addition, there is no longer an analytical expression for for an arbitrary configuration of magnetic anisotropy and magnetic field axis for $M(B/T)$ and $\chi T(T)$. Therefore, we use a simulation program, called PHI [324], which allows to characterize the values of the anisotropy parameters (see next section) by fitting the experimental measurements of $M(B/T)$ and $\chi T(T)$. However, I managed to develop analytical formula for the magnetization of a paramagnetic system with axial anisotropy, under a magnetic field parallel to the direction of the axial anisotropy.

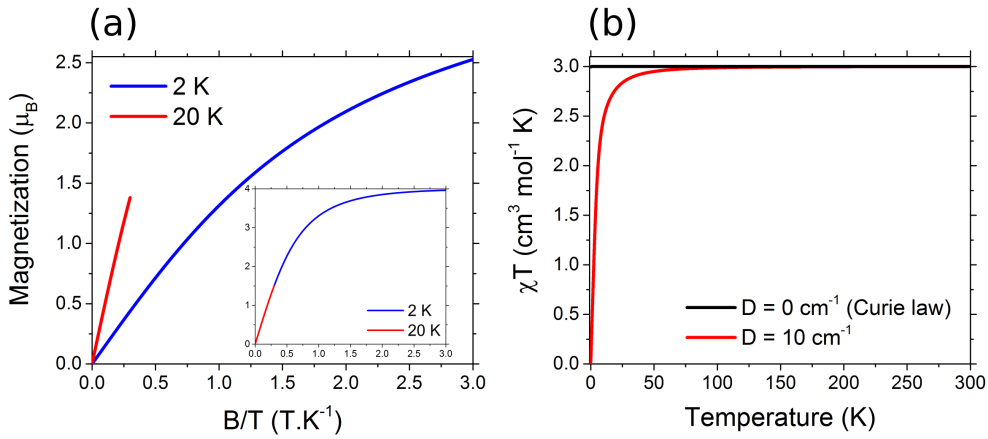


Figure 5.3: (a) $M(B/T)$ for $T = 2$ K (blue) and $T = 20$ K (red) with $D = 10$ cm^{-1} . In inset, $M(B/T)$ for $D = 0$ cm^{-1} . (b) $\chi T(T)$ for $D = 0$ cm^{-1} (black) and $D = 10$ cm^{-1} (red). The curves have been simulated by PHI.

5.2 The Spin Hamiltonian formalism

The Spin Hamiltonian (SH) [1, 26] is an effective Hamiltonian developed by Pryce for describing the energy of the different levels of the ground state. The purpose is to describe and model the macroscopic properties of the paramagnetic system. Also, this Hamiltonian

assumes that there is a sufficiently large gap between the electronic ground state and the excited states. Indeed, the effect of magnetic anisotropy on energy levels is felt only in the lower energy sector. The SH is constructed by time-independent perturbation method and only concerns spin variables. In this section, we show how this Hamiltonian is derived, its properties and how to simulate and fit magnetization curves using the *PHI* software.

5.2.1 Origin of the magnetic anisotropy

The origins of magnetic anisotropy are: spin-orbit coupling (SOC) and magnetic dipole interaction. In crystalline materials, the SOC induces a magneto-crystalline anisotropy. Thus the magnetization tends to orient itself in certain directions or crystallographic planes. The magnetic dipolar interaction induces a shape anisotropy which therefore depends on the shape of the object (e.g. a compass needle). In the case of magnetic molecules, the anisotropy is modified according to the metallic/ion center, i.e: competition between the SOC and crystal field (CF). Due to CF, the symmetry of the environment of the metallic center breaks the degeneracy of its orbitals. For $3d$ (resp. $4f$) orbitals case, the CF (resp. SOC as perturbation) dominates the SOC (resp. CF as a perturbation).

5.2.2 The Pryce's Spin Hamiltonian

The energy levels of the ground state are generally sufficient to describe the magnetic properties of a molecular magnet even at room temperature. In addition, it is necessary to take into account excited states within the ground state multiplet ^{2S+1}L to properly describe the energy of the ground state. We will show that in the case where the complex undergoes a distortion leading to a lowering of symmetry, the SOC not only disturbs the energy of the ground state but also lifts the degeneracy of this ground state in the absence of any external magnetic field. It is therefore important to calculate the energies of the levels resulting from the ground state by the combined effect of the SOC and a distortion. The total Hamiltonian is the following :

$$\hat{H} = \hat{H}_0 + \hat{V} \quad (5.2a)$$

$$\hat{H}_0 = \sum_{i=1}^{n_{\text{electrons}}} \left(\frac{\hat{p}_i^2}{2m_e} - \frac{Z_i e^2}{r_i} \right) + \sum_{i<j}^n \frac{e^2}{r_{ij}} + \hat{V}_{CF} \quad (5.2b)$$

$$\hat{V} = \mu_B \vec{B}(\hat{L} + g_e \hat{S}) + \lambda \hat{L} \cdot \hat{S} \quad (5.2c)$$

Where \hat{V}_{CF} is the crystal field potential, $\mu_B = 9.27 \times 10^{-24}$ J/T is the Bohr magneton, $g_e \simeq 2$ is the Lande factor for a free electron and λ is the SO constant for the magnetic ion. We need to construct an effective Hamiltonian, relating only to the space of functions of the ground state, and which makes it possible to take into account the effect of states excited by a perturbative approach. For light atoms ($Z < 30$), we consider the LS coupling (Russell-Saunders approximation) [26, 236, 247], it is appropriate to define the basis vectors in the decoupled basis, i.e., $|\alpha, L, M_L, S, M_S\rangle$, where α describes collective variables of the system. Subsequently, and for the sake of simplicity, we can separate the variables which depend on the spin in one ket and the other variables (radial and angular dependences) in another

ket as a tensorial product:

$$|\alpha, L, M_L, S, M_S\rangle = |\alpha, L, M_L\rangle \otimes |S, M_S\rangle = |K\rangle \otimes |S, M_S\rangle. \quad (5.3)$$

a) First-order perturbation term: In the following, we get rid of the symbol of the tensor product. The first-order energy shift is :

$$E^{(1)} = \langle K, S, M_S | \hat{V} | K, S, M_S \rangle \quad (5.4a)$$

$$E^{(1)} = \langle K, S, M_S | [\mu_B \vec{B}(\hat{L} + g_e \hat{S}) + \lambda \hat{L} \cdot \hat{S}] | K, S, M_S \rangle \quad (5.4b)$$

Since in this case, the expectation value of \hat{L} for an orbitally non-degenerate state is zero (all the terms in the form of $\langle K | \hat{L} | K \rangle = 0$). It leads to the final formula :

$$E^{(1)} = g_e \mu_B \vec{B} \langle K, S, M_S | \hat{S} | K, S, M_S \rangle \quad (5.4c)$$

The last term is called the Zeeman matrix of a "pure" spin characterized by the factor g_e . Clearly, the SOC does not contribute to the first-order correction of the energy. Thus, in the absence of SOC with the excited states, the ground state is magnetically isotropic.

b) Second-order perturbation term: The second-order energy shift is :

$$E^{(2)} = \sum_{K' \neq K} \sum_{M_{S'} \neq M_S} \frac{\langle K, S, M_S | \hat{V} | K', S, M_{S'} \rangle \langle K', S, M_{S'} | \hat{V} | K, S, M_S \rangle}{E_0^{(0)} - E_0^{(K')}} \quad (5.5a)$$

The sum goes over all orbital states. Superscripts (0) indicate zero-order energies. The following calculations are a bit heavy but not difficult. I will briefly describe the calculation tips. Already, it is necessary in what follows to write the operator \hat{V} by putting everything that depends on \hat{L} in one term and \hat{S} in the other ($(\mu_B \vec{B} + \lambda \hat{L}) \cdot \hat{S} + (\mu_B \vec{B} g_e \hat{S})$). Then, we can only focus on the term $\langle K, S, M_S | \hat{V} | K', S, M_{S'} \rangle$ in the equation 5.5a. Finally we take into account the orthogonality of the basis $\langle K | K' \rangle = \delta_{K, K'}$. We finally get:

$$E^{(2)} = \sum_{K' \neq K} \sum_{M_{S'} \neq M_S} \frac{\langle S, M_S | \mu_B \vec{B} + \lambda \hat{S} | S, M_{S'} \rangle \langle K | \hat{L} | K' \rangle \langle K' | \hat{L} | K \rangle \langle S, M_{S'} | \mu_B \vec{B} + \lambda \hat{S} | S, M_S \rangle}{E_0^{(0)} - E_0^{(K')}} \quad (5.5b)$$

Now that we have this result, we are almost done. In what follows, we will introduce a new mathematical object, the second order tensor $[\Lambda]$ whose definition is as follows:

$$\Lambda_{u,v} = \sum_{K' \neq K} \frac{\langle K | \hat{L}_u | K' \rangle \langle K' | \hat{L}_v | K \rangle}{E_0^{(0)} - E_0^{(K')}} \quad (5.5c)$$

Where $u, v = x, y, z$. With the previous result, the equation 5.5b leads to a simpler form:

$$E^{(2)} = \sum_{M_{S'} \neq M_S} \langle S, M_S | \mu_B \vec{B} + \lambda \hat{S} | S, M_{S'} \rangle [\Lambda] \langle S, M_{S'} | \mu_B \vec{B} + \lambda \hat{S} | S, M_S \rangle \quad (5.5d)$$

The last step consists in introducing a closing relation of the base ($\sum_{M_{S'}} \langle S, M_{S'} | S, M_{S'} \rangle = \mathbb{1}$), and then to simplify the calculation as much as possible, and we arrive at the following final formula:

$$E^{(2)} = \langle S, M_S | \mu_B^2 \vec{B} [\Lambda] \vec{B} + \lambda^2 \hat{S} [\Lambda] \hat{S} + 2\mu_B \lambda \vec{B} [\Lambda] \hat{S} | S, M_S \rangle \quad (5.5e)$$

The first term on the right-hand side of equation 5.5e represents temperature-independent paramagnetism. It is zero for $M_S \neq M_{S'}$ and constant for all $M_S = M_{S'}$. It does not create an energy difference between the ground state levels and will be omitted. Obviously, the second and third terms only contain the spin variables. By adding the results obtained in the equations 5.4c and 5.5e, we arrive at:

$$\hat{H}_{spin} = \hat{S}[D]\hat{S} + \mu_B B[g]\hat{S} \quad (5.6a)$$

with the following definitions:

$$[D] = \lambda^2[\Lambda] \quad (5.6b)$$

$$[g] = g_e \hat{1} + 2\lambda[\Lambda] \quad (5.6c)$$

$[D]$ is the magnetic anisotropy tensor and $[g]$ is the g -factor tensor. Some important remarks should be made. First, The Pryce's method of derivation is the first derivation of a microscopic SH because the D and g tensors are expressed in terms of microscopic parameters, that is, the energy-level splitting and the SOC parameter. An other is the deviation of the effective g factor from its free-electron value. It comes from the fact that the SOC produces an effective magnetic field which is added vectorially to the external field and admixes the ground state with certain excited states. The impact of this interaction is inversely proportional to the energy separation of the zero-order states engaged in the mixing. In the case of spin $S > 1$, higher order terms can intervene and the general form of the SH to be considered is then:

$$\hat{H}_{spin} = \sum_{k,q} B_k^q \hat{O}_k^q + \mu_B \vec{B}[g]\hat{S} \quad (5.6d)$$

Where the operators \hat{O}_k^q are spin operators called Stevens operators which translate the symmetry of the system (because of the CF) and it can be demonstrated that $k < 2S$. In the case of Fe^{II} ion where $S = 2$, there are two values of q (0 and 2). In addition, there are two relationships between the anisotropy parameters with the Stevens operators and are given by:

$$D = 3B_2^0 O_2 \quad (5.6e)$$

$$E = 3B_2^2 O_2 \quad (5.6f)$$

5.2.3 Properties of the Spin Hamiltonian

In practice, by removing a constant term, the trace of the tensor $[D]$ is 0. In addition, we will suppose that it is possible to diagonalize the tensors $[g]$ and $[D]$ in the same system of eigen axes. The eigenvalues of the tensor $[g]$ are noted g_x , g_y and g_z . The eigenvalues of the tensor $[D]$ are noted D_{xx} , D_{yy} and D_{zz} , such as $\text{Tr}[D] = D_{xx} + D_{yy} + D_{zz} = 0$. By circular permutation of the axes x , y and z , one chooses them in such a way that $|D_{zz}|$ is greater than $|D_{xx}|$ and $|D_{yy}|$. Then we define:

$$D = \frac{3}{2} D_{zz} \quad (5.7a)$$

$$E = \frac{|D_{xx} - D_{yy}|}{2} \quad (5.7b)$$

D is called the axial anisotropy or the zero-field splitting (ZFS) and E is called the rhombic anisotropy. Now, we arrive to our final result which is the following:

$$\hat{H}_{spin} = \mu_B(g_x B_x \hat{S}_x + g_y B_y \hat{S}_y + g_z B_z \hat{S}_z) + D[\hat{S}_z^2 - \frac{S(S+1)}{3}] + E[\hat{S}_x^2 - \hat{S}_y^2] \quad (5.7c)$$

where we added a constant term ($\frac{S(S+1)}{3}$) so that the barycenter of the levels remains unchanged. This effective Hamiltonian makes it possible to easily account for the anisotropy of a complex, and clearly shows the existence of a lifting of degeneracy of the ground state (due to ZFS) in the absence of a magnetic field if $[D] \neq [0]$.

5.2.4 Calculation of magnetization curves using the *PHI* software

PHI [324]¹ is a computer program designed by *N. Chilton* and co-workers, for the calculation of the magnetic properties of anisotropic paramagnetic coordination complexes. The range of possibilities offered by *PHI* is really impressive: magnetization curves, magnetic susceptibility, electron paramagnetic resonance curves, Zeeman field energy levels, etc. In my work, I will confine myself exclusively to the calculation of magnetization curves and magnetic susceptibility. In all the cases, the program takes as input the phenomenological parameters of the SH, i.e. S , L , D , E , $g_{x/y/z}$ described in equation 5.7c, this is the *simulation* mode. In addition, given the range of computational possibilities, it is also necessary to enter the initial conditions specific to each experiment: direction of the magnetic field ($\vec{B}(\theta, \phi)$) with respect to the magnetic axis of the molecule for the magnetization curves, the temperature sweep rate for the susceptibility, etc. Then, the program will calculate in order: the eigenvalues (E_i), the partition function ($Z = \sum_{i=1}^{2S+1} \exp(-\beta \cdot E_i)$) and the free energy of the system ($F = -k_B T \log Z$) and finally we can extract the two measured quantities²:

$$M = \frac{\partial F}{\partial B} \quad (5.8a)$$

$$\chi = \lim_{B \rightarrow 0} \frac{\partial M}{\partial B} \quad (5.8b)$$

The other available mode is the *fit* mode. Indeed, *PHI* is able to extract the parameters of the SH from an experimental $M(B)$ and/or $\chi T(T)$ curve(s) as input. It uses as convergence criterion, χ^2 function³, defined as (for magnetization curves):

$$\chi^2 = \sum_{p=1}^{points} (M_{exp,p} - M_{calc,p})^2 \quad (5.9)$$

5.2.5 Exact calculation of magnetization curves

Although *PHI* is a very powerful tool, it is generally more convenient for data analysis to have analytic formula. In this section, I will therefore develop analytical expressions

¹You can download the software at: <http://www.nfchilton.com/phi.html>.

²In *PHI*, all formulas and quantities are expressed in CGS units.

³The χ^2 is called the residual function and is absolutely not related to the magnetic susceptibility.

for $M(B)$ in anisotropic systems without rhombicity (E). I will first present the general matrix with the magnetic field which can be in any directions for $S = 2$. Then, the special case where $\vec{B} \parallel (\mathbf{OZ})$ in which I show that an analytic expression exists for $S = 2$ and a generalization could be done for any spin (integer or half-integer). Finally, I will check with *PHI* that my formula are correct.

5.2.5.1 $E = 0, \vec{B}(\theta, \phi), S = 2$

By posing $\vec{B} = B(\sin \theta \cos \phi, \sin \theta \sin \phi, \cos \theta)$, by developing the scalar product and by using the ladder operators $\sigma_{\pm} = \sigma_x \pm i\sigma_y$, the SH becomes in terms of Pauli matrices:

$$H = D(\sigma_z^2 - 2) + g\mu_B B \cos \theta \sigma_z + \frac{g\mu_B B}{2} (\exp(-i\phi)\sigma_+ + \exp(i\phi)\sigma_-) \sin \theta \quad (5.10)$$

The corresponding matrix in the $|2, M_S = -2 \rightarrow 2\rangle$ is:

$$\begin{pmatrix} 2D - 2g\mu_B B \cos(\theta) & g\mu_B B \sin(\theta) \exp(i\phi) & 0 & 0 & 0 \\ g\mu_B B \sin(\theta) \exp(-i\phi) & -D - g\mu_B B \cos(\theta) & \frac{\sqrt{6}}{2} g\mu_B B \sin(\theta) \exp(i\phi) & 0 & 0 \\ 0 & \frac{\sqrt{6}}{2} g\mu_B B \sin(\theta) \exp(-i\phi) & -2D & -D + g\mu_B B \cos(\theta) & g\mu_B B \sin(\theta) \exp(i\phi) \\ 0 & 0 & \frac{\sqrt{6}}{2} g\mu_B B \sin(\theta) \exp(-i\phi) & -D - g\mu_B B \cos(\theta) & g\mu_B B \sin(\theta) \exp(i\phi) \\ 0 & 0 & 0 & g\mu_B B \sin(\theta) \exp(-i\phi) & 2D + 2g\mu_B B \cos(\theta) \end{pmatrix}$$

This is the developed form of the matrix and I have not found a way to solve it with an analytical expression. However, it is possible to get an exact expression for the simplest case which is the one where the magnetic field is along the z magnetic axis. The effect of E is to add off-diagonal terms to the preceding matrix and this mixes the states $M_{S'} = M_S \pm 2$ with conditions such that $\sigma_+ |S, M_S = +S\rangle = 0$ and $\sigma_- |S, M_S = -S\rangle = 0$.

5.2.5.2 $E = 0, \vec{B} \parallel (\mathbf{OZ}), S = 2$

The SH becomes:

$$H = D(\sigma_z^2 - 2) + g\mu_B B_z \cdot \sigma_z \quad (5.11)$$

In this case, the diagonalization of 5.11 is quite simple with the eigenvalues which are $E_i = (2D - 2g\mu_B B_z; -D - g\mu_B B_z; -2D; -D + g\mu_B B_z; 2D + 2g\mu_B B_z)$. The calculation of the partition function gives:

$$Z = \exp\left(\frac{2D}{k_B T}\right) + 2 \exp\left(\frac{D}{k_B T}\right) \cosh\left(\frac{g\mu_B B_z}{k_B T}\right) + 2 \exp\left(\frac{-2D}{k_B T}\right) \cosh\left(\frac{2g\mu_B B_z}{k_B T}\right) \quad (5.12)$$

After calculating the free energy, the magnetization is :

$$M = \frac{2g \exp\left(\frac{D}{k_B T}\right) \sinh\left(\frac{g\mu_B B_z}{k_B T}\right) + 4g \exp\left(\frac{-2D}{k_B T}\right) \sinh\left(\frac{2g\mu_B B_z}{k_B T}\right)}{\exp\left(\frac{2D}{k_B T}\right) + 2 \exp\left(\frac{D}{k_B T}\right) \cosh\left(\frac{g\mu_B B_z}{k_B T}\right) + 2 \exp\left(\frac{-2D}{k_B T}\right) \cosh\left(\frac{2g\mu_B B_z}{k_B T}\right)} \quad (5.13)$$

5.2.5.3 $E = \mathbf{0}$, $\vec{B} \parallel (\text{OZ})$, S is integer

Equation 5.10 becomes simply:

$$H = D(\sigma_z^2 - \frac{S(S+1)}{3}) + g\mu_B B_z \cdot \sigma_z \quad (5.14)$$

This Hamiltonian is diagonal in the $|S; M_S\rangle$ basis and thus the eigenvalues are:

$$E_{M_S} = D(M_S^2 - \frac{S(S+1)}{3}) + g\mu_B B_z \cdot M_S \quad (5.15)$$

The partition function is (after some calculation):

$$Z(M_S) = \exp(\frac{DS(S+1)}{3k_B T}) \left\{ 1 + 2 \sum_{M_S=1}^{M_S=S} \exp(-\frac{DM_S^2}{k_B T}) \cosh(\frac{g\mu_B B M_S}{k_B T}) \right\} \quad (5.16)$$

And the magnetization is:

$$M = \frac{2g \sum_{M_S=1}^{M_S=S} M_S \exp(-\frac{DM_S^2}{k_B T}) \sinh(\frac{g\mu_B B M_S}{k_B T})}{1 + 2 \sum_{M_S=1}^{M_S=S} \exp(-\frac{DM_S^2}{k_B T}) \cosh(\frac{g\mu_B B M_S}{k_B T})} \quad (5.17)$$

The equation 5.13 could be found with the equation 5.17 simply with $S = 2$. Figure 5.4 shows that the agreement between the analytical formula and the *PHI* simulations is excellent. Figure 5.4-a is a curve without magnetic anisotropy and the Brillouin function is well found. Concerning figure 5.4-b, I tried to see the high and low temperature limits. For D very small compared to $k_B T$ ($D = 1 \text{ cm}^{-1}$, $T = 1000 \text{ K}$, $g = 2$), we need a huge magnetic field for the Zeeman energy to saturate the iron magnetization. In the case where D is comparable to $k_B T$ ($D = 11 \text{ cm}^{-1}$, $T = 50 \text{ K}$, $g = 2$), we need a magnetic field around 150 T (still huge) to be able to saturate the magnetisation of the compound. In the last case, where D is much larger than $k_B T$ ($D = 50 \text{ cm}^{-1}$, $T = 1 \text{ K}$, $g = 2$), we see a phenomenon called the quantum jump of the magnetization [317]. In figure 5.4-c the calculation of the energy levels of M_S as a function of the magnetic field is presented. At $B = 0 \text{ T}$, the levels are separated by the ZFS. As the field increases, the energy of the levels is modified until a certain field value is reached, which is called the level crossing field. The change of magnetization from 0 to $2\mu_B$ is due to the crossing of the levels $M_S = 0$ and $M_S = \pm 1$ and then the jump to $4\mu_B$ is due to the crossing of the levels $M_S = \pm 1$ and $M_S = \pm 2$.

5.2.5.4 $E = \mathbf{0}$, $\vec{B} \parallel (\text{OZ})$, S is half-integer

The calculation of the magnetization for a half-integer spin is a bit different. First, we need to change the indexing of the sum on M_S (also half-integer), to an indexing on k (integer). The general expression for a half-integer spin S is such that for any $k \in \mathbb{N}$: $S = k + \frac{1}{2}$. The values of $M_S \in [-(k + \frac{1}{2}); -(k + \frac{1}{2}) + 1; \dots; (k + \frac{1}{2}) - 1; (k + \frac{1}{2})]$. We have then for the eigenvalues:

$$\forall k \in \mathbb{N} \Gamma E_{M_S}(k) = D(M_S^2 - \frac{(k + \frac{1}{2})(k + \frac{3}{2})}{3}) + g\mu_B B_z M_S \quad (5.18)$$

The trick to calculate the partition function is to consider the fact that there is an even number of terms in the sum, then there is an even (resp. odd) number of spin projections for a half-integer (resp. integer) spin, we arrive to the following equation for the partition function:

$$Z(k) = 2 \exp\left(\frac{D(k + \frac{1}{2})(k + \frac{3}{2})}{3k_B T}\right) \sum_{n=0}^{n=k} \exp\left(-\frac{D((k + \frac{1}{2}) - n)^2}{k_B T}\right) \cosh\left(\frac{g\mu_B B_z(k + \frac{1}{2}) - n}{k_B T}\right) \quad (5.19)$$

And finally, we get:

$$M(k) = g \frac{\sum_{n=0}^{n=k} (k + \frac{1}{2} - n) \exp\left(-\frac{D((k + \frac{1}{2}) - n)^2}{k_B T}\right) \sinh\left(\frac{g\mu_B B_z(k + \frac{1}{2}) - n}{k_B T}\right)}{\sum_{n=0}^{n=k} \exp\left(-\frac{D((k + \frac{1}{2}) - n)^2}{k_B T}\right) \cosh\left(\frac{g\mu_B B_z(k + \frac{1}{2}) - n}{k_B T}\right)} \quad (5.20)$$

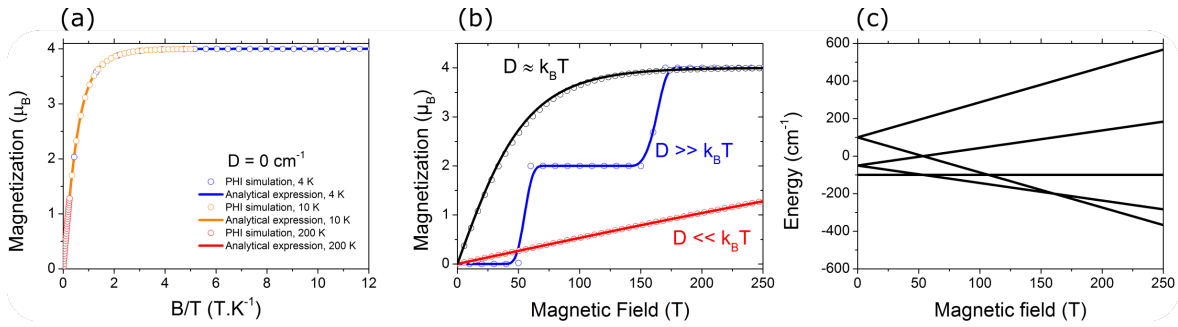


Figure 5.4: (a) $M(B/T)$ for $S = 2$ and $D = 0$ at three different temperatures. (open circles PHI; (full lines) from equation 5.17. (b) $M(B)$. (black) $D = 11 \text{ cm}^{-1}$, $T = 50 \text{ K}$, $g = 2$; (blue) $D = 50 \text{ cm}^{-1}$, $T = 1 \text{ K}$, $g = 2$; (red) $D = 1 \text{ cm}^{-1}$, $T = 1000 \text{ K}$, $g = 2$. (c) Zeeman energy diagram obtained by PHI.

5.3 Magnetic properties of a powder of Fe-Phen

At this point, it is useful to recall that the Fe-Phen molecule (HS at any temperature) has been synthesized [229] as a reference for the Fe-Pyrz [227, 228] molecule (LS at low temperature in its bulk form) whose magnetic anisotropy can be investigated at low temperatures. The measurements of the magnetic properties of a powder of Fe-Phen were measured using SQUID (Superconducting Quantum Interferometer Device) in the 2–250 K temperature range for $\chi T(T)$ and the 0–4.5 T magnetic field range. The measurement is made by measuring the leakage field of the material which is then converted via calibration curves into magnetization measurement. Figure 5.5-a shows the thermal variation of the $\chi T(T)$ product between 2 and 250 K and has the expected behavior for an $S = 2$ state. Upon cooling from 250 K to 60 K, $\chi T(T)$ is constant ($3.28 \text{ cm}^3 \text{ mol}^{-1} \text{ K}$) as expected from the Curie Law of a paramagnetic compound. Below 60 K, $\chi T(T)$ is not constant and then it decreases to $0.9 \text{ cm}^3 \text{ mol}^{-1} \text{ K}$ at $T = 2 \text{ K}$. The magnetization as a function of the applied magnetic field was measured at $T = 2, 4$ and 6 K . As visible in figure 5.5-b, the $M = f(B/T)$ curves shows

a non-negligible ZFS. Now we want to extract the D and E parameters, respectively by fitting $\chi T(T) = f(T)$ and $M = f(B/T)$ curves using the *PHI* package. It gives the following parameters: $g_{Fe-Phen} = 2.10$, $D_{Fe-Phen} = 11.4 \text{ cm}^{-1}$ and $|E_{Fe-Phen}| = 1.2 \text{ cm}^{-1}$ (with the ratio $|\frac{E_{Fe-Phen}}{D_{Fe-Phen}}| = 0.1$). No reasonable fit could be obtained with a negative D value. These values of the ZFS parameters lead to the low-lying energy spectrum depicted in the insert of figure 5.5-a with the $M_S = 0$ lying lower which corresponds to a situation with a hard axis of magnetization ($D > 0$). The expression for the energy levels of the M_S sub-levels for $S = 2$ are:

$$\begin{aligned} E_0 &= -2\sqrt{D^2 + 3E^2} \\ E_{-1} &= -D - 3E \\ E_{+1} &= -D + 3E \\ E_{-2} &= 2D \\ E_{+2} &= 2\sqrt{D^2 + 3E^2} \end{aligned} \quad (5.21)$$

According to the previous equations and the inset of figure 5.5, the anisotropy barrier is about $4D$ (DM_S^2) i.e. 46.4 cm^{-1} which corresponds to a temperature of 66.7 K consistent with the change of behavior in $\chi T(T)$.

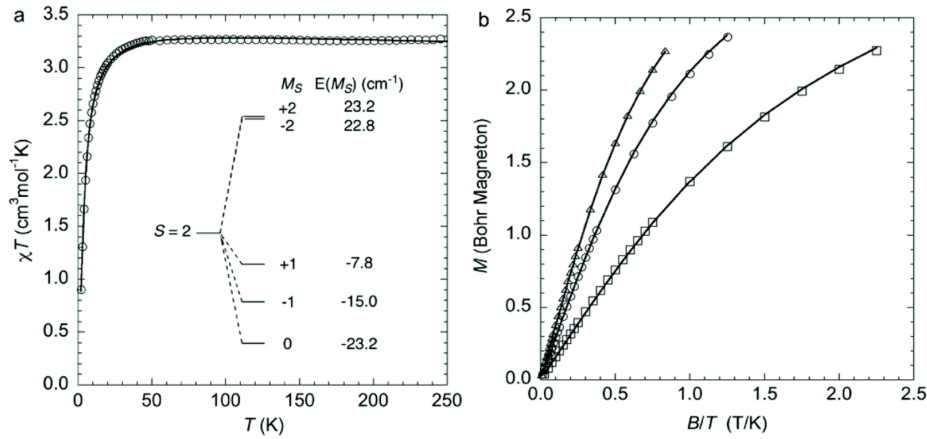


Figure 5.5: (a) Thermal variation of $\chi T(T)$. (inset): Energy spectrum of the M_S sub-levels due to ZFS of $S = 2$. (b) $M(B/T)$ at $T = 2 \text{ K}$ (square), 4 K (circle) and 6 K (triangle). The continuous lines correspond to the best fit using the *PHI* software.

5.4 XAS and XMCD measurements of an ultrathin layer of Fe-Pyrz on Cu(111)

5.4.1 XAS, XMCD and magnetization measurement on Fe-Pyrz

In this section, we will discuss the behavior of a sample of $0.6 \pm 0.15 \text{ ML}$ of Fe-Pyrz on Cu(111). The sensitivity of the SQUID does not allow measuring the magnetization of a monolayer of molecules. The investigations of the magnetic properties were therefore carried out using XAS and XMCD. The XAS data at 1.7 K , 4.2 K and 10 K show the presence of a mixed HS/LS state. Since only HS molecules participate in the magnetization, the sample

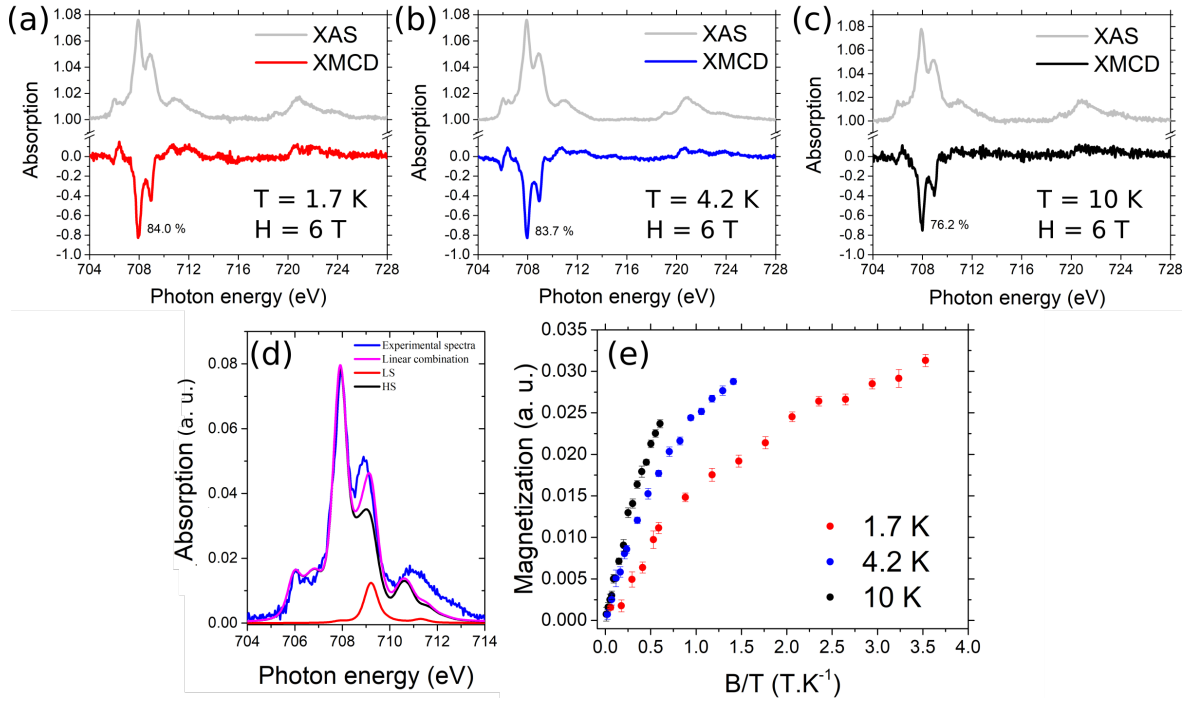


Figure 5.6: Normalized XAS (grey) and XMCD signals at L_3 edge of Fe^{II} of 0.6 ± 0.15 ML of Fe-Pyrz on Cu(111). (a) 1.7 K; (b) 4.2 K. (c) 10 K. A linear background has been subtracted for all the spectra and the signal is normalized to the background value at 707.9 eV. (d) XAS spectrum of L_3 edge of Fe^{II} with deconvolution after 2 hours irradiation with X-rays and deconvolution corresponding to 90% of HS proportion. (e) Variation of the maximum intensity of the XMCD spectrum at the L_3 edge of Fe^{II} as a function of $\frac{B}{T}$ (raw data).

was irradiated with X-rays that allows, due to the SOXIESST effect, a LS to HS transformation [144, 288, 325] and after two hours of illumination, the sample reaches a steady state with 90% fraction of the HS state (with an initial HS proportion of 75.0 ± 0.7 %) as shown in figures 5.6-a/b/c. A linear fit of the experimental XAS data at 1.7 K is displayed in figure 5.6-d. By using left σ^- and σ^+ circularly polarized light and a high magnetic field (6.0 T), we can measure the corresponding XMCD spectrum (figures 5.6-a/b/c) that gives direct information on the magnetic properties of the molecular layer. The XMCD spectra have been normalized by the corresponding XAS ($\frac{\sigma^+ + \sigma^-}{2}$) jump at the L_3 edge and to the HS proportion. The signal can therefore be read as the percentage of the maximum XAS signal. We can also measure the maximum intensity of this spectrum, at 707.9 eV, as a function of the applied magnetic field. We therefore obtain curves (in arbitrary units) directly proportional to the magnetization. Figure 5.6-e displays for 1.7 K, 4.2 K and 10 K, the averaged measurements over two full magnetic cycles (from -6 T to +6 T and from +6 T to -6 T), where the error bars correspond to the standard deviations of the measurements. In order to better emphasize the difference with a Brillouin paramagnetic behavior, we have represented this signal as a function of the B/T ratio, for which the three sets of data should collapse into the same curve in the absence of magnetic anisotropy in the molecule. To obtain quantitative values on the axial anisotropy ($D_{\text{Fe-Pyrz}}$), we have fitted these data by using the *PHI* software, in a SH framework. I will detail, in the next subsections, the

other important parameters for the fitting of these magnetization curves, namely, the effective g -factor ($g_{Fe-Pyrz}$), the normalization factor (N_f) which normalizes the variation of XMCD signal in arbitrary units to μ_B units and the angle between the magnetic field and the principal anisotropy axis of the complex (θ).

5.4.1.1 The effective g -factor

By XMCD sum rules [246, 255–257], we can extract the effective g -factor. Before that, two remarks must be made. Firstly, the calculation of sum rules implies the knowledge of the number of holes in the ground state. It should be equal to 6 in the case of an isolated Fe^{II} ion. However, the chemical bonding creates an electronic delocalization which makes the number of holes ≤ 6 or ≥ 6 depending on the nature of the ligand (donor or acceptor). Only ORCA [291] or charge transfer multiplets calculation can give this number. Secondly, and in general, the orbital sum rule described in equation 2.14a works very well (except for the error on the hole number). According to the publication of Piamonteze et al. [326] for Fe^{II} , the spin sum rule gives an error of at least 10%. These errors can come from a small energy separation of the $L_{3,2}$ edges, intermixing between the $L_{3,2}$ edges, the hole number and $\langle \hat{T}_z \rangle$. This is why, in order to extract the correction to the Lande factor of the free electron, the ratio of the equations (2.14a/2.14b) will be used. Thus, we get rid of the number of holes, the r integral and the dipolar term $\langle \hat{T}_z \rangle$ and thus g depends only on p and q integrals.

In figure 5.7 shows the XMCD signal for the three different temperatures with the integrals shown in dotted. We then extracted the values of p and q and applied the sum rules, we find by averaging the different g -values obtained for the difference XMCD spectra that

$g_{eff} = (2 + \frac{\langle \hat{L}_z \rangle}{\langle \hat{S}_z \rangle}) = 2.2 \pm 0.2$. This value is very close to what our collaborators calculated theoretically (see next sections).

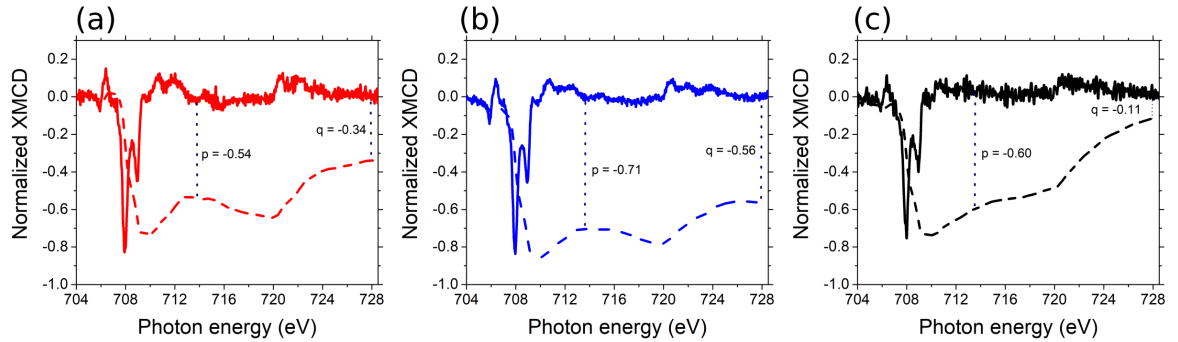


Figure 5.7: Normalized XMCD (in full lines) signal at L_3 edge of Fe^{II} at three different temperatures. The integral is represented in dashed lines. The p and q values (vertical points) taken at 713.6 eV and 727.8 eV respectively. (a) 1.7 K; (b) 4.2 K; (c) 10 K.

5.4.1.2 The normalization factor

As the XMCD signal, in arbitrary units, is only proportional to magnetization, we must take into account a new parameter that I call **normalization factor** or N_f . To find the best N_f

value, a systematic fitting of our data for several N_f values has been made and for each fit the χ^2 -residual is determined. As shown in figure 5.8-b, the minimum of χ^2 is obtained for N_f equals to 105. By multiplying the XMCD values by 105, we obtain the experimental points to adjust by PHI (scatters in figures 5.8-c/d) directly in μ_B units.

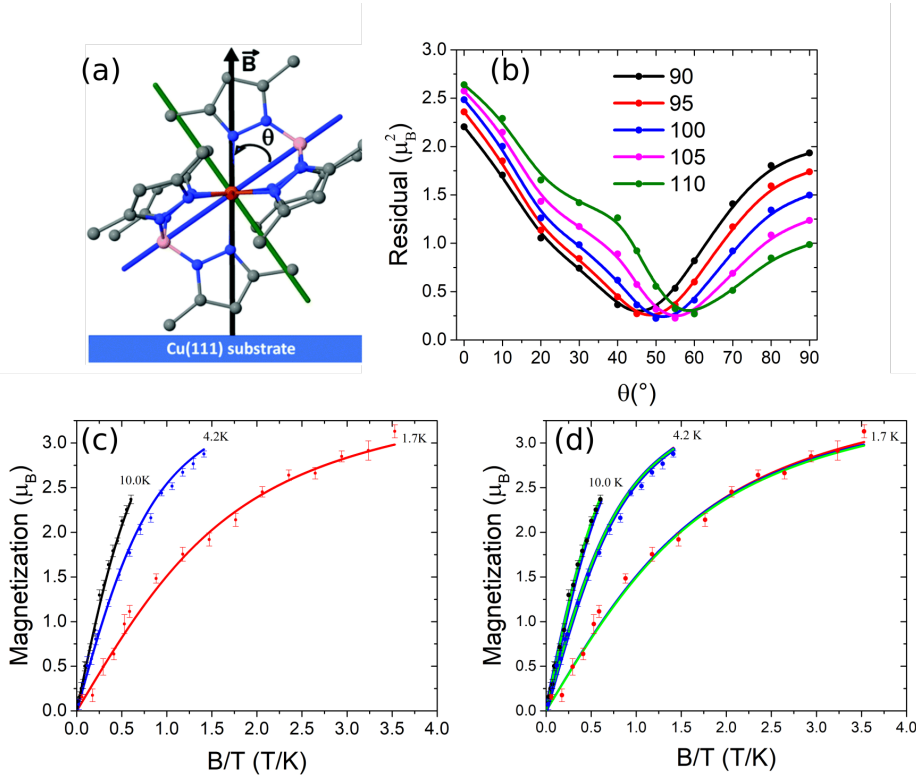


Figure 5.8: (a) $[D]$ tensor axes for Fe-Pyrz (x (red), y (green) and z (blue)); \vec{B} is shown parallel to the normal to the substrate, making an angle θ of 50° with the z -axis (blue) as found from the fit of the magnetic data of Fe-Pyrz on Cu(111). The drawing gives, therefore, the orientation of the molecule on Cu(111). (b) χ^2 as a function of θ from 0° to 90° for different N_f values. (c) Data points represent the XMCD signal at 707.9 eV as a function of B/T . Red at 1.7 K, blue at 4.2 K and black dots at 10.0 K. The full lines represent the best fit curves for $g_{Fe-Pyrz}$ fixed to 2.2, $D_{Fe-Pyrz} = 7.6 \pm 1 \text{ cm}^{-1}$ and $\theta = 50 \pm 10^\circ$. (d) Simulated magnetization data for Fe-Pyrz on Cu(111) with the following sets of $(g_{Fe-Pyrz}, D_{Fe-Pyrz}, \theta) = (2.12, 7.5 \text{ cm}^{-1}, 50^\circ), (2.04, 7.9 \text{ cm}^{-1}, 55^\circ), (2.00, 8.6 \text{ cm}^{-1}, 60^\circ)$.

5.4.1.3 The angle between the magnetic field and the principal anisotropy axis

Since our molecules self-organize on the surface, a very important point is the orientation of the axis of magnetic anisotropy (B-Fe-B, axis of symmetry C_3) with respect to the normal to the surface (θ) (see figure 5.8-a). So, after determining the normalization factor and the effective g -factor, I tried to fit my data with several θ and see for which ones the χ^2 is minimized. I have found that the χ^2 for angles between 40 and 60° are very close, with a minimum at 50° . The full lines in figure 5.8-c shows the best fit over the three temperatures data, giving $\theta = 50 \pm 10^\circ$ and $D_{Fe-Pyrz} = 7.6 \pm 1 \text{ cm}^{-1}$. The sensitivity of the different parameters was checked by performing the calculations for different values of g , D and θ , as shown in figure 5.8-d. The values used for the calculation of the magnetization curves in

the last figure are in the error bar, as depicted in the caption of figure 5.8-d. Moreover, the angle θ , in this study, can be compared with the reported value obtained from a structural study, done by reference [226] of the same molecule deposited on Au(111). In the latter case, an angle close to 70° (20° with the substrate) was found, but both the two-dimensional lattice and the STM images on Au(111) (see chapter 4) were different from those measured on Cu(111). Only a grazing incidence X-ray diffraction study on this system could confirm in the future this particular orientation of the molecules with respect to the substrate.

5.5 *Ab initio* calculations

Our collaborators (*M. Atanasov*, *T. Mallah* and *F. Neese*) performed theoretical calculations following the procedure explained in these references [291, 327–333]. The goal was to compare the magnitude and the nature of the magnetic anisotropy of the two complexes and to check whether Fe-Phen can be considered as a reasonable reference for Fe-Pyrz. Here, I will discuss the main results of the calculations. For more details about the calculations, please refer to these references: [231, 291, 329, 330].

5.5.1 Is Fe-Phen a good reference for Fe-Pyrz ?

The calculations give, for the two compounds, almost the same value for the axial ZFS parameter and a slightly different value for the rhombic one: $D_{Fe-Pyrz} = 8.9 \text{ cm}^{-1}$, $E_{Fe-Pyrz} = 0.62 \text{ cm}^{-1}$, $\left| \frac{E_{Fe-Pyrz}}{D_{Fe-Pyrz}} \right| = 0.07$ and $D_{Fe-Phen} = 10.0 \text{ cm}^{-1}$, $E_{Fe-Phen} = 1.1 \text{ cm}^{-1}$, $\left| \frac{E_{Fe-Phen}}{D_{Fe-Phen}} \right| = 0.11$. The E/D ratio is an important quantity because it fixes the energy separation between the M_S sub-levels. The principal values of the g -matrix were found to be almost identical for the two complexes ($g_{Fe-Pyrz,x} = 2.00$, $g_{Fe-Pyrz,y} = 2.10$, $g_{Fe-Pyrz,z} = 2.12$ and $g_{Fe-Phen,x} = 1.99$, $g_{Fe-Phen,y} = 2.12$, $g_{Fe-Phen,z} = 2.17$), close to the average values found for Fe-Phen from magnetization data. The calculations reproduce well the ZFS parameters obtained from the fit of the experimental magnetic data of Fe-Phen. They are suitable to account for the value of the axial ZFS parameter of Fe-Pyrz in its HS state and can, therefore, be compared with the experimental value for the molecules assembled on Cu(111). The main result is that the magnetic anisotropy of molecules of Fe-Pyrz is almost not altered, i.e. $7.6 \pm 1 \text{ cm}^{-1}$ for the molecule on Cu(111) and 8.9 cm^{-1} for the calculation in bulk, leading to the preliminary conclusion that **the molecules do not sustain large structural deformation even when adsorbed on a metallic substrate**. However, in order to gain a deeper insight into the effect of structural deformation on the magnetic anisotropy of Fe-Phen, one needs to determine which structural parameters affect most magnetic anisotropy, which can be done by analyzing the results of the *ab initio* calculations.

5.5.2 The magnetic axis frame of Fe-Pyrz and Fe-Phen

Figure 5.9-a is a top view of the molecules in the plane perpendicular to the C_3 axis (phenyl and dimethyl groups were erased for clarity). The first result concerns the orientation of

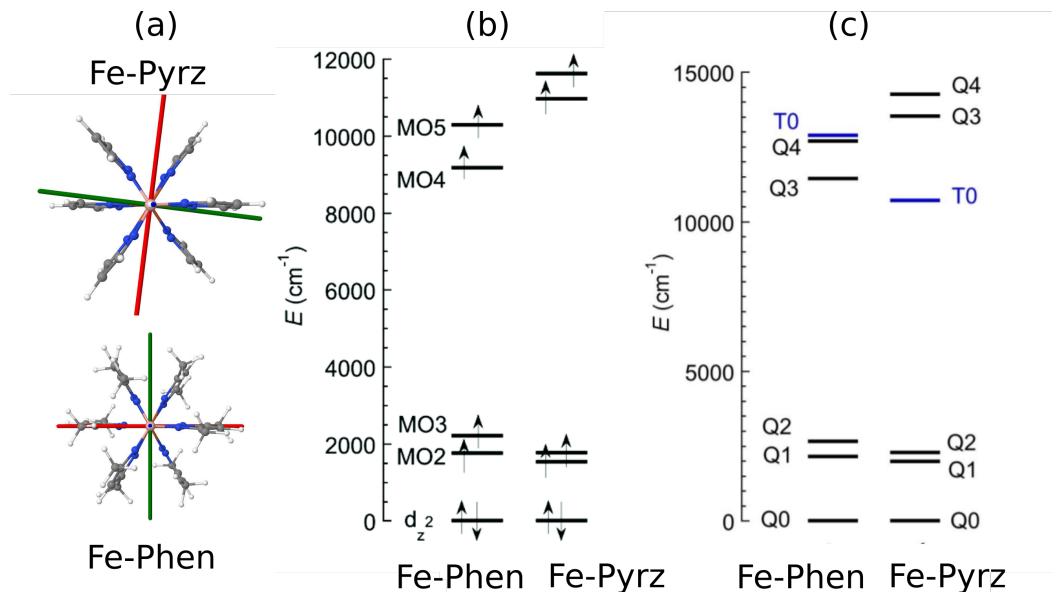


Figure 5.9: (a) $[D]$ view along the C_3 of the $[D]$ tensor axes for Fe-Pyrz and Fe-Phen (x (red), y (green) and z (blue)). (b) Energy diagram of the one electron molecular orbital for Fe-Phen and Fe-Pyrz obtained from *ab initio* ligand field theory (AILFT) calculations by ORCA. The composition of the MOs is given in table 5.1. (c) NEVPT2 energy of the electronic states before SOC for Fe-Phen and Fe-Pyrz.

the ZFS $[D]$ tensor axes with respect to the molecular frame. The calculations show that the $[D]$ tensor axes are collinear for the two compounds. The principal axis (z , blue axis in figure 5.8-a) is found along the pseudo three-fold axis direction B–Fe–B of the two complexes, and the y (green) and x (red) axes deviate by less than 2° . Indeed, the location of the x axis in Fe-Pyrz is situated between two pyrazoles groups where for Fe-Phen, the y direction is along the pyrazoles groups. Whereas the location of the hard magnetization axis for Fe-Phen allows proposing an orientation of the molecules on Cu(111) with the pseudo three-fold axis making an angle of $50 \pm 10^\circ$ with the normal to the plane ($40 \pm 10^\circ$ with the substrate).

5.5.3 Role of the torsion angle

The slight differences in the structural parameters of the coordination sphere of Fe-Pyrz and Fe-Phen, namely, the Fe–N bond distances and $\widehat{\text{NFeN}}$ angles, barely affect the axial ZFS parameter D , and the slight change of the rhombic parameter is not significant due to the uncertainties in its calculation. The orientation of the principal anisotropy axis and its hard nature are the same for the two compounds. However, we will show that the relevant structural to rationalize the positive D value is the torsion $\widehat{\text{BFeNN}}$ angles (Ψ) between the pseudo three-fold symmetry axis and the five-membered pyrazole rings of the tridentate ligand. Indeed, this angle (also called dihedral angle) is the angle between two planes (B–Fe–N) and (Fe–N–N) such that the first nitrogen belongs to the coordination sphere and is directly connected to Fe and the second nitrogen (connected to the first one) belongs to pyrazole and is itself connected to bohr (see figure 5.10). In a non-distorted case, the two planes should be in the same plane and the torsion angle is zero. For Fe-Pyrz and Fe-Phen, these angles hardly deviate from zero (from 1.65° to 5.69° , see figure 5.10-b) because they

are imposed by the tridentate $(\text{Pz})_3\text{BH}$ capping ligands; they are almost the same for the two complexes. This can be confirmed by examining their molecular orbital (MO) energy diagrams as shown in figure 5.9-b and also electronic structures in figure 5.9-c obtained from *ab initio* calculations.

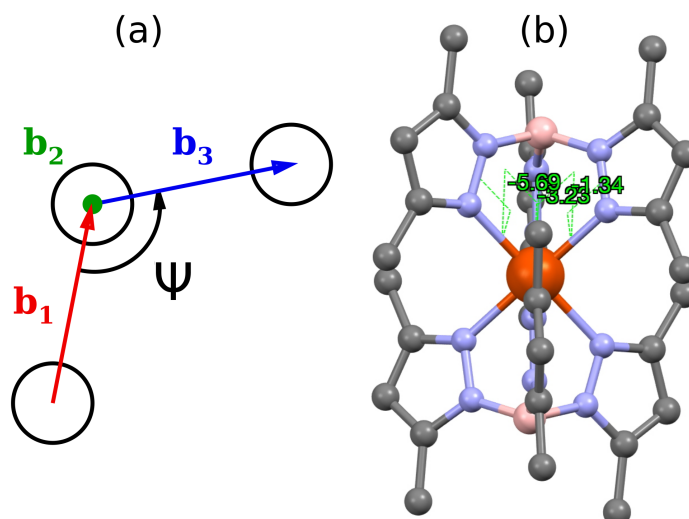


Figure 5.10: (a) Dihedral angle defined by three consecutive vectors (shown in red, green, and blue) connecting four atoms. From this perspective, the second vector (in green) leaves the page. (b) The Ψ angles for Fe-Pyrz.

5.5.3.1 Molecular orbitals energy diagram

For Fe-Pyrz and Fe-Phen, the orbital energy diagrams follow the expected scheme for a trigonal symmetry (D_{3d}) where the d orbitals transform as the irreducible representation $A_1(z^2)$, $e(xz, yz)$ and $e(xy, x^2 - y^2)$. As schematised in figure 5.9-b, we find that the lowest MO is a pure d_{z^2} orbital, then a set of two nearly degenerate MOs (MO2 and MO3) very close in energy at around 2000 cm^{-1} and then another set of two orbitals (MO4 and MO5) with close energies at around 11000 cm^{-1} . The composition of the different MOs is given in table 5.1. The splitting within the two sets (MO2, MO3) and (MO4, MO5) reflects the deviation from the trigonal symmetry. The d_{z^2} orbital is almost non-bonding. Indeed, it has zero overlap with the σ -like nitrogen atom orbitals which point almost exactly in its nodal cone (Figure 5.11-a), the $\widehat{\text{NFeN}}$ angles being very close to 54.7° (magic angle for the octahedron). In addition, the π -like orbitals of the N atoms are almost orthogonal to d_{z^2} because the torsion angles are very close to 0° also leading to an almost zero overlap where a strict orthogonality is obtained for Ψ equal to 0° as depicted in figure 5.11-b.

MOs	Composition of MOs of Fe-Pyrz	Composition of MOs of Fe-Phen
MO1	d_{z^2}	d_{z^2}
MO2	$0.08d_{xy}+0.59d_{yz}-0.80d_{x^2-y^2}$	$-0.73d_{xy}+0.68d_{yz}-0.05d_{xz}-$ $0.06d_{x^2-y^2}$
MO3	$-0.84d_{xy}-0.54d_{xz}+0.08d_{x^2-y^2}$	$-0.06d_{xy}+0.04d_{yz}+0.61d_{xz}+0.79d_{x^2-y^2}$
MO4	$0.53d_{xy}+0.08d_{yz}-$ $0.83d_{xz}+0.10d_{x^2-y^2}$	$-0.09d_{xy}-0.08d_{yz}+0.78d_{xz}-$ $0.61d_{x^2-y^2}$
MO5	$0.10d_{xy}-0.80d_{yz}-0.08d_{xz}+0.58d_{x^2-y^2}$	$-0.68d_{xy}-0.72d_{yz}-0.1d_{xz}+0.06d_{x^2-y^2}$

Table 5.1: Composition of the one electron AILFT MOs for Fe-Pyrz and Fe-Phen

5.5.3.2 Electronic structure energy diagram

In order to facilitate the following analysis, it is useful to recall the expressions of the d orbitals in terms of the spherical harmonics $Y_l^{m_l}$:

$$\begin{aligned}
d_{z^2} &= Y_2^0 \\
d_{xz} &= \frac{1}{\sqrt{2}}(Y_2^{-1} - Y_2^1) \\
d_{yz} &= \frac{i}{\sqrt{2}}(Y_2^{-1} + Y_2^1) \\
d_{xy} &= \frac{i}{\sqrt{2}}(Y_2^{-2} + Y_2^2) \\
d_{x^2-y^2} &= \frac{1}{\sqrt{2}}(Y_2^{-2} - Y_2^2)
\end{aligned} \quad (5.22)$$

Considering the electronic structure of the two complexes and particularly comparing the composition of the ground ($Q0$) and excited quintet states (table 5.2 and figure 5.9-c), it is possible to rationalize the sign of D for the two complexes. It is worth reminding that, for states with the same spin multiplicity, two determinants are coupled by the SOC if the excitation involves $|\Delta m_l| = 0$ or 1 (and not 2), with a negative contribution to D when $|\Delta m_l| = 0$ (involving the $\hat{L}_z \hat{S}_z$ term) and a positive one when $|\Delta m_l| = \pm 1$ (involving $1/2 (\hat{L}_+ \hat{S}_- + \hat{L}_- \hat{S}_+)$ term). Excitation involving $|\Delta m_l| = 2$ cannot be coupled by the SOC. From table 5.2, we show that the four quintet and the first triplet excited states all contribute positively to D and account almost for the major contributions to the overall D values for the two compounds because this contribution, within the second order perturbation theory, is inversely proportional to the energy separation between the ground and the excited states with which it is coupled by SOC. The wave functions of the ground states for Fe-Pyrz and Fe-Phen are a single determinant in the frame of the magnetic axes and are identical for the two complexes with two electrons with opposite spins in the orbital $|d_{xy}, d_{yz}, d_{xz}, d_{x^2-y^2}|$, in the hole formalism (meaning d_{z^2} in the electron formalism). Therefore, all the (four) quintet excited states are d_{z^2} obtained by excitations from the orbital ($m_l = 0$) to one of the other four ones ($m_l = \pm 1$) with, therefore, d_{z^2} change of the value of $|m_l|$ by 1. As shown from the calculations, the excitations never involve a $|\Delta m_l| = 0$, rationalizing the fact that all the quintet excited states bring only positive contributions to D [334, 335]. For example and if we consider the case of Fe-Pyrz, the first excited quintet state is composed by: $0.64|d_{xy}, d_{yz}, d_{z^2}, d_{xz}|$ and $0.35|d_{xy}, d_{z^2}, d_{xz}, d_{x^2-y^2}|$ meaning an excitation from d_{z^2} to $d_{x^2-y^2}$ and d_{yz} respectively. The first excitation cannot couple the two determinants by SOC ($|\Delta m_l|=2$, cf Y_l^m decomposition in equation 5.22), while the second brings a positive contribution to D ($|\Delta m_l|=1$). Examining the remaining three quintet ex-

cited states leads to the same result. The first excited triplet state ($T1$) has a non-negligible positive contribution to D (around 3 cm^{-1}), the same type of analysis can be made as for the quintet state. To summarize, the two excitations, from $Q0$ to $Q1$ and $Q0$ to $Q2$, lead to a change of ± 1 of the value of the orbital momentum m_l , which corresponds to a positive contribution to D . Finally, the fact that the d_{z^2} orbital has the lowest energy is responsible for the positive D values for Fe-Pyrz and Fe-Phen.

States	Composition of the states of Fe-Pyrz (contribution to D)	Composition of the states of Fe-Phen (contribution to D)
$Q0$	$ d_{xy}, d_{yz}, d_{xz}, d_{x^2-y^2} $	$ d_{xy}, d_{yz}, d_{xz}, d_{x^2-y^2} $
$Q1$	$0.64 d_{xy}, d_{yz}, d_{z^2}, d_{xz} ,$ $0.35 d_{xy}, d_{z^2}, d_{xz}, d_{x^2-y^2} $ (2.51)	$0.52 d_{yz}, d_{z^2}, d_{xz}, d_{x^2-y^2} ,$ $0.47 d_{xy}, d_{z^2}, d_{xz}, d_{x^2-y^2} $ (3.78)
$Q2$	$0.70 d_{yz}, d_{z^2}, d_{xz}, d_{x^2-y^2} ,$ $0.28 d_{xy}, d_{yz}, d_{z^2}, d_{x^2-y^2} $ (1.88)	$0.61 d_{xy}, d_{yz}, d_{z^2}, d_{xz} ,$ $0.39 d_{xy}, d_{yz}, d_{z^2}, d_{x^2-y^2} $ (2.37)
$Q3$	$0.70 d_{xy}, d_{yz}, d_{z^2}, d_{x^2-y^2} ,$ $0.28 d_{yz}, d_{z^2}, d_{xz}, d_{x^2-y^2} $ (0.78)	$0.60 d_{xy}, d_{yz}, d_{z^2}, d_{x^2-y^2} ,$ $0.38 d_{xy}, d_{yz}, d_{z^2}, d_{xz} $ (1.02)
$Q4$	$0.64 d_{xy}, d_{z^2}, d_{x^2-y^2}, d_{xz} ,$ $0.34 d_{xy}, d_{yz}, d_{z^2}, d_{xz} $ (0.73)	$0.52 d_{xy}, d_{z^2}, d_{x^2-y^2}, d_{xz} ,$ $0.47 d_{yz}, d_{z^2}, d_{xz}, d_{x^2-y^2} $ (0.77)

Table 5.2: Composition and contribution (in cm^{-1}) to the axial anisotropy parameter D (between brackets) of the quintet states for Fe-Pyrz and Fe-Phen.

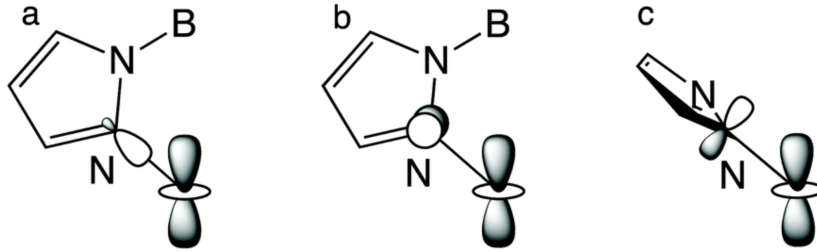


Figure 5.11: Scheme of the potential interaction between the d_{z^2} orbital on one hand and nitrogen atom orbitals coordinated to Fe: (a) with the σ axial orbital for $\Psi = 0^\circ$, (b) with the π -like orbitals for $\Psi = 0^\circ$ and (c) for $\Psi = 90^\circ$, showing in this last case the presence of non-zero overlap making the d_{z^2} orbital antibonding.

5.5.4 How to tune the magnetic anisotropy ?

The small differences in the bond distances and angles cannot much affect the energy of the d_{z^2} orbital with regard to MO2 and MO3 and cannot, therefore, much affect the magnitude of D . Only if the relative energies of d_{z^2} , on one hand, and MO2 and MO3, on the

other hand, are reversed, a negative D value could be obtained. Such a change occurs only if Ψ changes from close to zero to a large value. Indeed, in such a case, the first order orbital angular momentum $m_l = |1|$ in the nearly degenerate ground state (5E) and the fact that the excitation between the ground and the first excited states involve no change in the value of the orbital momentum lead to a negative contribution to D [334, 335]. Such a change in the energy of the d_{z^2} orbital requires an overlap with the π orbital of the nitrogen atoms that may occur if the value of Ψ changes. One can already suggest, at this stage, that a large change of Ψ in the family of complexes to which Fe-Pyrz and Fe-Phen belong is unexpected because the tridentate (Pz)₃BH ligand imposes a rigid geometry around Fe precluding a deviation by more than a few degrees from zero. We examined the Cambridge Crystallographic Data Centre and reference [82] and found that for hexacoordinate complexes with any derivative of the (Pz)₃HB tridentate ligand and different metal ions (Fe^{II}, Co^{II} and Ni^{II}), the Ψ values are never larger than 9°. This supports a rather high degree of rigidity against deformation, leading to the conclusion that the axial anisotropy of the family of [Fe^{II}((Pz)₃BH)₂]-related complexes should not be easily altered by their environment. However, in order to check the proposed model we examined the molecular structure of a Fe^{II} complex [Fe(ptz)₆]²⁺, ptz is propyltetrazole (see figure 5.12-a for a view of the structure) that was shown to have a negative D value (-14.8 cm⁻¹) from electron paramagnetic resonance measurements [336]. If one considers only the first coordination sphere FeN₆ for the three complexes, namely, Fe-N bond distances and \widehat{NFeN} angles, one finds that they are very close. The negative D value for [Fe(ptz)₆]²⁺ cannot, therefore, be justified only on this basis. The examination of the torsion angles of [Fe(ptz)₆]²⁺ (defined here as the angle between the three-fold axis of the molecule and the plane of the tetrazole five-membered ligand) reveals that they are completely different; they are equal to 63.3° for [Fe(ptz)₆]²⁺ (Figure 5.12-a), while between 1.7° and 5.7° for Fe-Pyrz and Fe-Phen. In order to prove that the change in magnetic anisotropy from the hard to easy axis is mainly governed by this torsion angle, we performed *ab initio* calculations on [Fe(ptz)₆]²⁺ that give a negative D value and therefore an easy axis of magnetization for the complex (Figures 5.12-b/c). The MO energy diagram shows that the orbital with a major contribution from d_{z^2} does not have the lowest energy anymore as expected from the onset of an overlap with the nitrogen atom π orbitals due to the change of the torsion angle as depicted in figure 5.12-c. This is responsible for the negative D value in this complex.

5.6 Conclusion

The measurement of the magnetic anisotropy of Fe-Pyrz in its high spin state ($S = 2$) by XMCD when assembled as an organized monolayer on Cu(111) shows the presence of a hard axis of magnetization (positive axial zero-field splitting - ZFS - parameter D). Combining magnetization measurements, on a reference compound, Fe-Phen, and *ab initio* wave function based theoretical calculations, we demonstrate that the magnetic anisotropy of the assembled molecules is not affected when they are present at the substrate/vacuum interface. Comparing our results with those of a reported complex having an almost identical FeN₆ coordination sphere but an easy axis of magnetization (corresponding to a negative D value), we show that the nature of the magnetic anisotropy (easy/hard axis) is governed by the torsion angle (Ψ) defined by the relative orientation of the pyrazole five-membered rings to the pseudo three-fold axis of the molecules. When Ψ is close to zero, D is found to

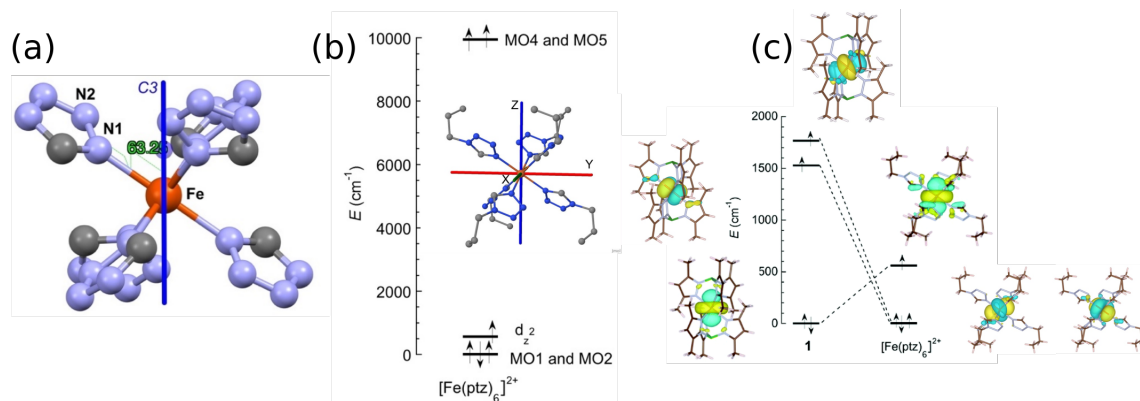


Figure 5.12: (a) View of the crystal structure of $[\text{Fe}(\text{ptz})_6]^{2+}$ showing the torsion angle (Ψ) at 63.25° . (b) Energy diagram of the one electron molecular orbitals for $[\text{Fe}(\text{ptz})_6]^{2+}$ obtained from *ab initio* ligand field theory (AIFLT) calculations by ORCA. The MO1 and MO2 on one hand and the MO4 and MO5 on the other hand are almost degenerate. In the inset of the figure is the orientation of the $[D]$ tensor axes for $[\text{Fe}(\text{ptz})_6]^{2+}$. (c) Relative energies of the three low-lying MOs for Fe-Pyrz and $[\text{Fe}(\text{ptz})_6]^{2+}$, with the sketch of the MOs having a majority contribution from d_{z^2} .

be positive and rationalized by wave function based theoretical calculations, while when this angle is much larger (63° as for $[\text{Fe}(\text{ptz})_6]^{2+}$), D is found to be negative [76, 336]. For Fe-Pyrz and Fe-Phen, because the five membered pyrazole rings of the tridentate ligands $(3,5\text{-(CH}_3)_2\text{Pz)}_3\text{BH}$ coordinated to Fe cannot rotate freely around the Fe–N bond and cannot deviate by more than a few degrees from 0° when the complex is placed in a dissymmetric environment, the axial magnetic anisotropy cannot be highly affected as demonstrated here when the molecules are organized at the metal/vacuum interface. However, as shown by the examination of the structure of a series of complexes belonging to this family, the torsion angle can vary within a very small range (from 0° to 9°), which may slightly affect the magnetic anisotropy. This is the origin of the robust magnetic anisotropy of this family of compounds.

SWITCHING AND MAGNETIC PROPERTIES OF SPIN-CROSSOVER MOLECULES/FERROMAGNETIC INTERFACES

For the use of SCO molecules in multifunctional spintronic devices [16, 17, 337], it is mandatory to study their properties in close contact with a ferromagnetic electrode. However, understanding the properties of on-surface SCO of thin-films remains relatively difficult because of fragmentation of molecules on surfaces, especially on magnetic surfaces which are rather reactive transition metals [147, 175]. Moreover, it is generally accepted in the literature that the spin transport and magnetic properties in hybrid ferromagnet/molecular materials are strongly affected by interactions between both materials. It is therefore important to study the so-called spinterface [17, 18, 180, 338, 339] as it was previously demonstrated for single molecular magnets [177, 319, 340–349] (SMM) or other organic systems [19, 316, 350], on various magnetic substrates. For example, within SMMs, the most studied class of magnetic molecules on magnetic surfaces was that of phthalocyanines namely TbPc₂ [341, 343–345], MnPc [177, 346, 349], CuPc [347], FePc [342, 346, 347, 351]. The coupling can be ferromagnetic (FM) or antiferromagnetic (AFM) and is of the superexchange type and mediated via the organic ligands. For the MnPc system [177], the coupling is strong up to 300 K.

Another interest for the SCO class of molecules is to achieve the so-called *active* molecular spinterface [17–19, 181, 338, 339]. Indeed, the strong hybridization between the SCO molecules and the 3d ferromagnet forms hybrid interface states (HISs) [17, 18, 180, 338, 339, 352]. In principle, the control of magnetic properties of these HISs is possible by changing the spin-state via an external stimulus and this could find direct application in spintronic devices like spin valves and tunnel junctions [27, 350, 353]. However, the strong coupling needed to obtain a HIS seems contradictory with keeping the SCO properties, which requires a priori a rather decoupled molecule. In the literature, the only reference of SCO molecules on a ferromagnetic surface is the Fe(phen)₂(NCS)₂ (phen = 1,10-phenanthroline) on Co bilayer islands on Cu(111) [156, 188, 189]. The investigation of this system was performed using scanning tunneling microscopy (STM) and spin-polarized STM (SP-STM). It was revealed that some of the molecules undergo fragmentation. However, for the intact

molecules in the HS state, the SP-STM demonstrated the presence of spin-polarized density of states close to the Fermi level and density functional theory calculations (DFT) revealed the spin-polarization at the Fermi level to be higher than that of the substrate (84 %). Finally, it was also shown theoretically [189] that irrespectively of the spin-state, the molecule is ferromagnetically coupled to Co atoms via indirect ferromagnetic superexchange pathway across the two NCS groups [156, 188, 189]. The ferromagnetic coupling is calculated to persist even when introducing several Cu spacer-layers [156, 188, 189, 194, 195]. Concerning the switching property, an important conclusion of the theoretical work is that it should be easier to switch between HS and LS on a cobalt surface as compared to a copper one, but without experimental demonstration [189].

In this chapter, using STM, XAS and XMCD, we investigate the magnetic interaction and the switching properties of ultrathin film of paramagnetic spin-crossover compound ($\text{Fe}^{\text{II}}((3,5-(\text{CH}_3)_2\text{Pz})_3\text{BH})_2$ molecules deposited on Co/Cu(111) and also on in-plane and out-of-plane magnetized Co/Au(111). We will also investigate the modification of the switching and magnetic behavior of the molecule/ferromagnetic interface by introducing several decoupling layers, namely copper and gold.

6.1 Fe-Pyrz on ferromagnetic cobalt surface

In this section, by using STM we will study the Fe-Pyrz/Co/Cu(111) interface. Then, by XAS and XMCD, we will study the thermal and light-induced switching behavior as well as the magnetism of Fe-Pyrz molecules on ferromagnetic surfaces, namely, Co/Au(111) with cobalt magnetization in-plane (IP) and also with out-of-plane (OP) magnetization.

6.1.1 STM of Fe-Pyrz on Co/Cu(111)

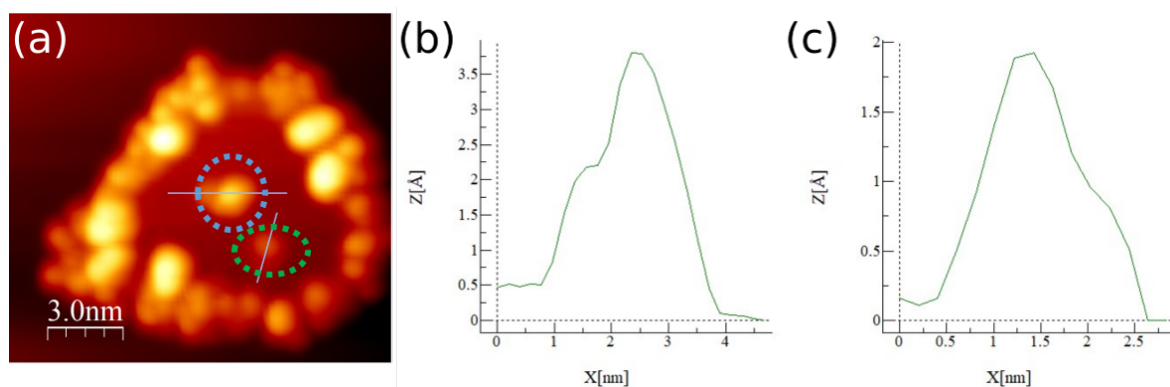


Figure 6.1: (a) STM image ($15 \times 14 \text{ nm}^2$) of Fe-Pyrz molecules on a Co island on Cu(111) at 20 pA and -1.5 V. (b) Height profile for the molecule in blue circle in (a). (c) Height profile for the molecule in green circle in (a).

The preparation of this sample is done as follows: first, a submonolayer deposition of cobalt on copper is realized on the sample at room temperature; then, the molecules are deposited on the sample held at low temperature (4.7 K). This was followed by annealing of

the system at room temperature. The fact that we observe almost all the molecules on cobalt islands after annealing shows that the adsorption energy of Fe-Pyrz is larger on cobalt than on copper. This is probably due to the stronger interactions between the methyl group and Co surface, as compared to copper. Even if the molecule and the nature of the coupling is rather different, one can note that this result is consistent with density functional theory (DFT) calculations done for $\text{Fe(phen)}_2(\text{NCS})_2$ reported by [186, 189]. Finally, as shown in figure 6.1-a, on the Co island, the molecules exhibits different orientations evidenced by the different profiles shown in figure 6.1-b/c. This observation has several important consequences. First, it means that the energy barriers between the different molecular configurations are high, what can prevent a spin switch, which requires a (small) change of configuration. Second, the spinterface is inhomogeneous, with a priori different properties for different molecular configurations.

6.1.2 Sample preparation and determination of cobalt and molecular coverages for Fe-Pyrz/Co/Au(111) system

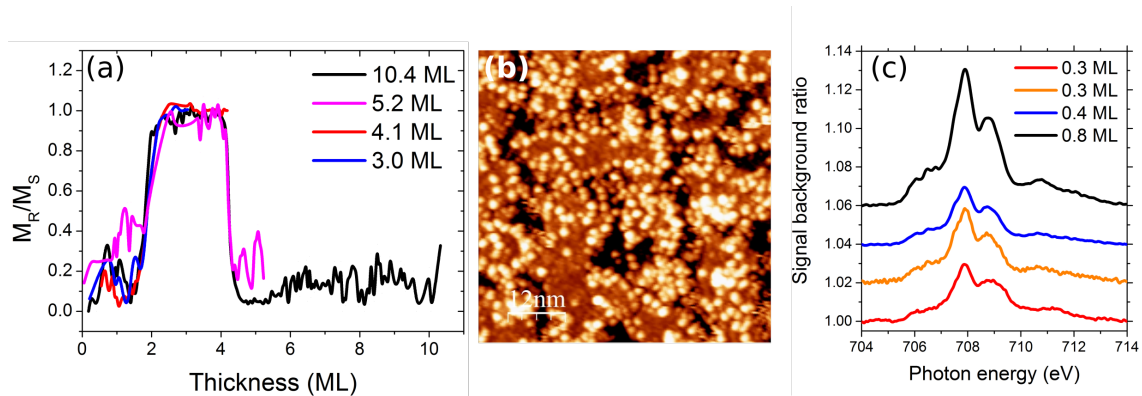


Figure 6.2: (a) The cobalt squareness ($\frac{M_R}{M_S}$) as a function of the layer thickness for the different samples studied in the chapter; (b) STM image for Fe-Pyrz/Co/Au(111); (c) XA spectra for the different coverages on Co/Au(111). Red: 0.3 ± 0.08 ML of Fe-Pyrz on 10.4 ML cobalt thickness (in-plane); Orange: 0.3 ± 0.08 ML of Fe-Pyrz on 4.1 ML cobalt thickness (out-of-plane); Blue: 0.4 ± 0.12 ML of Fe-Pyrz on 3.0 ML cobalt thickness (out-of-plane); Black: 0.8 ± 0.22 ML of Fe-Pyrz on 3.0 ML cobalt thickness (out-of-plane). A linear background has been subtracted for all the spectra and the signal is normalized to the background value at 707.9 eV. The spectra have been shifted for more clarity.

The deposition of cobalt and molecules is explained in chapter 2. The calibration of the cobalt thickness was determined by MOKE as shown in figure 6.2-a (black). We thus have deposited 10.4 ML of cobalt on Au(111) which corresponds to an in-plane (IP) cobalt magnetization. However, the calibration of the molecular coverage is a bit more delicate. Indeed, in order to extract the coverage on the different Co thicknesses, the calibration of the molecular thickness was done by knowing the experimental ratio between the backgrounds of 0.9 ML of Fe-Pyrz on Cu(111) (chapter 3) and Co/Au(111). In the following table is summarized the maximum of the XAS at the peak of the HS (707.9 eV), the background value at the same energy, the edge-jump in absolute and in percentage, the normalized edge-jump with respect to the Cu(111) background at 707.9 eV and at 300 K.

Sample (ML)	Maximum (a.u.)	Background (a. u.)	Edge-jump (a.u.)	Edge-jump (%)	Normalized edge-jump (%)	Coverage (ML)
Co(10.4)	1.491	1.448	0.043	3 %	3.6 %	0.3 ± 0.08
Co(4.1)	1.131	1.085	0.046	4.3 %	3.9 %	0.3 ± 0.08
Co(3.0)	2.049	1.983	0.066	3.3 %	5.5 %	0.4 ± 0.12
Co(3.0)	1.868	1.744	0.125	7.1 %	10.4 %	0.8 ± 0.22

Table 6.1: In the first column is represented the different areas of Co on which Fe-Pyrz has been evaporated and measured by XAS. Remember that on Co(3.0 ML), there are two thicknesses of molecules. The second (resp. third) column represents the maximum (resp. background) intensity of the L_3 -edge of Fe^{II} and the fourth column is the difference in absolute between the two previous ones. The fifth column represents the intensity in percentage of the background of the respective samples. The sixth column is the normalization of column five with respect to Cu(111) background. The seventh column is the molecular coverage. The error bar was determined as the error bar we had on the calibration of 0.5 ± 0.1 ML of Fe-Pyrz on Cu(111) (25 %) multiplied by the ratio of the absolute edge-jumps at the L_3 -edge of the fourth column and on Cu(111).

In the following, I will detail the calculation algorithm for the sample on 10.4 ML of Co, as shown in figure 6.2-c (red). We recall that the edge-jump in arbitrary units is simply calculated as the difference between the maximum and the background value at L_3 -edge, while the edge-jump in percentage is calculated as the ratio of this difference to the background value. By doing this, we find a percentage of 3 % for the L_3 edge-jump. Then, the background value at the same energy of 0.9 ML of Fe-Pyrz/Cu(111) is equal to 1.196. Thus, the normalized edge-jump value in percentage with respect to the Cu(111) background is calculated as follows: $\frac{1.448}{1.196} \times 3\% = 3.6\%$. Thus, since 5.4 % corresponds to 0.5 ± 0.1 ML on Cu(111), we deduce a thickness of around 0.3 ± 0.08 ML. Note that the edge-jumps in percentage of Fe-Pyrz at 707.9 eV (without normalization to the Cu(111) background), are different on the different Co zones but this does not necessarily indicate a difference in molecular coverage. Indeed, this difference is due to different contributions from the Co/Au backgrounds. Nevertheless and as shown in the previous table, the ratio of absolute edge-jumps at 707.9 eV is proportional to the ratio of molecular coverage. Moreover, as shown in figure 6.2-a, we have prepared two other samples with the out-of-plane (OP) cobalt magnetization with 4.1 ML (red) and 3.0 ML (blue) thicknesses. By the same analysis, we calculate the molecular coverages such as: on the first one, 0.3 ± 0.08 ML thickness (orange in figure 6.2-c) of molecules were deposited, while on the second one, we prepared two zones, one with 0.4 ± 0.12 ML and the other with 0.8 ± 0.22 ML as shown in blue and black in figure 6.2-c, respectively.

We notice that the XAS spectrum is appreciably the same (same edge-jump and same multiplet structure) and looks like the usual XAS spectra on Cu(111) (slightly distorted octahedron) which is an indication that the molecules are not decomposed on the different surfaces. Finally, it can be seen from the STM images that the molecules on Co/Au(111) (shown in figures 6.2-b) adopt rather random configurations, in a similar way than on Co islands on Cu(111).

6.1.3 Thermal and light-induced switching properties for Fe-Pyrz/Co/Au(111) interface

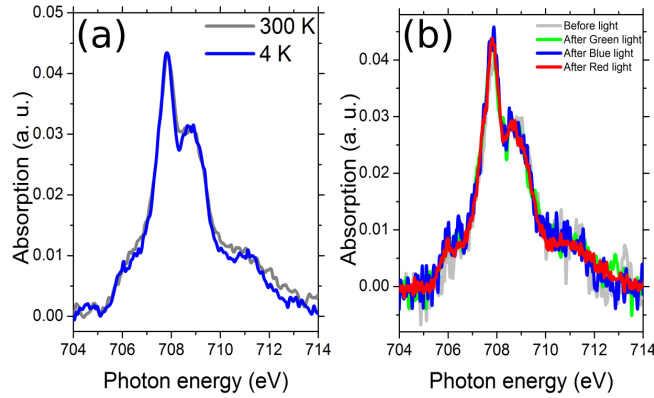


Figure 6.3: XAS at the L_3 edges of Fe^{II} after a linear background subtraction. (a) high and low temperatures. (b) At low temperature with different wavelengths i.e. 405 nm (blue), 532 nm (green) and 640 nm (red). The measurements were done on the Fe-Pyrz(0.3 ML)/Co(10.4 ML)/Au(111) sample.

Figure 6.3-a/b shows the L_3 XA spectra of Fe^{II} on 0.3 ± 0.08 ML of Fe-Pyrz on 10.4 ML of Co/Au(111), for high (grey) and low (blue) temperatures and under light illumination. It can be seen that the HS to LS transition by decreasing the temperature does not occur, even partially. Moreover, at low temperature, there is no wavelength in the visible range that allows the molecules to switch from HS to LS as observed for this molecule in submonolayer on Cu(111) and Au(111) [325]. This spin-state blocking is necessarily due to the fact that the substrate influences the energy barrier between the HS and LS states which is much too large to allow the molecule to switch [185, 189, 211, 214].

6.1.4 XMCD and magnetic hysteresis measurements for Fe-Pyrz/Co/Au(111) interface

After having studied the thermal and light-induced SCO behaviors, we will study the magnetic behavior of these molecules on the different substrates. Figure 6.4-a/b shows XAS (in grey) and XMCD spectra (colored) taken at low temperature (4 K) and high magnetic field for the $L_{2,3}$ edges for 0.3 ± 0.08 ML of Fe-Pyrz on cobalt with in-plane magnetization (resp. out-of-plane) as shown in red (resp. orange). The direction of the magnetic field is parallel to the photon wavevector and perpendicular to the sample surface ($\theta = 0^\circ$). The XMCD curves were normalized compared to the edge-jump of XAS and of the HS proportion. We find that the XMCD percentages are 68.1 % and 72.3 % for the sample with in-plane and out-of-plane cobalt magnetization respectively.

Then, we made full magnetic cycle measurements from -5.5 T to 5.5 T and from -1.2 T to 1.2 T for Fe-Pyrz and cobalt respectively, as shown in figures 6.4-c/d. A word about the processing of these XMCD curves for Iron(II) (and the following ones): indeed, to reduce the noise, we have decided to average the negative and positive fields branches (average of the branches from 5.5 T to 0 T and from 0 T to -5.5 T) of the curves and to display a symmetrized figure. In addition, the raw curves obtained are in arbitrary units, we have

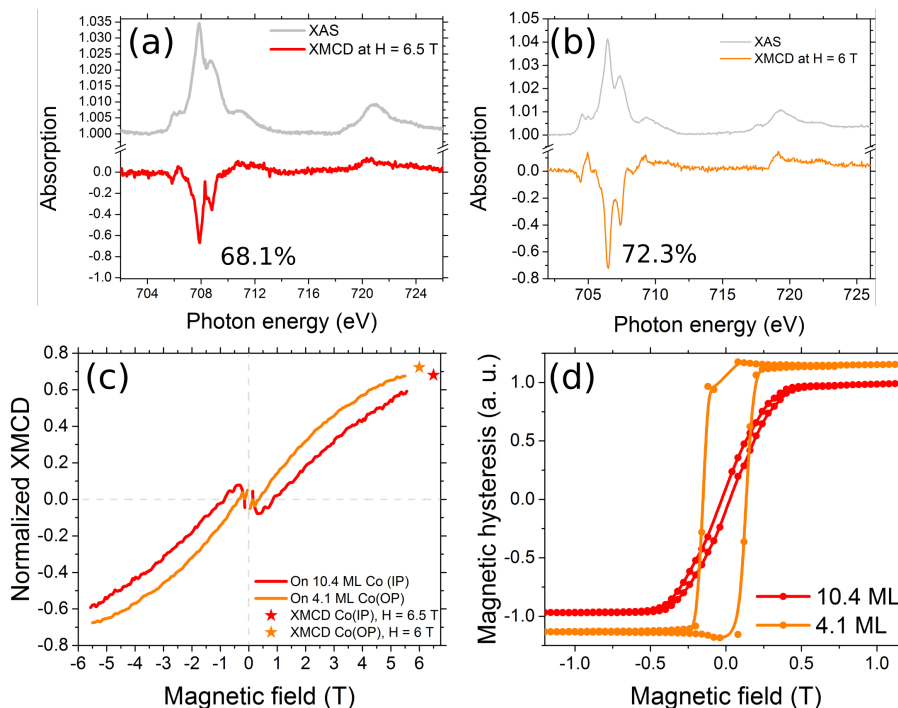


Figure 6.4: XAS (grey) and XMCD (color) for 0.3 ML of Fe-Pyrz at the $L_{2,3}$ edge of Fe^{II} at 4 K on: (a) 10.4 ML Co(IP) at 6.5 T; (b) 4.1 ML Co(OP) at 6 T; (c) XMCD signal from -5.5 T to 5.5 T and normalized with respect to the XMCD percentage at 6.5 T (red) and 6 T (orange) and to the HS fraction (100 %). The stars represent the XMCD percentage shown in (a) and (b); (d) $M(B)$ (in arbitrary units) for 10.4 ML Co(IP) (red) and for 4.1 ML (orange), at the Co L_3 -edge. The magnetic field is normal to the surface ($\theta = 0^\circ$).

normalized them with respect to the absolute XAS edge-jump at 707.9 eV and at high field (6.5 T or 6 T, see star symbol in the figure 6.4-c) and to the percentage of HS molecules for each sample (100 % HS here). Concerning the figure 6.4-c, we observe on Co(IP) (red) that the normalized XMCD signal of Fe-Pyrz is negative below 0.9 T (that we will call the exchange field). Regarding the hysteresis cycles of cobalt (figure 6.4-d) and if we look only at the low magnetic field part below the exchange field, it appears that the sign of XMCD is positive when that of cobalt is negative. Similarly, we can see on the magnetization curve on the Co(OP) (orange), that the sign of XMCD on iron is negative below 0.3 T while it is positive on cobalt. So, we can make the preliminary conclusion: for the first time and by means of XMCD measurement, we have direct evidence of antiferromagnetic (AFM) coupling between molecules and the Co magnetic moments, for a surface-supported SCO molecule and does not depend on the magnetization direction of the cobalt. The dipolar origin of this exchange interaction can be *a priori* excluded. It is more likely, as shown on phthalocyanine systems, that this coupling is of superexchange type [177, 186, 188, 189, 341, 345, 348] and mediated by the pyrazole ligands on Co areas (IP or OP).

Unfortunately, the large noise around zero field in the magnetic hysteresis process on the DEIMOS beamline avoids to conclude on a remnant magnetization at the Fe^{II} L_3 -edge. Therefore, in order to know if we could open a magnetic hysteresis cycle on the molecules for the out-of-plane cobalt magnetization samples (3.0 ML and 4.1 ML), we have measured the remanent magnetization, namely the XMCD at zero field, after submitting the sample

to a magnetic *history* from 1 T to 0 T (resp. -1 T to 0 T), for the L_3 edge of Fe-Pyrz as shown in figures 6.5-a/d (resp. figures 6.5-b/c) and the $L_{2,3}$ edges of cobalt (grey in inset of the figures 6.5-a/b).

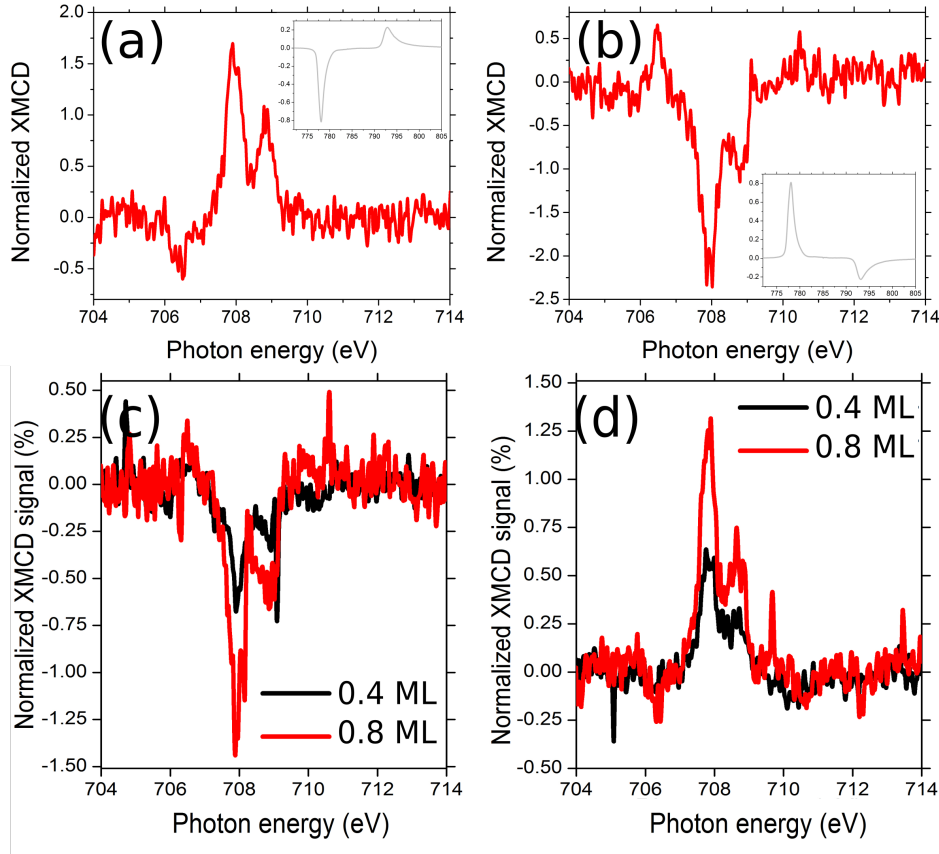


Figure 6.5: Normalized XMCD signal at zero field for L_3 edge of Fe^{II} (a) from 1 T \rightarrow 0 T; (b) from -1 T \rightarrow 0 T. In inset of (a) and (b) is shown the $L_{2,3}$ edges of cobalt at zero field; Normalized XMCD signal at L_3 edge of Fe^{II} at zero field for 0.4 ± 0.12 ML (red) and 0.8 ± 0.22 ML (black) from: (c) -1 T \rightarrow 0 T; (d) from 1 T \rightarrow 0 T. The measurements in (a) and (b) were made for 0.3 ± 0.08 ML of Fe-Pyrz on 4.1 ML of Co(OP) while (c) and (d) were made on for 0.4 ± 0.12 ML (red) and 0.8 ± 0.22 ML (black) on 3.0 ML Co(OP).

It is clear that the signs of the XMCDs for cobalt and Fe-Pyrz are opposite at zero field and thus confirms the existence of the AFM coupling between the Fe^{II} ion and the cobalt and a magnetic cycle opening of at least some of the molecules the on cobalt out-of-plane magnetization. Furthermore, in order to know what is the influence of the molecular thickness on the AFM coupling, we performed XMCD measurements at remanence on the 3.0 ML cobalt system. From figures 6.5-c/d, we see that in percentage XMCD, the thin sample (red) has more signal than the thick sample (black). This suggests the existence of two populations of HS molecules: some that are coupled with Co and others that are likely decoupled or not coupled at all. Moreover, it confirms that this effect is an interface effect and that it will probably disappear by increasing the thickness of the molecular layer.

Finally, in order to know up to what temperature the magnetic coupling remains persistent, we performed XMCD measurements in remanence on the 0.4 ± 0.12 ML sample on

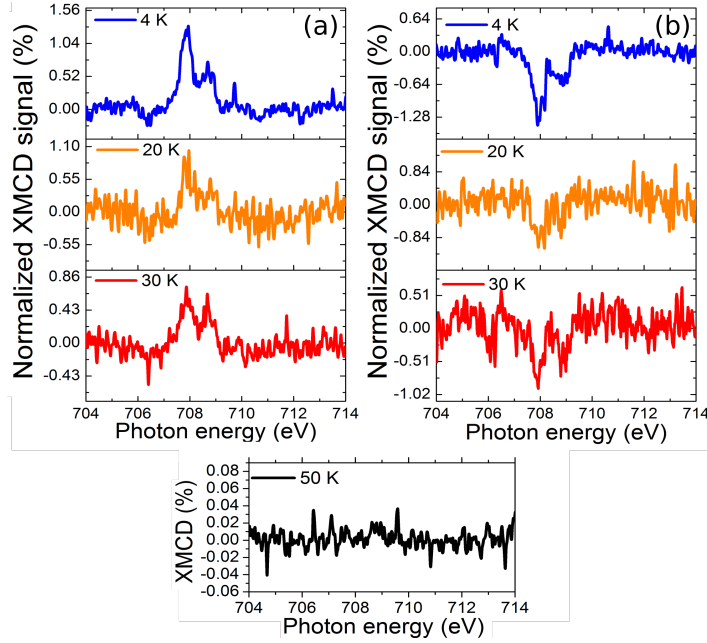


Figure 6.6: Temperature-dependant normalized XMCD at L_3 edge of Fe^{II} at zero field at 4 K (blue), 20 K (orange), 30 K (red) and 50 K (black) from 1 T \rightarrow 0 T (a) and from -1 T \rightarrow 0 T (b). The measurements were done on the Fe-Pyrz(0.4 ML)/Co(3.0 ML)/Au(111) sample.

3.0 ML of cobalt (OP), as shown in figures 6.6-a/b, from 1 T to 0 T (a) and from -1 T to 0 T (b), respectively. The temperature-dependant XMCD measurements show that the XMCD signal decreases while increasing temperature and remains up to 40/50 K. Thus, we can deduce a value of the magnetic exchange coupling energy to be around 3 or 4 meV.

6.2 Effect of different decoupling layers on the switching and magnetic properties between Fe-Pyrz and Co/Au(111)

In this section, we will study the effect of different decoupling layers (copper and gold) between Fe-Pyrz and cobalt to see if the thermal and light-induced switching properties of the molecules can be restored or not. Indeed, it was shown by reference [186] that for the $\text{Fe}(\text{phen})_2(\text{NCS})_2$ SCO molecule chemisorbed on Cu(001), the spin-state was locked to the HS state, and the addition of a nitrogen overlayer on the copper substrate (Cu_2N) reduces the chemical interaction between the molecule and the substrate, facilitating the SCO behavior. Following this idea, we will first look, in section 6.2.1, at different thicknesses of copper decoupling layers [185, 186, 189], namely, 1.0 ± 0.2 ML of copper or Cu(1 ML), 1.9 ± 0.36 ML of copper or Cu(1.9 ML) on Co(10.4 ML) and 1.2 ± 0.25 ML of copper or Cu(1.2 ML) on Co(4.1 ML). Then, in section 6.2.2, we will see the effect of a thick decoupling layer of gold on the magnetism and the SCO behavior between Fe-Pyrz and Co/Au(111).

6.2.1 Copper as a decoupling layer

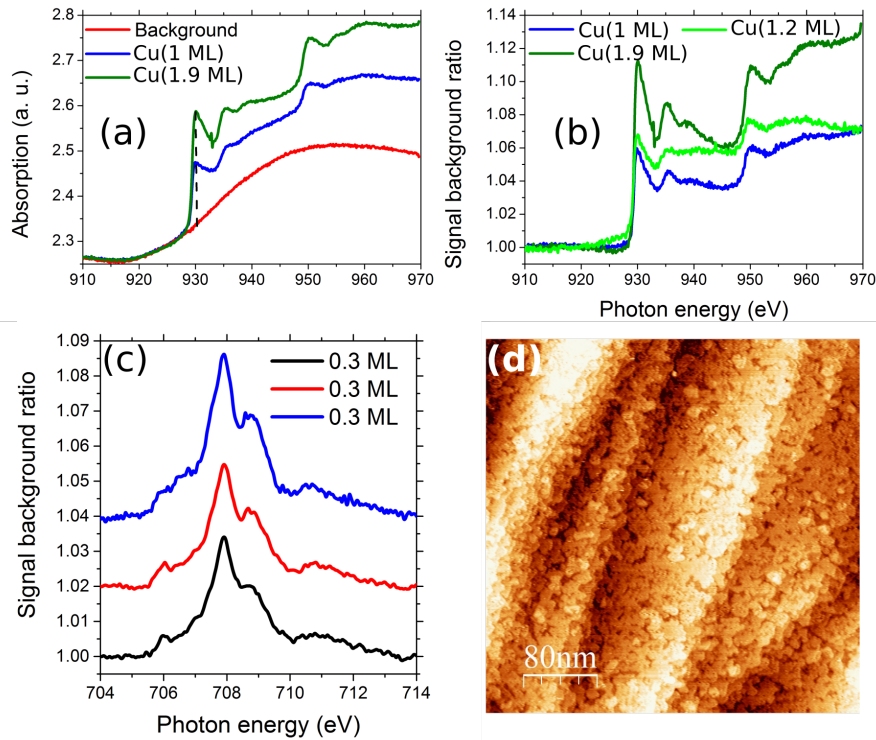


Figure 6.7: (a) $L_{2,3}$ edges of copper for Cu(1 ML) (blue), Cu(1.9 ML) (olive) and the background (red). The vertical dotted line at 930 eV represents the edge-jump intensity; (b) Normalized XAS at the $L_{2,3}$ edges of copper for Cu(1 ML) (blue), Cu(1.9 ML) (olive) and Cu(1.2 ML) (green and presented later). The background has been subtracted and normalized to the edge-jump intensity at 930 eV; (c) Normalized XAS at the L_3 edge of Fe^{II} at 290 K of 0.3 ± 0.08 ML of Fe-Pyrz on: Cu(1 ML) zone (black), Cu(1.9 ML) zone (red) and Cu(1.2 ML) zone (blue). A linear background has been subtracted and normalized to the edge-jump intensity at 707.9 eV and the spectra were shifted for clarity; (d) STM image ($400 \times 400 \text{ nm}^2$) at room temperature for Fe-Pyrz/Cu(1 ML)/Co/Au(111) at 10 pA and -2.0 V.

In this section, we will study two systems: i) the first one is the one with 10.4 ML of cobalt (cf. figure 6.2-a in black), on which we have evaporated a Cu decoupling layer wedge (two thicknesses); ii) the second sample is the one with 4.1 ML of cobalt (cf. figure 6.2-a in red), on which we have evaporated copper.

The Cu thicknesses were determined both by STM images and the XAS spectra (see figure 6.7-a/b). First, we realised a calibration by STM measurements. We evaporated copper for 40 minutes on a bare gold substrate, which leads to a Cu coverage of 0.5 ± 0.1 ML on Au(111), as shown in figure 2.13-g (chapter 2). The Cu on Co(10.4 ML)/Au(111) was sublimated for 82 minutes for the thin part and 162 min for the thicker part under the same evaporation conditions. For this same sample the XAS spectra at the Cu $L_{2,3}$ -edge have been recorded on both area of Cu. In figure 6.7-a is shown the XAS spectra at the Cu $L_{2,3}$ -edge on a bare copper (which is used as background for subtraction to obtain figure 6.7-b), and on the two areas of Cu (thin decoupling layer in blue, thick decoupling layer in olive). At 930 eV, we determined the absolute edge-jumps and their ratio which has a value of 1.8.

From the STM calibration and the ratio of the Cu- L_3 edge-jump, we thus determined the Cu coverage to be 1.0 ± 0.2 ML and 1.9 ± 0.4 ML on the Co(10.4 ML)/Au(111) sample. For the Cu decoupling layer grown on Co(4.1 ML)/Au(111), only the Cu-edge is used (see figure 6.7-b in green). The ratio with the Cu(1 ML)/ Co(10.4 ML)/Au(111) sample being 1.2, a thickness of 1.2 ± 0.3 ML is determined.

Sample (ML)	Maximum (a.u.)	Background (a. u.)	Edge-jump (a.u.)	Edge-jump (%)	Normalized edge-jump (%)	Coverage (ML)
Cu(1)	1.459	1.401	0.049	3.5 %	4.1 %	0.3 ± 0.08
Cu(1.9)	1.411	1.363	0.048	3.5 %	4.0 %	0.3 ± 0.08
Cu(1.2)	1.025	0.977	0.047	4.9 %	4.0 %	0.4 ± 0.12

Table 6.2: In the first column is represented the different Cu ares on which Fe-Pyrz has been evaporated and measured by XAS. The second (resp. third) column represents the maximum (resp. background) intensity of the L_3 -edge of Fe^{II} and the fourth column is the difference in absolute between the two previous ones. The fifth column represents the intensity in percentage of the background of the respective samples. The sixth column is the normalization of column five with respect to Cu(111) background. The seventh column is the molecular coverage.

Besides that, the calibration of the molecular thickness was done by knowing the experimental ratio between the backgrounds on Cu(111) and Cu(1 ML)/Co(10.4 ML)/Au(111), Cu(1.9 ML)/Co(10.4 ML)/Au(111) and Cu(1.2 ML)/Co(4.1 ML)/Au(111), as described in the first section. The values are reported in the previous table. Following this method, it gives exactly the same coverage as the one deduced directly on cobalt, namely, 0.3 ± 0.08 ML on Cu(1 ML), Cu(1.9 ML) and Cu(1.2 ML). Indeed, this result is natural since the evaporation of Fe-Pyrz on Cu(1 ML)/Co(10.4 ML), Cu(1.9 ML)/Co(10.4 ML) (resp. Cu(1.2 ML)/Co(4.1 ML)) was done concomitantly with the evaporation of the molecules on Co(10.4 ML) (resp. Co(4.1 ML)) i.e. on the same substrate. Moreover, this also confirms that this method is suitable for the calculation of molecular coverage.

Furthermore, the shape of the XAS signal in figure 6.7-c is very typical of a Fe^{II} ion on Cu(111) (slightly distorted octahedron) which is an indication that the molecules are not fragmented on the different surfaces. Finally, it can be seen from the STM image, in figure 6.7-d, that the molecules on Cu/Co/Au system form compact and small domains which pleads in favor of an organization of the molecules on the surface even if we were not able to measure directly by STM the molecular lattice.

6.2.1.1 Thermal and light-induced switching properties

Figure 6.8 shows the L_3 XA spectra of Fe^{II} on Cu(1 ML) (a/b) and on Cu(1.9 ML) (c/d) for high (grey) and low (blue) temperatures in figures 6.8-a/c and by using different wavelengths as shown in figures 6.8-b/d. Regarding the thermal transition, it can be seen that the spin-state is pinned to the HS state at any temperatures, in spite of having introduced the decoupling layers. Moreover, as shown in figures 6.8-b/d, at low temperature, there is no wavelength in the visible range that allows the molecules to switch from HS to LS

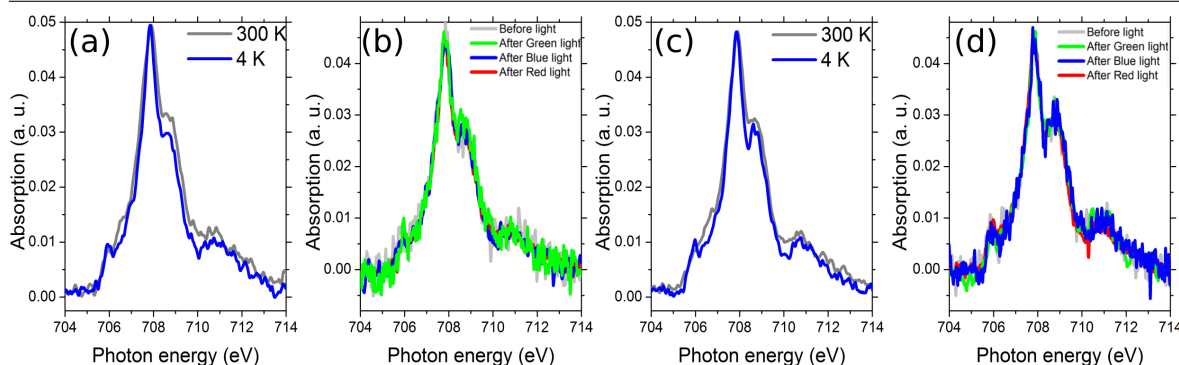


Figure 6.8: XAS at the L_3 edges of Fe^{II} after a linear background subtraction. On Cu(1 ML) zone: (a) high and low temperatures. (b) At low temperature with different wavelengths (405 nm, 532 nm and 640 nm); On Cu(1.9 ML) zone: (c) high and low temperatures. (d) At low temperature with different wavelengths.

as observed for this molecule in submonolayer on Cu(111) and Au(111). There are two reasons that we can invoke: first of all, the energy barrier between HS and LS is still too high, despite the fact that the copper decoupling layers have been introduced. In fact, the density of states of such thin Cu layers is different from the bulk Cu, inducing a stronger interaction between the molecule and the substrate [162]. Secondly, it can also be the direct consequence of a different lattice parameter, for those strained Cu layers, with an enhanced epitaxial constraint for the molecular layer. Only DFT calculations could confirm or refute these hypotheses. However, this result is very surprising comparing to what we found in the literature. Indeed, in reference [189], they have studied, by means of DFT, the spin-state behavior of $\text{Fe}(\text{phen})_2(\text{NCS})_2$ on Co(001) and Co(111). Their results show that the total energy difference between the HS and the LS states on Co(001) is reduced compared to the adsorbed molecule on Cu(001). Therefore, they expect that the magnetic substrates favor the switching of the molecule between the HS and the LS states and are therefore a most promising substrates for SCO for $\text{Fe}(\text{phen})_2(\text{NCS})_2$. However, this is not the case for Fe-Pyrz on Co.

6.2.1.2 XMCD and magnetic hysteresis measurements

Figure 6.9-a/b/c shows XAS (in grey) and XMCD (color) spectra taken at low temperature (4 K) and high magnetic field (6 or 6.5 T) for the $L_{2,3}$ edges for 0.3 ± 0.08 ML of Fe-Pyrz on Cu(1 ML)/Co(10.4 ML) (blue), on Cu(1.9 ML)/Co(10.4 ML) (olive) and on Cu(1.2 ML) (green). The direction of the magnetic field is parallel to the photon wavevector and perpendicular to the sample surface ($\theta = 0^\circ$). Even if the XAS spectra are the same on the different zones, they do not have the same XMCD percentage, namely, 68.1 % for Co(IP) zone, 72.1 % for Co(OP) (see figure 6.4-a/b), 90.5 % for Cu(1 ML) zone, 80.1 % for Cu(1.9 ML) zone and 85.8 % for Cu(1.2 ML) zone. With regard to the XMCD percentages, it indicates different magnetic behaviors of the molecules in the different areas and it seems that it does depend on the number of copper spacers. Then, we made full magnetic cycle measurements from -5.5 T to 5.5 T and from -1.2 T to 1.2 T for Fe-Pyrz and cobalt respectively, as shown in figures 6.9-e/f. We observe for Cu(1 ML) zone (blue), the signal is always positive unlike the Cu(1.9 ML) zone (olive) where the molecule has the usual paramagnetic behavior.

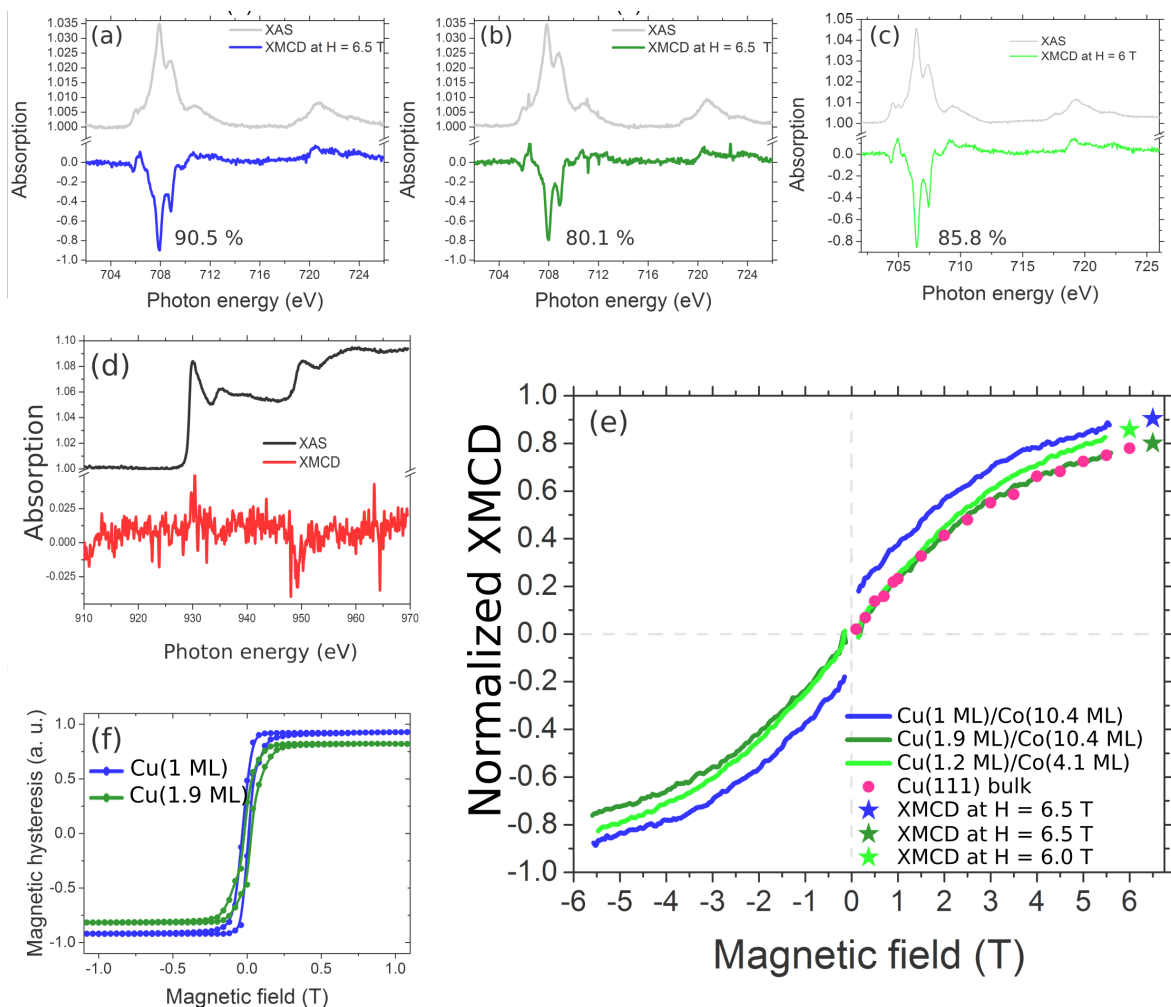


Figure 6.9: XAS (grey) and XMCD (color) at the $L_{2,3}$ edge of Fe^{II} at 4 K on: (a) Cu(1 ML) zone at 6.5 T; (b) Cu(1.9 ML) zone at 6.5 T; (c) Cu(1.2 ML) zone at 6 T; (d) XAS (black) and XMCD (red) signals at zero field for the $L_{2,3}$ edges of copper, coming from 1 T \rightarrow 0 T. (e) XMCD signal at the L_3 edge of Fe^{II} , from -5.5 T to 5.5 T, normalized with respect to the XMCD percentage at 6.5 T for (a) and (b) and at 6 T for (c) and to the HS fraction (100 %) on Cu(1 ML) zone (blue), Cu(1.9 ML) (olive) and on Cu(1.2 ML) zone (green). The stars represent the XMCD percentages shown in (a), (b) and (c). The magnetic data on Cu(111) (as in chapter 5) are shown in pink. (f) $M(B)$ (in arbitrary units) at the L_3 edge of Co for 10.4 ML Co(IP) on Cu(1 ML) (blue) and Cu(1.9 ML) (olive) zones.

Discussion on the magnetic coupling: Regarding the hysteresis cycles of cobalt (figure 6.9-f) acquired on the different copper zones, it appears that its sign is the same than the one of the molecular XMCD signal. Consequently, unlike the Fe-Pyrz molecules on bare cobalt case which shows the existence of an AFM coupling, these measurements show the existence of a ferromagnetic (FM) coupling between the molecules and the cobalt, once we put 1.0 ± 0.2 ML of Cu on Co and a return to the paramagnetic behavior with 1.9 ± 0.36 ML of Cu on Co. This paramagnetic behavior turns out to have almost the same magnetic anisotropy than the one studied in chapter 5. Indeed, if we superimpose the magnetization curves obtained on Cu(1.9 ML) and Cu(111) (figure 6.9-e in pink, normalized with respect to XMCD at 6 T and at 90 % of HS, see chapter 5), the agreement is total. The fact that the molecule has the same magnetic anisotropy on two surfaces for which the measured

switching behavior is radically different is counter intuitive at first glance. Indeed, the magnetic anisotropy energy is very small as compared to the energy barrier between the spin states and should be more sensitive to the details of the interface. However, we have given strong arguments in chapter 5 on the robustness of the magnetic anisotropy, whatever the strength of the interaction with the substrate, what seems to be directly demonstrated here. Concerning the Cu(1.2 ML) region, we have measured the XMCD at the Cu $L_{2,3}$ edge at remanance as shown in figure 6.9-d. A small but clear signal shows that the Cu is spin-polarized with an opposite sign with respect to the Co XMCD signal (cf. figure 6.5-a). This magnetic interaction between copper and cobalt, called interlayer exchange coupling (IEC), has been already demonstrated [193–196]. They showed that the sign of the coupling depends on the Cu spacer thicknesses and varies in an oscillatory fashion (about 9 Å period). Unfortunately, we did not measure the remanance XMCD of copper on Cu(1 ML) and Cu(1.9 ML). However, since this effect depends on the Cu spacer thickness, we can expect this spin-polarization on Cu(1 ML) but not on Cu(1.9 ML) (paramagnetic), since the thickness of this latter is higher than the others. From this discussion, we can draw a scheme that takes into account all these experimental evidences. As for Fe-Pyrz directly deposited on Co, there is a AFM coupling between Fe-Pyrz and the spin-polarized Cu. As just shown, the AFM coupling between Co and Cu gives rise finally to a ferromagnetic coupling between Co and Fe-Pyrz in the presence of the Cu 'decoupling' layer.

Discussion on the coupling mechanism: This coupling is certainly a superexchange-type coupling and mediated by the pyrazole ligands, whatever the spin-polarized surface (Co IP or OP, Cu interlayer). Unfortunately, it is very difficult to measure the XMCD K -edge for nitrogen due to the small amount of material. Such a magnetic coupling in a three-dimensional SCO molecule has already been observed by SP-STM and calculated by DFT to be ferromagnetic [156, 188, 189]. However, the sign of the coupling should obviously depends on the structural details of the molecule (number and nature of the atoms between the ferromagnet and the metal ion, angles between the different bonds...). Only DFT calculations on the Fe-Pyrz can confirm and explain the nature of the measured AFM coupling, based on a structural model for the molecular adsorption. More surprisingly, it is shown in reference [189] that this ferromagnetic coupling remains for few atomic layers of Cu overlayers. Indeed, a very similar result was obtained by reference [177] on a MnPc/Cu/Co/Cu(001) molecule, where the nature of the coupling (FM or AFM) depended on the number of decoupling layers of copper, until that disappeared and the molecule decoupled from the cobalt and regained its paramagnetic character. The authors argue that this change in the sign of the coupling is due IEC between the molecules and the Co and the sign change occurs in an oscillatory manner such as a RKKY-type interaction (Ruderman-Kittel-Kasuya-Yoshida) [194–196, 354–356]. Consequently, the AFM interaction of Fe-Pyrz on cobalt decreases in an oscillatory manner as a function of the number of copper layers. A scheme summarizing those results is depicted in figure 6.10.

6.2.2 Gold as a decoupling layer

The last system studied consists of (0.6 ML)Fe-Pyrz/(4.1 ML)Au/(5.2 ML)Co/Au(111). The calibration of the number of cobalt layers (5.2 ML) is shown from figure 6.2-b (magenta). In order to get the gold decoupling layer, we annealed the Co/Au(111) system gradually,

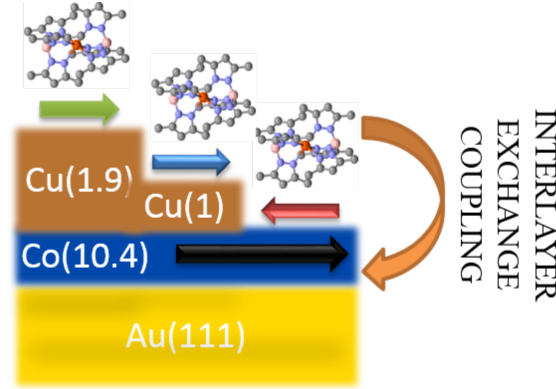


Figure 6.10: Diagram of the different magnetic couplings of Fe-Pyrz and Co. The black arrow represents the magnetization of cobalt. In red, the Fe-Pyrz magnetization where an AFM coupling can be seen. In blue, the Fe-Pyrz magnetization where we see a FM coupling. In green, the Fe-Pyrz magnetization where no coupling is seen (paramagnetic).

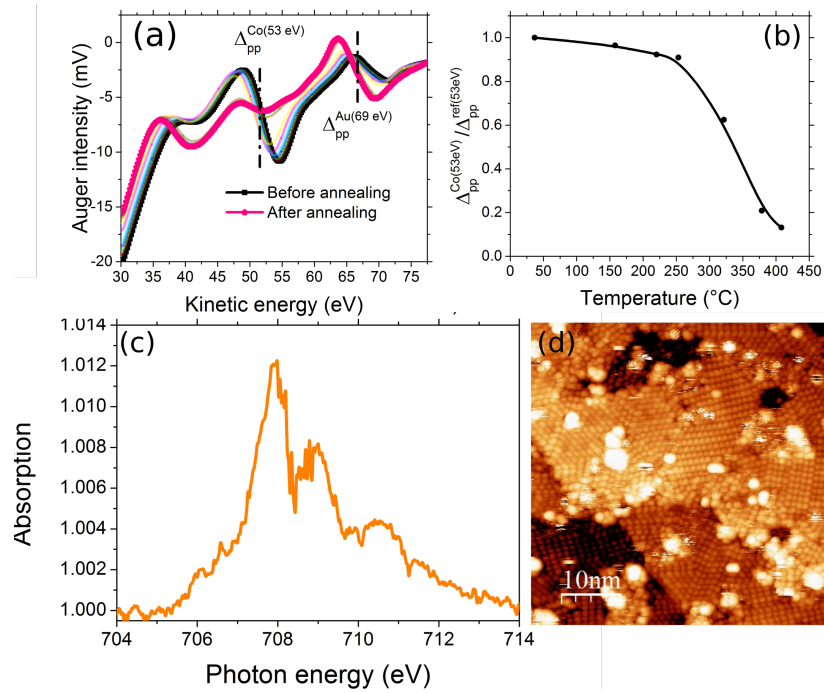


Figure 6.11: (a) Variation of the Auger intensity peaks as a function of kinetic energy of Auger electrons for cobalt at 53 eV and gold at 69 eV for the Co/Au(111) system while the sample is annealed up to 408°C. (b) Variation of the ratio between the peak-to-peak Δ_{pp} of cobalt while annealed ($\Delta_{pp}^{Co}(T)$) and the reference cobalt peak-to-peak before annealing ($\Delta_{pp}^{ref,Co}$) as a function of temperature. (c) Normalized XAS at the L_3 edge of Fe^{II} at 290 K for for 0.6 ± 0.1 ML of Fe-Pyrz/Au/Co/Au(111). A linear background has been subtracted and normalized to the edge-jump intensity at 707.9 eV; (d) 50×50 nm² STM image of Fe-Pyrz/Au/Co/Au(111) at $I = 20$ pA and $V = -2.5$ V for the measured sample in Synchrotron

using the PBN furnace, because it was shown already that there is an interlayer diffusion of gold atoms through the cobalt [357–361]. Thus, in order to calibrate the number of gold layers formed on the cobalt surface, we used Auger spectroscopy [362], a surface sensitive technique, to be able to follow the evolution of the Auger peaks of gold (Δ_{pp}^{Au} at 69 eV, with

Δ_{pp} is the absolute difference of the maximum and minimum values of the peak as shown dotted point in figure 6.11-a) and cobalt (Δ_{pp}^{Co} at 53 eV) as shown in figure 6.11-a. Indeed, it is clearly seen that at room temperature, the cobalt peak totally dominates that of gold (before annealing in the figure) and at around 350°C, the gold atoms start to diffuse through the cobalt and the Auger peak of gold starts to increase and we see a decrease in the cobalt peak (pink). The calibration of gold thickness is made as follows. First, before annealing (black in figures 6.11-a), we measured the reference signal of cobalt at 53 eV (Δ_{pp}^{ref}). These escaping electrons have a 100 % probability of being able to escape. By heating, to 378°C, a layer of gold is formed on top. Thus, the peak of the cobalt decreases while that of the gold increases (pink in figure 6.11-a). As a result, electrons escaping from the cobalt do not have a 100 % chance of escaping and the signal decreases exponentially with the thickness of gold covered (t_{Au}). The temperature evolution of the peak-to-peak intensity normalized to the peak-to-peak intensity before annealing ($\frac{\Delta_{pp}^{\text{Co}}}{\Delta_{pp}^{\text{ref}}}(T)$) is shown in figure 6.11-b. Assuming a negligible roughness of both Co and Au layers, we can write this quantity as follows: $\frac{\Delta_{pp}^{\text{Co}}(T)}{\Delta_{pp}^{\text{ref}}} = \exp(-\frac{t_{\text{Au}}}{\lambda_e})$. Where λ_e represents the inelastic mean free path of electrons escaping from cobalt and passing through gold. This value is equal to 5.3 Å and is derived from a database [363]. Thus, taking the measurement point at 378 °C with the $\frac{\Delta_{pp}^{\text{Co}}(T = 378^\circ\text{C})}{\Delta_{pp}^{\text{ref}}} = 0.21$, the thickness of gold is estimated to be 8.3 Å or 4.1 ML.

Moreover, the calibration of Fe-Pyrz molecules was done using the calibration on Au(111) (see chapter 4) in which 1.1%, corresponds to 0.5 ± 0.1 ML and gives 0.6 ± 0.1 ML. Furthermore, we can see that the spectra, shown in figure 6.11-c, looks like the usual spectra on Au(111), thus, we can conclude that there is no decomposition of the molecules on the surface. Finally, it can be seen from the STM images the Fe-Pyrz molecules on the Au/Co/Au(111) substrate are ordered with the coalescence of small domains of very different sizes as shown in figure 6.11-d.

6.2.2.1 Thermal and light-induced switching properties

Figure 6.12 shows the results obtained for the thermal transition (a) and for different wavelengths (b) at 405 nm, (c) at 532 nm and (d) at 640 nm as well as the SOXIESST (in grey for (b) and (c)). At high temperature, we have effectively all the molecules in the HS state and at 4 K, we obtain a proportion of HS which is 69 % quite comparable with submonolayer of Fe-Pyrz on Au(111) [325] despite the small domains observed. Concerning the light-induced effect, the results are again qualitatively and quantitatively the same as on a gold substrate with an anomalous HS to LS transition [325] under blue and green lights and no effect for red light. Before blue (resp. green) irradiation, the thermal state at 4 K has a HS proportion of 64 % (resp. 73 %). For the photoexcited state under blue (resp. green) illumination, we have 51 % (resp. 47 %) and finally for the SOXIESST, we obtain 67 % (resp. 74 %). As discussed earlier for the thermal state superstructure, the photoexcited state has a HS proportion of around 50 % which is very consistent with the photoexcited superstructure where one molecule over two ($S_{1/2}$ superstructure) is switched [223, 325] and this despite the smaller size of the molecule domains in our case.

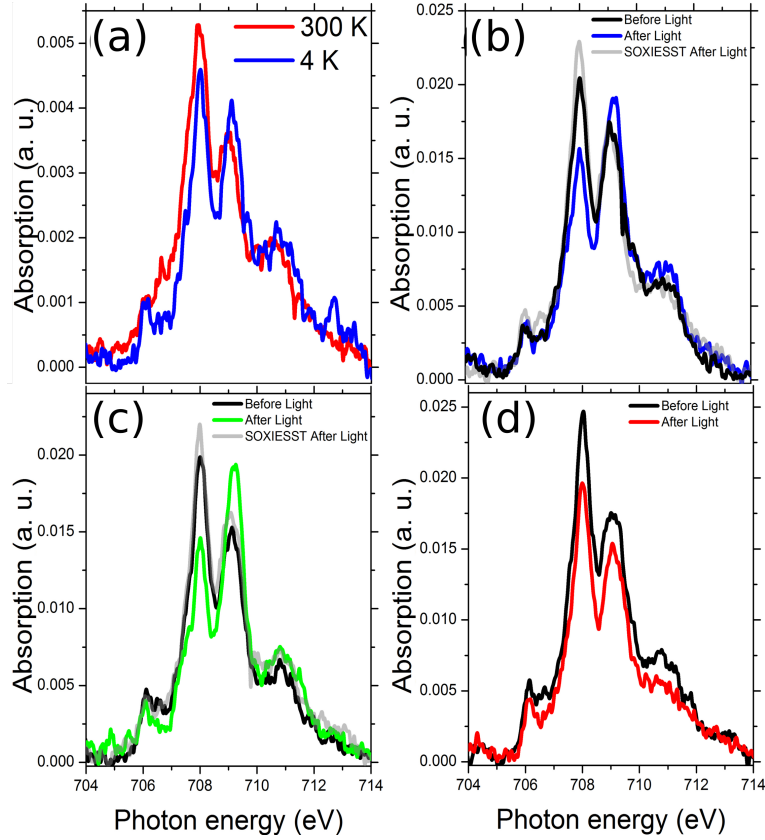


Figure 6.12: XAS at the L_3 edges of Fe^{II} after a linear background subtraction. (a) high and low temperatures; (b) Thermal state at low temperature (black), after 405 nm irradiation (blue) and after SOXIESST (grey); (c) Thermal state at low temperature (black), after 532 nm irradiation (blue) and after SOXIESST (grey); (d) Thermal state at low temperature (black), after 640 nm irradiation (red).

6.2.2.2 Magnetic properties

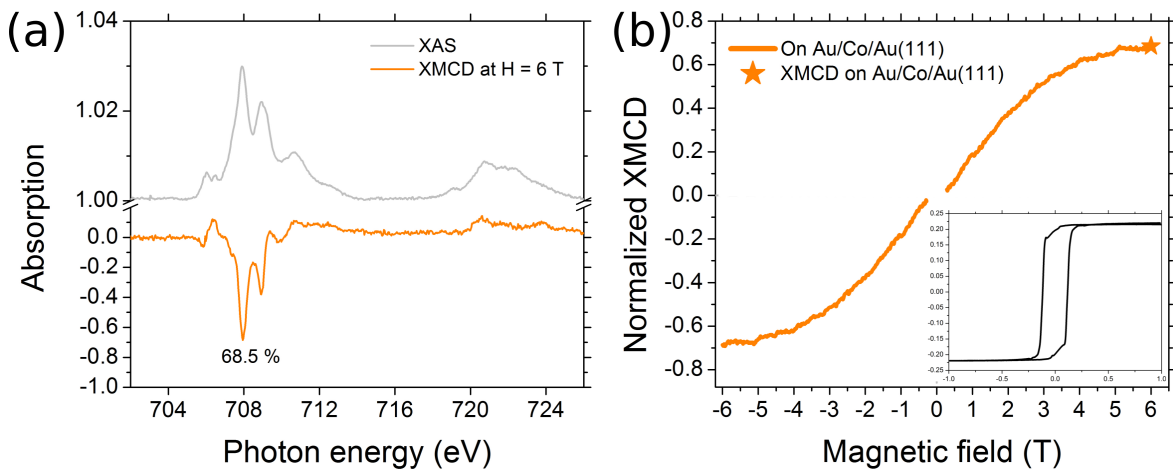


Figure 6.13: (a) Normalized XAS (grey) and XMCD (orange) signals at the $L_{2,3}$ edges of Fe^{II} at 4 K and at 6 T; (b) XMCD signal from -6 T to 6 T and normalized with respect to the XMCD percentage at 6 T and to the HS fraction (66 %). The star represents the XMCD percentage shown in (a). In inset, $M(B)$ (in arbitrary units) of cobalt. The magnetic field is normal to the surface.

The magnetic behavior of this sample has also been studied. Indeed, figure 6.13-a/b shows the XAS/XMCD (at 6 T) and the corresponding magnetic hysteresis cycle. Regarding the Co hysteresis cycle, it shows an easy axis of magnetization (out-of-plane) due to the formation of a second interface (Au/Co/Au) which increases the interface anisotropy [277, 358]. For the Fe-Pyrz, it can be seen that the molecule is not coupled to cobalt and adopts a paramagnetic behavior, what can be explained considering the larger Au thickness.

6.3 Conclusion

In this chapter, we have studied the growth of Fe-Pyrz molecules on Co/Cu(111), by STM. We have shown that the molecules were disordered on the Co islands. Our analyses indicate that the adsorption energy on Co is higher than on Cu(111) probably due to the stronger interactions between the methyl groups and Co. Since the molecules on the Co islands adopt different orientations, a good perspective is to couple this information obtained by STM with angular XMCD measurements in order to understand the obtained magnetization curves.

Secondly, we conducted XAS and XMCD studies at the $L_{2,3}$ edges of Fe^{II} and Co on the Fe-Pyrz/Co(IP/OP)/Au(111) system. XAS studies show that the molecules were pinned in the HS state at all temperatures, and light-induced switching is not effective. This is due to the fact that the energy barrier between HS and LS on Co is much larger than on Cu(111), Ag(111), Au(111) or HOPG, where switching under light and temperature has been well demonstrated. Moreover, the XAS spectra suggest that the molecules remain intact on all surfaces. The element-resolved XMCD measurements show that the spin of the molecules was antiferromagnetically coupled with the magnetic moments of Co. A consequence of the magnetic coupling on the Co(OP) is the possibility to open magnetic hysteresis on Fe-Pyrz. Indeed, the remanence magnetization of Fe-Pyrz has been demonstrated.

Thirdly, in the hope of reducing the HS to LS energy barrier and promoting switching, we conducted 1.0 ± 0.2 ML (called Cu(1 ML)), 1.9 ± 0.36 ML (Cu(1.9 ML)), 1.2 ± 0.25 ML (Cu(1.2 ML)) decoupling layers of Cu between Fe-Pyrz molecules and Co(IP/OP). These molecules were intact on the surface and seem to organize. Unfortunately, the molecules were always locked in the HS state regardless of the stimuli used. However, XMCD measurements at the Fe^{II} , Co and Cu $L_{2,3}$ edges show that in the Fe-Pyrz(0.3 ML)/Cu(1 ML)/Co(10.4 ML)/Au(111) and Fe-Pyrz(0.3 ML)/Cu(1.2 ML)/Co(4.1 ML)/Au(111) systems, the Fe-Pyrz spin was ferromagnetically coupled to that of Co through the spin-polarized electrons of Cu. This change of sign is due to the interlayer exchange coupling between the Fe-Pyrz spin (resp. Cu) and the magnetic moments of Cu (resp. Co) which are antiferromagnetically coupled and thus give a ferromagnetic coupling. On 1.9 ± 0.36 ML of Cu on Co, the molecule regains its paramagnetic behavior and retains its magnetic anisotropy as on a Cu(111) bulk. This confirms the robust character of its structure on the surface and thus of its magnetic anisotropy.

Finally, we concluded this chapter by studying the thermal and light-switching behavior of a system with gold as a decoupling layer. This sample was grown by controlled annealing of the Co/Au(111) system, which induces Au surfactant overlayers. We have measured that the molecules organised on Au(4.1 ML)/Co(5.2 ML)/Au(111), but with much smaller domain sizes than on Au(111). The thermal transition takes place and the light-induced switching from HS to LS has been demonstrated and quantitatively exhibits proportions of HS molecules in the photostationary state comparable to that on Au(111). This indicates that the Fe-Pyrz(0.6 ML)/Au(4.1 ML)/Co(5.2 ML)/Au(111) system recovers the behavior of submonolayer of Fe-Pyrz/Au(111). This is different from what we have found in copper. It is an open question to know if it is due to the higher thickness used for Au (5 ML instead of 2 ML) or to the nature of the metal (the misfit parameter between Au and Co is for example much larger than the one between Cu and Co). Furthermore, the molecules adopt a paramagnetic behavior and are completely decoupled from the magnetic moments of Co.

Dedicated DFT calculations would help rationalizing some of the results demonstrated in this chapter.

GENERAL CONCLUSIONS

In this thesis work, we have investigated how the spin transition of $\text{Fe}^{\text{II}}((3,5-(\text{CH}_3)_2\text{Pz})_3\text{BH})_2$ molecules is modified for thin films adsorbed on solid surfaces. This work required a strong experimental part (XAS and STM) and also different numerical simulations (*QUANTY*, *PHI*, *kinetic Monte Carlo*). Firstly, we find that the molecules keep their integrity on the different substrates studied and that, except on Co, they self-assembled in the form of dense molecular network.

In chapter 3, the thermal bistability of ultrathin films of $\text{Fe}^{\text{II}}((3,5-(\text{CH}_3)_2\text{Pz})_3\text{BH})_2$ on Cu(111) and Highly Oriented Pyrolytic Graphite (HOPG) surfaces was studied as a function of the molecular thickness. Whatever the molecular coverages (between sub-monolayer to a few monolayers), the thermal transition is partial. Nonetheless, the measured thermal conversion curve shows, for the first time, the appearance of a thermal hysteresis loops for 3.0 ML and 1.4 ML ultrathin films of SCO adsorbed on Cu(111) and HOPG, respectively. This is an indication of the strong cooperative effects despite the substrate influence. Complementary, kinetic Monte Carlo simulations in the framework of the mechanoelastic model have been realised. Their novelty is to introduce not only the intermolecular interaction but also a molecule-substrate interaction. Qualitatively, the experiments are well reproduced by the simulations. In addition, we have investigated numerically the influence of the molecule-substrate interaction strength on the thermal transition. We find that as we increase the substrate interaction, the residual fraction of HS molecule at low temperature increases. Moreover, as we decrease the molecule-substrate interaction, the number of layers needed to have a complete switching is decreased. Interestingly, we show that the distribution of HS molecules inside each layer is not homogeneous over the film thickness and more specifically, we highlight the role of the interface layer. Indeed, the residual fraction of HS molecule at low temperature in the interface layer depends greatly on the competition between intermolecular and the molecule-substrate interactions. These results demonstrate the interplay between interfacial and bulk effects in the SCO properties at the ultrathin film levels (few molecular layers), giving rise to new paradigms that may be important to consider to realize electronic or spintronic devices with such molecular layers.

In chapter 4, we investigate the light-induced properties of $\text{Fe}^{\text{II}}((3,5-(\text{CH}_3)_2\text{Pz})_3\text{BH})_2$ in direct contact with Au(111), Ag(111), Cu(111) and HOPG. For sub-monolayer coverage, using blue or green light, an anomalous light transition from HS \rightarrow LS is evidenced. This anomalous light-induced effect has never been reported before. A model implying a mediation of the excitation through the substrate is proposed to explain this anomalous transition. For higher molecular coverage, we have shown that the LIESST effect is recovered, confirming the influence of the substrate on the anomalous light transition. Moreover, it appears that the switching is more efficient on HOPG than on Cu(111). All together, this demonstrates the role of the molecule/substrate interface on the modification of the light-induced switching properties. Finally, we demonstrate the existence of light-induced thermal hysteresis (LITH) on both surfaces for more than one molecular monolayer. For sub-monolayer, the light excitation increases the temperature range of the thermal hysteresis. This could be the signature of hidden phases. These findings could open new potentialities to design information storage devices at the nanoscale: write information with light ON and then erase it with temperature.

In chapter 5, we investigate the robustness of the magnetic anisotropy of $\text{Fe}^{\text{II}}((3,5-(\text{CH}_3)_2\text{Pz})_3\text{BH})_2$ on Cu(111) in comparison with a bulk reference which is the HS $\text{Fe}^{\text{II}}((3-(\text{Ph})\text{Pz})_3\text{BH})_2$ molecule. For the bulk compound, a positive D value is determined both by magnetic susceptibility measurements and *ab initio* calculations. This indicates the presence of a hard magnetization axis corresponding to the B-Fe-B axis. On the submonolayer of the SCO molecule on Cu(111), XMCD measurements revealed the existence of magnetic anisotropy. Using *PHI* software to simulate our data, a positive D value similar to the bulk's one is extracted thus confirming the presence of a hard magnetization axis for the molecules in the 2D network on Cu(111). The magnetic anisotropy is almost not affected by the substrate/vacuum interface. Comparing the $\text{Fe}^{\text{II}}((3,5-(\text{CH}_3)_2\text{Pz})_3\text{BH})_2$ molecules to other metal complexes, it appears that the torsion angle between the pseudo three-fold symmetry axis and the five-membered pyrazole rings of the tridentate ligand governs the hard or easy nature of the magnetization axis. Indeed, the torsion angle directly plays on the overlapping of the d_{z^2} orbital with the π or σ -like orbitals of the ligands. So, for torsion angle smaller than 9° as observed for any derivative of the $(\text{Pz})_3\text{BH}$ tridentate ligand and different metal ions (Fe^{II} , Co^{II} and Ni^{II}), a positive D value is expected. On the contrary for larger torsion angle, such as in $[\text{Fe}(\text{ptz})_6]^{2+}$ (ptz = propyltetrazole) complex, an easy axis of magnetization, i.e. a negative D value, is observed. Thus, the robustness of the magnetization axis for $[\text{Fe}^{\text{II}}((\text{Pz})_3\text{BH})_2]$ -related complexes comes from the rigidity of the tridentate ligands.

Finally, in chapter 6, we studied the properties of submonolayers of SCO molecules either directly on a ferromagnetic layer or on a decoupling layer. We firstly found by STM that the molecules show no organisation and multiple orientations on a cobalt surface. By XAS measurement, we demonstrate that the molecules are completely HS-locked by the effect of the substrate, indicating that the energy barrier between the two states is higher on Co than on other noble metals. In addition, XMCD measurements demonstrate the existence of an antiferromagnetic coupling between the molecules and the Co magnetic moments, whatever the orientation of the Co magnetization. For out-of-plane Co magnetization, we even demonstrate the existence of a remnant magnetization at the Fe^{II} L_3 edge, up to about 40 K. Then, in order to promote the switching and reduce the energy barrier between the two states, we decided to intercalate different thicknesses of copper between the molecules and the cobalt. If the molecules are still locked in the HS state on the decoupling Cu layers (up to 2 ML), the sign of the magnetic coupling can change and become ferromagnetic. This is the first time that a coupling between SCO molecules and a ferromagnetic surface is demonstrated so directly. We have discussed this change of sign of the coupling as mediated by proximity induced spin polarization in the copper layer. Finally, a few ML gold decoupling layer have been used. In this case, no magnetic coupling is observed and the molecules switch under the effect of light and temperature, very similarly to what is observed on bulk gold. We believe that this work can be of interest for the spin-crossover and spintronic communities.

LIST OF PUBLICATIONS

1. Zhang, L. *et al.* Anomalous light induced spin state switching for Fe^{II} spin-crossover molecules in direct contact with metal surfaces. *Angewandte Chemie International Edition* **59**, 13341–13346 (2020).
2. Kelai, M. *et al.* Robust magnetic anisotropy of a monolayer of hexacoordinate Fe(II) complexes assembled on Cu(111). *Inorg. Chem. Front.* **8**, 2395–2404 (2021).
3. Kelai, M. *et al.* Thermal Bistability of an Ultrathin Film of Iron(II) Spin-Crossover Molecules Directly Adsorbed on a Metal Surface. *J. Phys. Chem. Lett.*, 6152–6158 (2021).
4. Tong, Y. *et al.* Voltage-Induced Bistability of Single Spin-Crossover Molecules in a Two-Dimensional Monolayer. *J. Phys. Chem. Lett.* **12**, 11029–11034 (2021).

BIBLIOGRAPHY

1. Kahn, O. *Molecular Magnetism* (VCH, 1993).
2. Long, G. J., Grandjean, F. & Reger, D. L. in *Spin Crossover in Transition Metal Compounds I* (eds Güthlich, P. & Goodwin, H.) 91–122 (Springer Berlin Heidelberg, Berlin, Heidelberg, 2004).
3. Güthlich, P., Gaspar, A. B. & Garcia, Y. Spin state switching in iron coordination compounds. *Beilstein J. Org. Chem.* **9**, 342–391 (2013).
4. Brooker, S. Spin crossover with thermal hysteresis: practicalities and lessons learnt. *Chem. Soc. Rev.* **44**, 2880–2892 (2015).
5. Real, J. A., Gaspar, A. B. & Muñoz, M. C. Thermal, pressure and light switchable spin-crossover materials. *Dalton Trans.*, 2062 (2005).
6. Létard, J.-F., Guionneau, P. & Goux-Capes, L. in *Spin Crossover in Transition Metal Compounds III* 221–249 (Springer-Verlag, Berlin/Heidelberg, 2004).
7. Bousseksou, A., Molnár, G. & Matouzenko, G. Switching of Molecular Spin States in Inorganic Complexes by Temperature, Pressure, Magnetic Field and Light: Towards Molecular Devices. *Eur. J. Inorg. Chem.* **2004**, 4353–4369 (2004).
8. Halcrow, M. A. The spin-states and spin-transitions of mononuclear iron(II) complexes of nitrogen-donor ligands. *Polyhedron* **26**, 3523–3576 (2007).
9. Bousseksou, A., Molnár, G., Salmon, L. & Nicolazzi, W. Molecular spin crossover phenomenon: recent achievements and prospects. *Chem. Soc. Rev.* **40**, 3313 (2011).
10. Ruiz, E. Charge transport properties of spin crossover systems. *Phys. Chem. Chem. Phys.* **16**, 14–22 (2014).
11. Gaspar, A. B., Ksenofontov, V., Seredyuk, M. & Güthlich, P. Multifunctionality in spin crossover materials. *Coordination Chemistry Reviews* **249**, 2661–2676 (2005).
12. Kahn, O. & Martinez, C. J. Spin-Transition Polymers: From Molecular Materials Toward Memory Devices. *Science* **279**, 44–48 (1998).
13. Lefter, C. *et al.* Charge Transport and Electrical Properties of Spin Crossover Materials: Towards Nanoelectronic and Spintronic Devices. *Magnetochemistry* **2**, 18 (2016).
14. Konstantinov, N. *et al.* Electrical read-out of light-induced spin transition in thin film spin crossover/graphene heterostructures. *J. Mater. Chem. C* **9**, 2712–2720 (2021).
15. Coronado, E., Galán-Mascarós, J., Monrabal-Capilla, M., García-Martínez, J. & Pardo-Ibáñez, P. Bistable Spin-Crossover Nanoparticles Showing Magnetic Thermal Hysteresis near Room Temperature. *Adv. Mater.* **19**, 1359–1361 (2007).
16. Cornia, A. & Seneor, P. The molecular way. *Nature Mater* **16**, 505–506 (2017).
17. Sanvito, S. Molecular spintronics. *Chem. Soc. Rev.* **40**, 3336 (2011).

18. Delprat, S. *et al.* Molecular spintronics: the role of spin-dependent hybridization. *J. Phys. D: Appl. Phys.* **51**, 473001 (2018).
19. Cinchetti, M., Dediu, V. A. & Hueso, L. E. Activating the molecular spinterface. *Nature Mater* **16**, 507–515 (2017).
20. Moodera, J. S., Koopmans, B. & Oppeneer, P. M. On the path toward organic spintronics. *MRS Bull.* **39**, 578–581 (2014).
21. Li, H. & Peng, H. Recent advances in self-assembly of spin crossover materials and their applications. *Current Opinion in Colloid & Interface Science* **35**, 9–16 (2018).
22. Verdaguer, M. Molecular Electronics Emerges from Molecular Magnetism. *Science* **272** (1996).
23. Molnár, G. *et al.* Molecular Spin Crossover Materials: Review of the Lattice Dynamical Properties. *Annalen Der Physik* **531**, 1900076 (2019).
24. Holovchenko, A. *et al.* Near Room-Temperature Memory Devices Based on Hybrid Spin-Crossover@SiO₂ Nanoparticles Coupled to Single-Layer Graphene Nanoelectrodes. *Adv. Mater.* **28**, 7228–7233 (2016).
25. Molnár, G., Rat, S., Salmon, L., Nicolazzi, W. & Bousseksou, A. Spin Crossover Nanomaterials: From Fundamental Concepts to Devices. *Adv. Mater.* **30**, 1703862 (2018).
26. Weissbluth, M. *Atoms and Molecules* (Academic Press, 1978).
27. *Magnetism and Accelerator-Based Light Sources: Proceedings of the 7th International School “Synchrotron Radiation and Magnetism”, Mittelwihr (France), 2018* (eds Bulou, H., Joly, L., Mariot, J.-M. & Scheurer, F.) (Springer International Publishing, Cham, 2021).
28. König, E. & Kremer, S. *Ligand Field* (Springer US, Boston, MA, 1977).
29. Hauser, A. in *Spin Crossover in Transition Metal Compounds II* 155–198 (Springer Berlin Heidelberg, Berlin, Heidelberg, 2004).
30. Murray, K. S. & Kepert, C. J. in *Spin Crossover in Transition Metal Compounds I* (eds Gülich, P. & Goodwin, H.) 195–228 (Springer Berlin Heidelberg, Berlin, Heidelberg, 2004).
31. Guionneau, P., Marchivie, M., Bravic, G., Létard, J.-F. & Chasseau, D. in *Spin Crossover in Transition Metal Compounds II* 97–128 (Springer Berlin Heidelberg, Berlin, Heidelberg, 2004).
32. Kusz, J., Gülich, P. & Spiering, H. in *Spin Crossover in Transition Metal Compounds II* 129–153 (Springer Berlin Heidelberg, Berlin, Heidelberg, 2004).
33. Slichter, C. P. & Drickamer, H. G. Pressure-Induced Electronic Changes in Compounds of Iron. *The Journal of Chemical Physics* **56**, 2142–2160 (1972).
34. McCusker, J. K., Rheingold, A. L. & Hendrickson, D. N. Variable-Temperature Studies of Laser-Initiated $^5T_2 \rightarrow ^1A_1$ Intersystem Crossing in Spin-Crossover Complexes: Empirical Correlations between Activation Parameters and Ligand Structure in a Series of Polypyridyl Ferrous Complexes, 13.

35. Alonso, J. A., Martínez-Lope, M. J., Casais, M. T. & Fernández-Díaz, M. T. Evolution of the JahnTeller Distortion of MnO_6 Octahedra in RMnO_3 Perovskites (R = Pr, Nd, Dy, Tb, Ho, Er, Y): A Neutron Diffraction Study. *Inorg. Chem.* **39**, 917–923 (2000).
36. Buron-Le Cointe, M. *et al.* Intermolecular control of thermoswitching and photo-switching phenomena in two spin-crossover polymorphs. *Phys. Rev. B* **85**, 064114 (2012).
37. Marchivie, M., Guionneau, P., Létard, J.-F. & Chasseau, D. Photo-induced spin-transition: the role of the iron(II) environment distortion. *Acta Crystallogr B Struct Sci* **61**, 25–28 (2005).
38. Guionneau, P. Crystallography and spin-crossover. A view of breathing materials. *Dalton Trans.* **43**, 382–393 (2014).
39. Chastanet, G. *et al.* A critical review of the T(LIESST) temperature in spin crossover materials - What it is and what it is not. *Chem.Sq.* **2**, 2 (2018).
40. Collet, E. & Guionneau, P. Structural analysis of spin-crossover materials: From molecules to materials. *Comptes Rendus Chimie* **21**, 1133–1151 (2018).
41. Herber, R. & Casson, L. M. Light-induced excited-spin-state trapping: evidence from variable temperature Fourier transform measurements. *Inorg. Chem.* **25**, 847–852 (1986).
42. Gütllich, P., Hauser, A. & Spiering, H. Thermal and Optical Switching of Iron(II) Complexes. *Angewandte Chemie International Edition in English* **33**, 2024–2054 (1994).
43. Chastanet, G., Lorenc, M., Bertoni, R. & Desplanches, C. Light-induced spin crossover—Solution and solid-state processes. *Comptes Rendus Chimie* **21**, 1075–1094 (2018).
44. Sorai, M. & Seki, S. Phonon coupled cooperative low-spin 1A_1 high-spin 5T_2 transition in $[\text{Fe}(\text{phen})_2(\text{NCS})_2]$ and $[\text{Fe}(\text{phen})_2(\text{NCSe})_2]$ crystals. *Journal of Physics and Chemistry of Solids* **35**, 555–570 (1974).
45. Brehm, G., Reiher, M. & Schneider, S. Estimation of the Vibrational Contribution to the Entropy Change Associated with the Low-to High-Spin Transition in $\text{Fe}(\text{phen})_2(\text{NCS})_2$ Complexes: Results Obtained by IR and Raman Spectroscopy and DFT Calculations. *J. Phys. Chem. A* **106**, 12024–12034 (2002).
46. Azzolina, G., Bertoni, R. & Collet, E. General Landau theory of non-symmetry-breaking and symmetry-breaking spin transition materials. *Journal of Applied Physics* **129**, 085106 (2021).
47. Paez-Espejo, M., Sy, M. & Boukheddaden, K. Elastic Frustration Causing Two-Step and Multistep Transitions in Spin-Crossover Solids: Emergence of Complex Antiferroelastic Structures. *J. Am. Chem. Soc.* **138**, 3202–3210 (2016).
48. Willenbacher, N. & Spiering, H. The elastic interaction of high-spin and low-spin complex molecules in spin-crossover compounds. *Journal of Physics C: Solid State Physics* **21**, 1423–1439 (1988).
49. Popa, A.-I., Stoleriu, L. & Enachescu, C. Tutorial on the elastic theory of spin crossover materials. *Journal of Applied Physics* **129**, 131101 (2021).

50. Spiering, H., Meissner, E., Köppen, H., Müller, E. W. & Gütlich, P. The effect of the lattice expansion on high spin low spin transitions. *Chemical Physics* **68**, 65–71 (1982).
51. Varret, F., Boukheddaden, K., Coddjovi, E., Enachescu, C. & Linares, J. in *Spin Crossover in Transition Metal Compounds II* 199–229 (Springer Berlin Heidelberg, Berlin, Heidelberg, 2004).
52. Kawamoto, T. & Abe, S. Thermal hysteresis loop of the spin-state in nanoparticles of transition metal complexes: Monte Carlo simulations on an Ising-like model. *Chem. Commun.*, 3933 (2005).
53. Wajnsflasz, J & Pick, R. *Low-spin-high-spin transitions in Fe^{2+} complexes* in *J. Phys. Colloq. Fr* **32** (1971), C1.
54. A. Bousseksou, J. Nasser, J. Linares, K. Boukheddaden & F. Varret. Ising-like model for the two-step spin-crossover. *J. Phys. I France* **2**, 1381–1403 (1992).
55. Hôo, B., Boukheddaden, K. & Varret, F. Two-variable macroscopic model for spin-crossover solids: Static and dynamic effects of the correlations. *The European Physical Journal B - Condensed Matter and Complex Systems* **17**, 449–457 (2000).
56. Dobrinescu, A., Enachescu, C. & Stancu, A. Ising-like model study of size dependence relaxation in spin crossover complexes. *Journal of Magnetism and Magnetic Materials* **321**, 4132–4138 (2009).
57. Kohlhaas, T., Spiering, H & Gütlich, P. Monte Carlo study of the two-step spin transition in $[Fe_xZn_{1-x}(2-pic)_3]Cl_2 \cdot EtOH$. *Zeitschrift für Physik B Condensed Matter* **102**, 455–459 (1997).
58. Atitoaie, A., Tanasa, R. & Enachescu, C. Size dependent thermal hysteresis in spin crossover nanoparticles reflected within a Monte Carlo based Ising-like model. *Journal of Magnetism and Magnetic Materials* **324**, 1596–1600 (2012).
59. Boukheddaden, K., Linares, J., Spiering, H. & Varret, F. One-dimensional Ising-like systems: an analytical investigation of the static and dynamic properties, applied to spin-crossover relaxation. *The European Physical Journal B - Condensed Matter and Complex Systems* **15**, 317–326 (2000).
60. Atitoaie, A., Tanasa, R., Stancu, A. & Enachescu, C. Study of spin crossover nanoparticles thermal hysteresis using FORC diagrams on an Ising-like model. *Journal of Magnetism and Magnetic Materials* **368**, 12–18 (2014).
61. Muraoka, A., Boukheddaden, K., Linares, J. & Varret, F. Two-dimensional Ising-like model with specific edge effects for spin-crossover nanoparticles: A Monte Carlo study. *Phys. Rev. B* **84**, 054119 (2011).
62. Varret, F. *et al.* The Ising-like model applied to switchable inorganic solids: discussion of the static properties. *Comptes Rendus Chimie* **6**, 385–393 (2003).
63. Gaina, R., Enachescu, C. & Cuza, A. I. Nucleation in Spin Transition Molecular Magnets: a Parallel Between Ising-like and Mechanoelastic Models. *Proceedings of the Romanian Academy* **18**, 215–222 (2016).

64. Nishino, M. *et al.* Macroscopic nucleation phenomena in continuum media with long-range interactions. *Sci Rep* **1**, 162 (2011).
65. Enachescu, C., Stoleriu, L., Stancu, A. & Hauser, A. Model for Elastic Relaxation Phenomena in Finite 2D Hexagonal Molecular Lattices. *Phys. Rev. Lett.* **102**, 257204 (2009).
66. Enachescu, C. *et al.* Cluster evolution in spin crossover systems observed in the frame of a mechano-elastic model. *EPL* **91**, 27003 (2010).
67. Stoleriu, L., Chakraborty, P., Hauser, A., Stancu, A. & Enachescu, C. Thermal hysteresis in spin-crossover compounds studied within the mechanoelastic model and its potential application to nanoparticles. *Phys. Rev. B* **84**, 134102 (2011).
68. Enachescu, C. & Hauser, A. Study of switching in spin transition compounds within the mechanoelastic model with realistic parameters. *Phys. Chem. Chem. Phys.* **18**, 20591–20599 (2016).
69. Nishino, M., Boukheddaden, K., Konishi, Y. & Miyashita, S. Simple Two-Dimensional Model for the Elastic Origin of Cooperativity among Spin States of Spin-Crossover Complexes. *Phys. Rev. Lett.* **98**, 247203 (2007).
70. Konishi, Y., Tokoro, H., Nishino, M. & Miyashita, S. Monte Carlo Simulation of Pressure-Induced Phase Transitions in Spin-Crossover Materials. *Phys. Rev. Lett.* **100**, 067206 (2008).
71. Nicolazzi, W., Pillet, S. & Lecomte, C. Two-variable anharmonic model for spin-crossover solids: A like-spin domains interpretation. *Phys. Rev. B* **78**, 174401 (2008).
72. Nicolazzi, W. & Pillet, S. Structural aspects of the relaxation process in spin crossover solids: Phase separation, mapping of lattice strain, and domain wall structure. *Phys. Rev. B* **85**, 094101 (2012).
73. Enachescu, C. & Nicolazzi, W. Elastic models, lattice dynamics and finite size effects in molecular spin crossover systems. *Comptes Rendus Chimie* **21**, 1179–1195 (2018).
74. Ndiaye, M., Belmouri, N. E. I., Linares, J. & Boukheddaden, K. Elastic Origin of the Unsymmetrical Thermal Hysteresis in Spin Crossover Materials: Evidence of Symmetry Breaking. *Symmetry* **13** (2021).
75. Milin, E. *et al.* Elastic Frustration Triggering Photoinduced Hidden Hysteresis and Multistability in a Two-Dimensional Photoswitchable Hofmann-Like Spin-Crossover Metal–Organic Framework. *Inorg. Chem.* **55**, 11652–11661 (2016).
76. Kusz, J., Zubko, M., Neder, R. B. & Gütllich, P. Structural phase transition to disorder low-temperature phase in $[\text{Fe}(\text{ptz})_6](\text{BF}_4)_2$ spin-crossover compounds. *Acta Crystallogr B Struct Sci* **68**, 40–56 (2012).
77. Singh, Y., Oubouchou, H., Nishino, M., Miyashita, S. & Boukheddaden, K. Elastic-frustration-driven unusual magnetoelastic properties in a switchable core-shell spin-crossover nanostructure. *Phys. Rev. B* **101**, 054105 (2020).

78. Traiche, R., Sy, M. & Boukheddaden, K. Elastic Frustration in 1D Spin-Crossover Chains: Evidence of Multi-Step Transitions and Self-Organizations of the Spin States. *J. Phys. Chem. C* **122**, 4083–4096 (2018).
79. Chorazy, S. *et al.* Octacyanidorhenate(V) Ion as an Efficient Linker for Hysteretic Two-Step Iron(II) Spin Crossover Switchable by Temperature, Light, and Pressure. *Angew. Chem.* **132**, 15871–15879 (2020).
80. Ridier, K., Molnár, G., Salmon, L., Nicolazzi, W. & Bousseksou, A. Hysteresis, nucleation and growth phenomena in spin-crossover solids. *Solid State Sciences* **74**, A1–A22 (2017).
81. Iasco, O. *et al.* The disentangling of hysteretic spin transition, polymorphism and metastability in bistable thin films formed by sublimation of bis(scorpionate) Fe^{II} molecules. *J. Mater. Chem. C* **5**, 11067–11075 (2017).
82. Halcrow, M. A. Structure: function relationships in molecular spin-crossover complexes. *Chem. Soc. Rev.* **40**, 4119–4142 (2011).
83. Pillet, S., Hubsch, J. & Lecomte, C. Single crystal diffraction analysis of the thermal spin conversion in [Fe(btr)₂(NCS)₂](H₂O): evidence for spin-like domain formation. *The European Physical Journal B - Condensed Matter and Complex Systems* **38**, 541–552 (2004).
84. Chong, C., Varret, F. & Boukheddaden, K. Evolution of self-organized spin domains under light in single-crystalline [Fe(ptz)₆](BF₄)₂. *Phys. Rev. B* **81**, 014104 (2010).
85. Slimani, A. *et al.* Visualization and quantitative analysis of spatiotemporal behavior in a first-order thermal spin transition: A stress-driven multiscale process. *Phys. Rev. B* **84**, 094442 (2011).
86. Slimani, A. *et al.* Velocity of the High-Spin Low-Spin Interface Inside the Thermal Hysteresis Loop of a Spin-Crossover Crystal, via Photothermal Control of the Interface Motion. *Phys. Rev. Lett.* **110**, 087208 (2013).
87. McGarvey, J. J. & Lawthers, I. Photochemically-induced Perturbation of the ¹A ↔ ⁵T Equilibrium in Fe^{II} Complexes by Pulsed Laser Irradiation in the Metal-to-ligand Charge-transfer Absorption Band. *J. Chem. Soc., Chem. Commun.*, 2 (1982).
88. Decurtins, S, Gutlich, P., Köhler, C. P., Spiering, H & Hauser, A. Light-Induced Excited Spin State Trapping in a Transition-Metal Complex: The Hexa-1-propyltetrazole-iron(II) tetrafluoroborate Spin-Crossover System. *Chemical Physics Letters* **105**, 4 (1984).
89. Hauser, A. Intersystem crossing in the [Fe(ptz)₆](BF₄)₂ spin-crossover system (ptz=1-propyltetrazole). *The Journal of Chemical Physics* **94**, 2741–2748 (1991).
90. McCusker, J. K. *et al.* Sub-picosecond ΔS = 2 intersystem crossing in low-spin ferrous complexes. *J. Am. Chem. Soc.* **114**, 6919–6920 (1992).
91. McCusker, J. K. *et al.* Subpicosecond ¹MLCT → ⁵T₂ Intersystem Crossing of Low-spin Polypyridyl Ferrous Complexes. *J. Am. Chem. Soc.* **115**, 298–307 (1993).

92. Marino, A. *et al.* The Role of Ligand-Field States in the Ultrafast Photophysical Cycle of the Prototypical Iron(II) Spin-Crossover Compound $[\text{Fe}(\text{ptz})_6](\text{BF}_4)_2$. *Angew. Chem. Int. Ed.* **53**, 3863–3867 (2014).
93. Hauser, A. Reversibility of light-induced excited spin state trapping in the $\text{Fe}(\text{ptz})_6(\text{BF}_4)_2$, and the $\text{Zn}_{1-x}\text{Fe}_x(\text{ptz})_6(\text{BF}_4)_2$ spin-crossover systems. *Chemical Physics Letters* **124**, 543–548 (1986).
94. Bertoni, R. *et al.* Ultrafast Light-Induced Spin-State Trapping Photophysics Investigated in $\text{Fe}(\text{phen})_2(\text{NCS})_2$ Spin-Crossover Crystal. *Acc. Chem. Res.* **48**, 774–781 (2015).
95. Bertoni, R. *et al.* Elastically driven cooperative response of a molecular material impacted by a laser pulse. *Nature Mater* **15**, 606–610 (2016).
96. Brady, C., McGarvey, J. J., McCusker, J. K., Toftlund, H. & Hendrickson, D. N. in *Spin Crossover in Transition Metal Compounds III* 1–22 (Springer-Verlag, Berlin/Heidelberg, 2004).
97. Cammarata, M. *et al.* Sequential Activation of Molecular Breathing and Bending during Spin-Crossover Photoswitching Revealed by Femtosecond Optical and X-Ray Absorption Spectroscopy. *Phys. Rev. Lett.* **113**, 227402 (2014).
98. Guionneau, P. & Collet, E. in *Spin-Crossover Materials* (ed Halcrow, M. A.) 507–526 (John Wiley & Sons Ltd, Oxford, UK, 2013).
99. Huse, N. *et al.* Femtosecond Soft X-ray Spectroscopy of Solvated Transition-Metal Complexes: Deciphering the Interplay of Electronic and Structural Dynamics. *J. Phys. Chem. Lett.* **2**, 880–884 (2011).
100. Jiang, Y. *et al.* Structural Dynamics upon Photoexcitation in a Spin Crossover Crystal Probed with Femtosecond Electron Diffraction. *Angew. Chem. Int. Ed.* **56**, 7130–7134 (2017).
101. Ridier, K. *et al.* Finite Size Effects on the Switching Dynamics of Spin-Crossover Thin Films Photoexcited by a Femtosecond Laser Pulse. *Adv. Mater.* **31**, 1901361 (2019).
102. Buhks, E., Navon, G., Bixon, M. & Jortner, J. Spin conversion processes in solutions. *J. Am. Chem. Soc.* **102**, 2918–2923 (1980).
103. Hauser, A., Enachescu, C., Daku, M. L., Vargas, A. & Amstutz, N. Low-temperature lifetimes of metastable high-spin states in spin-crossover and in low-spin iron(II) compounds: The rule and exceptions to the rule. *Coordination Chemistry Reviews* **250**, 1642–1652 (2006).
104. Hauser, A. Cooperative effects on the HS→LS relaxation in the $[\text{Fe}(\text{ptz})_6](\text{BF}_4)_2$ spin-crossover system. *Chemical Physics Letters* **192**, 65–70 (1992).
105. Boukheddaden, K., Shteto, I., Hôo, B. & Varret, F. Dynamical model for spin-crossover solids. II. Static and dynamic effects of light in the mean-field approach. *Phys. Rev. B* **62**, 14806–14817 (2000).

106. Enachescu, C. *et al.* Direct access to the photo-excitation and relaxation terms in photo-switchable solids: non-linear aspects. *Journal of Physics and Chemistry of Solids* **62**, 1409–1422 (2001).
107. Herber, R. H. VTFTIR and light-induced excited spin state trapping in n Fe(2,2'-bpy)₂(SCN)₂ and related spin-crossover compounds. *Inorg. Chem.* **26**, 173–178 (1987).
108. Létard, J.-F. *et al.* Structural, Magnetic, and Photomagnetic Studies of a Mononuclear Iron(II) Derivative Exhibiting an Exceptionally Abrupt Spin Transition. Light-Induced Thermal Hysteresis Phenomenon. *Inorg. Chem.* **37**, 4432–4441 (1998).
109. Matar, S. F., Guionneau, P. & Chastanet, G. Multiscale Experimental and Theoretical Investigations of Spin Crossover FeII Complexes: Examples of [Fe(phen)₂(NCS)₂] and [Fe(PM-BiA)₂(NCS)₂]. *International Journal of Molecular Sciences* **16**, 4007–4027 (2015).
110. Viquerat, B., Degert, J., Létard, J. F. & Freysz, E. Relaxation oscillations during the laser-induced spin state transition of a [Fe(PM-BiA)₂(NCS)₂] complex. *Phys. Rev. B* **87**, 024303 (2013).
111. Ichiyanagi, K. *et al.* Nature and mechanism of the photoinduced spin transition in [Fe(PM-BiA)₂(NCS)₂]. *Phys. Rev. B* **73**, 060408 (2006).
112. Kulmaczewski, R. *et al.* The role of symmetry breaking in the structural trapping of light-induced excited spin states. *Chem. Commun.* **53**, 13268–13271 (2017).
113. Enachescu, C., Stoleriu, L., Stancu, A. & Hauser, A. Competition between photoexcitation and relaxation in spin-crossover complexes in the frame of a mechanoelastic model. *Phys. Rev. B* **82**, 104114 (2010).
114. Desaix, A. *et al.* Light-induced bistability in spin transition solids leading to thermal and optical hysteresis. *Eur. Phys. J. B* **6**, 183–193 (1998).
115. Hauser, A., Guetlich, P. & Spiering, H. High-spin \rightarrow low-spin relaxation kinetics and cooperative effects in the hexakis(1-propyltetrazole)iron bis(tetrafluoroborate) and [Zn_{1-x}Fe_x(ptz)₆](BF₄)₂ (ptz = 1-propyltetrazole) spin-crossover systems. *Inorg. Chem.* **25**, 4245–4248 (1986).
116. Hauser, A., Jeftić, J., Romstedt, H., Hinek, R. & Spiering, H. Cooperative phenomena and light-induced bistability in iron(II) spin-crossover compounds. *Coordination Chemistry Reviews* **190–192**, 471–491 (1999).
117. Enachescu, C. *et al.* Photoexcitation and Relaxation Properties of a Spin-Crossover Solid in the Case of a Stable High-Spin State. *J. Phys. Chem. B* **110**, 5883–5888 (2006).
118. Ogawa, Y. *et al.* Dynamical Aspects of the Photoinduced Phase Transition in Spin-Crossover Complexes. *Phys. Rev. Lett.* **84**, 3181–3184 (2000).
119. Létard, J.-F. *et al.* Spin Crossover Properties of the [Fe(PM-BiA)₂(NCS)₂] Complex – Phases I and II. *Chemical Monthly* **134**, 165–182 (2003).

120. Varret, F., Boukheddaden, K., Jeftic, J. & Roubeau, O. A Macroscopic Approach to the Light-Induced Instability of Cooperative Photo-Switchable Systems. *Molecular Crystals and Liquid Crystals Science and Technology. Section A. Molecular Crystals and Liquid Crystals* **335**, 561–572 (1999).
121. Baldé, C., Desplanches, C., Gütlich, P., Freysz, E. & Létard, J. Effect of the metal dilution on the thermal and light-induced spin transition in $[\text{Fe}_x\text{Mn}_{1-x}(\text{bpp})_2](\text{NCSe})_2$: When T(LIESST) reaches $T_{1/2}$. *Inorganica Chimica Acta* **361**, 3529–3533 (2008).
122. Varret, F., Boukheddaden, K., Chastanet, G., Paradis, N. & Létard, J.-F. When T(LIESST) Meets Thermal Hysteresis – a Theoretical Approach. *European Journal of Inorganic Chemistry* **2013**, 763–769 (2013).
123. Koshino, K. & Ogawa, T. Theory of the photoinduced spin-state transitions in spin-crossover complexes. *Journal of Luminescence* **87–89**, 642–645 (2000).
124. Enachescu, C., Linares, J. & Varret, F. Comparison of static and light-induced thermal hystereses of a spin-crossover solid, in a mean-field approach [†]. *J. Phys.: Condens. Matter* **13**, 2481–2495 (2001).
125. Varret, F., Paez-Espejo, M. & Boukheddaden, K. Light-induced instability generated by photo-thermal effect in switchable molecular crystals. *EPL* **104**, 27003 (2013).
126. Gudyma, I. & Maksymov, A. Optically induced switching in spin-crossover compounds: microscopic and macroscopic models and their relationship. *Appl. Opt.* **51**, C55 (2012).
127. Plesca, D. *et al.* Unexpected Light-Induced Thermal Hysteresis in Matrix Embedded Low Cooperative Spin Crossover Microparticles. *Magnetochemistry* **7**, 59 (2021).
128. Jeftić, J. *et al.* Quasi-static nature of the light induced thermal hysteresis in $[\text{Fe}(\text{ptz})_6](\text{BF}_4)_2$ spin-transition solid. *Polyhedron* **20**, 1599–1606 (2001).
129. Light-Induced Bistability in the 2D Coordination Network $[\text{Fe}(\text{bbtr})_3][\text{BF}_4]_2$.
130. Chakraborty, P., Enachescu, C., Walder, C., Bronisz, R. & Hauser, A. Thermal and Light-Induced Spin Switching Dynamics in the 2D Coordination Network of $[\text{Zn}_{1-x}\text{Fe}_x(\text{bbtr})_3](\text{ClO}_4)_2$: The Role of Cooperative Effects. *Inorg. Chem.* **51**, 9714–9722 (2012).
131. Legrand, V. *et al.* Optical, Magnetic and Structural Properties of the Spin-Crossover Complex $[\text{Fe}(\text{btr})_2(\text{NCS})_2] \cdot \text{H}_2\text{O}$ in the Light-Induced and Thermally Quenched Metastable States. *Eur. J. Inorg. Chem.* **2007**, 5693–5706 (2007).
132. Enachescu, C. *et al.* First-order reversal curves analysis of rate-dependent hysteresis: The example of light-induced thermal hysteresis in a spin-crossover solid. *Phys. Rev. B* **72**, 054413 (2005).
133. Hauser, A., Hinek, R., Spiering, H. & Gütlich, P. The $[\text{Fe}(\text{etz})_6](\text{BF}_4)_2$ Spin-Crossover System—Part Two: Hysteresis in the LIESST Regime. *Chemistry – A European Journal* **2** (1996).
134. Sciortino, N. F. *et al.* Thermal- and Light-Induced Spin-Crossover Bistability in a Disrupted Hofmann-Type 3D Framework. *Inorg. Chem.* **53**, 7886–7893 (2014).

135. Enachescu, C. *et al.* Static and light induced hysteresis in spin-crossover compounds: experimental data and application of Preisach-type models. *Physica B: Condensed Matter* **306**, 155–160 (2001).
136. Enachescu, C. *et al.* Rate-dependent light-induced thermal hysteresis of $[\text{Fe}(\text{PM-BiA})_2(\text{NCS})_2]$ spin transition complex. *Journal of Applied Physics* **99**, 08J504 (2006).
137. Klokishner, S. & Linares, J. Effects of Intra- and Intercenter Interactions in Spin Crossover: Application of the Density Matrix Method to the Nonequilibrium Low-Spin-High-Spin Transitions Induced by Light. *J. Phys. Chem. C* **111**, 10644–10651 (2007).
138. Boonprab, T. *et al.* The First Observation of Hidden Hysteresis in an Iron(III) Spin-Crossover Complex. *Angew. Chem. Int. Ed.* **58**, 11811–11815 (2019).
139. Varret, F. *et al.* Light-induced thermal hysteresis and intensity thresholds in molecular switchable solids, by mean-field macroscopic master equation approach: Discussion of the experimental data obtained for Co–Fe Prussian Blue Analogues. *Polyhedron* **24**, 2857–2863 (2005).
140. Schmidt, R. D., Shultz, D. A., Martin, J. D. & Boyle, P. D. Goldilocks Effect in Magnetic Bistability: Remote Substituent Modulation and Lattice Control of Photoinduced Valence Tautomerism and Light-Induced Thermal Hysteresis. *J. Am. Chem. Soc.* **132**, 6261–6273 (2010).
141. Liu, X. J., Moritomo, Y., Kawamoto, T., Nakamoto, A. & Kojima, N. Optical hysteresis in a spin-crossover complex. *Phys. Rev. B* **67**, 012102 (2003).
142. Boukheddaden, K., Fourati, H., Singh, Y. & Chastanet, G. Evidence of Photo-Thermal Effects on the First-Order Thermo-Induced Spin Transition of $[\{\text{Fe}(\text{NCSe})(\text{py})_2\}_2(\text{m-bppyz})]$ Spin-Crossover Material. *Magnetochemistry* **5**, 21 (2019).
143. Renz, F., Spiering, H., Goodwin, H. A. & Gutlich, P. Light-perturbed hysteresis in an iron(II) spin-crossover compound observed by the Mössbauer effect. *Hyperfine Interactions* **126**, 155–158 (2000).
144. Collison, D. *et al.* Soft X-ray induced excited spin state trapping and soft X-ray photochemistry at the iron $L_{2,3}$ edge in $[\text{Fe}(\text{phen})_2(\text{NCS})_2]$ and $[\text{Fe}(\text{phen})_2(\text{NCSe})_2]$ (phen = 1,10-phenanthroline). *J. Chem. Soc., Dalton Trans.*, 4371–4376 (1997).
145. Kipgen, L. *et al.* Soft-x-ray-induced spin-state switching of an adsorbed Fe(II) spin-crossover complex. *J. Phys.: Condens. Matter* **29**, 394003 (2017).
146. Vankó, G., Renz, F., Molnár, G., Neisius, T. & Kárpáti, S. Hard-X-ray-Induced Excited-Spin-State Trapping. *Angew. Chem. Int. Ed.* **46**, 5306–5309 (2007).
147. Kumar, K. S. & Ruben, M. Sublimable Spin-Crossover Complexes: From Spin-State Switching to Molecular Devices. *Angew. Chem. Int. Ed.* **60**, 7502–7521 (2021).
148. Cavallini, M. *et al.* Micro- and Nanopatterning of Spin-Transition Compounds into Logical Structures. *Angew. Chem. Int. Ed.* **47**, 8596–8600 (2008).
149. Cavallini, M. Status and perspectives in thin films and patterning of spin crossover compounds. *Phys. Chem. Chem. Phys.* **14**, 11867 (2012).

150. Shepherd, H. J., Molnár, G., Nicolazzi, W., Salmon, L. & Bousseksou, A. Spin Crossover at the Nanometre Scale. *Eur. J. Inorg. Chem.* **2013**, 653–661 (2013).
151. Quintero, C. M. *et al.* Hybrid spin-crossover nanostructures. *Beilstein J. Nanotechnol.* **5**, 2230–2239 (2014).
152. Mallah, T. & Cavallini, M. Surfaces, thin films and patterning of spin crossover compounds. *Comptes Rendus Chimie* **21**, 1270–1286 (2018).
153. Hao, G. *et al.* Nonvolatile voltage controlled molecular spin state switching. *Appl. Phys. Lett.* **114**, 032901 (2019).
154. Davesne, V. *et al.* Hysteresis and change of transition temperature in thin films of $\text{Fe}\{[\text{Me}_2\text{Pyrz}]_3\text{BH}\}_2$, a new sublimable spin-crossover molecule. *The Journal of Chemical Physics* **142**, 194702 (2015).
155. Real, J. A., Muñoz, M. C., Faus, J. & Solans, X. Spin Crossover in Novel Dihydrobis(1-pyrazolyl)borate $[\text{H}_2\text{B}(\text{pz})_2]$ -Containing Iron(II) Complexes. Synthesis, X-ray Structure, and Magnetic Properties of $[\text{Fe}(\text{L})(\text{H}_2\text{B}(\text{pz})_2)_2]$ ($\text{L} = 1,10\text{-Phenanthroline}$ and $2,2'\text{-Bipyridine}$). *Inorg. Chem.* **36**, 3008–3013 (1997).
156. Gruber, M. *et al.* Spin crossover in $\text{Fe}(\text{phen})_2(\text{NCS})_2$ complexes on metallic surfaces. *The Journal of Chemical Physics* **146**, 092312 (2017).
157. Bernien, M. *et al.* Spin Crossover in a Vacuum-Deposited Submonolayer of a Molecular Iron(II) Complex. *J. Phys. Chem. Lett.* **3**, 3431–3434 (2012).
158. Salmon, L. *et al.* Re-investigation of the spin crossover phenomenon in the ferrous complex $[\text{Fe}(\text{HB}(\text{pz})_3)_2]$. *New J. Chem.* **33**, 1283 (2009).
159. Mahfoud, T. *et al.* Electrical properties and non-volatile memory effect of the $[\text{Fe}(\text{HB}(\text{pz})_3)_2]$ spin crossover complex integrated in a microelectrode device. *Appl. Phys. Lett.* **99**, 053307 (2011).
160. Rat, S. *et al.* Solvatomorphism and structural-spin crossover property relationship in bis[hydrotris(1,2,4-triazol-1-yl)borate]iron(ii). *CrystEngComm* **19**, 3271–3280 (2017).
161. Atzori, M. *et al.* Thermal and light-induced spin transition in a nanometric film of a new high-vacuum processable spin crossover complex. *J. Mater. Chem. C* **6**, 8885–8889 (2018).
162. Rohlf, S. *et al.* Influence of Substrate Electronic Properties on the Integrity and Functionality of an Adsorbed Fe(II) Spin-Crossover Compound. *J. Phys. Chem. C* **123**, 17774–17780 (2019).
163. Jasper-Tönnies, T. *et al.* Deposition of a Cationic Fe^{III} Spin-Crossover Complex on Au(111): Impact of the Counter Ion. *J. Phys. Chem. Lett.* **8**, 1569–1573 (2017).
164. Hayami, S. *et al.* First Observation of Light-Induced Excited Spin State Trapping for an Iron(III) Complex. *J. Am. Chem. Soc.* **122**, 7126–7127 (2000).
165. Galán-Mascarós, J. R. *et al.* Tuning Size and Thermal Hysteresis in Bistable Spin Crossover Nanoparticles. *Inorg. Chem.* **49**, 5706–5714 (2010).

166. Tanaka, D. *et al.* Thin films of spin-crossover coordination polymers with large thermal hysteresis loops prepared by nanoparticle spin coating. *Chem. Commun.* **50**, 10074–10077 (2014).
167. Volatron, F. *et al.* Spin-Crossover Coordination Nanoparticles. *Inorg. Chem.* **47**, 6584–6586 (2008).
168. Martinho, P. N., Rajnak, C. & Ruben, M. in *Spin-Crossover Materials* (ed Halcrow, M. A.) 375–404 (John Wiley & Sons Ltd, Oxford, UK, 2013).
169. Devid, E. J. *et al.* Spin Transition in Arrays of Gold Nanoparticles and Spin Crossover Molecules. *ACS Nano* **9**, 4496–4507 (2015).
170. Rubio-Giménez, V. *et al.* Effect of nanostructuration on the spin crossover transition in crystalline ultrathin films. *Chem. Sci.* **10**, 4038–4047 (2019).
171. Larionova, J. *et al.* Towards the Ultimate Size Limit of the Memory Effect in Spin-Crossover Solids. *Angew. Chem. Int. Ed.* **47**, 8236–8240 (2008).
172. Meded, V. *et al.* Electrical control over the Fe(II) spin crossover in a single molecule: Theory and experiment. *Phys. Rev. B* **83**, 245415 (2011).
173. Jiang, X. *et al.* Tunable spin-state bistability in a spin crossover molecular complex. *J. Phys.: Condens. Matter* **31**, 315401 (2019).
174. Gruber, M. & Berndt, R. Spin-Crossover Complexes in Direct Contact with Surfaces. *Magnetochemistry* **6**, 35 (2020).
175. Kipgen, L., Bernien, M., Tuczek, F. & Kuch, W. Spin-Crossover Molecules on Surfaces: From Isolated Molecules to Ultrathin Films. *Adv. Mater.* **33**, 2008141 (2021).
176. Djeghloul, F. *et al.* High Spin Polarization at Ferromagnetic Metal–Organic Interfaces: A Generic Property. *J. Phys. Chem. Lett.* **7**, 2310–2315 (2016).
177. Gruber, M. *et al.* Spin-Dependent Hybridization between Molecule and Metal at Room Temperature through Interlayer Exchange Coupling. *Nano Lett.* **15**, 7921–7926 (2015).
178. Rocha, A. R. *et al.* Towards molecular spintronics. *Nature Materials* **4**, 335–339 (2005).
179. Bellec, A., Lagoute, J. & Repain, V. Molecular electronics: Scanning tunneling microscopy and single-molecule devices. *Comptes Rendus Chimie* **21**, 1287–1299 (2018).
180. Barraud, C. *et al.* Unravelling the role of the interface for spin injection into organic semiconductors. *Nature Phys* **6**, 615–620 (2010).
181. Sanvito, S. The rise of spinterface science. *Nature Phys* **6**, 562–564 (2010).
182. Kuch, W. & Bernien, M. Controlling the magnetism of adsorbed metal–organic molecules. *J. Phys.: Condens. Matter* **29**, 023001 (2017).
183. Neaton, J. B., Hybertsen, M. S. & Louie, S. G. Renormalization of Molecular Electronic Levels at Metal-Molecule Interfaces. *Phys. Rev. Lett.* **97**, 216405 (2006).
184. Shi, S. *et al.* Study of molecular spin-crossover complex Fe(phen)₂(NCS)₂ thin films. *Appl. Phys. Lett.* **95**, 043303 (2009).

185. Miyamachi, T. *et al.* Robust spin crossover and memristance across a single molecule. *Nat Commun* **3**, 938 (2012).
186. Gueddida, S. & Alouani, M. Spin crossover in a single Fe(phen)₂(NCS)₂ molecule adsorbed onto metallic substrates: An *ab initio* calculation. *Phys. Rev. B* **87**, 144413 (2013).
187. Gruber, M. *Electronic and magnetic properties of hybrid interfaces : from single molecules to ultra-thin molecular films on metallic substrates* PhD Thesis (2014).
188. Gueddida, S. *et al.* Exchange Coupling of Spin-Crossover Molecules to Ferromagnetic Co Islands. *J. Phys. Chem. Lett.* **7**, 900–904 (2016).
189. Gueddida, S. & Alouani, M. Calculated impact of ferromagnetic substrate on the spin crossover in a Fe(1,10-phenanthroline)₂(NCS)₂ molecule. *Phys. Rev. B* **93**, 184433 (2016).
190. Tautz, F. Structure and bonding of large aromatic molecules on noble metal surfaces: The example of PTCDA. *Progress in Surface Science* **82**, 479–520 (2007).
191. Hoffmann, R. A chemical and theoretical way to look at bonding on surfaces. *Rev. Mod. Phys.* **60**, 601–628 (1988).
192. Gruber, M. *et al.* Spin state of spin-crossover complexes: From single molecules to ultrathin films. *Phys. Rev. B* **89**, 195415 (2014).
193. Schreyer, A. *et al.* Oscillatory exchange coupling in Co/Cu(111) superlattices. *Phys. Rev. B* **47**, 15334–15337 (1993).
194. Bruno, P. & Chappert, C. Oscillatory coupling between ferromagnetic layers separated by a nonmagnetic metal spacer. *Phys. Rev. Lett.* **67**, 1602–1605 (1991).
195. Stiles, M. D. Interlayer exchange coupling. *Journal of Magnetism and Magnetic Materials* **200**, 322–337 (1999).
196. Bauer, E., Duden, T. & Zdyb, R. Spin-polarized low energy electron microscopy of ferromagnetic thin films. *Journal of Physics D: Applied Physics* **35**, 2327–2331 (2002).
197. Naggert, H. *et al.* First observation of light-induced spin change in vacuum deposited thin films of iron spin crossover complexes. *Dalton Trans.* **40**, 6364 (2011).
198. Palamarciuc, T. *et al.* Spin crossover materials evaporated under clean high vacuum and ultra-high vacuum conditions: from thin films to single molecules. *Journal of Materials Chemistry* **22**, 9690 (2012).
199. Gopakumar, T. G. *et al.* Electron-Induced Spin Crossover of Single Molecules in a Bilayer on Gold. *Angew. Chem. Int. Ed.* **51**, 6262–6266 (2012).
200. Bernien, M. *et al.* Highly Efficient Thermal and Light-Induced Spin-State Switching of an Fe(II) Complex in Direct Contact with a Solid Surface. *ACS Nano* **9**, 8960–8966 (2015).
201. Gopakumar, T. G. *et al.* Spin-Crossover Complex on Au(111): Structural and Electronic Differences Between Mono- and Multilayers. *Chem. Eur. J.* **19**, 15702–15709 (2013).

202. Ossinger, S. *et al.* Vacuum-Evaporable Spin-Crossover Complexes in Direct Contact with a Solid Surface: Bismuth versus Gold. *J. Phys. Chem. C* **121**, 1210–1219 (2017).
203. Ossinger, S. *et al.* Effect of ligand methylation on the spin-switching properties of surface-supported spin-crossover molecules. *J. Phys.: Condens. Matter* **32**, 114003 (2020).
204. Naggert, H. *et al.* Vacuum-evaporable spin-crossover complexes: physicochemical properties in the crystalline bulk and in thin films deposited from the gas phase. *J. Mater. Chem. C* **3**, 7870–7877 (2015).
205. Poggini, L. *et al.* Surface effects on a photochromic spin-crossover iron(II) molecular switch adsorbed on highly oriented pyrolytic graphite. *Nanoscale* **11**, 20006–20014 (2019).
206. Warner, B. *et al.* Temperature- and Light-Induced Spin Crossover Observed by X-ray Spectroscopy on Isolated Fe(II) Complexes on Gold. *J. Phys. Chem. Lett.* **4**, 1546–1552 (2013).
207. Kipgen, L. *et al.* Evolution of cooperativity in the spin transition of an iron(II) complex on a graphite surface. *Nat Commun* **9**, 2984 (2018).
208. Wäckerlin, C. *et al.* Excited Spin-State Trapping in Spin Crossover Complexes on Ferroelectric Substrates. *J. Phys. Chem. C* **122**, 8202–8208 (2018).
209. Pronschinske, A. *et al.* Iron(ii) spin crossover films on Au(111): scanning probe microscopy and photoelectron spectroscopy. *Chem. Commun.* **49**, 10446 (2013).
210. Pronschinske, A. *et al.* Modification of Molecular Spin Crossover in Ultrathin Films. *Nano Lett.* **13**, 1429–1434 (2013).
211. Beniwal, S. *et al.* Surface-induced spin state locking of the $[\text{Fe}(\text{H}_2\text{B}(\text{pz})_2)_2(\text{bipy})]$ spin crossover complex. *J. Phys.: Condens. Matter* **28**, 206002 (2016).
212. Kumar, K. S. *et al.* Engineering On-Surface Spin Crossover: Spin-State Switching in a Self-Assembled Film of Vacuum-Sublimable Functional Molecule. *Adv. Mater.* **30**, 1705416 (2018).
213. Zhang, X. *et al.* The spin state of a molecular adsorbate driven by the ferroelectric substrate polarization. *Chem. Commun.* **50**, 2255 (2014).
214. Zhang, X. *et al.* Locking and Unlocking the Molecular Spin Crossover Transition. *Adv. Mater.* **29**, 1702257 (2017).
215. Zhang, X. *et al.* Indications of magnetic coupling effects in spin cross-over molecular thin films. *Chem. Commun.* **54**, 944–947 (2018).
216. Rohlf, S. *et al.* Light-Induced Spin Crossover in an Fe(II) Low-Spin Complex Enabled by Surface Adsorption. *J. Phys. Chem. Lett.* **9**, 1491–1496 (2018).
217. Jasper-Toennies, T. *et al.* Robust and Selective Switching of an Fe^{III} Spin-Crossover Compound on $\text{Cu}_2\text{N}/\text{Cu}(100)$ with Memristance Behavior. *Nano Lett.* **17**, 6613–6619 (2017).

218. Shalabaeva, V. *et al.* Unprecedented Size Effect on the Phase Stability of Molecular Thin Films Displaying a Spin Transition. *J. Phys. Chem. C* **121**, 25617–25621 (2017).
219. Shalabaeva, V. *et al.* Vacuum deposition of high-quality thin films displaying spin transition near room temperature. *J. Mater. Chem. C* **5**, 4419–4425 (2017).
220. Cailleau, H. *et al.* Structural dynamics of photoinduced molecular switching in the solid state. *Acta Crystallogr A Found Crystallogr* **66**, 189–197 (2010).
221. Collet, E. *et al.* Polymorphism in the spin-crossover ferric complexes [(TPA)Fe^{III}(TCC)]PF₆. *Acta Crystallogr B Struct Sci* **65**, 474–480 (2009).
222. Bairagi, K. *et al.* Temperature-, Light-, and Soft X-ray-Induced Spin Crossover in a Single Layer of Fe^{II}-Pyrazolylborate Molecules in Direct Contact with Gold. *J. Phys. Chem. C* **122**, 727–731 (2018).
223. Bairagi, K. *et al.* Molecular-scale dynamics of light-induced spin cross-over in a two-dimensional layer. *Nat Commun* **7**, 12212 (2016).
224. Haverkort, M. W., Zwierzycki, M. & Andersen, O. K. Multiplet ligand-field theory using Wannier orbitals. *Phys. Rev. B* **85**, 165113 (2012).
225. Haverkort, M. W. *et al.* Bands, resonances, edge singularities and excitons in core level spectroscopy investigated within the dynamical mean-field theory. *EPL (Europhysics Letters)* **108**, 57004 (2014).
226. Fourmental, C. *et al.* Importance of Epitaxial Strain at a Spin-Crossover Molecule–Metal Interface. *J. Phys. Chem. Lett.* **10**, 4103–4109 (2019).
227. Jesson, J. P., Trofimenko, S. & Eaton, D. R. Spectra and structure of some transition metal poly(1-pyrazolyl) borates. *J. Am. Chem. Soc.* **89**, 3148–3158 (1967).
228. Jesson, J. P., Trofimenko, S. & Eaton, D. R. Spin equilibria in octahedral iron(II) poly((1-pyrazolyl)-borates. *J. Am. Chem. Soc.* **89**, 3158–3164 (1967).
229. Eichhorn, D. M. & Armstrong, W. H. M{Hydrotris(3-phenylpyrazol-1-yl)borate}₂: sterically encumbered iron(II) and manganese(II) complexes. *Inorg. Chem.* **29**, 3607–3612 (1990).
230. Oliver, J. D., Mullica, D. F., Hutchinson, B. B. & Milligan, W. O. Iron-nitrogen bond lengths in low-spin and high-spin iron(II) complexes with poly(pyrazolyl)borate ligands. *Inorg. Chem.* **19**, 165–169 (1980).
231. Kelai, M. *et al.* Robust magnetic anisotropy of a monolayer of hexacoordinate Fe(II) complexes assembled on Cu(111). *Inorg. Chem. Front.* **8**, 2395–2404 (2021).
232. Groot, F. d. & Kotani, A. *Core level spectroscopy of solids Advances in condensed matter science* v. **6** (CRC Press, Boca Raton, 2008).
233. *Magnetism and Synchrotron Radiation: new Trends* (eds Beaurepaire, E., Bulou, H., Scheurer, F. & Kappler, J.-P.) (Springer Berlin Heidelberg, Berlin, Heidelberg, 2010).
234. *Magnetism: A Synchrotron Radiation Approach* (eds Beaurepaire, E. *et al.*) (Springer Berlin Heidelberg, Berlin, Heidelberg, 2006).

235. *Magnetism and Synchrotron Radiation: Towards the Fourth Generation Light Sources: Proceedings of the 6th International School "Synchrotron Radiation and Magnetism", Mittelwihr (France), 2012* (eds Beaurepaire, E., Bulou, H., Joly, L. & Scheurer, F.) (Springer International Publishing, Cham, 2013).
236. J. J. Sakurai, J. J. N. *Modern Quantum Mechanics (2nd Edition)* 2nd ed. (Addison Wesley, 2010).
237. Westre, T. E. *et al.* A Multiplet Analysis of Fe *K*-Edge $1s \rightarrow 3d$ Pre-Edge Features of Iron Complexes. *Journal of the American Chemical Society* **119** (1997).
238. Nozieres, P. & De Dominicis, C. T. Singularities in the X-Ray Absorption and Emission of Metals. One-Body Theory Exact Solution. *Phys. Rev.* **178**, 1097–1107 (1969).
239. Gunnarsson, O. & Schönhammer, K. Electron spectroscopies for Ce compounds in the impurity model. *Phys. Rev. B* **28**, 4315–4341 (1983).
240. Hu, Z. *et al.* Valence electron distribution in $\text{La}_2\text{Li}_{1/2}\text{Cu}_{1/2}\text{O}_4$, $\text{Nd}_2\text{Li}_{1/2}\text{Ni}_{1/2}\text{O}_4$, and $\text{La}_2\text{Li}_{1/2}\text{Co}_{1/2}\text{O}_4$. *Chemical Physics Letters* **297**, 321–328 (1998).
241. Wasinger, E. C., de Groot, F. M. F., Hedman, B., Hodgson, K. O. & Solomon, E. I. *L*-edge X-ray Absorption Spectroscopy of Non-Heme Iron Sites: Experimental Determination of Differential Orbital Covalency. *Journal of the American Chemical Society* **125** (2003).
242. Hocking, R. K. *et al.* Fe *L*-Edge XAS Studies of $\text{K}_4[\text{Fe}(\text{CN})_6]$ and $\text{K}_3[\text{Fe}(\text{CN})_6]$: A Direct Probe of Back-Bonding. *Journal of the American Chemical Society* **128** (2006).
243. De Groot, F. M. F., Fuggle, J. C., Thole, B. T. & Sawatzky, G. A. 2p x-ray absorption of 3d transition-metal compounds: An atomic multiplet description including the crystal field. *Phys. Rev. B* **42**, 5459–5468 (1990).
244. Thole, B. T. *et al.* 3d x-ray-absorption lines and the $3d^9 4f^{n+1}$ multiplets of the lanthanides. *Phys. Rev. B* **32**, 5107–5118 (1985).
245. Praetorius, C., Zinner, M., Hansmann, P., Haverkort, M. W. & Fauth, K. Exploring small energy scales with x-ray absorption and dichroism. *Phys. Rev. B* **93**, 165107 (2016).
246. Antonov, V. N., Shpak, A. P. & Yaresko, A. N. X-ray magnetic circular dichroism in d and f ferromagnetic materials: recent theoretical progress. Part I (Review Article). *Low Temperature Physics* **34**, 1–36 (2008).
247. Ballhausen, C. *Introduction to Ligand Field Theory* (McGraw-Hill, 1962).
248. Haverkort, M. H. *Forum - Quanty* 2020.
249. Glawion, S. *et al.* Two-Spinon and Orbital Excitations of the Spin-Peierls System TiOCl . *Phys. Rev. Lett.* **107**, 107402 (2011).
250. Pourousskii, L. V., Hansmann, P., Ferrero, M. & Georges, A. Theoretical Prediction and Spectroscopic Fingerprints of an Orbital Transition in CeCu_2Si_2 . *Phys. Rev. Lett.* **112**, 106407 (2014).

251. Willers, T. *et al.* Determining the In-Plane Orientation of the Ground-State Orbital of CeCu_2Si_2 . *Phys. Rev. Lett.* **109**, 046401 (2012).
252. Retegan, M. *Crispy: v0.7.3* 2019.
253. Krause, M. O. & Oliver, J. H. Natural widths of atomic *K* and *L* levels, *K* X-ray lines and several *K L L* Auger lines. *Journal of Physical and Chemical Reference Data* **8**, 329–338 (1979).
254. Figueroa, A. I. *et al.* Structural and magnetic properties of granular Co-Pt multilayers with perpendicular magnetic anisotropy. *Phys. Rev. B* **90**, 174421 (2014).
255. Van der Laan, G. & Figueroa, A. I. X-ray magnetic circular dichroism—A versatile tool to study magnetism. *Coordination Chemistry Reviews* **277–278**, 95–129 (2014).
256. Thole, B. T., Carra, P., Sette, F. & van der Laan, G. X-ray circular dichroism as a probe of orbital magnetization. *Phys. Rev. Lett.* **68**, 1943–1946 (1992).
257. Carra, P., Thole, B. T., Altarelli, M. & Wang, X. X-ray circular dichroism and local magnetic fields. *Phys. Rev. Lett.* **70**, 694–697 (1993).
258. Van der Laan, G. Relation between the angular dependence of magnetic x-ray dichroism and anisotropic ground-state moments. *Phys. Rev. B* **57**, 5250–5258 (1998).
259. Ohresser, P. *et al.* DEIMOS: A beamline dedicated to dichroism measurements in the 350–2500 eV energy range. *Review of Scientific Instruments* **85**, 013106 (2014).
260. Lagarde, B. *et al.* High efficiency multilayer gratings for monochromators in the energy range from 500 eV to 2500 eV. *Journal of Physics: Conference Series* **425**, 152012 (2013).
261. Joly, L. *et al.* Versatile variable temperature insert at the DEIMOS beamline for *in situ* electrical transport measurements. *J Synchrotron Rad* **23**, 652–657 (2016).
262. Bearden, J. A. & Burr, A. F. Reevaluation of X-Ray Atomic Energy Levels. *Rev. Mod. Phys.* **39**, 125–142 (1967).
263. Fuggle, J. C. & Mårtensson, N. Core-level binding energies in metals. *Journal of Electron Spectroscopy and Related Phenomena* **21**, 275–281 (1980).
264. Chen, C. T. *et al.* Experimental Confirmation of the X-Ray Magnetic Circular Dichroism Sum Rules for Iron and Cobalt. *Phys. Rev. Lett.* **75**, 152–155 (1995).
265. Binnig, G. & Rohrer, H. Scanning tunneling microscopy—from birth to adolescence. *Rev. Mod. Phys.* **59**, 615–625 (1987).
266. *Scanning Probe Microscopy* (eds Wiesendanger, R., von Klitzing, K. & Wiesendanger, R.) (Springer Berlin Heidelberg, Berlin, Heidelberg, 1998).
267. Bardeen, J. Tunnelling from a Many-Particle Point of View. *Phys. Rev. Lett.* **6**, 57–59 (1961).
268. Tersoff, J. & Hamann, D. R. Theory of the scanning tunneling microscope. *Phys. Rev. B* **31**, 805–813 (1985).

269. Ding, H. F., Pütter, S., Oepen, H. P. & Kirschner, J. Spin-reorientation transition in thin films studied by the component-resolved Kerr effect. *Phys. Rev. B* **63**, 134425 (2001).
270. Rodary, G. *et al.* Influence of grain boundaries on the magnetization reorientation transition in ultrathin films. *Phys. Rev. B* **75**, 184415 (2007).
271. Duden, T. & Bauer, E. Magnetic Domain Structure and Spin Reorientation Transition in the System Co/Au/W(110). *MRS Online Proceedings Library* **475**, 283–288 (1997).
272. Voigtländer, B., Meyer, G. & Amer, N. M. Epitaxial growth of thin magnetic cobalt films on Au(111) studied by scanning tunneling microscopy. *Phys. Rev. B* **44**, 10354–10357 (1991).
273. Allenspach, R., Stampanoni, M. & Bischof, A. Magnetic domains in thin epitaxial Co/Au(111) films. *Phys. Rev. Lett.* **65**, 3344–3347 (1990).
274. Oepen, H. P., Speckmann, M., Millev, Y. & Kirschner, J. Unified approach to thickness-driven magnetic reorientation transitions. *Phys. Rev. B* **55**, 2752–2755 (1997).
275. Oepen, H. P., Millev, Y. T. & Kirschner, J. The reorientation transition in Co/Au(111). *Journal of Applied Physics* **81**, 5044–5046 (1997).
276. Mishra, P., Qi, Z. K., Oka, H., Nakamura, K. & Komeda, T. Spatially Resolved Magnetic Anisotropy of Cobalt Nanostructures on the Au(111) Surface. *Nano Lett.* **17**, 5843–5847 (2017).
277. Bairagi, K. *Magnetic anisotropy and spin crossover at molecule-metal interfaces* PhD Thesis (2016).
278. Senthil Kumar, K. & Ruben, M. Emerging trends in spin crossover (SCO) based functional materials and devices. *Coordination Chemistry Reviews* **346**, 176–205 (2017).
279. Schleicher, F. *et al.* Linking Electronic Transport through a Spin Crossover Thin Film to the Molecular Spin State Using X-ray Absorption Spectroscopy Operando Techniques. *ACS Appl. Mater. Interfaces* **10**, 31580–31585 (2018).
280. Delgado, T. *et al.* The influence of the sample dispersion on a solid surface in the thermal spin transition of [Fe(pz)Pt(CN)₄] nanoparticles. *Phys. Chem. Chem. Phys.* **20**, 12493–12502 (2018).
281. Boukheddaden, K. & Bailly-Reyre, A. Towards the elastic properties of 3D spin-crossover thin films: Evidence of buckling effects. *EPL (Europhysics Letters)* **103**, 26005 (2013).
282. Slimani, A., Boukheddaden, K. & Yamashita, K. Effect of intermolecular interactions on the nucleation, growth, and propagation of like-spin domains in spin-crossover materials. *Phys. Rev. B* **92**, 014111 (2015).
283. Affes, K., Slimani, A., Maalej, A. & Boukheddaden, K. Electro-elastic modeling of thermal and mechanical properties of a spin crossover core/shell nanoparticle. *Chemical Physics Letters* **718**, 46–53 (2019).
284. Sethna, J. P. *et al.* Hysteresis and hierarchies: Dynamics of disorder-driven first-order phase transformations. *Phys. Rev. Lett.* **70**, 3347–3350 (1993).

285. Gear, C. W. *Numerical initial value problems in ordinary differential equations* (1971).
286. Enachescu, C., Nishino, M., Miyashita, S., Stoleriu, L. & Stancu, A. Monte Carlo Metropolis study of cluster evolution in spin-crossover solids within the framework of a mechanoelastic model. *Phys. Rev. B* **86**, 054114 (2012).
287. Knaak, T. *et al.* Fragmentation and Distortion of Terpyridine-Based Spin-Crossover Complexes on Au(111). *J. Phys. Chem. C* **123**, 4178–4185 (2019).
288. Davesne, V. *et al.* First glimpse of the soft x-ray induced excited spin-state trapping effect dynamics on spin cross-over molecules. *The Journal of Chemical Physics* **139**, 074708 (2013).
289. Schooneveld, M. M. v. & DeBeer, S. A close look at dose: Toward L-edge XAS spectral uniformity, dose quantification and prediction of metal ion photoreduction. *Journal of Electron Spectroscopy and Related Phenomena* **198**, 31–56 (2015).
290. Briois, V., Cartier dit Moulin, C., Sainctavit, P., Brouder, C. & Flank, A.-M. Full Multiple Scattering and Crystal Field Multiplet Calculations Performed on the Spin Transition Fe(phen)₂(NCS)₂ Complex at the Iron *K* and *L*_{2,3} X-ray Absorption Edges. *J. Am. Chem. Soc.* **117**, 1019–1026 (1995).
291. Neese, F. Software update: the ORCA program system, version 4.0. *WIREs Comput Mol Sci* **8** (2018).
292. Renz, F. *et al.* Hard-X-ray-Induced Thermal Hysteresis (HAXITH) in a Molecular Switchable Solid. *Eur. J. Inorg. Chem.* **2012**, 2653–2655 (2012).
293. Mori, T., Miyashita, S. & Rikvold, P. A. Asymptotic forms and scaling properties of the relaxation time near threshold points in spinodal-type dynamical phase transitions. *Phys. Rev. E* **81**, 011135 (2010).
294. Miyashita, S. *et al.* Threshold phenomena under photoexcitation of spin-crossover materials with cooperativity due to elastic interactions. *Phys. Rev. B* **80**, 064414 (2009).
295. Tong, Y. *et al.* Voltage-Induced Bistability of Single Spin-Crossover Molecules in a Two-Dimensional Monolayer. *J. Phys. Chem. Lett.* **12**, 11029–11034 (2021).
296. Johnson, P. B. & Christy, R. W. Optical Constants of the Noble Metals. *Phys. Rev. B* **6**, 4370–4379 (1972).
297. Petek, H. & Ogawa, S. Femtosecond time-resolved two-photon photoemission studies of electron dynamics in metals. *Progress in Surface Science* **56**, 239–310 (1997).
298. Pawlik, S., Bauer, M. & Aeschlimann, M. Lifetime difference of photoexcited electrons between intraband and interband transitions. *Surface Science* **377–379**, 206–209 (1997).
299. Molen, S. J. v. d. & Liljeroth, P. Charge transport through molecular switches. *Journal of Physics: Condensed Matter* **22**, 133001 (2010).
300. Tuchagues, J.-P., Bousseksou, A., Molnár, G., McGarvey, J. J. & Varret, F. in *Spin Crossover in Transition Metal Compounds III* 84–103 (Springer Berlin Heidelberg, Berlin, Heidelberg, 2004).

301. Kumagai, T. *et al.* Quantum tunneling in real space: Tautomerization of single porphycene molecules on the (111) surface of Cu, Ag, and Au. *The Journal of Chemical Physics* **148**, 102330 (2018).
302. Böckmann, H. *et al.* Direct Observation of Photoinduced Tautomerization in Single Molecules at a Metal Surface. *Nano Lett.* **16**, 1034–1041 (2016).
303. Greenaway, D. L., Harbeke, G., Bassani, F. & Tosatti, E. Anisotropy of the Optical Constants and the Band Structure of Graphite. *Phys. Rev.* **178**, 1340–1348 (3 1969).
304. Paradis, N. *et al.* Detailed Investigation of the Interplay Between the Thermal Decay of the Low Temperature Metastable HS State and the Thermal Hysteresis of Spin-Crossover Solids. *J. Phys. Chem. C* **119**, 20039–20050 (2015).
305. Chakraborty, P. *et al.* Persistent Bidirectional Optical Switching in the 2D High-Spin Polymer [Fe(bbtr)₃](BF₄)₂. *J. Am. Chem. Soc.* **134**, 4049–4052 (2012).
306. Ndiaye, M. M. *et al.* Hidden Hysteretic Behavior of a Paramagnetic Iron(II) Network Revealed by Light Irradiation. *Eur. J. Inorg. Chem.* **2018**, 305–313 (2018).
307. Létard, J.-F., Chastanet, G., Tokoro, H. & Ohkoshi, S.-i. Rubidium Manganese Hexacyanoferrate Solid Solutions: Towards Hidden Phases. *CIC* **6**, 34–39 (2016).
308. Wickman, H. H., Trozzolo, A. M., Williams, H. J., Hull, G. W. & Merritt, F. R. Spin-3/2 Iron Ferromagnet: Its Mössbauer and Magnetic Properties. *Phys. Rev.* **155**, 563–566 (1967).
309. Javier Tejada (auth.) Juan Bartolomé, F. L. J. F. F. e. *Molecular Magnets: Physics and Applications* 1st ed. (Springer-Verlag Berlin Heidelberg, 2014).
310. Benelli, C. Introduction to Molecular Magnetism, 465.
311. Leuenberger, M. N. & Loss, D. Quantum computing in molecular magnets. *Nature* **410**, 789–793 (2001).
312. Sessoll, R. Magnetic bistability in a metal-ion cluster. **365**, 3 (1993).
313. Perlepe, P. *et al.* Metal-organic magnets with large coercivity and ordering temperatures up to 242°C. *Science* **370**, 587–592 (2020).
314. Mannini, M. *et al.* Magnetic memory of a single-molecule quantum magnet wired to a gold surface. *Nature Mater* **8**, 194–197 (2009).
315. Tsukahara, N. *et al.* Adsorption-Induced Switching of Magnetic Anisotropy in a Single Iron(II) Phthalocyanine Molecule on an Oxidized Cu(110) Surface. *Phys. Rev. Lett.* **102**, 167203 (2009).
316. Campbell, V. E. *et al.* Engineering the magnetic coupling and anisotropy at the molecule-magnetic surface interface in molecular spintronic devices. *Nat Commun* **7**, 13646 (2016).
317. Gatteschi, D. & Sessoli, R. Quantum Tunneling of Magnetization and Related Phenomena in Molecular Materials. *Angew. Chem. Int. Ed.* **42**, 268–297 (2003).

-
318. Mannini, M. *et al.* Quantum tunnelling of the magnetization in a monolayer of oriented single-molecule magnets. *Nature* **468**, 417–421 (2010).
319. Wende, H. *et al.* Substrate-induced magnetic ordering and switching of iron porphyrin molecules. *Nature Mater* **6**, 516–520 (2007).
320. Liu, B. *et al.* An Iron-Porphyrin Complex with Large Easy-Axis Magnetic Anisotropy on Metal Substrate. *ACS nano* **11** **11**, 11402–11408 (2017).
321. Rolf, D., Lotze, C., Czekelius, C., Heinrich, B. W. & Franke, K. J. Visualizing Intramolecular Distortions as the Origin of Transverse Magnetic Anisotropy. *J. Phys. Chem. Lett.* **9**, 6563–6567 (2018).
322. Orbach, R. On the Theory of Spin-Lattice Relaxation in Paramagnetic Salts. *Proceedings of the Physical Society* **77**, 821–826 (1961).
323. Neese, F. & Pantazis, D. A. What is not required to make a single molecule magnet. *Faraday Discuss.* **148**, 229–238 (2011).
324. Chilton, N. F., Anderson, R. P., Turner, L. D., Soncini, A. & Murray, K. S. PHI: A powerful new program for the analysis of anisotropic monomeric and exchange-coupled polynuclear *d* - and *f* -block complexes. *J. Comput. Chem.* **34**, 1164–1175 (2013).
325. Zhang, L. *et al.* Anomalous light induced spin state switching for Fe^{II} spin-crossover molecules in direct contact with metal surfaces. *Angewandte Chemie International Edition* **59**, 13341–13346 (2020).
326. Piamonteze, C., Miedema, P. & de Groot, F. M. F. Accuracy of the spin sum rule in XMCD for the transition-metal L edges from manganese to copper. *Phys. Rev. B* **80**, 184410 (2009).
327. Angeli, C., Cimiraglia, R. & Malrieu, J.-P. N-electron valence state perturbation theory: a fast implementation of the strongly contracted variant. *Chemical Physics Letters* **350**, 297–305 (2001).
328. Angeli, C., Cimiraglia, R. & Malrieu, J.-P. *n* -electron valence state perturbation theory: A spinless formulation and an efficient implementation of the strongly contracted and of the partially contracted variants. *The Journal of Chemical Physics* **117**, 9138–9153 (2002).
329. Neese, F. Efficient and accurate approximations to the molecular spin-orbit coupling operator and their use in molecular g-tensor calculations. *The Journal of Chemical Physics* **122**, 034107 (2005).
330. Pantazis, D. A., Chen, X.-Y., Landis, C. R. & Neese, F. All-Electron Scalar Relativistic Basis Sets for Third-Row Transition Metal Atoms. *J. Chem. Theory Comput.* **4**, 908–919 (2008).
331. Maurice, R. *et al.* Universal Theoretical Approach to Extract Anisotropic Spin Hamiltonians. *J. Chem. Theory Comput.* **5**, 2977–2984 (2009).

332. Atanasov, M., Ganyushin, D., Pantazis, D. A., Sivalingam, K. & Neese, F. Detailed Ab Initio First-Principles Study of the Magnetic Anisotropy in a Family of Trigonal Pyramidal Iron(II) Pyrrolide Complexes. *Inorganic Chemistry* **50**, 7460–7477 (2011).
333. Atanasov, M., Zadrozny, J. M., Long, J. R. & Neese, F. A theoretical analysis of chemical bonding, vibronic coupling, and magnetic anisotropy in linear iron(II) complexes with single-molecule magnet behavior. *Chem. Sci.* **4**, 139–156 (2013).
334. Gomez-Coca, S., Cremades, E., Aliaga-Alcalde, N. & Ruiz, E. Mononuclear Single-Molecule Magnets: Tailoring the Magnetic Anisotropy of First-Row Transition-Metal Complexes. *J. Am. Chem. Soc.* **135**, 7010–7018 (2013).
335. Ruamps, R. *et al.* Origin of the Magnetic Anisotropy in Heptacoordinate Ni^{II} and Co^{II} Complexes. *Chem. Eur. J.* **19**, 950–956 (2013).
336. Feng, X. *et al.* Tristability in a Light-Actuated Single-Molecule Magnet. *J. Am. Chem. Soc.* **135**, 15880–15884 (2013).
337. Bogani, L. & Wernsdorfer, W. Molecular spintronics using single-molecule magnets. *Nanoscience and Technology* **7**, 8 (2009).
338. Djeghloul, F. *et al.* Direct observation of a highly spin-polarized organic spinterface at room temperature. *Sci Rep* **3**, 1272 (2013).
339. Djeghloul, F. *et al.* Highly spin-polarized carbon-based spinterfaces. *Carbon* **87**, 269–274 (2015).
340. Auwärter, W., Écija, D., Klappenberger, F. & Barth, J. V. Porphyrins at interfaces. *Nature Chem* **7**, 105–120 (2015).
341. Lodi Rizzini, A. *et al.* Coupling Single Molecule Magnets to Ferromagnetic Substrates. *Phys. Rev. Lett.* **107**, 177205 (2011).
342. Klar, D. *et al.* Oxygen-tuned magnetic coupling of Fe-phthalocyanine molecules to ferromagnetic Co films. *Phys. Rev. B* **88**, 224424 (2013).
343. Klar, D. *et al.* Antiferromagnetic coupling of TbPc₂ molecules to ultrathin Ni and Co films. *Beilstein J. Nanotechnol.* **4**, 320–324 (2013).
344. Malavolti, L. *et al.* Magnetism of TbPc₂ SMMs on ferromagnetic electrodes used in organic spintronics. *Chem. Commun.* **49**, 11506 (2013).
345. Lodi Rizzini, A. *et al.* Exchange Biasing Single Molecule Magnets: Coupling of TbPc₂ to Antiferromagnetic Layers. *Nano Lett.* **12**, 5703–5707 (2012).
346. Lodi Rizzini, A. *et al.* Coupling of single, double, and triple-decker metal-phthalocyanine complexes to ferromagnetic and antiferromagnetic substrates. *Surface Science* **630**, 361–374 (2014).
347. Avvisati, G. *et al.* Ferromagnetic and Antiferromagnetic Coupling of Spin Molecular Interfaces with High Thermal Stability. *Nano Lett.* **18**, 2268–2273 (2018).
348. Avvisati, G. *et al.* Superexchange pathways stabilize the magnetic coupling of MnPc with Co in a spin interface mediated by graphene. *Phys. Rev. B* **98**, 115412 (2018).

-
349. Avvisati, G., Gargiani, P., Mariani, C. & Betti, M. G. Tuning the Magnetic Coupling of a Molecular Spin Interface via Electron Doping. *Nano Lett.* **21**, 666–672 (2021).
350. Xiong, Z. H., Wu, D., Vardeny, Z. V. & Shi, J. Giant magnetoresistance in organic spin-valves. **427**, 4 (2004).
351. Annese, E., Casolari, F., Fujii, J. & Rossi, G. Interface magnetic coupling of Fe-phthalocyanine layers on a ferromagnetic surface. *Phys. Rev. B* **87**, 054420 (2013).
352. Baldo, M. A. & Forrest, S. R. Interface-limited injection in amorphous organic semiconductors. *Phys. Rev. B* **64**, 085201 (2001).
353. Petta, J. R., Slater, S. K. & Ralph, D. C. Spin-Dependent Transport in Molecular Tunnel Junctions. *Phys. Rev. Lett.* **93**, 136601 (2004).
354. Kasuya, T. A Theory of Metallic Ferro- and Antiferromagnetism on Zener's Model. *Progress of Theoretical Physics* **16** (1956).
355. Yosida, K. Magnetic Properties of Cu-Mn Alloys. *Phys. Rev.* **106**, 893–898 (1957).
356. Ruderman, M. A. & Kittel, C. Indirect Exchange Coupling of Nuclear Magnetic Moments by Conduction Electrons. *Phys. Rev.* **96**, 99–102 (1954).
357. Haag, N *et al.* Epitaxial growth of thermally stable cobalt films on Au(111). *New J. Phys.* **18**, 103054 (2016).
358. Kisielewski, M. *et al.* Magnetic Domains and Anisotropy in Ultrathin Au/Co/Au Wedges Deposited on Mica Substrates. *phys. stat. sol. (a)* **189**, 929–933 (2002).
359. Gentner, T., Scheurer, F., Detzel, T. & Bucher, J. in *Small Scale Structures* 58–60 (Elsevier, 1996).
360. Wawro, A *et al.* The growth modes of epitaxial Au/Co/Au sandwiches. *Thin Solid Films*, 4 (2002).
361. Padovani, S, Scheurer, F & Bucher, J. P. Burrowing self-organized cobalt clusters into a gold substrate. *Europhys. Lett.* **45**, 327–333 (1999).
362. Holloway, P. H. Thickness determination of ultrathin films by Auger electron spectroscopy. *Journal of Vacuum Science and Technology* **12**, 1418 (1975).
363. Powell, C. J. & Jablonski, A. Evaluation of Calculated and Measured Electron Inelastic Mean Free Paths Near Solid Surfaces. *Journal of Physical and Chemical Reference Data* **28**, 19–62 (1999).